

**ADVANCED KALMAN FILTERING WITH APPLICATIONS
TO POWER SYSTEM AND EPIDEMIOLOGICAL
DATA ANALYSIS**

Ph.D. Thesis

by

SUMANTA KUMAR NANDA



**DEPARTMENT OF ELECTRICAL ENGINEERING
INDIAN INSTITUTE OF TECHNOLOGY INDORE
May 2023**

Advanced Kalman Filtering with Applications to Power System and Epidemiological Data Analysis

A THESIS

*Submitted in partial fulfillment of the
requirements for the award of the degree*

of

DOCTOR OF PHILOSOPHY

by

SUMANTA KUMAR NANDA



**DEPARTMENT OF ELECTRICAL ENGINEERING
INDIAN INSTITUTE OF TECHNOLOGY INDORE**

May 2023



INDIAN INSTITUTE OF TECHNOLOGY INDORE

CANDIDATE'S DECLARATION

I hereby certify that the work which is being presented in the thesis entitled “**Advanced Kalman Filtering with Applications to Power System and Epidemiological Data Analysis**” in the partial fulfillment of the requirements for the award of the degree of DOCTOR OF PHILOSOPHY and submitted in the DEPARTMENT OF ELECTRICAL ENGINEERING, Indian Institute of Technology Indore, is an authentic record of my own work carried out during the time period from June 2019 to May 2023 under the supervision of Dr. Abhinoy Kumar Singh and Prof. Vimal Bhatia, Indian Institute of Technology Indore, India.

The matter presented in this thesis has not been submitted by me for the award of any other degree of this or any other institute.

Sumanta Kumar Nanda
Signature of the student with date 06/12/23
(SUMANTA KUMAR NANDA)

This is to certify that the above statement made by the candidate is correct to the best of our knowledge.

Dr. Abhinoy Kumar Singh
Signature of Thesis Supervisor with date 06/12/2023
(Dr. Abhinoy Kumar Singh)

Prof. Vimal Bhatia
Signature of Thesis Supervisor with date
(Prof. Vimal Bhatia)

Sumanta Kumar Nanda has successfully given his Ph.D. Oral Examination held on

Dr. Abhinoy Kumar Singh
Signature of Thesis Supervisor with date 06/12/2023
(Dr. Abhinoy Kumar Singh)

Prof. Vimal Bhatia
Signature of Thesis Supervisor with date 06/12/2023
(Prof. Vimal Bhatia)

ACKNOWLEDGEMENTS

My life has been filled with some of the best moments in the last four years. Over the course of this period, I have received support and encouragement from many people. The completion of this thesis would not have been possible without the patience and support of these individuals. I would like to extend my sincere gratitude to them. Firstly, I would like to express my deepest gratitude to my supervisors, Dr. Abhinoy Kumar Singh and Prof. Vimal Bhatia, for their excellent guidance, constant support, and positive encouragement over the years. I am truly thankful to them for spending their valuable time on my thesis work. From my supervisors, in addition to learning the technical aspects of my research, I also learned how to be positive during the research. My appreciation goes out to their patient mentoring and the wealth of knowledge they have imparted, not just in solving challenging problems but in writing and presenting papers clearly.

Furthermore, I am grateful to Dr. Taraknath Kobaku, for his insightful comments on research works. I would also like to thank my PSPC committee members Prof. Anand Parey, Prof. Amod C. Umarikar, Prof. Abhirup Datta, for their fruitful discussions and suggestions for my research. I extend my gratitude to Prof. Trapti Jain for generously granting access to the Smart Grid Research Facility. This facility is financially supported by the Department of Science and Technology (D.S.T), New Delhi, India, under the DST-FIST program SR/FST/ETI-400.

I am also thankful to my stochastic control system lab members, Guddu Kumar, Amit Kumar Naik, Yamalakonda Venu Gopal, and colleagues Adnan Iqbal, Suhel Khan, and Suvamit Chakraborty for their support. Finally, but by no means least, I dedicate this thesis to my family. In particular, special and sincere thanks to my parents for their continuous and unconditional support and love throughout my life. Thanks to my companion Dr. Somashree Pathy, for her continuous support and endless sacrifices. Completing this thesis was easier with her love and understanding. I also wish to acknowledge my parents-in-law for their selfless love and support.

SUMANTA KUMAR NANDA

Dedicated

to

My family and beloved late mother

ABSTRACT

Estimation is a popular computational tool for determining the internal states of a dynamical system from noisy measurements. A recursive process of estimation is called filtering. The conceptual filtering solution is obtained using unknown probability density functions (PDF). Several analytical filtering solutions have been presented in the literature by characterizing the unknown PDFs differently. The popularly known Kalman filter is an optimal analytical filter for linear dynamical systems. However, there is still a scope for exploring the development of an optimal nonlinear filter in the future. Thankfully, the popularly known Gaussian filtering provides a widely accepted suboptimal solution for nonlinear filtering problems. Some of the popular Gaussian filters are the extended Kalman filter (EKF), unscented Kalman filter (UKF), cubature Kalman filter (CKF), and cubature quadrature Kalman filter (CQKF).

This thesis mainly focuses on two directions: i) developing advanced filtering methods for handling various practical irregularities and ii) developing advanced power system state estimation (PSSE) methods for improving the PSSE accuracy in the monitoring of real-life power system networks. However, in the middle of the thesis work, the Covid-19 outbreak was witnessed, which was soon proved to be one of the deadliest pandemics of the last several centuries. Therefore, in the interest of scientific responsibility, a new research direction was chosen to develop an advanced algorithm for epidemiological state estimator (ESE) method.

In the first direction of the research, the use of state-of-art tools for data processing and transmission in modern filtering applications invites several irregularities in the measurement data. For example, cyber-physical systems, including communication channels and networks, often causes delays and invites cyber threats. Similarly, the noises are inherently non-Gaussian while ~~they are~~ forcefully assumed to be Gaussian. To handle various measurement irregularities, this thesis has two contributions, as follows: i) The thesis redesigns the linear Kalman filter for simultaneously handling the problems of the delay and non-Gaussian noises, and ii) the thesis redesigns the traditional nonlinear Gaussian filtering method for addressing the problems of jointly occurring delay and

cyber-attacks on the measurements.

The second focus of this thesis work is to utilize the knowledge of advanced filtering algorithms to enhance the efficacy of the state-of-art PSSE methods. Please note that the PSSE methods comprise a dynamical state space model of power system networks and estimation methods. The last decades have witnessed the applications of nonlinear Gaussian filters like EKF, UKF, and CKF for the PSSE. Moreover, parallel research is ongoing to utilize extensions of Gaussian filtering to handle various network uncertainties, including the lack of a precise state dynamical model, unknown noises, and non-Gaussian outliers. Considering these scopes of research, this thesis introduces two advancements in the PSSE methods, as discussed below: i) The accuracy of PSSE is improved by utilizing an advanced Gaussian filter named CQKF for estimating the dynamical states of the power system networks, ii) An advanced PSSE method is developed for addressing various uncertainties and irregularities in power system networks, including the lack of a precise state dynamical model, unknown noises, and non-Gaussian outliers

The third direction of this thesis is to contribute towards ESE algorithms for strengthening the fight against Covid-19. This direction of the research was the consequence of the scientific response that was observed at the time of Covid-19 outbreak across the world. In this direction, the thesis introduces an advanced ESE method composed of compartment-based pandemic models and nonlinear estimator. The proposed ESE method introduces a new compartment-based pandemic model and applies the CKF for estimating the compartment populations.

Contents

| | |
|---|-------------|
| ABSTRACT | i |
| LIST OF FIGURES | x |
| LIST OF TABLES | xiv |
| LIST OF ABBREVIATIONS | xvii |
| LIST OF SYMBOLS | xix |
| 1 Introduction | 1 |
| 1.1 Background | 1 |
| 1.2 Introduction to linear and nonlinear Kalman filtering | 4 |
| 1.2.1 Introduction to state space model | 5 |
| 1.2.2 Bayesian filtering framework | 6 |
| 1.3 Linear Kalman filter | 8 |
| 1.4 Nonlinear Gaussian filtering method | 10 |
| 1.5 Power system state estimator (PSSE) methodology | 13 |
| 1.5.1 Evolution of dynamic PSSE | 14 |
| 1.5.2 Methodology of hybrid measurement | 15 |
| 1.6 Epidemiological state estimator (ESE) methodology | 18 |
| 1.6.1 Agent-based epidemic modeling | 19 |
| 1.6.2 Compartment-based epidemic modeling | 19 |
| 1.7 Cyber-threats on measurement data | 20 |

| | | |
|----------|--|-----------|
| 1.8 | Motivation | 21 |
| 1.9 | Thesis objective | 22 |
| 1.10 | Approaches and methods | 23 |
| 1.10.1 | Model formulation | 23 |
| 1.10.2 | Design and selection of filters | 23 |
| 1.10.3 | Validation | 24 |
| 1.10.4 | Performance criteria | 24 |
| 1.11 | Contribution | 25 |
| 1.12 | Publications generated out of thesis work | 26 |
| 1.13 | Thesis organization | 27 |
| 2 | Literature Review | 29 |
| 2.1 | Gaussian Filtering | 29 |
| 2.1.1 | Derivative-based Gaussian filters | 30 |
| 2.1.2 | Derivative-free Gaussian filters | 31 |
| 2.2 | Filtering under various irregularities | 34 |
| 2.2.1 | Filtering with delayed measurements | 34 |
| 2.2.2 | Filtering with non-Gaussian noises | 35 |
| 2.2.3 | Filtering with cyber-attacked measurements | 36 |
| 2.3 | Power System state estimator | 37 |
| 2.3.1 | PSSE by ignoring various irregularities | 37 |
| 2.3.2 | PSSE with various real-life irregularities | 37 |
| 2.4 | Epidemiological state estimator | 38 |
| 2.5 | Summary | 39 |
| 3 | Kalman Filtering with Delayed Measurements in Non-Gaussian Environments | 43 |
| 3.1 | Modified Kalman filtering for delayed measurements and non-Gaussian noises | 45 |
| 3.1.1 | Prediction | 45 |
| 3.1.2 | Update | 46 |

| | | |
|----------|---|------------|
| 3.2 | Simulation and results | 56 |
| 3.2.1 | Example-1 | 57 |
| 3.2.2 | Example-2 | 62 |
| 3.3 | Discussion and conclusion | 64 |
| 4 | Gaussian Filtering with False Data Injection and Randomly Delayed Measurements | 71 |
| 4.1 | Introduction | 71 |
| 4.2 | Problem Description | 73 |
| 4.3 | Design methodology of GFDF | 76 |
| 4.4 | Stability of the GFDF | 81 |
| 4.5 | Simulation and Results | 85 |
| 4.5.1 | Example-1: Multiple sinusoids estimation | 86 |
| 4.5.2 | Example-2: Power system state estimation | 88 |
| 4.6 | Discussion and Conclusion | 93 |
| 5 | Dynamic State Estimation of Power System Using Forecasting-Aided Cubature Quadrature Kalman Filter | 95 |
| 5.1 | Introduction | 95 |
| 5.2 | Dynamic power system model | 96 |
| 5.3 | Forecasting-aided modified CQKF-based PSSE | 97 |
| 5.4 | Simulation and result | 102 |
| 5.4.1 | Case-1: Study of various benchmark electric power system under random voltage fluctuation. | 103 |
| 5.4.2 | Case-2: To study handling of sudden load change and temporary sensor failure | 106 |
| 5.5 | Discussion and conclusion | 108 |
| 6 | Self-Adaptive Forecasting-Aided Gaussian Filtering-based Power System State Estimation under non-Gaussian Outliers | 111 |
| 6.1 | Problem formulation | 113 |

| | | |
|----------|---|------------|
| 6.2 | FSMCGF-Based PSSE method | 115 |
| 6.2.1 | Prediction | 115 |
| 6.2.2 | Update | 116 |
| 6.3 | Simulation and result | 123 |
| 6.3.1 | Case-5: Consistency evaluation | 131 |
| 6.4 | Discussion and conclusion | 133 |
| 7 | Kalman-based Compartment Estimation for Covid-19 Pandemic using Advanced Epidemic Model | 136 |
| 7.1 | Compartment based SEIRRPV model for analyzing Covid-19 spread . . | 139 |
| 7.1.1 | Parameters involved in Covid-19 pandemic | 140 |
| 7.1.2 | Mathematical representation | 143 |
| 7.2 | Problem formulation | 146 |
| 7.3 | Mathematical analysis of the Proposed epidemic Model | 148 |
| 7.3.1 | Basic reproduction rate \mathcal{R}_0 | 151 |
| 7.3.2 | Sensitivity analysis \mathcal{S} | 153 |
| 7.3.3 | Stability analysis | 153 |
| 7.4 | Cubature Kalman filter (CKF)-based epidemic state estimator | 164 |
| 7.5 | Simulation and Results | 164 |
| 7.5.1 | Case-1: Vaccinated model validation through real-data of epidemic outbreak in Delhi caused by SARS-COV-2 virus | 166 |
| 7.5.2 | Case-2: Comparison with <i>SIR</i> family models | 168 |
| 7.6 | Discussion | 169 |
| 7.7 | Conclusion | 170 |
| 8 | Discussion and Conclusion | 172 |
| 8.1 | Discussion | 172 |
| 8.2 | Conclusion | 173 |
| 8.3 | Future Research Scope | 174 |
| A | Simplifying Eq. (3.23) in terms of Eq. (3.27) | 177 |

B Simplifying Eq. (6.15) in terms of Eq. (6.17) 179

C Analytical steps of filtering 180

D Innovation and residual covariance 182

 D.1 Innovation covariance 182

 D.2 Residual covariance 182

BIBLIOGRAPHY 184

List of Figures

| | | |
|------|---|----|
| 1.1 | A simple diagram for the Bayesian filtering framework | 7 |
| 1.2 | Schematic representation of recursive the Bayesian filter in each recursion. | 8 |
| 1.3 | A schematic diagram of power system grid. | 15 |
| 1.4 | π -port network model for power system. | 16 |
| 1.5 | A SIR epidemic model. | 20 |
| 3.1 | Flow chart for implementing the proposed extension of the Kalman filter for delayed measurements and non-Gaussian noises. Please note that $k = k + 1$ leads to a new iteration of estimation algorithm that finally leads to recursive state estimation. | 53 |
| 3.2 | Example-1: Comparison of true and estimated states obtained from MDKF for 1-delay and 0.3 probability of delay. | 59 |
| 3.3 | Example-1: RMSE plots for 1-delay with probability of delay 0.3. | 60 |
| 3.4 | Example-1: RMSE plots for 1-delay with probability of delay 0.5. | 60 |
| 3.5 | Example-1: RMSE plots for 2-delay with probability of delay 0.3. | 61 |
| 3.6 | Example-1: RMSE plots for 2-delay with probability of delay 0.5. | 61 |
| 3.7 | Example-1: Average RMSE plots for varying Gaussian coefficient (κ_g) with 1-delay and probability of delay 0.3. | 63 |
| 3.8 | Example-2: Comparison of true and estimated states obtained from MDKF for 1-delay and 0.3 probability of delay: (a) State-1 and (b) State-2. | 65 |
| 3.9 | Example-2: RMSE plots for 1-delay with probability of delay 0.3: (a) State-1 and (b) State-2. | 65 |
| 3.10 | Example-2: RMSE plots for 1-delay with probability of delay 0.5. | 66 |

| | | |
|------|---|-----|
| 3.11 | Example-2: RMSE plots for 2-delay with probability of delay 0.3. | 66 |
| 3.12 | Example-2: RMSE plots for 2-delay with probability of delay 0.5. | 67 |
| 3.13 | Example-2: Average RMSE plots for varying Gaussian coefficient (κ_g) with 1-delay and probability of delay 0.3. | 67 |
| 4.1 | Case 1: Average of RMSE comparison of CKF, MLCKF, CKF_FA, CKF_GD, and GFDF against varying delay probabilities. | 87 |
| 4.2 | Case 2: Average of RMSE comparison of CKF, MLCKF, CKF_FA, CKF_GD, and GFDF against varying delay probabilities. | 87 |
| 4.3 | IEEE 14 bus benchmark. | 90 |
| 4.4 | RMSE comparison of CKF, CKF_FA, CKF_GD, CKF_DM, and GFDF at Bus-9 for 0.3 delay probabilities. | 91 |
| 4.5 | RMSE comparison of CKF, CKF_FA, CKF_GD, CKF_DM, and GFDF at Bus-9 for 0.5 delay probabilities. | 92 |
| 5.1 | Modified CQKF-based PSSE algorithm. | 101 |
| 5.2 | Case-1: True and estimate plots at bus-9 (subscripts 14, 30, and 118 represent the 14-, 30-, and 118-bus networks, respectively): (a) Voltage magnitude V (p.u.) and (b) Phase angle δ (radian). | 104 |
| 5.3 | Case-1: MAE (in 10^{-2}) for voltage magnitude (V) and phase angle (δ) of all buses for the proposed (CQKF) and existing PSSE methods. The modified CQKF-base PSSE method voltage magnitude (V) shown in black color and phase angle (δ) shown in green color. | 105 |
| 5.4 | True and estimate plots at bus-9 of 14-bus under load changing and sensor failure condition. | 107 |
| 6.1 | Modified MC-based PSSE algorithm | 121 |
| 6.2 | Case-1: True and estimate plots at bus-9 (subscripts 14, 30, and 118 represent the 14-, 30-, and 118-bus networks, respectively). | 126 |

6.3 Case-2: MAE (in 10^{-3}) for voltage magnitude (V) and phase angle (δ) of all buses for the proposed (FSMCGF) and existing PSSE methods: (a) 14-bus, (b) 30-bus, and (c) 118-bus. **The proposed FSMCGF-base PSSE method voltage magnitude (V) shown in black color and phase angle (δ) shown in magenta color.** 128

6.4 Case-4: True and estimate plots at bus-2 for the sudden load change condition with non-Gaussian measurement. 132

6.5 Case-5: NEES plot for consistency evaluation for 14-bus. 133

7.1 Infection flow graph *SEIRRPV* epidemic model 145

7.2 Block diagram of *SEIRRPV* epidemic model. 146

7.3 Case-1: Estimates of different compartments in form of population ratio (a) infected compartment, (b) recovered people from infected compartment, (c) vaccinated people compartment. 167

7.4 Case-1: RMSE based performance comparison between *SEIRRPV* and *SIRV* model 168

7.5 Case-2: RMSE of different compartments by *SEIRRPV* model. 169

List of Tables

| | | |
|-----|---|-----|
| 3.1 | Example-1: 1-delay: Average RMSE of different filters as the delay probability varies. | 62 |
| 3.2 | Example-1: Correlation between the true and estimated states obtained for different filters with varying κ_g | 62 |
| 3.3 | Example-2: 1-delay: Average RMSE of different filters as the delay probability varies. | 64 |
| 3.4 | Example-2: Correlation between the true and estimated states obtained for different filters with varying κ_g | 64 |
| 3.5 | Computational time of the proposed MDKF with other existing filter, such as DKF, and KF. | 68 |
| 4.1 | α_k and β_k values for different attacks. | 75 |
| 4.2 | Relative computational time of the proposed GFDF with other existing filter, such as MLCKF, CKF_FA, CKF_GD, CKF | 88 |
| 4.3 | PMU and RTU measurements locations for the IEEE 14-bus benchmark power system networks. | 89 |
| 4.4 | Performance indices (in 10^{-3}) of the proposed GFDF-based PSSE with the existing benchmark filters obtained by averaging the voltage magnitude (\mathbf{V}) and phase angle δ across all buses. | 91 |
| 4.5 | Comparison of computational time for different filters. | 92 |
| 5.1 | PMU and RTU measurements locations for the considered IEEE 14-, 30-, and 118-bus power system networks. | 102 |

| | | |
|-----|---|-----|
| 5.2 | Case-1: Estimation error performance indices (in 10^{-5}) of the modified CQKF-based PSSE with the existing PSSEs obtained by averaging the voltage magnitude (V) and phase angle δ across all buses. | 105 |
| 5.3 | Case-2: Performance indices (in 10^{-3}) of all PSSEs obtained by averaging the voltage magnitude (V) and phase angle δ across all buses for 14-bus power system. | 107 |
| 6.1 | Case-3: Average of error performance (in 10^{-4}) and computational time (in ms) comparison for voltage (V) and phase angle (δ) of all buses. | 130 |
| 6.2 | Case-3: Comparison of average of MAEs for different PSSEs (in 10^{-3}) with Gaussian noise co-efficient κ_g for the states. | 130 |
| 6.3 | Case-3: Comparison of average of MAEs for different PSSEs (in 10^{-3}) with noise mis-assumption factor γ_Q and γ_R for the V , and δ states. | 131 |
| 7.1 | Epidemic parameters values considered. | 165 |
| 7.2 | Average % RMSE comparison of the <i>SEIRRPV</i> and <i>SIRV</i> model using real-data. | 166 |
| 7.3 | %RMSE for different models with 1000 Monte-Carlo simulations. | 168 |
| 7.4 | Sensitive index for different epidemic parameters | 169 |

List of Abbreviations

| | |
|---------|---|
| ACKF | Adaptive cubature kalman filter |
| AGF | Adaptive Gaussian filter |
| ARIMA | Auto-regressive integrated moving average |
| CPS | Cyber-physical system |
| CQKF | Cubature quadrature Kalman filter |
| DKF | Delayed Kalman filter |
| DPSSE | Dynamic Power System State Estimator |
| DSE | Dynamic State Estimator |
| EKF | Extended Kalman filter |
| ESE | Epidemiological State Estimator |
| FACQKF | Forecasting-aided Cubature quadrature Kalman filter |
| FAGF | Forecasting-aided Gaussian filter |
| FDI | False data injection |
| FSMCGF | Forecasting-aided self-adaptive maximum correntropy Gaussian filter |
| FSMCCKF | Forecasting-aided self-adaptive maximum correntropy cubature Kalman filter |
| GF | Gaussian filter |
| HPSSE | Hybrid power system state estimator |
| HSE | Hybrid state estimator |
| ICU | Intensive care units |
| KF | Kalman filter |
| LB | Lower bound |

| | |
|---------|---|
| MAE | Mean of absolute error |
| MAXE | Maximum absolute error |
| MC | Maximum correntropy |
| MDKF | Modified delayed Kalman filter |
| MMSE | Minimum mean square error |
| MSE | Mean square error |
| NASPI | North American Synchro-Phasor Initiative |
| NEES | Normalised estimation error squared |
| NPI | Non-pharmaceutical intervention |
| PDF | Probability density functions |
| PMU | Phasor measurement unit |
| PSSE | Power system state estimator |
| RMSE | Root mean square error |
| RTPCR | Real-time polymerase chain reaction |
| RTU | Remote terminal unit |
| SIR | Susceptible-infected-recovered |
| SIRP | Susceptible-infected-recovered-pass away |
| SEIRP | Susceptible-exposed-infected-recovered-pass away |
| SEIRRP | Susceptible-exposed-infected-recovered from exposed-recovered from infection-pass away |
| SEIRRPV | Susceptible-exposed-infected-recovered from exposed-recovered from infection-pass away-vaccinated |
| SCADA | supervisory control and data acquisition |
| SGA | Sage-Husa adaptive |
| SHAKF | Sage-Husa adaptive Kalman filter |
| SQKF | Szegő quadrature Kalman filter |
| UB | Upper bound |
| UKF | Unscented Kalman filter |
| WLS | Weighted least square |

List of Symbols

| | |
|--|--|
| \mathbf{x}_k | State variable |
| \mathbf{y}_k | Measurement variable |
| \mathbf{z}_k | Delayed Measurement variable |
| n | Dimension of state variable |
| m | Dimension of measurement variable |
| \mathbb{R} | n-dimensional column vector of all real numbers |
| $\mathbb{E}[\cdot]$ | Statistical expectation operator |
| $\mathcal{N}(\cdot)$ | Gaussian distribution |
| \mathbb{I} | Identity matrix |
| \mathcal{F} | Linear state transition matrix |
| \mathcal{H} | Linear measurement transition matrix |
| $\mathcal{f}(\cdot)$ | General nonlinear function of process model |
| $\mathcal{h}(\cdot)$ | General nonlinear function of measurement model |
| $\mathcal{h}^r(\cdot), \mathcal{h}^p(\cdot)$ | General nonlinear function of RTU, and PMU measurement model, respectively |
| $\mathbf{y}^r(\cdot), \mathbf{y}^p(\cdot)$ | General RTU, and PMU measurement model, respectively |
| $\mathbf{R}^r(\cdot), \mathbf{R}^p(\cdot)$ | General RTU, and PMU measurement noise covariances, respectively |
| t_k | k^{th} sampling instant |
| τ | Sampling interval |
| N_{int} | Number of intermediate instants between two immediate sampling instants |
| Δt | Time interval between two consecutive intermediate instants |
| Δ_k | False data injected at time T_k |

| | |
|--|--|
| N_{ru} | Number of intermediate instants between $t_k - \tau_d$ to t_k |
| \mathcal{B} | Generalized statistical measure |
| T | Number of time steps |
| M_c | Number of Monte-Carlo runs |
| \mathcal{Q}_k | Process noise |
| \mathcal{V}_k | Measurement noise |
| \mathbf{Q}_k | Covariance of process noise |
| \mathbf{R}_k | Covariance of measurement noise |
| \mathbf{K}_k | Kalman gain |
| \mathbf{P} | State error Covariance |
| \mathbf{V} | Per unit voltage magnitude state variable |
| δ | Voltage angle in radian state variable |
| ξ | Set of deterministic sample points |
| \mathbf{W} | Set of deterministic weights associated with sample points |
| N_s | Number of deterministic sample points |
| \mathbf{I}_n | n-dimensional identity matrix |
| $chol(\cdot)$ | Cholesky decomposition |
| $f_{\mathcal{Q}_k}, f_{\mathcal{V}_k}$ | PDF of state, and measurement noises, respectively $\hat{\mathbf{x}}_{k k}, \hat{\mathbf{x}}_{k k-1}$ are the estimated state and predicted state, respectively, at time t_k |
| $\mathbf{P}_{k k}, \mathbf{P}_{k k-1}$ | Estimated, and predicted error covariance, respectively at t_k |
| $\hat{\mathbf{y}}_{k k-1}, \hat{\mathbf{z}}_{k k-1}$ | Priori measurement under undelayed and delayed measurement, respectively |
| $\mathbf{P}_{k k-1}^{yy}$ | Measurement error covariance |
| $\mathbf{P}_{k k-1}^{xy}$ | Cross-covariance of state and measurement |
| \mathbf{S} | Measurement or innovation covariance |
| \mathbf{e} | Error value |
| σ | Kernel band-width |
| L, \mathcal{L} | Gaussian and maximum log-likelihood, respectively |
| $\mathbf{K}, \mathbf{C}, \hat{\mathbf{C}}$ | Gaussian Kernel, correntropy and Kernel estimator, respectively |

| | |
|--|--|
| J | Cost function |
| E_{rr}, χ | Second norm of error and threshold parameter for fixed-point iteration |
| N_b | Total number of buses in power network |
| N_r | Number of buses having RTUs |
| N_p | Number of buses having PMUs |
| $\mathbf{P}^i, \mathbf{Q}^i$ | Active and reactive power injected at a power bus |
| $\mathbf{P}^f, \mathbf{Q}^f$ | Active and reactive power flow between two different buses |
| G, B | Real and imaginary values of bus admittance matrix |
| g, b | Real and imaginary values of series branch admittance matrix |
| g_0, b_0 | Real and imaginary values of half shunt admittance matrix |
| $\mathbf{V}_r, \mathbf{V}_i$ | Real and imaginary values of voltage phasor variable |
| $\mathbf{I}_r, \mathbf{I}_i$ | Real and imaginary values of current phasor variable |
| $\epsilon_{k k-1}^x, \hat{\epsilon}_{k k-1}^x$ | Predictive and estimated state errors, respectively |
| $\epsilon_{k k-1}^y, \hat{\epsilon}_{k k-1}^y$ | Innovation and residual measurement |
| $\mathfrak{L}_k, \mathfrak{T}_k$ | Level factor and trend factor for smoothness |
| α_k, β_k | Bernoulli random variables |
| $G_{d,k}$ | Geometric random variable for modeling d -delay at time t_k |
| d | Maximum unknown delay |
| κ_g | Gaussian co-efficient |
| $\gamma_{\mathbf{Q}}, \gamma_{\mathbf{R}}$ | Noise mis-assumption factor |
| Δt | Time interval between two consecutive intermediate instants |
| (r, j) | A past instant $t = t_r + j\Delta t$ |
| $p_{(r,j)}$ | Probability of $\beta_{(r,j)} = 1$ |
| p | Probability of no delay |
| $\ \cdot\ $ | Norm |
| \mathcal{D}, \mathcal{W} | Estimated, and desire value state-measurement augmented model |
| $\mathbf{S}^p, \mathbf{S}^r$ | Cholesky decomposition of \mathbf{P} and \mathbf{R} , respectively |
| σ | Kernel width |

| | |
|-------------------------------|---|
| κ_g | Gaussian co-efficient |
| γ_Q | Adaptive process noise co-efficient |
| γ_R | Adaptive process noise co-efficient |
| L | Lyapunov function |
| Γ_i | Probability of i^{th} delay |
| Δ_k | Random false data is injected at time t_k |
| $\hat{\delta}, \Sigma_\delta$ | Mean and covariance of false data injection |
| (r, j) | A past instant $t = t_r + j\Delta t$ |
| p | Probability of no delay |
| $\ \cdot\ $ | Norm |
| α_e, α | Infection rate from exposed and infected compartments, respectively |
| β | Recovery rate |
| γ_e, γ | Reinfection rate |
| μ | Mortality rate |
| κ | Incubation rate |
| ρ | Recovery rate of exposed compartment |
| Ω | Vaccination rate |
| ν | Vaccination inefficacy rate |
| \mathcal{S} | Sensitivity |
| \mathcal{R} | Basic reproduction rate |
| sup | Supremum function |
| \mathbf{N}_g | Negative of next generation matrix |

Chapter 1

Introduction

1.1 Background

State estimation is a process of determining states (more specifically, hidden/latent states) from available noisy measurements [1][2][3]. A recursive process of state estimation is referred to as filtering. The estimation and filtering algorithms are of huge significance in various engineering domains of cyber-physical systems, including power systems [4][5], epidemiological transmission dynamics [6],[7], target tracking [2], network control and communication systems [8], space technology [9], fault diagnosis [10], biomedical system [11], robotics [12], industrial diagnosis and prognosis [13], navigation [14], financial modeling and monitoring [15], weather forecasting [16], *etc.* Kalman filter (KF) [3], developed in the 1960s, has been a leading tool for state estimation applications for the past fifty years. Hereafter, we will use the term ‘filtering,’ which may also refer to estimation.

The discussion on the evolution of filtering theory should start much before the Kalman filter, *e.g.*, the Wiener filtering [2],[17]. However, our discussion begins with Kalman filtering [3] since contemporary practitioners hardly choose to investigate the former developments (apart from the commonly known mean square estimator).

The Kalman filtering was traditionally developed for an extensively simplified problem formulation with the following significant simplifications: i) assuming a linear dynamical system, ii) Gaussian approximation of arbitrary and unknown noises, and iii) exceedingly flawless measurements [2],[18],[19].

Although the Kalman filter is limited to linear dynamical systems, the practical systems are inherently nonlinear [20]. A linear approximation of the inherently nonlinear dynamical systems can sometimes be sufficiently accurate for applying the Kalman filter. However, in many practical problems, such an approximation needs to be more accurate, rendering the application of Kalman filtering impractical. [21]. Similarly, the noises are naturally non-Gaussian, and a Gaussian approximation barely accurately characterizes the real noises, leading to poor accuracy [18],[22]. Conclusively, the first two simplifications mentioned above were well-known and understood in the filtering theory since the early days. Thus, after developing the KF, we observed some prompt attempts in the literature to address them. For example, a nonlinear extension of Kalman filter, named extended Kalman filter (EKF), was developed in the sixties, just a few years after the Kalman filter was developed. Similarly, we find some discussions [23] on non-Gaussian noises for a long time, although an efficient solution could be developed only a decade ago.

Unlike the first two challenges, such as the problems of nonlinear dynamical systems and non-Gaussian noises, the third challenge, *i.e.*, the problem of various measurement flaws, gradually evolved in the filtering problems. More specifically, this challenge developed with extensive using advanced tools and methodologies for data processing, propagation, transmission, *etc.* For instance, the development of cyber-physical systems drew practitioners' attention to their utility in data processing. However, using cyber-physical systems in data processing often influences delay. Similarly, data processing through cyber-physical systems invites the possibility of cyber-attacks [24][25]. Furthermore, the evolution of reliable networks and communication channels enabled the practitioners to transmit and propagate the measurement data before the estimator used it [26][27][28]. However, such transmission and propagation of measurement data influence the occurrences of missing measurements (*e.g.*, due to packet losses) and delay (*e.g.*, due to propagation time and queuing). Summarizing this discussion, we cite two particular measurement flaws or irregularities, including delays in measurements and cyber-attacks, evolving with extensive uses of advanced scientific

tools for data processing, propagation, and transmission. The possible increasing uses of internet-of-things (IoT) and clouds in the future may further generalize and intensify such problems. Thus, this is when we start attempting to develop advanced filtering algorithms to address these concerns.

This thesis aims to contribute to the three challenges mentioned earlier, including the problems of nonlinear dynamical systems, non-Gaussian noises, and various irregularities in measurement data. In this regard, the thesis first contributes to traditional Kalman filtering by redesigning it to address two irregularities simultaneously, including non-Gaussian noises and delay in measurement. Then, it studies the extensions of Kalman filtering for nonlinear dynamical systems. Subsequently, it redesigns the traditional nonlinear filtering method to handle two data irregularities simultaneously, including the cyber-attack and delay.

After contributing to advancing the linear and nonlinear filtering algorithms for handling various data irregularities, the thesis explores the practical applications of filtering and further contributes to the application side. Out of several practical applications of filtering, this thesis chooses to contribute to filtering applications in power systems. Within the power system, the author believes the power system state estimation (PSSE) is one of the most crucial applications of filtering. An efficient PSSE helps in the accurate monitoring of power grids, which, in turn, provides a key to a reliable energy management strategy. In the PSSE, the thesis contributes with two advancements, as discussed below.

- In one of the contributions, the thesis enhances the PSSE accuracy by implementing an advanced nonlinear filter, having better accuracy than the previously tested filters in the PSSE.
- In another contribution, the thesis introduces an advanced PSSE method to address the following drawbacks of the existing PSSE methods: i) arbitrary and ambiguous assignment of an unknown process model for PSSE, ii) Gaussian approximation of non-Gaussian measurement noises, and iii) inaccurate selection of arbitrary and unknown noises.

On a different note, the author would like to mention that the world witnessed one of the deadliest pandemics of the last century while the thesis work was ongoing. In the fight against this pandemic, the scientific communities across the world united and contributed with all their knowledge. The author also joined this fight with his limited knowledge, particularly the limited knowledge of filtering algorithms, considering it as his scientific responsibility. As a result, as a part of this thesis work, the author contributed by developing a compartment estimation algorithm, also known as the epidemiological state estimator (ESE) method, for a pandemic model. Interestingly, this contribution introduced a new pandemic model for ESE application, which fits into the scientific standards of the twenty-first century in the fight against the pandemic. An efficient ESE gives competent monitoring and prediction (to some extent) of the pandemic spread, which can further help frame the administrative strategies for curbing or slowing the Covid-19 spread.

Following the above discussions, in the coming parts of this chapter, we introduce the linear and nonlinear Kalman filtering methods, PSSE, and ESE methodology. Thereafter, we discuss the motivation, objective, approach, and contributions of this thesis. Finally, we highlight the publications generated out of this thesis and the thesis organization.

1.2 Introduction to linear and nonlinear Kalman filtering

The linear Kalman filter, as well as its nonlinear extensions, is a model-based computational tool that is implemented over a state space model. They are designed under the Bayesian filtering framework, consisting of prediction and update steps. The prediction and update steps obtain prior and posterior probability density functions (PDFs). The prior and posterior PDFs are assumed to be Gaussian during the filtering. In the linear Kalman filter, the Gaussian nature of PDFs is retained over time in linear Kalman filtering. However, in a simplified form of the Bayesian framework, called Gaussian filtering, the prior and posterior PDFs are assumed to be Gaussian at each time-step. Hereafter, we will often refer to the term ‘Gaussian filtering’ for ‘nonlinear Kalman filtering.’ In the subsequent parts of this section, we introduce the state space model, Bayesian framework, linear Kalman filter, and nonlinear Gaussian filtering

method.

Kalman filter is an optimal estimator method that uses a probabilistic approach to effectively filter out noises in the process and measurements model. It can handle incomplete state information and measurement information and still provide an accurate estimate of the unknown states. This feature of the Kalman filter makes it suitable for real-time state estimation or target tracking applications over other machine learning and artificial intelligence methods.

1.2.1 Introduction to state space model

Kalman filter is a model-based computational tool [2] that requires the state space model of dynamical systems. The state space model consists of the process and measurement models with the following descriptions:

- Process model: It characterizes the dynamical behavior of the states. Moreover, it consists of noises to compensate for the modeling errors of the true dynamics.
- Measurement model: It characterizes the mathematical relationship between the observed data and the unknown states. It additionally has a noise component to compensate for the observation errors, which may be due to device and data processing errors.

Considering the above descriptions, the general forms of the process and measurement models are either linear or nonlinear models [1][29]. A standard state space model for a linear dynamical system is given as follows:

Process model

$$\mathbf{x}_k = \mathcal{F}_{k-1}\mathbf{x}_{k-1} + \mathcal{Q}_{k-1}. \quad (1.1)$$

Measurement model

$$\mathbf{y}_k = \mathcal{H}_k\mathbf{x}_k + \mathcal{V}_k. \quad (1.2)$$

Where $\mathbf{x}_k \in \mathbb{R}^n$ with dimension n and $\mathbf{y}_k \in \mathbb{R}^m$ with dimension m are state and measurement vectors, respectively, at k^{th} instant, represented by t_k , i.e., $k \in \{0, 1, \dots, N\}$

with N being the number of time steps. \mathcal{F}_k and \mathcal{H}_k are constants with appropriate dimensions, while \mathcal{Q}_k and \mathcal{V}_k represent process and measurement noises, respectively.

If either process or measurement or both are non-linearly dependent, then the system is called a nonlinear dynamic system with the following state space model:

Process model

$$\mathbf{x}_k = \mathcal{F}_{k-1}(\mathbf{x}_{k-1}) + \mathcal{Q}_{k-1}. \quad (1.3)$$

Measurement model

$$\mathbf{y}_k = \mathcal{H}_k(\mathbf{x}_k) + \mathcal{V}_k. \quad (1.4)$$

where $\mathbf{x}_k \in \mathbb{R}^n$ and $\mathbf{y}_k \in \mathbb{R}^m$ are the state and measurement variables, respectively $\forall k \in \{1, 2, \dots\}$. Moreover, $\mathcal{F}_k: \mathbf{x}_{k-1} \rightarrow \mathbf{x}_k$ and $\mathcal{H}_k: \mathbf{x}_k \rightarrow \mathbf{y}_k$ denote general mathematical functions in a non-linear state-space model and carry constant values in linear dynamic systems, while \mathcal{Q}_k and \mathcal{V}_k represent the process and measurement noises, respectively.

To this end, the author defines the filtering objective as a recursive process of estimating the unknown states $\mathbf{x}_k \forall k \in \{1, 2, \dots\}$, as the measurement \mathbf{y}_k is sequentially received $\forall k \in \{1, 2, \dots\}$. Kalman filtering method is based on the Bayesian probabilistic approach to compute optimal state estimate.

1.2.2 Bayesian filtering framework

The objective of Bayesian filtering [2] framework is to determine the posterior PDF $P(\mathbf{x}_k | \mathbf{y}_{1:k})$ [21][30] using the dynamical system model. A simple diagram of the Bayesian framework is presented for understanding the Bayesian filtering framework in Fig. 1.1. This objective is achieved in two steps: prediction and update, as discussed below [20], [21],[31].

Prediction:

The prediction step determines the prior PDF $P(\mathbf{x}_k | \mathbf{y}_{1:k-1})$ to predict the desired state at the next time interval based on the current state estimate and the system model. In this

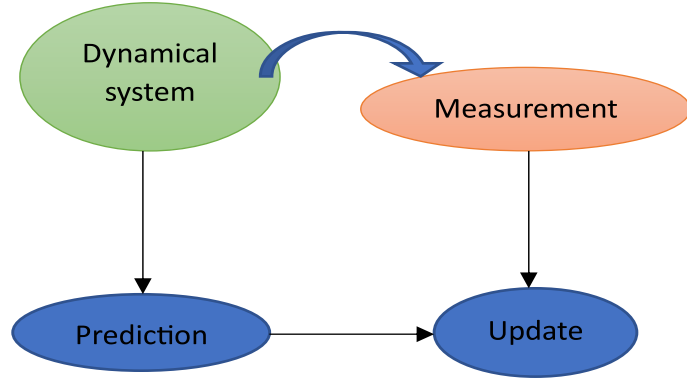


Figure 1.1: A simple diagram for the Bayesian filtering framework

regard, it utilizes the popularly known Chapman-Kolmogorov [18] equation, giving

$$P(\mathbf{x}_k|\mathbf{y}_{1:k-1}) = \int_{\mathbb{R}^n} P(\mathbf{x}_k|\mathbf{x}_{k-1})P(\mathbf{x}_{k-1}|\mathbf{y}_{1:k-1})d\mathbf{x}_{k-1}. \quad (1.5)$$

Update:

The update step obtains the desired posterior PDF $P(\mathbf{x}_k|\mathbf{y}_{1:k})$ by correcting the predicted PDF $P(\mathbf{x}_k|\mathbf{y}_{1:k-1})$ using the information received from the latest measurement \mathbf{y}_k , arriving at t_k [2][1]. In this regard, it applies the popularly known Baye's rule, which gives

$$P(\mathbf{x}_k|\mathbf{y}_{1:k}) = P(\mathbf{x}_k|\mathbf{y}_{1:k-1}, \mathbf{y}_k) = \frac{1}{\mathcal{E}_k} P(\mathbf{y}_k|\mathbf{x}_k)P(\mathbf{x}_k|\mathbf{y}_{1:k-1}), \quad (1.6)$$

where $P(\mathbf{y}_k|\mathbf{x}_k)$ is the measurement likelihood function and \mathcal{E}_k is a normalization constant, given as

$$\mathcal{E}_k = P(\mathbf{y}_k|\mathbf{y}_{1:k-1}) = \int_{\mathbb{R}^n} P(\mathbf{y}_k|\mathbf{x}_k)P(\mathbf{x}_k|\mathbf{y}_{1:k-1})d\mathbf{x}_k.$$

A schematic representation of the Bayesian filter is shown in Fig. 1.2. From Eqs. (1.3) and (1.4), it can be inferred that the probabilistic approach offered by the Bayesian filtering framework falls short in providing an analytical estimate of \mathbf{x}_k .

Hereafter, for better readability, the author considers the following notational

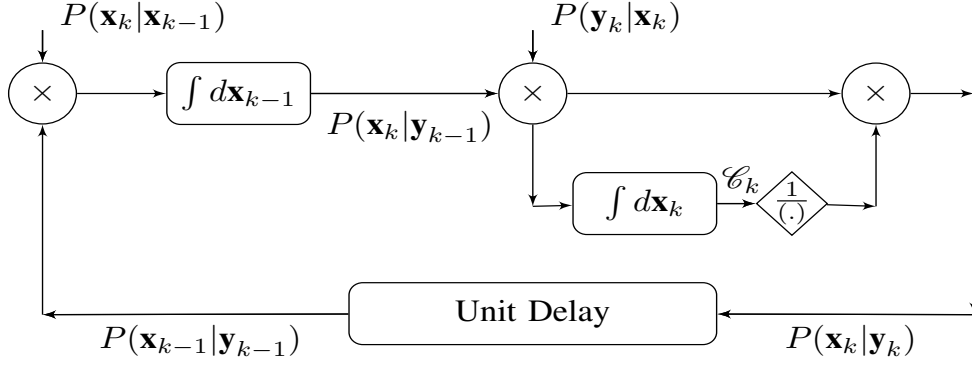


Figure 1.2: Schematic representation of recursive the Bayesian filter in each recursion.

simplicity: $P(\mathbf{x}_k | \mathbf{y}_{1:k-1})$ is denoted as $P(\mathbf{x}_{k|k-1})$, while $P(\mathbf{x}_k | \mathbf{y}_{1:k})$ is denoted as $P(\mathbf{x}_{k|k})$.

1.3 Linear Kalman filter

The linear Kalman filter recursively computes the optimal estimates using the dynamical system model and available noisy measurement while minimizing the mean square error. It implements the Bayesian filtering framework [3], which is based on Gaussian approximations of various PDFs and noises.

- Kalman filter approximates the various conditional PDFs that appeared in the Bayesian filtering as Gaussian, *i.e.*,

$$P(\mathbf{x}_{k|k-1}) \approx \mathcal{N}(\mathbf{x}_k; \hat{\mathbf{x}}_{k|k-1}, \mathbf{P}_{k|k-1}), \quad (1.7)$$

$$P(\mathbf{x}_{k|k}) \approx \mathcal{N}(\mathbf{x}_k; \hat{\mathbf{x}}_{k|k}, \mathbf{P}_{k|k}), \quad (1.8)$$

and

$$P(\mathbf{y}_{k|k-1}) \approx \mathcal{N}(\mathbf{y}_k; \hat{\mathbf{y}}_{k|k-1}, \mathbf{P}_{k|k-1}^{\mathbf{y}\mathbf{y}}), \quad (1.9)$$

where $\mathcal{N}(\cdot)$ represents the Gaussian distribution, whereas $\hat{\mathbf{x}}_{k|k-1}$, $\hat{\mathbf{x}}_{k|k}$, $\mathbf{P}_{k|k-1}$, and $\mathbf{P}_{k|k}$ denote the prior estimate, posterior estimate, prior covariance, and posterior covariance of \mathbf{x}_k , respectively, while $\hat{\mathbf{y}}_{k|k-1}$ and $\mathbf{P}_{k|k-1}^{\mathbf{y}\mathbf{y}}$ denote the predicted estimate and covariance of \mathbf{y}_k , respectively.

- The noises \mathcal{Q}_k and \mathcal{V}_k are assumed uncorrelated and approximated as zero-mean

Gaussian with covariances \mathbf{Q}_k and \mathbf{R}_k , respectively. Thus, we get $\mathbb{E}[\mathcal{Q}_k] = \mathbb{E}[\mathcal{Z}_k] = \mathbb{E}[\mathcal{Q}_k \mathcal{Z}_k^T] = 0$, $\mathcal{Q}_k \sim \mathcal{N}(0, \mathbf{R}_k)$ and $\mathcal{Z}_k \sim \mathcal{N}(0, \mathbf{Q}_k)$, where $\mathbb{E}[\cdot]$ denotes the statistical expectation operator, while $\mathbf{Q}_k = \mathbb{E}[\mathcal{Q}_k \mathcal{Q}_k^T]$ and $\mathbf{R}_k = \mathbb{E}[\mathcal{Z}_k \mathcal{Z}_k^T]$.

With the above approximations, [20] [21], the Kalman filter involves prediction and update steps. In prediction step, the filter predicts the current state estimate based on the previous state estimate and the system's dynamics model. In the following update step, optimal estimates are determined by employing the minimum mean square error method based on the available state prediction and the mismatch between actual and predicted measurements. The computational aspects for the Kalman filtering are discussed below.

Prediction

The objective is to compute the prior estimate and covariance, denoted as $\hat{\mathbf{x}}_{k|k-1}$ and $\mathbf{P}_{k|k-1}$, as [3], [2]

$$\begin{aligned}\hat{\mathbf{x}}_{k|k-1} &= \mathcal{F}_{k-1} \hat{\mathbf{x}}_{k-1|k-1} \\ \mathbf{P}_{k|k-1} &= \mathcal{F}_{k-1} \mathbf{P}_{k-1|k-1} \mathcal{F}_{k-1}^T + \mathbf{Q}_k,\end{aligned}\tag{1.10}$$

where $\hat{\mathbf{x}}_{k-1|k-1}$ and $\mathbf{P}_{k-1|k-1}$ are posterior estimates and covariance at a previous instant, i.e., $(k-1)^{th}$ instant.

Update

This step computes the posterior estimate and covariance [3], $\hat{\mathbf{x}}_{k|k}$ and $\mathbf{P}_{k|k}$, respectively. In this regard, it updates the prior estimate and covariance, $\hat{\mathbf{x}}_{k|k-1}$ and $\mathbf{P}_{k|k-1}$, respectively, using the noisy information of \mathbf{y}_k . However, the computation of $\hat{\mathbf{x}}_{k|k}$ and $\mathbf{P}_{k|k}$ requires the measurement estimate, a mismatch between actual and estimated measurement (innovation) and innovation covariance, denoted as $\hat{\mathbf{y}}_{k|k-1}$, $\boldsymbol{\varepsilon}_{k|k-1}^y$ and $\mathbf{P}_{k|k-1}^{yy}$, respectively, as well as the cross-covariance between the state and measurement, $\mathbf{P}_{k|k-1}^{xy}$. Therefore, before determining the desired $\hat{\mathbf{x}}_{k|k}$ and $\mathbf{P}_{k|k}$, $\hat{\mathbf{y}}_{k|k-1}$, $\boldsymbol{\varepsilon}_{k|k-1}^y$, $\mathbf{P}_{k|k-1}^{yy}$, and $\mathbf{P}_{k|k-1}^{xy}$ are determined as

$$\begin{aligned}
\hat{\mathbf{y}}_{k|k-1} &= \mathcal{H}_k \hat{\mathbf{x}}_{k|k-1} \\
\boldsymbol{\varepsilon}_{k|k-1}^y &= \mathbf{y}_k - \hat{\mathbf{y}}_{k|k-1} \\
\mathbf{P}_{k|k-1}^{yy} &= \mathcal{H}_k \mathbf{P}_{k|k-1} \mathcal{H}_k^T + \mathbf{R}_k \\
\mathbf{P}_{k|k-1}^{xy} &= \mathbf{P}_{k|k-1} \mathcal{H}_k^T.
\end{aligned} \tag{1.11}$$

Subsequently, $\hat{\mathbf{x}}_{k|k}$ and $\mathbf{P}_{k|k}$ are obtained as [2],[17]

$$\begin{aligned}
\hat{\mathbf{x}}_{k|k} &= \hat{\mathbf{x}}_{k|k-1} + \mathbf{K}_k \boldsymbol{\varepsilon}_{k|k-1}^y \\
\mathbf{P}_{k|k} &= (\mathbb{I} - \mathbf{K}_k \mathcal{H}_k) \mathbf{P}_{k|k-1} + \mathbf{K}_k \mathbf{R}_k \mathbf{K}_k^T,
\end{aligned} \tag{1.12}$$

where \mathbb{I} denotes an identity matrix, and \mathbf{K}_k represents the Kalman gain, given as $\mathbf{K}_k = \mathbf{P}_{k|k-1}^{xy} (\mathbf{P}_{k|k-1}^{yy})^{-1}$.

1.4 Nonlinear Gaussian filtering method

Nonlinear Gaussian filtering method As discussed, Gaussian filtering simplifies the Bayesian filtering and extension of Kalman filtering for nonlinear dynamical systems. The prediction and update steps for Gaussian filtering are discussed below.

Prediction:

Similar to linear Kalman filter, nonlinear Gaussian filtering computes the prior PDF using $\hat{\mathbf{x}}_{k|k-1}$ and $\mathbf{P}_{k|k-1}$, as [20],[21]

$$\hat{\mathbf{x}}_{k|k-1} \approx \int_{\mathbb{R}^n} \boldsymbol{\rho}_{k-1}(\mathbf{x}_{k-1}) \mathcal{N}(\mathbf{x}_{k-1}; \hat{\mathbf{x}}_{k-1|k-1}, \mathbf{P}_{k-1|k-1}) d\mathbf{x}_{k-1}, \tag{1.13}$$

$$\begin{aligned}
\mathbf{P}_{k|k-1} &= \mathbb{E}[(\mathbf{x}_k - \hat{\mathbf{x}}_{k|k-1})(\mathbf{y}_k - \hat{\mathbf{y}}_{k|k-1})^T] \\
&\approx \int_{\mathbb{R}^n} \boldsymbol{\rho}_{k-1}(\mathbf{x}_{k-1}) \boldsymbol{\rho}_{k-1}(\mathbf{x}_{k-1})^T \mathcal{N}(\mathbf{x}_{k-1}; \hat{\mathbf{x}}_{k-1|k-1}, \mathbf{P}_{k-1|k-1}) d\mathbf{x}_{k-1} \\
&\quad - (\hat{\mathbf{x}}_{k-1|k-1})(\hat{\mathbf{x}}_{k-1|k-1})^T + \mathbf{Q}_k.
\end{aligned} \tag{1.14}$$

Update:

Building upon the updating technique of the linear Kalman filter, this particular step involves the computation of the posterior estimate and covariance [20], [21], denoted as $\hat{\mathbf{x}}_{k|k}$ and $\mathbf{P}_{k|k}$, respectively. The computation of $\hat{\mathbf{x}}_{k|k}$ and $\mathbf{P}_{k|k}$ requires computing

measurement estimate, $\hat{\mathbf{y}}_{k|k-1}$, measurement covariance, $\mathbf{P}_{k|k-1}^{\mathbf{y}\mathbf{y}}$, and the cross-covariance between the state and measurement, $\mathbf{P}_{k|k-1}^{\mathbf{x}\mathbf{y}}$, which are obtained as

$$\hat{\mathbf{y}}_{k|k-1} = \mathbb{E}[(\mathbf{h}_k(\mathbf{x}_k) + \mathbf{v}_k) | \mathbf{y}_{1:k-1}] \approx \int_{\mathbb{R}^n} \mathbf{h}_k(\mathbf{x}_k) \mathcal{N}(\mathbf{x}_k; \hat{\mathbf{x}}_{k|k-1}, \mathbf{P}_{k|k-1}) d\mathbf{x}_k, \quad (1.15)$$

$$\begin{aligned} \mathbf{P}_{k|k-1}^{\mathbf{y}\mathbf{y}} &= \mathbb{E}[(\mathbf{y}_k - \hat{\mathbf{y}}_{k|k-1})(\mathbf{y}_k - \hat{\mathbf{y}}_{k|k-1})^T] \\ &\approx \int_{\mathbb{R}^n} \mathbf{h}_k(\mathbf{x}_k) \mathbf{h}_k(\mathbf{x}_k)^T \mathcal{N}(\mathbf{x}_k; \hat{\mathbf{x}}_{k|k-1}, \mathbf{P}_{k|k-1}) d\mathbf{x}_k - (\hat{\mathbf{y}}_{k-1|k-1})(\hat{\mathbf{y}}_{k-1|k-1})^T + \mathbf{R}_k, \end{aligned} \quad (1.16)$$

$$\begin{aligned} \mathbf{P}_{k|k-1}^{\mathbf{x}\mathbf{y}} &= \mathbb{E}[(\mathbf{x}_k - \hat{\mathbf{x}}_{k|k-1})(\mathbf{y}_k - \hat{\mathbf{y}}_{k|k-1})^T] \\ &\approx \int_{\mathbb{R}^n} \mathbf{x}_k \mathbf{h}_k(\mathbf{x}_k)^T \mathcal{N}(\mathbf{x}_k; \hat{\mathbf{x}}_{k|k-1}, \mathbf{P}_{k|k-1}) d\mathbf{x}_k - (\hat{\mathbf{x}}_{k|k-1})(\hat{\mathbf{y}}_{k|k-1})^T. \end{aligned} \quad (1.17)$$

Subsequently, $\hat{\mathbf{x}}_{k|k}$ and $\mathbf{P}_{k|k}$ are determined as

$$\hat{\mathbf{x}}_{k|k} = \hat{\mathbf{x}}_{k|k-1} + \mathbf{K}_k(\mathbf{y}_k - \hat{\mathbf{y}}_{k|k-1}), \quad (1.18)$$

$$\mathbf{P}_{k|k} = \mathbf{P}_{k|k-1} - \mathbf{K}_k \mathbf{P}_{k|k-1}^{\mathbf{y}\mathbf{y}} \mathbf{K}_k^T, \quad (1.19)$$

where \mathbf{K}_k denotes the Kalman gain [2], given as

$$\mathbf{K}_k = \mathbf{P}_{k|k-1}^{\mathbf{x}\mathbf{y}} (\mathbf{P}_{k|k-1}^{\mathbf{y}\mathbf{y}})^{-1}. \quad (1.20)$$

To this end, the non-linear Gaussian filtering [30] can be implemented through Eqs. (1.15) to (1.20). However, Eqs. (1.15) to (1.17) involve Gaussian weighted integrals of the form

$$I(\mathbb{F}) = \int_{\mathbb{R}^n} \mathbb{F}(\mathbf{x}) \mathcal{N}(\mathbf{x}; \hat{\mathbf{x}}, \mathbf{P}) d\mathbf{x}, \quad (1.21)$$

where \mathbf{x} is a random variable with mean $\hat{\mathbf{x}}$ and covariance \mathbf{P} , and $\mathbb{F} : \mathbb{R}^n \rightarrow \mathbb{R}^n$ is a simple function. The numerical methods used for integral approximation are generally defined for standard Gaussian, *i.e.*, for $\mathcal{N}(\mathbf{x}; \mathbf{0}_{n \times 1}, \mathbb{I}_n)$, with \mathbb{I}_n being an n -dimensional unit matrix and $\mathbf{0}_{n \times 1}$ being an n -dimensional array of all zero elements. The author denotes this integral as $I_0(\mathbb{F})$, *i.e.*,

$$I_0(\mathbb{F}) = \int_{\mathbb{R}^n} \mathbb{F}(\mathbf{x}) \mathcal{N}(\mathbf{x}; \mathbf{0}_{n \times 1}, \mathbb{I}_n) d\mathbf{x}. \quad (1.22)$$

The analytical solutions of such integrals exist for linear systems, having constant $\mathcal{f}_k : \mathbf{x}_{k-1} \rightarrow \mathbf{x}_k$ and $\mathcal{h}_k : \mathbf{x}_k \rightarrow \mathbf{y}_k$. Such a solution is popularly known as Kalman filter [3]. However, in the case of nonlinear systems, $\mathcal{f}_k : \mathbf{x}_{k-1} \rightarrow \mathbf{x}_k$ and $\mathcal{h}_k : \mathbf{x}_k \rightarrow \mathbf{y}_k$ (either or both) are nonlinear. Subsequently, the desired integral (Eq. (1.22)) appears in the form of a ‘*nonlinear function* \times *Gaussian distribution*,’ which is mostly intractable [17]. Consequently, the Gaussian filtering fails to accomplish an analytical solution. In this regard, two approaches are popular: the derivative-based Gaussian filtering [1] and derivative-free Gaussian filtering [20].

The nonlinear dynamics are locally linearized using the derivatives in the derivative-based Gaussian filtering. Subsequently, the linear Kalman filtering-based approach is applied. The readers may refer to [1],[17] for a detailed filtering algorithm for the derivative-based Gaussian filtering, popularly known as EKF. On the other hand, the derivative-free Gaussian filters utilize numerical methods for approximating $I_0(\mathbb{F})$ with the help of deterministically chosen sets of sample points and weights. Let us denote the sets of sample points and weights as $\boldsymbol{\xi}$ and \mathbf{W} , respectively. Then, $I_0(\mathbb{F})$ is approximated as

$$I_0(\mathbb{F}) \approx \sum_{i=1}^{N_s} \mathbf{W}_i \mathbb{F}(\boldsymbol{\xi}_i), \quad (1.23)$$

where N_s is the number of sample points, and $\boldsymbol{\xi}_i$ and $\mathbf{W}_i \forall i \in \{1, 2, \dots, N_s\}$ are the i^{th} sample point and weight, respectively. The same numerical method can be extended for $\mathcal{N}(\mathbf{x}; \hat{\mathbf{x}}, \mathbf{P})$ by transforming $\boldsymbol{\xi}$ with mean $\hat{\mathbf{x}}$ and covariance \mathbf{P} . Subsequently, the desired intractable integral $I(\mathbb{F})$ is approximated as

$$I(\mathbb{F}) \approx \sum_{i=1}^{N_s} \mathbf{W}_i \mathbb{F}(\hat{\mathbf{x}} + \boldsymbol{\Sigma} \boldsymbol{\xi}_i), \quad (1.24)$$

where $\boldsymbol{\Sigma} \boldsymbol{\Sigma}^T = \mathbf{P}$. The author refers to [20],[21],[17] for a detailed filtering algorithm of the derivative-free Gaussian filtering.

The conventional Kalman filter technique is an optimal estimator but relies on the assumption that measurements are received sequentially without any anomalies, such as i) delayed measurement [26], ii) false data injected in measurement [32][33], iii) unknown

or varying statistical noise information [19][34] and iii) non-Gaussian noise[35][36]. The traditional Kalman filter obtains the optimal state estimate by minimizing the mean square error cost function between the state prediction and sequential non-delayed measurements, assuming known statistical information on noise, *i.e.*, \mathbf{Q}_k and \mathbf{R}_k . Hence, delays, false data injection, or unknown noise statistics can harm the estimation accuracy. Furthermore, the conventional Kalman filter only captures up to second-order statistics, which can be inadequate for non-Gaussian distributions. Nonlinear state dynamics also face similar limitations, requiring extensions to the Kalman filter (for linear systems) and Gaussian filter (for nonlinear systems) to achieve accurate state estimation.

Despite above mentioned limitations, the Gaussian filtering is probably the most widely implemented nonlinear filtering method, as it provides a good trade-off between accuracy and computational demand. This thesis is solely focused on Gaussian filtering method whenever it comes to nonlinear filtering.

As discussed previously, the author also contribute to practical applications of Gaussian filtering, particularly in the PSSE design applications. Furthermore, as a scientific responsibility during the Covid-19 outbreak [38][39], the author also decided to contribute to ESE design applications using Gaussian filter to effectively monitor the spread of Covid-19. Thus, in the subsequent discussions, we also introduce the PSSE and ESE methods.

The above advantages encourage using Gaussian filters in complex networks, such as PSSE design applications and ESE design applications. When the Kalman filter is used for the said applications, there is still scope for modification in the filtering method for better estimation performance.

1.5 Power system state estimator (PSSE) methodology

The states of a power system describe its operating condition, including factors such as overload and overvoltage, by monitoring power flows through transmission lines, transformers, substations, and voltage readings at different nodes. From a mathematical standpoint, once the bus voltage magnitudes and phase angles are known, all these quantities can be computed. Therefore, the state of a power system can be defined as the

set of bus voltage magnitudes and phase angles [40][4][5].

1.5.1 Evolution of dynamic PSSE

With the help of power system state estimator, system operators can assess voltage magnitudes and angles at each power system bus bar using a limited number of available redundant raw measurement data, such as voltage, current, and power. Prof. F. Schweppe introduced the idea of state estimation at energy control centers of electric utilities and independent system operators (ISOs) in the 1970s [41],[42],[43].

A few buses have voltage and power meters to satisfy the observable conditions. These measurements are accessed from remotely located remote terminal units (RTU) to control centers using supervisory control and data acquisition (SCADA) technology [4]. Traditionally, PSSE was static before digitization. State estimation tools, such as the weighted least squares (WLS) method, were implemented to estimate the system states [41],[42],[43]. One measurement snap scan takes around 2-4 secs, and an offline WLS method takes approximately 10-15 secs for a single scan estimation [4][5]. However, such static PSSE methods suffered from several drawbacks, such as time skewness in RTU measurements and estimates lag from real-time values by several seconds. Consequently, the static PSSE can be more accurately stated as a tool for quasi-steady-state operating conditions.

The 2003 blackout in the northeastern United States of America and Canada [44] sparked interest in deploying Phasor Measurement Units (PMUs) in power systems. An investigation into blackouts conducted afterward determined that several factors led to the blackouts, including insufficient situational awareness, inefficient monitoring and control systems, and inability to perform transient state analysis of the power system parameters. In 2007, the north American synchro-phasor initiative (NASPI) was launched to promote using PMUs in the power industry [45].

PMUs are advanced measurement devices that provide time-synchronized and highly precise measurements of voltage and current phasors at high speeds, typically 30 to 60 data packets per second, even under fast sampling scenarios. This is a significant improvement over traditional SCADA systems, which are limited to one measurement per

second. The high-speed and precise measurements of PMUs help track the transients in the power system and enable the development of a dynamic power system state estimator (DPSSE), also known as the dynamic state estimator (DSE) method.

Although using Phasor Measurement Units (PMUs) in power systems is becoming popular, a power system equipped entirely with PMUs is likely to be less practical in the near future due to its high cost. As a result, there is a trend toward using a combination of RTUs and PMUs for generating the measurements. Such a power system state estimator is called a hybrid power system state estimator (HPSSE) or hybrid state estimator (HSE).

The present thesis implements both RTUs and PMUs for the PSSE, and from now on, we will use the term ‘PSSE’ for either ‘DPSSE’ or ‘HPSSE.’

1.5.2 Methodology of hybrid measurement

In the PSSE design applications, the state \mathbf{x}_k is an array of voltage magnitudes \mathbf{V}_k (p.u) and phase angles δ_k (radian) for all the bus-bars at time t_k [40]. A schematic representation of power system grid is shown in Fig. 1.3. It depicts that the measurement data packets from remotely located RTUs and time-synchronized PMUs are transmitted to the control center through a router.

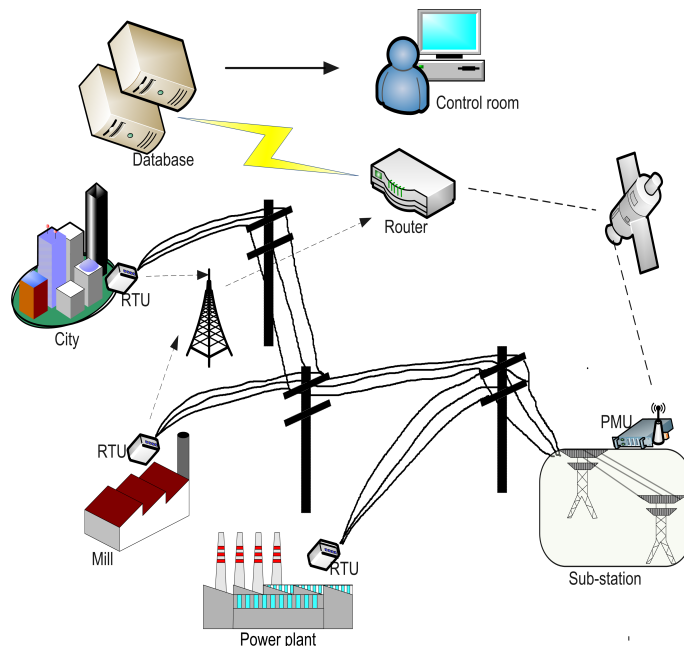


Figure 1.3: A schematic diagram of power system grid.

The measurements from RTUs and PMUs are discussed below:

Let us denote N_{br} and N_{bp} as the number of buses with RTUs and PMUs, respectively, out of N_b number of buses of a power network. Considering $l \in \{1, 2, \dots, N_{br}\}$ and $m \in \{1, 2, \dots, N_b\}$, the RTU sensors consist of the following: i) slack bus voltage magnitude \mathbf{V}_l , ii) active and reactive power injections at the l^{th} line, denoted as \mathbf{P}_l^i and \mathbf{Q}_l^i , respectively, and iii) active and reactive power flows between the l^{th} and m^{th} lines, denoted as $\mathbf{P}_{l,m}^f$ and $\mathbf{Q}_{l,m}^f$, respectively [4][5][46]. The RTU and PMU measurements are computed from the π -port network shown in Fig. 1.4 using Kirchoff's law as given below: The RTU

$$\begin{cases} \mathbf{V}_l = \sqrt{\mathbf{V}_{r,l}^2 + \mathbf{V}_{i,l}^2}, \\ \mathbf{P}_l^i = \mathbf{V}_{r,l} \sum_{l \in \mathbb{N}_l} (G_{lm} \mathbf{V}_{r,m} - B_{lm} \mathbf{V}_{i,m}) + \mathbf{V}_{i,l} \sum_{j \in \mathbb{N}_l} (G_{lj} \mathbf{V}_{i,j} + B_{lj} \mathbf{V}_{r,j}), \\ \mathbf{Q}_l^i = \mathbf{V}_{i,l} \sum_{l \in \mathbb{N}_l} (G_{lm} \mathbf{V}_{r,m} - B_{lm} \mathbf{V}_{i,m}) - \mathbf{V}_{r,l} \sum_{l \in \mathbb{N}_l} (G_{lm} \mathbf{V}_{i,m} + B_{lm} \mathbf{V}_{r,m}), \\ \mathbf{P}_{l,m}^f = (\mathbf{V}_{r,l}^2 + \mathbf{V}_{i,l}^2)(g_{lm_0} + g_{lm}) - \mathbf{V}_{r,l} \mathbf{V}_{r,m} g_{lm} - \mathbf{V}_{i,l} \mathbf{V}_{i,m} g_{lm} - \mathbf{V}_{i,l} \mathbf{V}_{r,m} b_{lm} + \mathbf{V}_{r,l} \mathbf{V}_{i,m} b_{lm}, \\ \mathbf{Q}_{l,m}^f = -(\mathbf{V}_{r,l}^2 + \mathbf{V}_{i,l}^2)(b_{lm_0} + b_{lm}) - \mathbf{V}_{i,l} \mathbf{V}_{r,m} g_{lm} + \mathbf{V}_{r,l} \mathbf{V}_{i,m} g_{lm} + \mathbf{V}_{r,l} \mathbf{V}_{r,m} b_{lm} + \mathbf{V}_{i,l} \mathbf{V}_{i,m} b_{lm}, \end{cases} \quad (1.25)$$

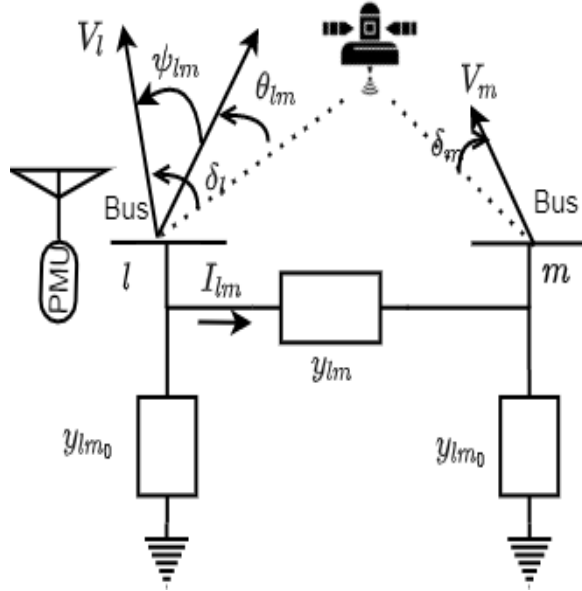


Figure 1.4: π -port network model for power system.

measurements data follow Eq. (1.25), where $G + jB$, $g + jb$, and $g_0 + jb_0$ represent the line parameters, particularly the bus admittance matrix, the admittance of series branch, and half shunt admittance, respectively. Similarly, the PMUs installed at buses $l_j \in$

$\{l_1, l_2, \dots, N_{bp}\}$ measure the voltage phasor ($\mathbf{V}_{r,l}$ and $\mathbf{V}_{i,l}$) and the current flows ($\mathbf{I}_r^{l,m}$ and $\mathbf{I}_i^{l,m}$) $\forall m \in \{1, 2, \dots, N_b\}$. Similar to the RTU models provided in Eq. (1.25), we get the PMU models as [47]

$$\begin{aligned}\mathbf{I}_r^{l,m} &= \mathbf{V}_{r,l} g_{l,m}^0 \mathbf{V}_{i,l} b_{l,m}^0 + (\Delta \mathbf{V}_r) g_{l,m} - (\Delta \mathbf{V}_i) b_{l,m}, \\ \mathbf{I}_i^{l,m} &= \mathbf{V}_{i,l} g_{l,m}^0 \mathbf{V}_{r,l} b_{l,m}^0 + (\Delta \mathbf{V}_i) g_{l,m} - (\Delta \mathbf{V}_r) b_{l,m}.\end{aligned}\tag{1.26}$$

where $l_j \in \{l_1, l_2, \dots, N_{bp}\}$, $m \in \{1, 2, \dots, N_b\}$, $\Delta \mathbf{V}_r = \mathbf{V}_{r,l} - \mathbf{V}_{r,m}$, and $\Delta \mathbf{V}_i = \mathbf{V}_{i,l} - \mathbf{V}_{i,m}$, with N_{bp} representing the number of buses having a PMU. Please note that the RTU and PMU buses may not be connected to all other buses. Thus, the corresponding values of m may be ignored, and the corresponding model equations of RTU and PMU may be neglected. Following the preceding discussions and employing Kirchhoff's laws over the π -port model [47][48], the RTU and PMU measurements are expressed as

$$\mathcal{R}^r = \left[\mathbf{V}_l | \mathbf{P}_l^i | \mathbf{Q}_l^i | \mathbf{P}_{l,m}^f | \mathbf{Q}_{l,m}^f \right],\tag{1.27}$$

$$\mathcal{R}^p = \left[\mathbf{V}_{r,l} | \mathbf{V}_{i,l} | \mathbf{I}_r^{l,m} | \mathbf{I}_i^{l,m} \right],\tag{1.28}$$

where \mathcal{R}^r and \mathcal{R}^p are the sub-operators of \mathcal{R} , denoting RTU and PMU measurements readings, respectively. Please note that the time index k has been removed to improve readability. Moreover, the superscripts i and f represent power injection and flow, respectively.

For PSSE, the measurement is received from PMUs and RTUs and processed through a router to a database as data packets. Please note that RTUs have different sample times from PMUs. As the PMU is faster, we consider the sample time of PSSE equal to the sample time of PMU. As part of the augmented dynamical operator \mathcal{R}_k , data is collected in packets from installed PMUs and from the latest available RTUs measurements at t_k time instant [4][49]. Hence, the overall measurement data *i.e.*, augmented \mathbf{y}_k , augments the RTU measurements \mathbf{y}_k^r and PMU measurements \mathbf{y}_k^p , giving $\mathbf{y}_k = [\mathbf{y}_k^r \ \mathbf{y}_k^p]^T$. Consequently, the dynamic operator \mathcal{R}_k is composed of the sub-operators \mathcal{R}_k^r and \mathcal{R}_k^p

for RTU measurements and PMU measurements, respectively. Similarly, the augmented measurement noise covariance is expressed as $\mathbf{R}_k = \text{diag}([\mathbf{R}_k^r \ \mathbf{R}_k^p])$, where \mathbf{R}_k^r and \mathbf{R}_k^p are the noise covariances of RTU and PMU measurements, respectively.

As mentioned above, for a stochastic control expert, the PSSE problem is a typical state estimation over the state space model particularly derived for power system networks. As we will see in the next chapter, the state-of-art PSSE methods utilize advanced nonlinear Gaussian filters like EKF, UKF, and CKF in [46],[49], and [48]. As we will conclude in the coming chapter, EKF, UKF, and CKF are not the most accurate state estimation methods. Thus, improving the PSSE accuracy by replacing the EKF, UKF, and CKF with their more accurate alternatives is possible.

In addition to the above discussion, the growing usage of electric vehicles, traction loads, and distributed energy resources (DERs), such as solar, wind, and others, introduce harmonics and frequent load fluctuations into the grid. As a result, the contemporary power grids are highly unpredictable and do not follow a deterministic model. Consequently, real-time monitoring and control of power systems are critical for efficient energy management to ensure a secure, reliable, and stable power delivery.

1.6 Epidemiological state estimator (ESE) methodology

Unlike power systems, the models for dynamics of biological processes, such as the transmission of a new pandemic, is not well established. Consistent effort still ongoing to achieve models that sufficiently characterize the dynamics [6][50],[51],[52],[53][54],[55]. As a scientific responsibility, this thesis models highly contagious Coronavirus epidemics to monitor, identify, and suggest strategic measures to the government agencies that may be needed to combat the virus. Our contribution is timely as the world is directly or indirectly affected by the Covid-19 pandemic. Policymakers encourage scientific research and knowledge-based analyses and conclusions to help make policy decisions that can help contain the pandemic. A mathematical model for an epidemic is generally classified as i)an agent-based epidemic model and ii) a compartment-based epidemic model. We provide more details about the two model classes in the subsequent discussions.

1.6.1 Agent-based epidemic modeling

Under agent-based epidemic modeling, we consider every individual in the population as a separate agent and monitor the individuals interaction with other individuals over time as an agent. The models under this category are generally complex and computationally inefficient. They can capture the heterogeneity of individual behavior and the influences of social networks between its population [56][57]. Such models also consider spatial heterogeneity and individual differences in susceptibility and behavior. However, such models are complex and data-sensitive.

1.6.2 Compartment-based epidemic modeling

The compartment-based epidemic model categorizes the total population into different compartments based on the infection level in individuals. The model tracks the flow of individuals between two compartments and the number of individuals in each compartment over time. The most elementary model of compartmental based epidemic model is SIR model [6]. Using this model, each individual is classified into one of three compartments based on their disease status, such as susceptible (S), infected (I), and recovered (R). A simple diagram of the *SIR* model is shown in Fig. 1.5. Later developments under this category of models have mostly been an extension of SIR epidemic model. Thus compartment-based epidemic model is popularly known as SIR-family of epidemic modeling. A few advanced models diversified the traditional SIR models by introducing compartments like exposed (E), vaccinated (V), and by further segmenting the recovered compartment into recovered from asymptomatic infection (R_e) and recovered from symptomatic infection (R) compartments, which, in their abbreviated forms, are named as *SIRP* [54],[55] *SEIR* [58], *SEIRP* [59], *SEIRRP* [60], *SIRV* [61] epidemic models, respectively. Please note that the model involves both R_e and R. The first R in model abbreviation stands for R_e , following by the recovered from infected compartment R.

Developing a mathematical model that considers various disease-influencing parameters is crucial to simulate real-world epidemic scenarios accurately. Such a model can be used to estimate and analyze the impact and consequences of various

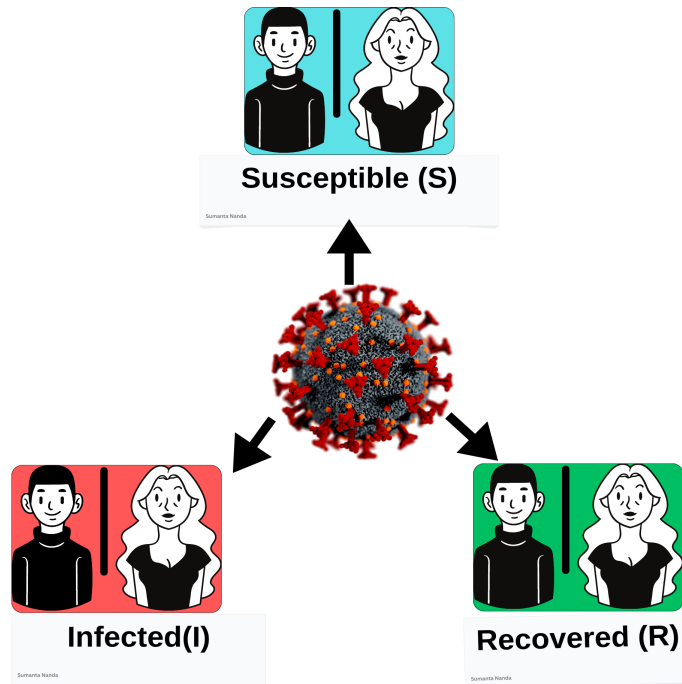


Figure 1.5: A SIR epidemic model.

government decisions on containing the transmission of the epidemic. Additionally, this enables decision-makers and government agencies to conduct a comparative analysis to determine whether implementing a particular decision is justifiable from a socio-economic perspective.

The simplicity, robustness, and computational efficiency of compartment-based epidemic model make it popular among researchers for tracking the disease dynamics of highly contagious diseases, such as Covid-19 pandemic. Thus, our research focuses on contributing to the compartment-based epidemic modeling itself.

1.7 Cyber-threats on measurement data

The modern way of dealing with data often involves cyber-physical systems, which generally integrate physical systems with intelligent communication infrastructure and embedded software. Often, state-of-the-art control systems incorporate a wireless communication network to transfer measurement data from geographically distant sensors (or other measuring devices) to the remote estimator [62]. However, these components may have inherent threats and vulnerabilities, rendering them susceptible to

malicious exploitation and manipulation by cyber-attackers. Thus, risk identification has emerged as a critical task in counteracting cyber-attacks. The cyber-attacker, or intruder, often inducts false measurement data into the advanced sensors to adversely affect the estimator's performance. As cyber-attack manipulates the measurements with false data injection (FDI), we often call it an FDI attack. We will frequently use the term "FDI attack" to refer to the cyber-attack.

Although we have cyber-security methods and systems developed, we may not trust them to overrule the FDI attacks completely. Thus, the futuristic filters should be competently robust to address the FDI attacks.

While Gaussian filtering has a broad spectrum of applications, the efficacy of the estimator can be adversely affected in the presence of system irregularities, such as erroneous measurements (delayed or missing or non-Gaussian or falsely injected data), ill-defined physical process model and non-Gaussian process noise.

1.8 Motivation

Following the previous discussions, we identify the following motivations for this thesis work.

- As discussed previously, the state-of-the-art filtering problems often witness measurement irregularities, such as delay measurements and non-Gaussian noises. Thus, an advanced Kalman filter is required for handling contemporary filtering problems and should be robust enough to handle such irregularities.
- The traditional nonlinear Gaussian filtering method ignores the delay and cyber-attack, while such measurement irregularities are often likely to appear in state-of-the-art filtering applications that involve cyber-physical systems for processing and transmitting the measurement data.
- The increased usage of electric vehicles, traction loads, and distributed energy resources (DERs) has made the power grid highly unpredictable, with a scenario that randomly changes and does not follow a deterministic model. Therefore, accurate PSSE must incorporate sudden and random changes in loading conditions.

- An actual power grid witnesses various irregularities, including temporal failures of one or more sensors, non-Gaussian outliers, and unknown statistical information about noises. The existing PSSE failed to address these irregularities collectively.
- While pursuing the research for this thesis, the world witnessed the outbreak of one of the deadliest pandemic of the last several centuries in terms of Covid-19. The heartbreaking chaos worldwide strongly motivated beyond the planned framework for the thesis and contributed to the fight against Covid-19. While a section of the scientific community with specific expertise was busy developing medicines and vaccines for containing Covid-19, reducing the pandemic's spread rate was necessary to minimize the losses before medicines and vaccines were developed. Henceforth, it was necessary to have efficient analytical methods to help the administrative authorities frame efficient strategies to reduce the rate of spread.

1.9 Thesis objective

The author outlines the following objectives for this thesis based on the above discussed motivations.

- Develop an advanced Kalman filtering algorithm for handling two measurement irregularities together, particularly the delay in measurement and non-Gaussian noises.
- Redesigning the traditional nonlinear Gaussian filtering method for simultaneously addressing unknown delays (in measurements) and cyber-attacks (on measurement systems).
- Introducing a new PSSE technique by replacing the contemporary estimators with a relatively more accurate estimator.
- Developing a robust PSSE to address non-Gaussian outliers along with the noise adaptivity.

- As a scientific responsibility, develop an advanced ESE method for efficiently monitoring the transmission of pandemics, notably the Covid-19 pandemic, which can help in efficient strategy making.

1.10 Approaches and methods

As discussed through the motivations and objectives, this thesis aims to contribute into three different classes as discussed below: C1: Advanced linear and nonlinear filtering methods to overcome various irregularities. C2: Advanced PSSE methods in order to improve the accuracy as well as to improve the robustness against various uncertainties. C3: Develop efficient methods for analyzing the spread of Covid-19 pandemic as a scientific responsibility of a researcher in the era of Covid-19 outbreak.

In the subsequent discussions, we highlight the methods and approaches adopted for the contributions in the three classes.

1.10.1 Model formulation

For the contributions under the C1 class, we reformulated the traditional measurement models to incorporate the possibilities of the concerned measurement irregularities. On the other handle, for class C2, we adopted the models of PSSE from the literature. Finally, for class C3, we introduced a new pandemic model with more compartments in order to efficiently monitor the Covid-19 spread.

1.10.2 Design and selection of filters

For class C1, we re-derived the traditional Gaussian filtering method for the reformulated measurement model. For class C2, we have two contributions with the following methods: i) a Gaussian filter, named CQKF, is adopted from the literature with improved accuracy as compared to those already tested in PSSE literature, and then that Gaussian filter is implemented over the PSSE models to improve the PSSE accuracy

and ii) a Gaussian filter is first advanced to handle various uncertainties, and then, the advanced filter is applied to the PSSE models to mitigate various limitations of the traditional PSSE methods. Finally, for contribution C3, a Gaussian filter, CKF, is adopted from the literature and applied to the newly developed pandemic model in this thesis.

1.10.3 Validation

The developed methods are simulated in MATLAB over a computer with a 64-bit operating system, 32 GB RAM, and Intel i5, 3.40GHz processor configuration. For the contributions under C2, various IEEE benchmark power system test bus systems are considered. To conduct an extensive simulation-based study, 14-, 30-, and 118-bus networks from the American electric power system (in the Midwest) are tested. It helps us investigate the efficacy of the proposed PSSE under complex networks. Finally, the contribution under C3 is investigated over real-data of Covid-19 pandemic in Delhi, the capital city of India, between 17 January 2021 and 26 April 2021, during which the city was witnessing its second wave of Covid-19.

1.10.4 Performance criteria

Estimation performance

Considering the complexity and severity of real-life problems, the author considers a large number of Monte-Carlo (M_c) simulations for analyzing the state estimator behavior under various different uncertain conditions. For validating the performances of different contributions, one or more of various metrics, including the root mean square error (RMSE), % RMSE, Mean square error, mean of absolute error (MAE), maximum absolute error (MAXE), and computational time are chosen. The performance metrics, such as RMSE, MSE, MAE, and MAXE, are expressed as

$$\text{RMSE}(\mathbf{x}_k) = \sqrt{\frac{1}{M_c} \sum_{i=1}^{M_c} \left\| \hat{\mathbf{x}}_{k|k}^i - \mathbf{x}_k \right\|_2^2} \quad (1.29)$$

$$\%RMSE(\mathbf{x}_k) = \sqrt{\frac{1}{M_c} \sum_{i=1}^{M_c} \left(\frac{x_k(i) - \hat{x}_{k|k}(i)}{x_k(i)} \times 100 \right)^2}, \quad (1.30)$$

$$MSE(\mathbf{x}_k) = \frac{1}{M_c} \sum_{i=1}^{M_c} \left\| \hat{\mathbf{x}}_{k|k}^i - \mathbf{x}_k^i \right\|_2^2 \quad (1.31)$$

$$MAE(\mathbf{x}_k) = \frac{1}{M_c} \sum_{i=1}^{M_c} \left| \hat{\mathbf{x}}_{k|k}^i - \mathbf{x}_k^i \right| \quad (1.32)$$

$$MAXE(\mathbf{x}_k) = \max \left| \hat{\mathbf{x}}_{k|k}^i - \mathbf{x}_k^i \right| \quad \forall i \in \{1, 2, \dots, M_c\} \quad (1.33)$$

where $|\cdot|$, and $\|\cdot\|$ denotes first and second norm, respectively.

1.11 Contribution

The main contributions of this thesis are summarized below.

- This thesis provides a detailed and up-to-date literature review on the nonlinear filtering, PSSE, and ESE, including the contributions available for handling various real-life pragmatic problems.
- A modified Kalman filter is proposed to address the problems of delayed measurements and non-Gaussian outliers in a noisy environment.
- A CQKF-based advanced PSSE method is designed to improve the accuracy of the existing PSSE methods, which utilize EKF, UKF, and CKF.
- An advanced Gaussian filtering-based PSSE algorithm is developed to address various potential irregularities in power system models.
- Lastly, as a scientific responsibility, an advanced compartment-based stochastic epidemic model is introduced. Subsequently, the CKF is implemented to estimate the compartmental state dynamics to develop an advanced ESE method.

1.12 Publications generated out of thesis work

Journal papers:

1. Sumanta Kumar Nanda, Guddu Kumar, Vimal Bhatia, and Abhinoy Kumar Singh, “Kalman Filtering with Delayed Measurements in Non-Gaussian Environments,” IEEE Access, vol. 9, pp. 123231-123244, 2021, doi: 10.1109/ACCESS.2021.3107466.
2. Sumanta Kumar Nanda, Guddu Kumar, Vimal Bhatia, and Abhinoy Kumar Singh. “Kalman-based compartmental estimation for Covid-19 pandemic using advanced epidemic model.” Biomedical Signal Processing and Control, Elsevier, 104727, 2023, doi: 10.1016/j.bspc.2023.104727.
3. Sumanta Kumar Nanda, Guddu Kumar, Amit Kumar Naik, Mohamed Abdel-Hafez, Vimal Bhatia, Ondrej Krejcar, and Abhinoy Kumar Singh, “Gaussian Filtering with False Data Injection and Randomly Delayed Measurements,” IEEE Access, (Under review).
4. Sumanta Kumar Nanda, Amit Kumar Naik, Vimal Bhatia, Taraknath Kobaku, and Abhinoy Kumar Singh, “Dynamic State Estimation of Power System Using forecasting-aided Cubature Quadrature Kalman filter,” international journal of adaptive control and signal processing (Under review).
5. Sumanta Kumar Nanda, Vimal Bhatia, Taraknath Kobaku, and Abhinoy Kumar Singh, “Self-Adaptive Forecasting-aided Gaussian Filtering-based Power System State Estimation under non-Gaussian Outliers,” IEEE Transactions on Instrumentation and Measurement, (under review).

Conferences:

1. Sumanta Kumar Nanda, Vimal Bhatia, and Abhinoy Kumar Singh, “Performance analysis of Cubature rule based Kalman filter for target tracking,” 2020 IEEE 17th India Council International Conference (INDICON). IEEE, 2020.

1.13 Thesis organization

The rest of the thesis is structured as follows. The thesis consists of eight chapters, including the present one. Continuing from this chapter, the second chapter briefly overviews the remarkable developments in estimation and filtering with their application in PSSE and ESE methods. A brief discussion of the Bayesian framework of the nonlinear filtering follows it. Chapter 3 contributes to the estimation with delayed measurements. Chapter 4 developed an advanced Gaussian filtering to deal with false data injection and randomly delayed measurement. Chapter 5 discusses the proposed KF-based PSSE without any irregularity in measurement. Chapter 6 includes the development of a robust and adaptive PSSE method performing under possible system dynamics and measurement model irregularities. In Chapter 7, an advanced epidemic model is formulated, and its stability issues with evaluating the dominant parameters impacting the disease transmission. The last chapter of this thesis, Chapter 8, briefs the discussions and conclusions of the thesis. Moreover, it includes the scope of future works. In the end, an appendix is provided, which includes the algorithms developed in different chapters.

Chapter 2

Literature Review

As discussed in the previous chapter, this thesis aims to contribute in the following directions: i) advancing the traditional linear and nonlinear filtering methods for handling data irregularities like delay, cyber-attack, and non-Gaussian noises, ii) advancing the PSSE methods to improve the accuracy and handle the uncertainties of the temporary power system networks, and iii) developing advanced ESE methods for improving the efficacy in monitoring the pandemic spread like the spread of Covid-19. Therefore, the review in this chapter is classified into the following: i) Gaussian filtering methods, ii) filtering with various measurement irregularities, including delayed measurements, cyber-attacks, and non-Gaussian noises, iv) PSSE methods, and v) Advanced ESE methods.

2.1 Gaussian Filtering

The previous chapter introduced two Gaussian filtering approaches: derivative-free Gaussian filtering and derivative-based Gaussian filtering. As discussed previously, the derivative-based Gaussian filtering is an extension of linear Kalman filter, where the nonlinear functions are locally linearized. The popularly known extended Kalman filter (EKF) [17] and its extensions [63][64][65] are the prevalent developments under this approach.

The derivative-free Gaussian filters, as discussed previously, propagate the estimate and covariance directly through nonlinear functions. However, in this case, the mean computations involve intractable integrals, which are numerically approximated during

the filtering using deterministic sets of sample points and associated weights. The literature witnesses various derivative-free Gaussian filters using various numerical approximation methods, giving different sets of sample points and associated weights. The derivative-free Gaussian filters outperform the derivative-based Gaussian filters in accuracy and numerical stability.

In the subsequent discussions, we review the various developments under the derivative-based Gaussian filtering and the derivative-free Gaussian filtering.

2.1.1 Derivative-based Gaussian filters

As discussed above, the popular contributions under the derivative-based Gaussian filtering include the EKF and its variants, which are reviewed below.

Extended Kalman filter (EKF)

The EKF was developed in the sixties [17], within a few years after the development of the linear Kalman filter. The EKF is the earliest developed nonlinear Gaussian filter, still widely popular in practical applications and academic developments. As discussed previously, the EKF locally linearizes the nonlinear dynamic models by computing the first-order derivative in terms of Jacobian. Subsequently, it applies the concept of linear Kalman filtering over the locally linearized nonlinear dynamical models.

The EKF has a broad range of practical applications, such as in wireless sensor networks [66], state of charge estimation in Lithium-ion batteries widely used in electric vehicles [67], identification of online parameters for permanent magnet synchronous motor drive [68], spoofing resilient power system state estimation [69], biomedical systems [70],[71], [72], epidemic state estimation [73],[74], [75], *etc.*

Despite being used in widespread practical applications, the EKF has several drawbacks. For example, derivative computation requires the system dynamics to be continuous and differentiable. Similarly, the first-order linearization of the nonlinear dynamical systems causes poor accuracy and numerical instability [63]. This problem

becomes severe, particularly if the sampling interval is large. Please note that the sampling interval is often system/device property, which the practitioners cannot flexibly command to mitigate these drawbacks. Nevertheless, despite these drawbacks, the EKF widely attracts practitioners due to its simplicity of implementation and small computational demand. Moreover, many variants [76],[77], and [78] of the traditional EKF are developed to mitigate its drawbacks up to some extent.

2.1.2 Derivative-free Gaussian filters

In the previous chapter, we discussed how derivative-free Gaussian filtering involves intractable integrals, which are difficult to solve analytically and are usually approximated numerically during the filtering. Various Gaussian filters are developed in the literature using different numerical approximation methods. We review some of the major developments in the subsequent discussions.

Unscented Kalman filter (UKF) and its variants

One of the earliest and most popular derivative-free filters is the UKF [63], developed in the nineties. The UKF utilizes unscented transformation-based numerical approximation to approximate intractable integrals using a set of sigma points and weights [63]. The UKF is more accurate and numerically stable than the derivative-based EKF.

In the literature, the UKF has been widely used in handling real-life problems, *i.e.*, [79],[80],[81]. More specifically, [79] applies the UKF for state of charge estimation in an adaptive cell model, [49] implements the UKF for estimation of dynamic states for power system networks, [81] applies the UKF for biomedical systems, and [55],[82] use the UKF for ESE design applications.

Cubature Kalman filter (CKF)

Arasaratnam *et al.* [64] introduced the cubature Kalman filter (CKF) as an alternative EKF and UKF. The CKF decomposes the intractable integral into spherical and radial components, approximating the spherical integral using the third-degree

spherical-cubature rule. In contrast, the radial integral is approximated using the first-order Gauss-Laguerre quadrature rule. The resulting numerical approximation method is called third-degree spherical-radial rule, which the CKF utilizes to approximate the intractable integral with relatively improved accuracy compared to the UKF.

The CKF utilized lower orders of the spherical-cubature and Gauss-Laguerre quadrature rules, leaving away the scope of further improving the accuracy by advancing the orders of the spherical-cubature and Gauss-Laguerre quadrature rules. As a result, a series of developments appeared by improving the orders of two numerical approximation rules. This thesis briefly reviews a few other major developments below.

Cubature Quadrature Kalman filter (CQKF)

The Cubature quadrature Kalman filter (CQKF) is developed to enhance estimation accuracy while slightly increasing computational demand [83]. It adopts the integral decomposition approach from CKF and retains the third-degree spherical cubature rule for approximating the spherical integral. However, it utilizes a higher-order Gauss-Laguerre quadrature rule to approximate the radial integral. Subsequently, the CQKF introduces a new numerical approximation method, named cubature quadrature rule, by combining the third-degree spherical cubature rule and higher-order Gauss-Laguerre quadrature rule. The sample points generated through this rule are referred to as cubature quadrature points. using higher-order Gauss-Laguerre quadrature rule helps improve the accuracy at the cost of increased computational demand.

Some other popular extensions of the CKF and CQKF are the square-root CKF [64], square-root CQKF [84], transformed CQKF [85], simplex-spherical CKF [86], simplex-spherical CQKF [87], and exponential-fitted CKF [88]. Furthermore, the widespread practical application of the CKF and its extensions are reflected in [89],[90],[91]. For example, [90] used the CKF in underwater target tracking applications, [89] implemented the CKF for continuous glucose monitoring, while [91] performed fault diagnosis using the CKF [92].

Other popular Gaussian filters

The Gauss-Hermite filter (GHF) [65] utilizes the univariate Gauss-Hermite quadrature rule for numerically approximating the intractable integrals. In this filter, the sample

points generated for approximating the intractable integrals are often known as quadrature points. As the practical problems are mostly multivariate, the GHF utilizes the product rule [65] to extend the univariate Gauss-Hermite quadrature rule into a multivariate domain. However, for the product rule, the number of quadrature points increases exponentially with the increasing system dimension [93]. Therefore, the GHF suffers from the curse of dimensionality problem and becomes inapplicable for high-dimensional systems. To reduce the computational demand, there are two popular variants of the GHF available in the literature, which are discussed below.

- Sparse-grid Gauss-Hermite filter (SGHF) [93]: The SGHF replaces the product rule with Smolyak rule, reducing the number of multivariate quadrature points. Interestingly, it reduced the computational demand significantly without damaging the accuracy.
- Adaptive sparse-grid Gauss-Hermite filter (ASGHF) [94]: The ASGHF utilizes the adaptive-sparse grid method to extend the univariate quadrature rule into a multivariate domain. The adaptive-sparse grid method considers varying nonlinearity across different dimensions. Subsequently, it reduces the number of the multivariate quadrature points further. As a result, the ASGHF further reduces the computational demand compared to the GHF and SGHF without harming the accuracy.

Some other popular contributions to GHF-based filtering are square-root Gauss-Hermite filter [95], generalized GHF [96], and multi-sparse grid GHF [97]. Similar to the square-root unscented Kalman filter, the square-root Gauss-Hermite filter eliminates the need for Cholesky decomposition computations. The generalized GHF improves the accuracy further. However, the multi-sparse grid GHF reduces the computational demand further, considering that some of the subspaces of the unknown states are uncorrelated.

The GHF and its variants are among the most accurate Gaussian filters in the literature. However, despite the reduced computational demands for filtering applications in general,

the SGHF and the ASGHF, computational demand is still too large for high-dimensional systems, a limiting constraint for their practical applications widely.

2.2 Filtering under various irregularities

The linear and nonlinear Kalman filters ignore various real-life irregularities, such as the delay in measurements, non-Gaussian noises, and possible cyber-attacks in the measurement systems by intruders. Interestingly, the literature witnesses various developments in traditional linear and nonlinear filtering methods to address these problems. In the subsequent discussions, the author briefly reviews various contributions for handling the occurrences of one or more of such irregularities.

2.2.1 Filtering with delayed measurements

Measurement delays that may appear due to data propagation, queuing, *etc.*, can cause inaccurate information and adversely impact the filtering accuracy. If the delay is known, a simple time shift can solve the problem. However, unknown delays can be challenging, especially without time-stamping or clock access. In the literature, such a delay is known as a random delay.

The literature pertaining to state estimation with delayed measurements has a rich history [98],[99],[100],[101],[102]. In [98], Zhang et al. extended the Kalman filter by introducing a re-organized innovation approach to deal with multiple delays. Later, robust and adaptive Kalman filtering techniques were re-derived to deal with delayed measurements [103], [99], [100]. Sun et al. [101] introduced another popular approach by stochastically modeling the delayed measurements in terms of possible non-delayed measurements.

For handling delay in nonlinear filtering, [104], [105][106][107], [108] are some popular techniques. For instance, [104] and [105] re-derived the EKF and UKF for handling delays up to one sampling interval. Later, the same approach was extended for handling delays up to two sampling intervals [106]. To address higher delays, Singh *et al.* [107] re-derived the traditional Gaussian filtering method for handling large delays.

However, these developments assume: i) delay is an integer multiple of the sampling

interval, ii) if not known deterministically, stochastic models of the delay are known, and iii) modeling errors and measurement errors can be characterized by Gaussian approximated noises. Real-life problems often fail to satisfy these assumptions. Note that the delay in measurements is not guided by the sampling intervals, which causes a fractional delay [109] and [110].

The above-mentioned nonlinear Gaussian filtering literature for handling delayed measurements requires a stochastic model with a sequence of delay probabilities. It makes them less applicable to real-life problems with unknown probabilities and leads to poor estimation accuracy. To overcome these limitations, Abhinoy *et al.* [111] used the likelihood-based approach to overcome these limitations to determine the unknown probabilistic information about the delay. Subsequently, it implemented the delay model-based filtering approach. This algorithm is called the fractionally delayed Kalman filter.

2.2.2 Filtering with non-Gaussian noises

In general, noises are inherently non-Gaussian, while they are assumed as Gaussian in the traditional Gaussian filtering method. In some cases, they may be closely approximated as Gaussian but not always, resulting in poor accuracy of the traditional Gaussian filtering. More importantly, certain outliers in the process and measurements are mostly non-Gaussian.

The Non-Gaussian outliers in state may result from abrupt changes in the system's behavior, external disturbances, or system malfunctions. Similarly, non-Gaussian outliers in measurement data can arise from factors like data transmission quantization, impulse noise in telephone channels, atmospheric noise caused by lightning flashes, radio frequency interference, thunderstorms, and more [112][113].

This data irregularity is handled by leveraging information-theoretic learning [22],[114] with correntropy maximization. It maximizes the nonlinear and local similarity between related random variables in a joint space. This is controlled by the Kernel bandwidth and is rooted in Renyi's entropy [114]. Although these methods are useful for non-Gaussian noise, they have not been extensively tested for estimation and

filtering. Recently, Chen *et al.* [35] proposed a reformulated Kalman filtering approach that uses the maximum correntropy criterion.

In recent years, there has been a growing interest in utilizing the maximum correntropy (MC)-based design methodology [22] to handle non-Gaussian noises in real-life applications that typically involve nonlinear systems. As a result, there have been various contributions [115],[116],[117],[118],[119],[120] that have redesigned well-known nonlinear Gaussian filters such as the EKF, UKF, CKF, and GHF to incorporate this criterion.

Some other recent design criteria have also been tested for handling non-Gaussian noises. For example, Huber-based cost function [36] and minimum entropy criterion-based [121],[122] design have already been tested in the filtering literature. To further improve robustness and accuracy, a versatile criterion called the generalized maximum correntropy with freely changing Kernel shape by considering generalized Gaussian density has been developed in [123],[124],[125].

2.2.3 Filtering with cyber-attacked measurements

The filtering accuracy is significantly impacted by the precision of the measurements, which is vulnerable in cyber-physical systems due to the threat of deliberate tampering and distortion through cyber-attacks [126], [127]. Intruder mainly focuses: i) false data injection (FDI), which involves injecting false data together with true measurements [128], ii) time asynchronous measurements (data replay attacks), which entail introducing time delays in measurement propagation, and iii) denial-of-services, which entails blocking any measurement availability [129], [130]. The primary focus of this thesis is on filtering with FDI attacks.

In the literature, [128] extends the traditional EKF to handle FDI attacks, but this method is not suitable for other Gaussian filters like the UKF, CKF, and GHF, which offer higher accuracy. Later, [33] and [32] introduce a generalized Gaussian filtering method to handle FDI attacks by reformulating the measurement model stochastically to incorporate the possibility of FDI attacks and re-deriving the traditional Gaussian filtering accordingly. Since [33] and [32] are generalized extensions of Gaussian filtering, they can

be applied to any existing Gaussian filters, such as the EKF, UKF, CKF, and GHF.

2.3 Power System state estimator

The author classified PSSEs literature survey into without irregularities and with irregularities as given below:

2.3.1 PSSE by ignoring various irregularities

In the year 1970, Larson et al. [131], [132] proposed sequential processing of redundant measurement, and subsequently, Kalman filter is applied for the estimation [133]. Da Silva *et al.* [134], for the first time, introduced the concept of a forecasting-aided dynamic state estimator using Kalman filter, which was later improvised with the advent of PMU and other intelligent electronic devices using nonlinear Gaussian filtering methods. In the later developments, Gaussian filtering methods, such as EKF, UKF, and CKF, are exploited for dynamic state estimation of the power system states [46],[49],[48],[135],[136].

Numerous variants of nonlinear Kalman filtering algorithms, such as EKF, UKF, and CKF, have been used to address the critical problems of DSE in nonlinear power system networks. The EKF forms a Jacobian matrix, which computes the partial derivatives to locally linearize the power system dynamic model. Due to the derivative-based local linearization of the nonlinear PSSE models, the EKF exhibits poor estimation accuracy and a low convergence rate [30] [21]. For solving the nonlinear dynamic equations, the UKF and CKF methods replace the Jacobian matrix-based linearization technique with a simpler and more stable numerical approximation approach. The UKF uses unscented transformation-based numerical approximation [49], while the CKF utilizes a relatively more accurate alternative named third-order spherical-radial cubature rule [30].

2.3.2 PSSE with various real-life irregularities

The aforementioned Gaussian filter-based PSSE methods have drawbacks, such as requiring unknown mathematical models of state dynamics, unknown statistical information on noises, and ignoring non-Gaussian outliers in process and measurements. The typical reasons for non-Gaussian outliers are changing demands and power

generation, instrument failures, communication limitations, uncertainties of electronic devices, *etc.* [40].

The Gaussian filter-based PSSE has been extended to overcome these limitations to improve estimation accuracy, adaptability, and robustness for real-time monitoring of complex power networks. One such extension is Holt's double exponential smoothing, used for state prediction in power systems. Additionally, the concept of SHAKF [137] is utilized in the power system monitoring for adaptive noise estimation. As described, the adaptive Gaussian filter-based PSSE method integrates time-dependent, mathematically derived, exact statistical information relevant to noise covariance. In contrast, the traditional Gaussian filter-based PSSE assumes that the covariances are constant over time, which may accidentally work for the actual power network but is selected through trial and error. However, the reality is not the same. Readers are suggested to follow [138],[139]. Finally, Maximum correntropy (MC) and minimum entropy (ME)-based design criteria are used to address the irregularity of non-Gaussian outliers in [125],[117], and [140].

2.4 Epidemiological state estimator

Knowledge-based mathematical disease dynamics models are popular to characterize the repercussions of diseases using mathematical models [6][53][54],[55] [58],[59],[60],[61]. Among such mathematical models, compartmental-based models are the most popular [53]. They categorize the total population into different compartments based on the infection level in an individual. As discussed in Chapter 1, the simplest compartment-based model is *SIR* model [6]. The compartment-based models utilize a few parameters, such as infection rate, recovery rate, recovery rate from disease, *etc.* The superiority of compartment-based models improves as the number of parameters influencing disease transmission increases. In this regard, later developments (after *SIR* model) incorporated more compartments, including susceptible (S), exposed (E), infected (I), recovered from exposed (R), recovered from infected (R), passed away (P), and vaccinated (V) compartments. Much like the renowned *SIR* models, epidemic models are commonly referred to by their compartmental names represented in abbreviated form.

Later developments introduced *SIRP* [54],[55] *SEIR* [58], *SEIRP* [59], *SEIRRP* [60], *SIRV* [61], model to characterize the nonlinear disease dynamics.

Literature on epidemic model state estimation witnesses recursive least square estimation [60], maximum likelihood method [141], and Markov chain Monte-Carlo [142]. Sameni et al. [60] used recursive least square estimation method by minimizing linear least square cost function. These methods are often dependent on accuracy of the measurement data. Hasan et al. [54] developed an EKF-based ESE method using *SIRP* model. As discussed previously, in the EKF, the partial derivatives are computed to locally linearize the highly nonlinear epidemic model, which has poor accuracy and stability in estimating the compartmental populations. Later UKF-based ESE integrated epidemic model replaced Jacobian matrix-based linearization with simpler, more stable unscented transformation-based numerical approximations [55]. A *SEIRP* model was proposed to investigate the dynamic behavior of the Covid-19 pandemic [59]. Later, Xinhe et al. developed an EKF-based ESE method for *SEIRP* epidemic model by incorporating reinfection rate to estimate the Covid-19 compartments [73]. Similarly, Jialu et al. [141] introduced an EKF-based estimation of *SEIRP* model, where the model parameters were obtained using maximum likelihood method [141]. The above-discussed estimation methods, such as the EKF, UKF, and their extensions, used in the [54],[55],[141],[73] are known for their poor accuracy and stability. Thus, introducing an efficient estimation method can further improve the accuracy.

2.5 Summary

- The Gaussian filtering provides a range of filters that can help achieve good trade-offs between accuracy and computational demand. However, the Gaussian filtering traditionally ignores various irregularities, and thus, it often underperforms in practical applications.
- The optimal linear Kalman filter conventionally fails to account for a range of real-life irregularities, such as measurement data irregularities and performance

degradation caused by non-Gaussian outliers. These irregularities significantly degrade estimation accuracy.

- The linear Kalman filter conventionally fails to account for a range of real-world applicability scenarios, such as measurement data irregularities and performance degradation caused by non-Gaussian outliers. These irregularities often manifest in practical applications and can significantly impact accuracy. Examples of such measurement irregularities include delayed and cyber-attacked measurements.
- The cyber-physical system is susceptible to measurement irregularities, such as delayed and cyber-attacked measurements. The system implements suboptimal Gaussian filters, but the presence of measurement irregularities adversely impacts the estimator's performance.
- The state-of-the-art PSSE methods use mixed measurements from remotely located RTUs and PMUs. The recent literature has witnessed applications of different Gaussian filters over the PSSE state space model to enhance accuracy.
- As discussed above, a branch of the recent research on PSSE methods focused on advancing the Gaussian filtering methods to improve accuracy. However, this is insufficient for handling various network uncertainties in the PSSE. Such network uncertainties may include the lack of a precise state dynamical model, unknown and time-varying noises, and non-Gaussian outliers. Therefore, parallel research also focuses on addressing such uncertainties in the PSSE.
- As a need of the hour, during the outbreak of Covid-19, an immediate shift of research was witnessed on containing the Covid-19 spread. Within the scope of filtering knowledge, developing advanced ESE methods was crucial for developing efficient monitoring algorithms for Covid-19 spread, which could later help in framing efficient administrative strategies for containing the Covid-19 spread. The ESE methods are composed of compartment-based models and nonlinear estimators. They can estimate various compartment populations (of pandemic

models), including susceptible, exposed, infected, recovered, and deceased populations.

Chapter 3

Kalman Filtering with Delayed Measurements in Non-Gaussian Environments

As discussed previously, the Kalman filter recursively estimates the unknown dynamical states of a system when noisy measurements are received sequentially from individual or centralized sensors. Several real-life applications of the linear Kalman filter have been discussed in previous chapters: target tracking localization in mobile robots and autonomous vehicles, estimating speech and audio signals in signal processing, *etc.*

Following the discussions in the previous chapters, we highlight two problems of Kalman filter below: i) state and measurements are assumed to be Gaussian distributed, and ii) measurements are the non-delayed *i.e.*, the measurement received by the estimator at time t_k must be generated at the same time t_k .

To understand the problems arising from delayed measurements, please note that the estimation accuracy of Kalman filter depends on the accuracy of the estimated innovation term $\varepsilon_{k|k-1}^y = \mathbf{y}_k - \hat{\mathbf{y}}_{k|k-1}$. With τ_d delay, \mathbf{y}_k carries information about the states at $t_k - \tau_d$. However, $\hat{\mathbf{y}}_{k|k-1}$, obtained by propagating $\hat{\mathbf{x}}_{k-1|k-1}$ through state space model, estimates the same information at t_k . Thus, \mathbf{y}_k and $\hat{\mathbf{y}}_{k|k-1}$ carry the state information separated by τ_d in time, resulting in an inaccurate innovation term $\varepsilon_{k|k-1}^y$. Inaccurate innovation results in poor filtering performance. Please note that τ_d is generally unknown [99, 100],[143, 144] to the practitioners; therefore, a simple time-shift cannot be applied to

solve the delay problem. A time-varying delay with unknown τ_d is known as random delay [99],[100],[143],[144], which is of interest in this chapter.

To understand the problem of non-Gaussian noises, please note that the Kalman filtering algorithm discussed in Eq. (1.10) to (1.12) compensates the noises with up to the second order of statistical measures (please note that the mean, representing the first order statistical measure, is zero). Therefore, it is accurate for Gaussian noises, which can only be characterized by the first and second order statistical measures. However, in the case of non-Gaussian noises, higher order statistical measures are also significant, and ignoring them results in poor accuracy [112],[145].

The Kalman filter is also subjected to several other limitations, including modeling process dynamics in discrete-time and uncorrelated noises. However, this chapter focuses on the aforementioned restrictions, such as non-delayed measurements in the presence of non-Gaussian noises, which are known to decrease estimation accuracy in conventional Kalman filter.

In particular, sudden changes in system behavior, external disturbances, or system failures can cause non-Gaussian outliers in state estimates. Similarly, various factors such as quantization during data transmission, impulse noise in telephone channels, atmospheric noise caused by lightning flashes, radio frequency interference, thunderstorms, and so on [112, 113, 146] can lead to non-Gaussian outliers in measurement data. In addition, network systems and multiplexed communication channels can induce time delays in measurements [104],[106],[147],[148].

This chapter introduces a new extension of the Kalman filter to deal with the problems of unknown delayed measurements in the presence of non-Gaussian noises. To the best of the authors' knowledge, no filtering method has been discussed in the literature to address the two problems together. Unlike the above discussed delay algorithms, the proposed extension allows a fractional delay. Moreover, the proposed filter does not require apriori knowledge of the delay probabilities. Instead, it implements a likelihood-based approach to identify the delay stochastically. This delayed Kalman filtering approach is reformulated using maximum correntropy criterion for estimation

to capture the higher order statistics, which are generally non-Gaussian. The proposed correntropy maximization based formulation fails to deliver a closed-form solution. Therefore, a fixed-point iterative method is implemented to determine an approximate solution numerically. The proposed algorithm is simulated for two delayed measurement filtering problems with non-Gaussian noises. The performance analysis shows an improved accuracy for the proposed extension compared to the existing Kalman filtering techniques.

3.1 Modified Kalman filtering for delayed measurements and non-Gaussian noises

From the detailed discussion in chapter 1, we redesign the traditional Kalman filtering approach to deal with delayed measurements in the presence of non-Gaussian noises. The proposed Kalman filtering is also performed in two steps: prediction and update. To address the delayed measurements, it implements a likelihood based approach to identify the unknown delay of τ_d . Based on the identified τ_d , it uses \mathbf{y}_k received at t_k to update the states at a past instant $t_k - \tau_d$ from which \mathbf{y}_k actually arrives. Thereafter, a further time update is performed from $t_k - \tau_d$ to t_k to determine the estimated state at t_k . Moreover, to deal with non-Gaussian noises, the measurement update step of the proposed algorithm is designed under the correntropy maximization criterion [35].

3.1.1 Prediction

The sensor-induced non-Gaussian noises influence only the update step. This step is also called a time update. Therefore, the existing literature for handling the sensor-induced non-Gaussian noises, such as [35], adopts the prediction step directly from the ordinary Kalman filter and redesigns the measurement update step under the correntropy maximization criterion. We apply a similar approach and continue with the Gaussian noise assumption for the time update step. It should be mentioned that the process model is not unique and depends on the practitioner's hypotheses. Therefore, it can be amended to allow the Gaussian approximation to closely represent the actual modeling error. However, the same is not valid for the measurement model, and efficient handling of the sensor-induced non-Gaussian noises becomes important.

As discussed earlier, the proposed filtering method considers a fractional delay, i.e., the delay can be a fractional multiple of sampling interval. Therefore, intermediate sampling instants are also considered, unlike the traditional Kalman filter, which should improve the accuracy. We denote N_{int} as the number of intermediate instances between two immediate sampling instants. If T is the sampling interval, the intermediate instants are separated by $\Delta t = T/N_{int}$. We use the notation $t_{k-1}^j = t_{k-1} + j\Delta t \forall j \in \{1, 2, \dots, N_{int}\}$ for j^{th} intermediate instant between t_{k-1} and t_k . Hence, at $j = N_{int}$, $t_k^{N_{int}}$ represents t_{k+1} . In the remaining part of this chapter, we use the following notations to denote a statistical measure \mathcal{B} at $t_k + j\Delta t$:

$$\begin{aligned}\mathcal{B}_{t_k+j\Delta t} &= \mathcal{B}_{(k,j)} \\ \mathcal{B}_{t_k+j\Delta t}|y_{t_{k'}} &= \mathcal{B}_{(k,j)|(k')} \\ \mathcal{B}_{t_k+j\Delta t}|y_{t_{k'}+j'\delta} &= \mathcal{B}_{(k,j)|(k',j')}.\end{aligned}\tag{3.1}$$

Therefore, at $j = 0$ and $j = N_{int}$, we can write

$$\begin{aligned}\mathcal{B}_{(k,0)|(k)} &= \mathcal{B}_{k|k} \\ \mathcal{B}_{(k,N_{int})|(k)} &= \mathcal{B}_{k+1|k}.\end{aligned}\tag{3.2}$$

The proposed algorithm determines the time update parameters, i.e., $\hat{\mathbf{x}}_{k|k-1}$ and $\mathbf{P}_{k|k-1}$, through intermediate steps. Please follow [111] for a detailed discussion.

3.1.2 Update

In this step, the measurement is updated. As discussed earlier, the objective of the update step is to determine the posterior estimate of parameters at t_k , i.e., $\hat{\mathbf{x}}_{k|k}$ and $\mathbf{P}_{k|k}$, using \mathbf{y}_k . Please note that \mathbf{y}_k ideally gives the state information at t_k to be used to determine the desired parameters. However, due to delay, it carries the state information from a delayed instant $t_k - \tau_d$ instead of t_k . Therefore, it is appropriate to determine the posterior estimated parameters at $t_k - \tau_d$ instead of t_k , with τ_d being unknown. The proposed algorithm adopts a likelihood based approach from [111] to identify τ_d .

As the measurement equation is linear, the predicted estimate and covariance of \mathbf{x}_k at any intermediate instant t_{k-1}^j can be easily transformed to obtain the predicted estimate and covariance of \mathbf{y}_k at t_{k-1}^j . Let us denote the predicted estimate and covariance of \mathbf{y}_k at t_{k-1}^j as $\hat{\mathbf{y}}_{(k-1,j)|(k-1)}$ and $\mathbf{S}_{(k-1,j)|(k-1)}$, respectively. It is worth mentioning that the predicted estimate and covariance of \mathbf{x}_k are available for all past intermediate instants. Thus, before the measurement \mathbf{y}_k is received at t_k , we can obtain $\hat{\mathbf{y}}_{(i-1,j)|(k-1)}$ and $\mathbf{S}_{(i-1,j)|(k-1)} \forall i \in \{1, 2, \dots, k\}$ and $j \in \{1, 2, \dots, N_{int}\}$, which can be used to determine the Gaussian likelihood of \mathbf{y}_k at any past intermediate instant. Thus, without harming the generality of the proposed algorithm for handling the sensor-induced non-Gaussian noises, we adopt the Gaussian likelihood for determining the likelihood of \mathbf{y}_k arriving from a past intermediate instant.

To this end, let us consider a delayed instant $t_r + j\Delta t$, i.e., $t_r \in \{t_1, t_2, \dots, t_{k-1}\}$. Then, the Gaussian likelihood that \mathbf{y}_k arrives from a past instant $t_r + j\Delta t$ due to the delay can be given as

$$L_{(r,j)}(\mathbf{y}_k) \sim ((2\pi)^m \det(\mathbf{S}_{(r,j)|(r)}))^{-\frac{1}{2}} \times \exp\left(-\frac{(\boldsymbol{\varepsilon}_{(r,j)|(r)}^y)^T (\mathbf{S}_{(r,j)|(r)})^{-1} \boldsymbol{\varepsilon}_{(r,j)|(r)}^y}{2}\right), \quad (3.3)$$

where $\det(\mathbf{S}_{(r,j)|(r)})$ denotes the determinant of $\mathbf{S}_{(r,j)|(r)}$ and $\boldsymbol{\varepsilon}_{(r,j)|(r)}^y = \mathbf{y}_k - \hat{\mathbf{y}}_{(r,j)|(r)}$. The log-likelihood function can be written as

$$\log(L_{(r,j)}(\mathbf{y}_k)) \sim -\frac{1}{2} \left(m \log(2\pi) + \log(\det(\mathbf{S}_{(r,j)|(r)})) + \mathfrak{B}_{(r,j)|(r)} \right), \quad (3.4)$$

where $\mathfrak{B}_{(r,j)|(r)} = (\boldsymbol{\varepsilon}_{(r,j)|(r)}^y)^T (\mathbf{S}_{(r,j)|(r)})^{-1} \boldsymbol{\varepsilon}_{(r,j)|(r)}^y$. Furthermore, additive and multiplicative of the constant terms are removed as they do not affect index of the maximum log-likelihood [111]. Thus, Eq. 3.4 can be re-written as

$$\mathcal{L}_{(r,j)}(\mathbf{y}_k) \sim -\log(\det(\mathbf{S}_{(r,j)|(r)})) - \mathfrak{B}_{(r,j)|(r)}.$$

For analytical simplification, a negative log-likelihood can be taken as

$$\mathcal{L}_{(r,j)}(\mathbf{y}_k) \sim \log(\det(\mathbf{S}_{(r,j)|(r)})) + \mathfrak{B}_{(r,j)|(r)}. \quad (3.5)$$

To compute the likelihood $\mathcal{L}_{(r,j)}(\mathbf{y}_k)$ for \mathbf{y}_k arriving from $t_r + j\Delta t$, let us recall Eq. (1.11), which infers that

$$\begin{aligned} \hat{\mathbf{y}}_{(r,j)|(r)} &= \mathcal{H}_{(r,j)} \hat{\mathbf{x}}_{(r,j)|(r)} \\ \mathbf{S}_{(r,j)|(r)} &= \mathcal{H}_{(r,j)} \mathbf{P}_{(r,j)|(r)} (\mathcal{H}_{(r,j)})^T + \mathbf{R}_{(r,j)}. \end{aligned} \quad (3.6)$$

Subsequently,

$$\begin{aligned} \boldsymbol{\varepsilon}_{(r,j)|(r)}^y &= \mathbf{y}_k - \mathcal{H}_{(r,j)} \hat{\mathbf{x}}_{(r,j)|(r)} \\ \mathfrak{B}_{(r,j)|(r)} &= (\mathbf{y}_k - \mathcal{H}_{(r,j)} \hat{\mathbf{x}}_{(r,j)|(r)})^T \left(\mathcal{H}_{(r,j)} \mathbf{P}_{(r,j)|(r)} (\mathcal{H}_{(r,j)})^T \right. \\ &\quad \left. + \mathbf{R}_{(r,j)} \right)^{-1} (\mathbf{y}_k - \mathcal{H}_{(r,j)} \hat{\mathbf{x}}_{(r,j)|(r)}). \end{aligned} \quad (3.7)$$

Substituting $\mathbf{S}_{(r,j)|(r)}$ and $\mathfrak{B}_{(r,j)|(r)}$ into Eq. (3.5) from Eq. (3.6) and (3.7), we get

$$\begin{aligned} \mathcal{L}_{(r,j)}(\mathbf{y}_k) &\sim \log \left(\det \left(\mathcal{H}_{(r,j)} \mathbf{P}_{(r,j)|(r)} (\mathcal{H}_{(r,j)})^T + \mathbf{R}_{(r,j)} \right) \right) \\ &\quad + (\mathbf{y}_k - \mathcal{H}_{(r,j)} \hat{\mathbf{x}}_{(r,j)|(r)})^T \left(\mathcal{H}_{(r,j)} \mathbf{P}_{(r,j)|(r)} (\mathcal{H}_{(r,j)})^T \right. \\ &\quad \left. + \mathbf{R}_{(r,j)} \right)^{-1} (\mathbf{y}_k - \mathcal{H}_{(r,j)} \hat{\mathbf{x}}_{(r,j)|(r)}). \end{aligned} \quad (3.8)$$

Remark 3.1.1 $\mathcal{L}_{(r,j)}(\mathbf{y}_k)$ is a negative likelihood; therefore, a minimum of $\mathcal{L}_{(r,j)}(\mathbf{y}_k)$ gives the maximum likelihood estimate.

From the likelihood theory, a delayed measurement \mathbf{y}_k can be considered to have arrived from the past instant where the likelihood is maximum, i.e., $\mathcal{L}_{(r,j)}(\mathbf{y}_k)$ is minimum. $\mathcal{L}_{(r,j)}(\mathbf{y}_k)$ can be computed for every delayed instant, i.e., $\forall t_r \in \{t_1, t_2, \dots, t_{k-1}\}$ and $\forall j \in \{1, 2, \dots, N_{int}\}$. Subsequently, the time instant $t_{r^*} + j^* \Delta t$ from which \mathbf{y}_k arrives can

be obtained from (r^*, j^*) , if

$$(r^*, j^*) \sim \underset{(r,j)}{\operatorname{arg\,min}} L_{(r,j)}(\mathbf{y}_k). \quad (3.9)$$

Subsequently, τ_d can be given as $t_k - (t_{r^*} + j^* \Delta t)$.

The likelihood analysis concludes that \mathbf{y}_k arrives with τ_d delay, i.e., from a past instant $t_{r^*} + j^* \Delta t = t_k - \tau_d$. Therefore, we use \mathbf{y}_k to update the posterior estimate parameters at $t_{r^*} + j^* \Delta t$ instead of t_k . The proposed Kalman filtering algorithm adopts a maximum correntropy [114][22] based posterior estimation to deal with non-Gaussian noises. In this regard, let us define an error function

$$\mathbf{e}_{(r^*, j^*)} = \begin{bmatrix} \hat{\mathbf{x}}_{(r^*, j^*)|(k)} \\ \mathbf{y}_k \end{bmatrix} - \begin{bmatrix} \mathbb{I} \\ \mathcal{H}_{(r^*, j^*)} \end{bmatrix} \mathbf{x}_{(r^*, j^*)} = \mathbf{U}_{(r^*, j^*)} - \mathbf{V}_{(r^*, j^*)}. \quad (3.10)$$

The objective is to maximize the correntropy between $\mathbf{U}_{(r^*, j^*)}$ and $\mathbf{V}_{(r^*, j^*)}$, given as the first moment of Kernel of $\mathbf{e}_{(r^*, j^*)}$ [114],[22]. We choose the commonly accepted Gaussian Kernel, given as [149, 150]

$$K_{\mathbf{U}, \mathbf{V}}(i) = G_{\sigma}(\mathbf{e}_{(r^*, j^*)}(i)) = \exp\left(-\frac{\mathbf{e}_{(r^*, j^*)}(i)^2}{2\sigma^2}\right), \quad (3.11)$$

where $\sigma > 0$ is Kernel width, $\mathbf{e}_{(r^*, j^*)}(i)$ is the i^{th} element of $\mathbf{e}_{(r^*, j^*)}$ with $i \in \{1, 2, \dots, l_s\}$, i.e., $l_s = n + m$. Subsequently, the correntropy, i.e., the first moment of Kernel, is approximated using the sample mean based approach as

$$\hat{C}_{\mathbf{U}, \mathbf{V}} = \frac{1}{l_s} \sum_{l=1}^{l_s} G_{\sigma}(\mathbf{e}_{(r^*, j^*)}(i)), \quad (3.12)$$

where $C_{\mathbf{U}, \mathbf{V}}$ denotes the correntropy between $\mathbf{U}_{(r^*, j^*)}$ and $\mathbf{V}_{(r^*, j^*)}$. Therefore, the correntropy maximization problem reduces to the problem of maximizing $\frac{1}{l_s} \sum_{l=1}^{l_s} G_{\sigma}(\mathbf{e}_{(r^*, j^*)}(i))$. To maintain consistency across different i , we prefer standardized

error. Subsequently, we define the cost function as

$$\mathbf{J}_{(r^*,j^*)} = \frac{1}{l_s} \sum_{l=1}^{l_s} G_\sigma(\bar{\mathbf{e}}_{(r^*,j^*)}(l)). \quad (3.13)$$

where $\bar{\mathbf{e}}_{(r^*,j^*)}$ is standardized $\mathbf{e}_{(r^*,j^*)}$.

To standardize the error function $\mathbf{e}_{(r^*,j^*)}$, we re-write Eq. (6.7) as

$$\mathbf{e}_{(r^*,j^*)} = \begin{bmatrix} \hat{\mathbf{x}}_{(r^*,j^*)|(k)} - \mathbf{x}_{(r^*,j^*)} \\ \mathcal{V}_{(r^*,j^*)} \end{bmatrix}. \quad (3.14)$$

Subsequently, the error covariance can be given as

$$\mathbb{E} \left[\mathbf{e}_{(r^*,j^*)} \mathbf{e}_{(r^*,j^*)}^T \right] = \begin{bmatrix} \mathbf{P}_{(r^*,j^*)|(k)} & \mathbf{0} \\ \mathbf{0} & \mathbf{R}_{(r^*,j^*)} \end{bmatrix}, \quad (3.15)$$

where $\mathbb{E}[\cdot]$ denotes the estimate. If $\mathbf{S}_{(r^*,j^*)|(k)}^p$ and $\mathbf{S}_{(r^*,j^*)}^r$ represent the Cholesky decomposition of $\mathbf{P}_{(r^*,j^*)|(k)}$ and $\mathbf{R}_{(r^*,j^*)}$, respectively, then

$$\begin{aligned} \mathbb{E} \left[\mathbf{e}_{(r^*,j^*)} \mathbf{e}_{(r^*,j^*)}^T \right] &= \begin{bmatrix} \mathbf{S}_{(r^*,j^*)|(k)}^p (\mathbf{S}_{(r^*,j^*)|(k)}^p)^T & \mathbf{0} \\ \mathbf{0} & \mathbf{S}_{(r^*,j^*)}^r (\mathbf{S}_{(r^*,j^*)}^r)^T \end{bmatrix} \\ &= \mathbf{S}_{(r^*,j^*)|(k)} (\mathbf{S}_{(r^*,j^*)|(k)})^T. \end{aligned} \quad (3.16)$$

Note that $\mathbf{S}_{(r^*,j^*)|(k)}$ represents the Cholesky decomposition of $\mathbb{E} \left[\mathbf{e}_{(r^*,j^*)} \mathbf{e}_{(r^*,j^*)}^T \right]$. Please note that the Kalman estimator is unbiased, i.e., $\mathbb{E}[\mathbf{e}_{(r^*,j^*)}] = \mathbf{0}$. Subsequently, the standardized error $\bar{\mathbf{e}}_{(r^*,j^*)}$ can be obtained as

$$\bar{\mathbf{e}}_{(r^*,j^*)} = (\mathbf{S}_{(r^*,j^*)|(k)})^{-1} \mathbf{e}_{(r^*,j^*)}. \quad (3.17)$$

Substituting $\mathbf{e}_{(r^*,j^*)}$ from Eq. (6.7), we can write

$$\begin{aligned}\bar{\mathbf{e}}_{(r^*,j^*)} &= \mathbf{S}_{(r^*,j^*)|(k)}^{-1} \begin{bmatrix} \hat{\mathbf{x}}_{(r^*,j^*)|(k)} \\ \mathbf{y}_k \end{bmatrix} - \mathbf{S}_{(r^*,j^*)|(k)}^{-1} \begin{bmatrix} \mathbb{I} \\ \mathcal{H}_{(r^*,j^*)} \end{bmatrix} \mathbf{x}_{(r^*,j^*)} \\ &= \mathcal{D}_{(r^*,j^*)} - \mathcal{W}_{(r^*,j^*)} \mathbf{x}_{(r^*,j^*)}.\end{aligned}\quad (3.18)$$

Substituting $\bar{\mathbf{e}}_{(r^*,j^*)}$ into Eq. (3.13), the cost function can be re-written as

$$\mathbf{J}_{(r^*,j^*)} = \frac{1}{l_s} \sum_{l=1}^{l_s} G_{\sigma} \left(\mathcal{D}_{(r^*,j^*)}(l) - \mathcal{W}_{(r^*,j^*)}(l) \mathbf{x}_{(r^*,j^*)} \right), \quad (3.19)$$

where $\mathcal{D}_{(r^*,j^*)}(l)$ and $\mathcal{W}_{(r^*,j^*)}(l)$ represent l^{th} element of $\mathcal{D}_{(r^*,j^*)}$ and $\mathcal{W}_{(r^*,j^*)}$, respectively. The value of $\mathbf{x}_{(r^*,j^*)}$ that maximizes $\mathbf{J}_{(r^*,j^*)}$ is the desired posterior estimate of \mathbf{x} at $t_{r^*} + j^* \Delta t$, i.e.,

$$\hat{\mathbf{x}}_{(r^*,j^*)|(k)} = \arg \max_{\mathbf{x}_{(r^*,j^*)}} \mathbf{J}_{(r^*,j^*)} \quad (3.20)$$

Therefore, $\hat{\mathbf{x}}_{(r^*,j^*)|(k)}$ is a solution of

$$\frac{d\mathbf{J}_{(r^*,j^*)}}{d\mathbf{x}_{(r^*,j^*)}} = 0. \quad (3.21)$$

Solution to a similar cost function is derived in [35] at t_k for non-delayed measurements.

The same solution holds at the delayed instant $t_{r^*} + j^* \Delta t$ as well, which gives

$$\begin{aligned}\mathbf{x}_{(r^*,j^*)} &= g(\mathbf{x}_{(r^*,j^*)}) \\ &= \left(\sum_{l=1}^{l_s} G_{\sigma} \left(\bar{\mathbf{e}}_{(r^*,j^*)}(l) \right) \left(\mathcal{W}_{(r^*,j^*)}(l) \right)^T \mathcal{W}_{(r^*,j^*)}(l) \right)^{-1} \\ &\quad \times \left(\sum_{l=1}^{l_s} G_{\sigma} \left(\bar{\mathbf{e}}_{(r^*,j^*)}(l) \right) \left(\mathcal{W}_{(r^*,j^*)}(l) \right)^T \mathcal{D}_{(r^*,j^*)}(l) \right).\end{aligned}\quad (3.22)$$

Please note that $g(\mathbf{x}_{(r^*,j^*)})$ is an exponential function of $\mathbf{x}_{(r^*,j^*)}$ due to $G_{\sigma}(\bar{\mathbf{e}}_{(r^*,j^*)}(l))$. Therefore, Eq. (3.22) fails to offer a closed-form solution. We adopt a fixed-point iteration based numerical method from [35] to solve this equation. In this regard, we re-write Eq.

(3.22) as

$$\mathbf{x}_{(r^*,j^*)} = \left(\mathcal{W}_{(r^*,j^*)}^T \boldsymbol{\vartheta}_{(r^*,j^*)} \mathcal{W}_{(r^*,j^*)} \right)^{-1} \left(\mathcal{W}_{(r^*,j^*)}^T \boldsymbol{\vartheta}_{(r^*,j^*)} \mathcal{D}_{(r^*,j^*)} \right), \quad (3.23)$$

where

$$\boldsymbol{\vartheta}_{(r^*,j^*)} = \text{diag} \left(\boldsymbol{\vartheta}_{(r^*,j^*)}^x \quad \boldsymbol{\vartheta}_{(r^*,j^*)}^y \right), \quad (3.24)$$

with

$$\boldsymbol{\vartheta}_{(r^*,j^*)}^x = \text{diag} \left(\bar{\mathbf{e}}_{(r^*,j^*)}(1), \dots, \bar{\mathbf{e}}_{(r^*,j^*)}(n) \right) \quad (3.25)$$

$$\boldsymbol{\vartheta}_{(r^*,j^*)}^y = \text{diag} \left(\bar{\mathbf{e}}_{(r^*,j^*)}(n+1), \dots, \bar{\mathbf{e}}_{(r^*,j^*)}(n+m) \right). \quad (3.26)$$

A solution to Eq. (3.23) is derived in [35] at the non-delayed instant t_k . However, the same derivation can be extended for the delayed instant $t_{r^*} + j^* \Delta t$ as well, which gives

$$\mathbf{x}_{(r^*,j^*)} = \hat{\mathbf{x}}_{(r^*,j^*)|(k-1)} + \bar{\mathbf{K}}_{(r^*,j^*)} (\mathbf{y}_k - \mathcal{H}_{(r^*,j^*)} \hat{\mathbf{x}}_{(r^*,j^*)|(k-1)}), \quad (3.27)$$

where

$$\bar{\mathbf{K}}_{(r^*,j^*)} = \bar{\mathbf{P}}_{(r^*,j^*)|(k-1)} \mathcal{H}_{(r^*,j^*)}^T \left(\bar{\mathbf{S}}_{(r^*,j^*)|(k-1)} \right)^{-1} \quad (3.28)$$

$$\bar{\mathbf{S}}_{(r^*,j^*)|(k-1)} = \mathcal{H}_{(r^*,j^*)} \bar{\mathbf{P}}_{(r^*,j^*)|(k-1)} \mathcal{H}_{(r^*,j^*)}^T + \bar{\mathbf{R}}_{(r^*,j^*)} \quad (3.29)$$

$$\bar{\mathbf{P}}_{(r^*,j^*)|(k-1)} = \mathbf{S}_{(r^*,j^*)|(k-1)}^p \left(\boldsymbol{\vartheta}_{(r^*,j^*)}^x \right)^{-1} \left(\mathbf{S}_{(r^*,j^*)|(k-1)}^p \right)^T \quad (3.30)$$

$$\bar{\mathbf{R}}_{(r^*,j^*)} = \mathbf{S}_{(r^*,j^*)}^r \left(\boldsymbol{\vartheta}_{(r^*,j^*)}^y \right)^{-1} \left(\mathbf{S}_{(r^*,j^*)}^r \right)^T. \quad (3.31)$$

Note that $\mathbf{x}_{(r^*,j^*)}$ depends on $\bar{\mathbf{K}}_{(r^*,j^*)}$ in Eq. (3.27), and $\bar{\mathbf{K}}_{(r^*,j^*)}$ further depends on $\mathbf{x}_{(r^*,j^*)}$ due to $\bar{\mathbf{P}}_{(r^*,j^*)|(k-1)}$, $\boldsymbol{\vartheta}_{(r^*,j^*)}^x$ and $\boldsymbol{\vartheta}_{(r^*,j^*)}^y$. Therefore, Eq. (3.28) also does not provide a closed-form solution. To this end, we use the fixed-point iteration method to find the

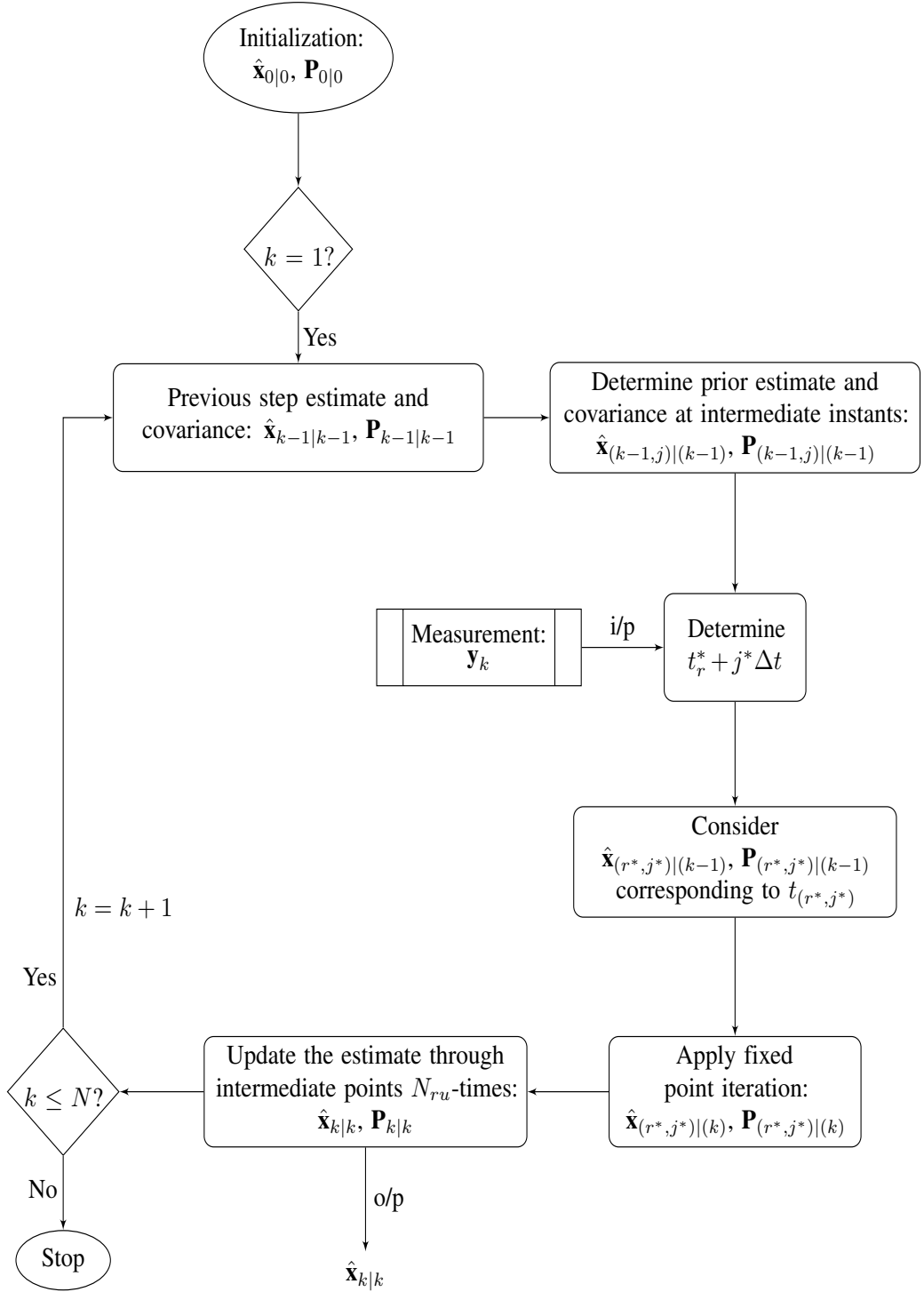


Figure 3.1: Flow chart for implementing the proposed extension of the Kalman filter for delayed measurements and non-Gaussian noises. Please note that $k = k + 1$ leads to a new iteration of estimation algorithm that finally leads to recursive state estimation.

solution numerically. The steps to be implemented for this iterative method are shown in Algorithm 3. It should be noted that the steps presented in Algorithm 3 are similar to the Kalman filter iteration, which makes it simple for practitioners to understand.

It gives the desired posterior estimates at the delayed instant $t_{r^*} + j^* \Delta t$, i.e., $\hat{\mathbf{x}}_{(r^*, j^*)|(k)}$ and $\mathbf{P}_{(r^*, j^*)|(k)}$, based on the information received from the delayed measurement \mathbf{y}_k . Following the notations in Eq. (3.2), $\hat{\mathbf{x}}_{(k-1)|(k-1)}$ and $\mathbf{P}_{(k-1)|(k-1)}$ used in Algorithm 3 are simply $\hat{\mathbf{x}}_{(k-1,0)|(k-1)}$ and $\mathbf{P}_{(k-1,0)|(k-1)}$, respectively. Finally, $\hat{\mathbf{x}}_{k|k-1}$ and $\mathbf{P}_{k|k-1}$ are obtained as $\hat{\mathbf{x}}_{(k-1, N_{int})|(k-1)}$ and $\mathbf{P}_{(k-1, N_{int})|(k-1)}$, respectively. It should be noted that

Algorithm 1 Pseudo code for computing $\hat{\mathbf{x}}_{(r^*, j^*)|(k)}$ and $\mathbf{P}_{(r^*, j^*)|(k)}$.

Input: $\hat{\mathbf{x}}_{(r^*, j^*)|(k-1)}$, $\mathbf{P}_{(r^*, j^*)|(k-1)}$, n , m and χ

Output: $\hat{\mathbf{x}}_{(r^*, j^*)|(k)}$ and $\mathbf{P}_{(r^*, j^*)|(k)}$

Initialization: $\hat{\mathbf{x}}_{(r^*, j^*)|(k-1)}(1) = \hat{\mathbf{x}}_{(r^*, j^*)|(k-1)}$, $E_{rr} = 1000$ (any large value) and $t = 1$

- 1: **while** $E_{rr} > \chi$ **do**
 - 2: $\mathbf{S}_{(r^*, j^*)|(k)}^p = \text{Chol}(\mathbf{P}_{(r^*, j^*)|(k)})$, $\mathbf{S}_{(r^*, j^*)}^r = \text{Chol}(\mathbf{R}_{(r^*, j^*)})$, and $\mathbf{S}_{(r^*, j^*)|(k)} = \text{Chol}(\text{diag}(\mathbf{P}_{(r^*, j^*)|(k)}, \mathbf{R}_{(r^*, j^*)}))$ from Eq. (3.16)
 - 3: $\mathcal{D}_{(r^*, j^*)} = (\mathbf{S}_{(r^*, j^*)|(k)})^{-1} \begin{bmatrix} \hat{\mathbf{x}}_{(r^*, j^*)|(k)} \\ \mathbf{y}_k \end{bmatrix}$
 - 4: $\mathcal{W}_{(r^*, j^*)} = (\mathbf{S}_{(r^*, j^*)|(k)})^{-1} \begin{bmatrix} \mathbb{I} \\ \mathcal{H}_{(r^*, j^*)} \end{bmatrix}$
 - 5: $\bar{\mathbf{e}}_{(r^*, j^*)} = \mathcal{D}_{(r^*, j^*)} - \mathcal{W}_{(r^*, j^*)} \hat{\mathbf{x}}_{(r^*, j^*)|(k-1)}(t)$
 - 6: $\vartheta_{(r^*, j^*)}^x = \text{diag}(\bar{\mathbf{e}}_{(r^*, j^*)}(1), \dots, \bar{\mathbf{e}}_{(r^*, j^*)}(n))$
 - 7: $\vartheta_{(r^*, j^*)}^y = \text{diag}(\bar{\mathbf{e}}_{(r^*, j^*)}(n+1), \dots, \bar{\mathbf{e}}_{(r^*, j^*)}(n+m))$
 - 8: $\bar{\mathbf{R}}_{(r^*, j^*)} = \mathbf{S}_{(r^*, j^*)}^r (\vartheta_{(r^*, j^*)}^y)^{-1} (\mathbf{S}_{(r^*, j^*)}^r)^T$
 - 9: $\bar{\mathbf{P}}_{(r^*, j^*)|(k-1)} = \mathbf{S}_{(r^*, j^*)|(k-1)}^p (\vartheta_{(r^*, j^*)}^x)^{-1} (\mathbf{S}_{(r^*, j^*)|(k-1)}^p)^T$
 - 10: $\bar{\mathbf{S}}_{(r^*, j^*)|(k-1)} = \mathcal{H}_{(r^*, j^*)} \bar{\mathbf{P}}_{(r^*, j^*)|(k-1)} \mathcal{H}_{(r^*, j^*)}^T + \bar{\mathbf{R}}_{(r^*, j^*)}$
 - 11: $\bar{\mathbf{K}}_{(r^*, j^*)} = \bar{\mathbf{P}}_{(r^*, j^*)|(k-1)} \mathcal{H}_{(r^*, j^*)}^T (\bar{\mathbf{S}}_{(r^*, j^*)|(k-1)})^{-1}$
 - 12: $\hat{\mathbf{x}}_{(r^*, j^*)|(k)}(t+1) = \hat{\mathbf{x}}_{(r^*, j^*)|(k-1)} + \bar{\mathbf{K}}_{(r^*, j^*)} \times (\mathbf{y}_k - \mathcal{H}_{(r^*, j^*)} \hat{\mathbf{x}}_{(r^*, j^*)|(k-1)})$
 - 13: $E_{rr} = \frac{\|\hat{\mathbf{x}}_{(r^*, j^*)|(k)}(t+1) - \hat{\mathbf{x}}_{(r^*, j^*)|(k)}(t)\|}{\|\hat{\mathbf{x}}_{(r^*, j^*)|(k)}(t)\|}$
 - 14: $t = t + 1$
 - 15: **end while**
 - 16: $\hat{\mathbf{x}}_{(r^*, j^*)|(k)} = \hat{\mathbf{x}}_{(r^*, j^*)|(k)}(t)$
 - 17: $\mathbf{P}_{(r^*, j^*)|(k)} = (\mathbb{I} - \bar{\mathbf{K}}_{(r^*, j^*)} \mathcal{H}_k) \mathbf{P}_{(r^*, j^*)|(k-1)} (\mathbb{I} - \bar{\mathbf{K}}_{(r^*, j^*)} \mathcal{H}_k)^T + \bar{\mathbf{K}}_{(r^*, j^*)} \mathbf{R}_k \bar{\mathbf{K}}_{(r^*, j^*)}^T$
 - 18: **return** $\hat{\mathbf{x}}_{(r^*, j^*)|(k)}$ and $\mathbf{P}_{(r^*, j^*)|(k)}$
-

the practical problems mostly desire real-time filtering, which uses \mathbf{y}_k to determine the posterior estimate and covariance at t_k , i.e., $\hat{\mathbf{x}}_{k|k}$ and $\mathbf{P}_{k|k}$. However, the proposed filtering algorithm gives the estimate and covariance at a delayed instant $t_{r^*} + j^* \Delta t$, i.e., $\hat{\mathbf{x}}_{(r^*, j^*)|(k)}$ and $\mathbf{P}_{(r^*, j^*)|(k)}$. To perform a real-time filtering, we propose to determine $\hat{\mathbf{x}}_{k|k}$ and $\mathbf{P}_{k|k}$ by

recursively updating $\hat{\mathbf{x}}_{(r^*,j^*)|(k)}$ and $\mathbf{P}_{(r^*,j^*)|(k)}$ from $t_{r^*} + j^*\Delta t$ to t_k through intermediate instants. Please note that the number of intermediate steps between $t_{r^*} + j^*\Delta t$ and t_k is $N_{ru} = \tau_d/\Delta t$. Subsequently, we need N_{ru} number of recursive updates over $\hat{\mathbf{x}}_{(r^*,j^*)|(k)}$ and $\mathbf{P}_{(r^*,j^*)|(k)}$ to obtain $\hat{\mathbf{x}}_{k|k}$ and $\mathbf{P}_{k|k}$. The steps to be followed for this update are presented in Algorithm 2.

The filtering strategy designed above takes care of the delayed measurements and non-Gaussian noises in a single algorithm. It does not require any stochastic model for the delay to be known, which is an added advantage over most of the existing delayed filtering techniques, nor does it need to know the distribution of the Gaussian process. However, statistical information from the past instants must be stored, increasing the storage budget. Moreover, the computational complexity of Algorithm 3 and 2 are in addition to the computational requirement of the ordinary Kalman filter, which results in an increased computational time as well. A block diagram showing the steps for implementing the proposed filtering algorithm is shown in Fig. 3.1. The proposed filtering

Algorithm 2 Pseudo code for computing $\hat{\mathbf{x}}_{k|k}$ and $\mathbf{P}_{k|k}$ from $\hat{\mathbf{x}}_{(r^*,j^*)|(k)}$ and $\mathbf{P}_{(r^*,j^*)|(k)}$.

Input: $\hat{\mathbf{x}}_{(r^*,j^*)|(k)}$, $\mathbf{P}_{(r^*,j^*)|(k)}$ and N_{ru}

Output: $\hat{\mathbf{x}}_{k|k}$ and $\mathbf{P}_{k|k}$

Initialization: $\hat{\mathbf{x}}_{(r^*,j^*+0)|(k)} = \hat{\mathbf{x}}_{(r^*,j^*)|(k)}$, $\mathbf{P}_{(r^*,j^*+0)|(k)} = \mathbf{P}_{(r^*,j^*)|(k)}$ and $i = 1$

1: **while** $i \leq N_{ru}$ **do**

2: $\hat{\mathbf{x}}_{(r^*,j^*+i)|(k)} = \mathbf{F}_{(r^*,j^*+i)}\hat{\mathbf{x}}_{(r^*,j^*+i-1)|(k)}$

3: $\mathbf{P}_{(r^*,j^*+i)|(k)} = \mathbf{F}_{(r^*,j^*+i)}\mathbf{P}_{(r^*,j^*+i-1)|(k)}(\mathbf{F}_{(r^*,j^*+i)})^T + \mathbf{Q}_{(r^*,j^*+i)}$

4: $i = i + 1$

5: **end while**

6: $\hat{\mathbf{x}}_{k|k} = \hat{\mathbf{x}}_{(r^*,j^*+N_{ru})|(k)}$

7: $\mathbf{P}_{k|k} = \mathbf{P}_{(r^*,j^*+N_{ru})|(k)}$

8: **return** $\hat{\mathbf{x}}_{k|k}$ and $\mathbf{P}_{k|k}$

algorithm is possibly the first development under the delay filtering framework, including [111], designed under the correntropy maximization criterion. Moreover, the ordinary Kalman filter formulation for correntropy maximization in [35] differs substantially from our algorithm. Some of the major differences are as follows:

- In a very fundamental difference, the proposed algorithm has a cost function (Eq. (3.13)) different from [35] due to the delay. Thus, the design aspects of the two

algorithms are different.

- In [35], the fixed-point iteration is applied at t_k , when estimating the states using \mathbf{y}_k . However, our derivation shows that the fixed point iteration should be implemented on a past instant for the proposed algorithm.
- In [35], the fixed-point iteration is initialized with the latest posterior estimate. However, our derivation shows that it should be initialized with a different estimate associated with a hypothetically chosen intermediate instant.

We adopt the solutions of Eqs. (3.22) and (3.23) from [35]. It should be mentioned that [35] is designed for non-delayed measurements and observes a few equations similar to Eqs. (3.22) and (3.23) of this chapter. The equations that appeared in [35] do not have closed-form solutions similar to the Eqs. (3.22) and (3.23) of this chapter. However, [35] determines approximated solutions by using fixed point iteration technique. We have applied this technique for approximation as it does not harm the validity of the proposed algorithm for delayed measurements.

3.2 Simulation and results

In this section, the proposed MDKF method is simulated for two real-life filtering problems with delayed measurements in the presence of non-Gaussian noises. The performance of the proposed method is compared with the ordinary Kalman filter and a recently developed delayed Kalman filtering algorithm. The comparison is based on the root mean square error (RMSE). Please note that the delay is generally not much larger than the sampling interval. Therefore, the performance analysis is limited to the delay of up to two sampling intervals, i.e., 2-delay. We use the following abbreviations: KF for the ordinary Kalman filter, DKF for the existing delayed Kalman filter, and MDKF for the maximum correntropy based proposed delayed filter.

3.2.1 Example-1

State space model

We consider a system with the following state space model

$$\mathbf{x}_k = \begin{bmatrix} \cos \Theta & -\sin \Theta \\ \sin \Theta & \cos \Theta \end{bmatrix} \mathbf{x}_{k-1} + \mathbf{q}_k \quad (3.32)$$

$$\mathbf{y}_k = \mathcal{H}_k \mathbf{x}_k + \mathcal{V}_k, \quad (3.33)$$

with $\mathcal{H}_k = [1, 1]^T$. \mathbf{y}_k is a hypothetical non-delayed measurement that follows the general assumptions of the state space model. \mathbf{q}_k is the process noise, which follows $\mathbf{q}_k = \mathcal{N}(\mathbf{0}, \mathbf{Q}_k)$, where \mathcal{N} denotes Gaussian distribution. We consider the matrix \mathbf{Q}_k with all elements equally being 0.01. Furthermore, $f_{\mathcal{V}_k}$ is a non-Gaussian measurement noise, which is represented as a sum of two Gaussian PDFs, i.e., $f_{\mathcal{V}_k} = \kappa_g f_{\mathcal{V}_{1,k}} + (1 - \kappa_g) f_{\mathcal{V}_{2,k}}$, where $\kappa_g \in [0, 1]$ is a Gaussian coefficient. We assume $\mathcal{V}_{j,k} = \mathcal{N}(\mathbf{0}, \mathbf{R}_{j,k}) \forall j \in \{1, 2\}$, where $\mathbf{R}_{1,k}$ and $\mathbf{R}_{2,k}$ are taken as 0.01 and 100, respectively. It should be mentioned that a significantly small value for $\mathbf{R}_{1,k}$ compared to $\mathbf{R}_{2,k}$ means that $\mathcal{V}_{1,k}$ characterizes an impulse noise and $\mathcal{V}_{2,k}$ characterizes a Gaussian noise. Subsequently, \mathcal{V}_k models an impulsive (non-Gaussian) noise for a larger value of κ_g . However, as κ_g increases, \mathcal{V}_k tends to model Gaussian distribution.

True data simulation

The true states are generated using Eq. (3.32), with the initial state taken as $\mathbf{x}_0 = [1, 1]^T$. Please note that Eq. (3.33) shows the model for hypothetical non-delayed measurements. Therefore, it cannot be used to generate the simulated data of the desired delayed measurements. We use a modified stochastic model based on Bernoulli random variables incorporating the delay in the simulated measurement data. The modified model is based on an upper bound for delay, which is taken as d -time steps. Subsequently, the

measurement model to incorporate the delay is defined as

$$\mathbf{z}_k = \sum_{r=k-d}^{k-1} \sum_{j=0}^{N_{int}} \beta_{(r,j)} (\mathcal{H}_{(r,j)} \mathbf{x}_{(r,j)} + \mathcal{V}_{(r,j)}). \quad (3.34)$$

It should be mentioned that $\mathcal{H}_{(r,j)} \mathbf{x}_{(r,j)} + \mathcal{V}_{(r,j)}$ is a hypothetical non-delayed measurement at a delayed instant $t_r + j\delta$. To avoid multiple measurements at any sampling instant, we restrict $\beta_{(r,j)} = 1$ for only one combination of r and j at any time t_k . If we define $P(\beta_{(r,j)} = 1) = p_{(r,j)}$, then p represents the no-delay probability. We simulate for two different scenarios with $p = 0.7$ (probability of delay 0.3) and $p = 0.5$ (probability of delay 0.5). We equally distribute the remaining probabilities (representing the probability of delay) over all the past instants (including the intermediate instants) within d -delay. We use Eq. (3.34) with Eq. (3.32) to generate the simulated data of delayed measurements. Starting from \mathbf{x}_0 , Eq. (3.32) is used to obtain $\mathbf{x}_{(r,j)} \forall r \in \{k-1, k-1, \dots, k-d\}$ and $j \in \{N_{int}, N_{int}-1, \dots, 1\}$. Subsequently, Eq. (3.34) is used to generate a sequence of delayed measurements based on $\mathbf{x}_{(r,j)} \forall r \in \{k-1, k-1, \dots, k-d\}$ and $j \in \{N_{int}, N_{int}-1, \dots, 1\}$.

We consider 200 time steps for the true data simulation, and so, for the filtering. Wherever it is not specified, the simulation is performed for 1-delay with $\kappa_g = 0.9$ and $p = 0.7$. Please note that the stochastic model Eq. (3.34) is used for generating the true simulated data only, with no role in filtering.

Filter implementation and results

For filtering, the initial estimate $\hat{\mathbf{x}}_{0|0}$ is generated as a Gaussian random number with mean \mathbf{x}_0 and initial covariance $\mathbf{P}_{0|0} = \text{diag}([0.01, 0.01])$, where diag represents the diagonal matrix. As discussed earlier, the comparison of the proposed MDKF with KF and DKF is based on RMSE. The RMSE is obtained by implementing $M_c = 500$ Monte-Carlo simulations. The RMSE of the i^{th} element of state at k^{th} instant is computed from Eq.(1.29).

The simulation is performed for $\Theta = \pi/18$. The true and estimated states are obtained using the proposed MDKF for 1-delay with a probability of delay 0.3, which is shown in Fig. 3.2. A close match between the true and estimated plots concludes a successful

estimation for the proposed MDKF. The RMSE plots for the MDKF, DKF, and KF are

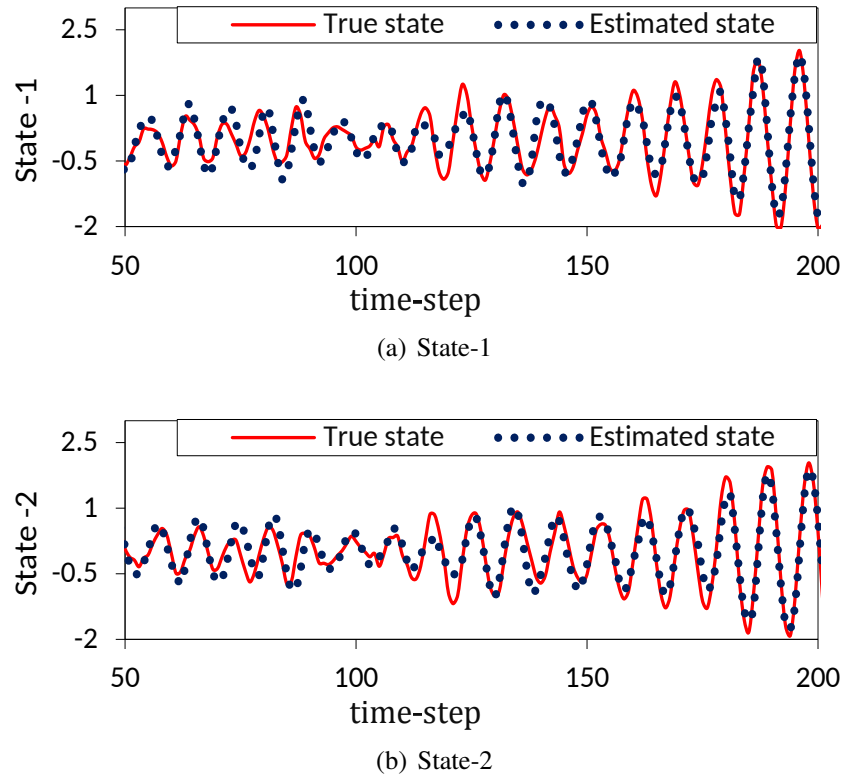
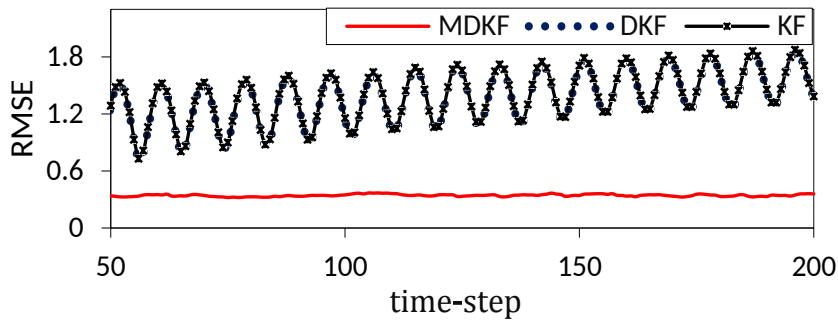


Figure 3.2: Example-1: Comparison of true and estimated states obtained from MDKF for 1-delay and 0.3 probability of delay.

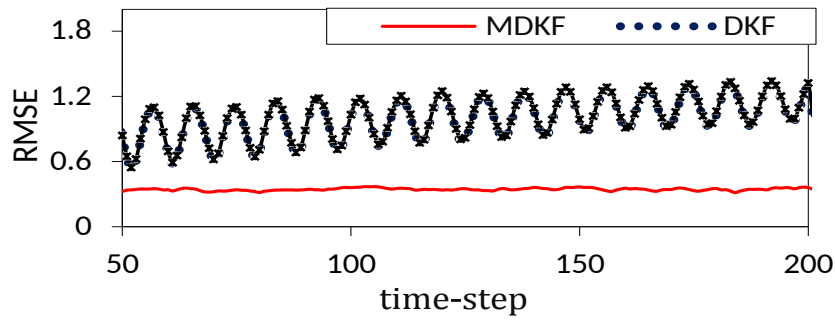
shown in Fig. 3.3 to 3.6. Fig. 3.3 and 3.4 show the performance of different filters with 1-delay and delay probability of 0.3 and 0.5, respectively. Fig. 3.5 and 3.6 show the RMSE plots for 2-delay with probability of delay as 0.3 and 0.5, respectively. Analysis of the performance of different filters for varying delay probability is shown in Table 3.1, which is restricted to 1-delay. The Table shows the average RMSE obtained for different filters as the probability of delay varies. The collective analysis of the RMSE plots (Fig. 3.3 to Fig. 3.6) and Table 3.1 conclude that the RMSE is smallest for the proposed MDKF, i.e., the accuracy is highest for the proposed MDKF. They also conclude that all filter performance deteriorates as either or both the delay and the delay probability increase.

Performance analysis for varying noise Gaussianity

We study the performance of different filters for varying Gaussianity of the measurement noise \mathcal{V}_k in Fig. 3.7. As discussed previously in this section, \mathcal{V}_k is more Gaussian distributed as κ_g increases. We plotted the average RMSE for varying κ_g in Fig. 3.7. The figure shows that the RMSE of all filters decreases as the κ_g increases,

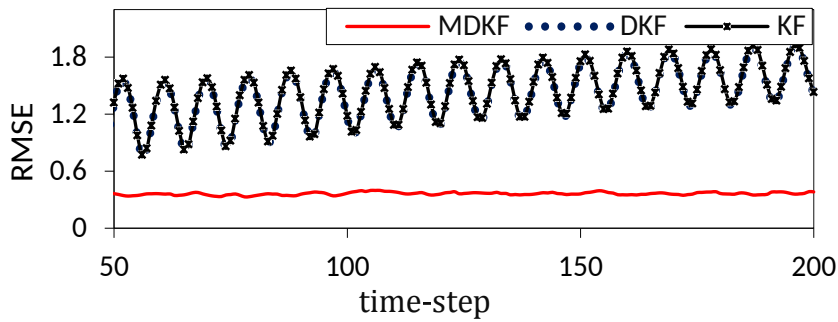


(a) State-1

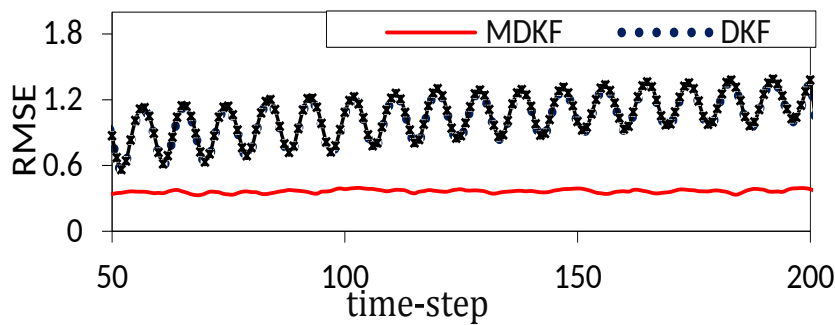


(b) State-2

Figure 3.3: Example-1: RMSE plots for 1-delay with probability of delay 0.3.

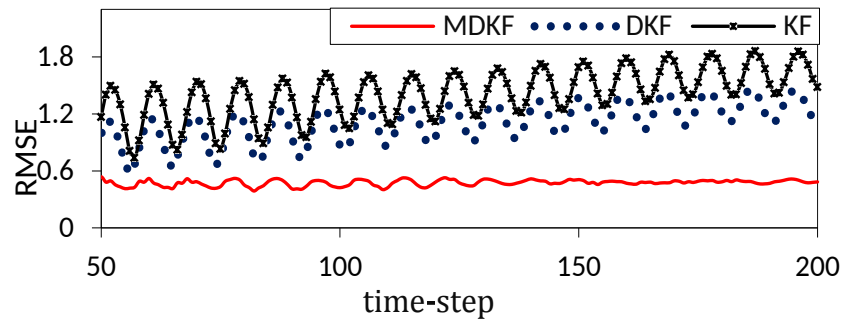


(a) State-1

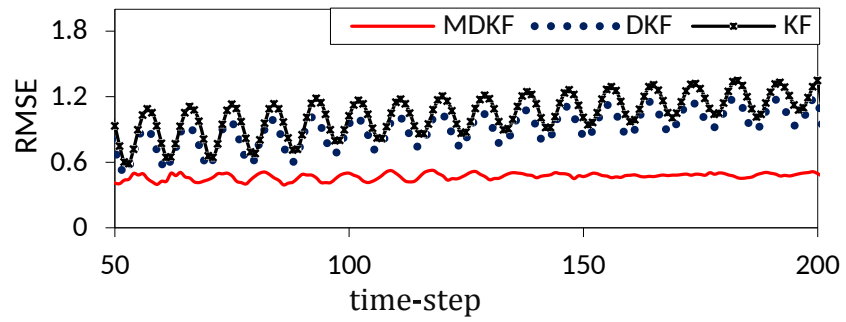


(b) State-2

Figure 3.4: Example-1: RMSE plots for 1-delay with probability of delay 0.5.

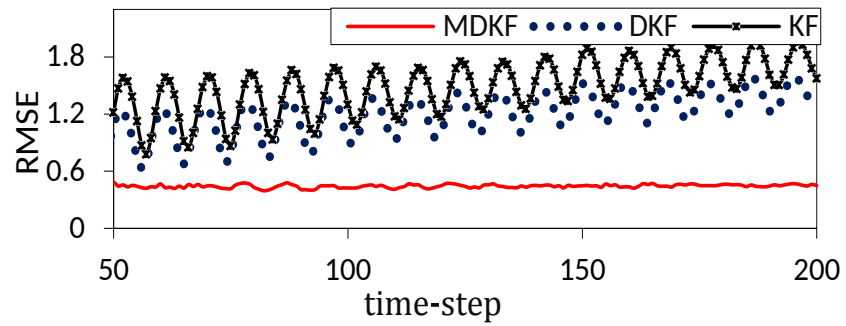


(a) State-1

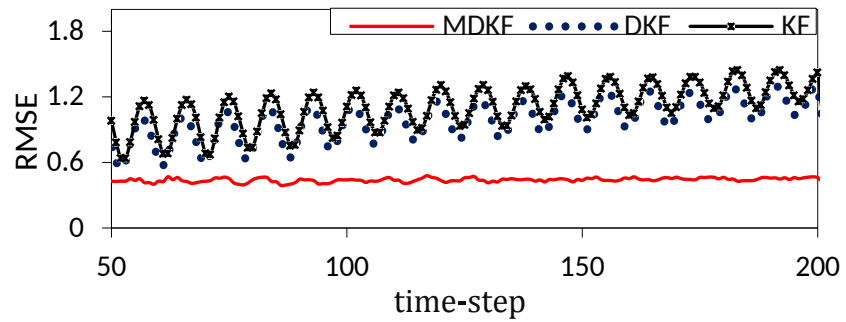


(b) State-2

Figure 3.5: Example-1: RMSE plots for 2-delay with probability of delay 0.3.



(a) State-1



(b) State-2

Figure 3.6: Example-1: RMSE plots for 2-delay with probability of delay 0.5.

i.e., as \mathcal{V}_k becomes more Gaussian distributed. Thus, we can conclude that the RMSE is reduced as \mathcal{V}_k tends to be more Gaussian distributed. Alternatively, we conclude that the performance of the filters degrades as \mathcal{V}_k deviates from Gaussianity. Interestingly, RMSE is the lowest for the proposed MDKF for all κ_g , which concludes that the proposed MDKF always outperforms the KF and DKF.

Table 3.1: Example-1: 1-delay: Average RMSE of different filters as the delay probability varies.

| Filter | 0.1 | 0.2 | 0.3 | 0.4 | 0.5 | 0.6 | 0.7 | 0.8 | 0.9 |
|--------|--------|--------|--------|--------|--------|--------|--------|--------|--------|
| MDKF | 0.3369 | 0.3374 | 0.3437 | 0.3516 | 0.3639 | 0.3652 | 0.3626 | 0.3519 | 0.3372 |
| DKF | 1.135 | 1.163 | 1.188 | 1.210 | 1.229 | 1.238 | 1.242 | 1.239 | 1.231 |
| KF | 1.152 | 1.181 | 1.207 | 1.229 | 1.248 | 1.257 | 1.260 | 1.247 | 1.247 |

Table 3.2: Example-1: Correlation between the true and estimated states obtained for different filters with varying κ_g .

| Filter | $\kappa_g = 0.1$ | $\kappa_g = 0.2$ | $\kappa_g = 0.3$ | $\kappa_g = 0.4$ | $\kappa_g = 0.5$ | $\kappa_g = 0.6$ | $\kappa_g = 0.7$ | $\kappa_g = 0.8$ | $\kappa_g = 0.9$ |
|--------|------------------|------------------|------------------|------------------|------------------|------------------|------------------|------------------|------------------|
| MDKF | 0.369 | 0.418 | 0.491 | 0.580 | 0.662 | 0.762 | 0.824 | 0.869 | 0.912 |
| DKF | -0.018 | -0.007 | 0.000 | 0.012 | 0.036 | 0.094 | 0.142 | 0.279 | 0.620 |
| KF | 0.006 | 0.007 | 0.008 | 0.010 | 0.013 | 0.017 | 0.025 | 0.043 | 0.137 |

Analysis of correlation between the true and estimated states

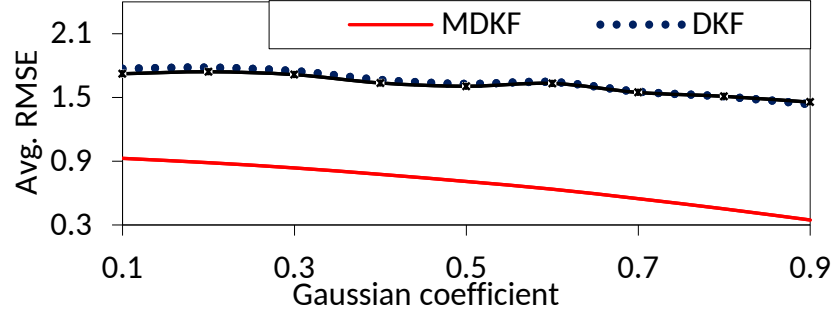
In practical problems, the correlation analysis between the true and estimated states is often important, *e.g.*, it is sometimes used for analyzing the time-shift between the true and estimated signals [144]. We show the correlation obtained using different filters for various κ_g values in Table 3.2. We restrict this study to 1-delay as a similar pattern is also expected for higher delays. This table concludes that the correlation is highest for the proposed MDKF. Alternatively, the true and estimated states are most correlated for the proposed MDKF. Table 3.2 also concludes that the correlation improves as κ_g increases, i.e., the noise \mathcal{V}_k is more Gaussian distributed.

3.2.2 Example-2

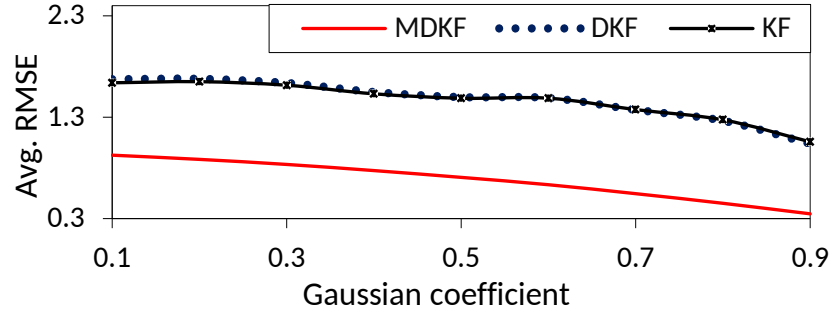
State space model

We consider a linear dynamic system with the following state space model

$$\mathbf{x}_k = \begin{bmatrix} 1 & T \\ 0 & 1 \end{bmatrix} \mathbf{x}_{k-1} + \mathbf{q}_k \quad (3.35)$$



(a) State-1



(b) State-2

Figure 3.7: Example-1: Average RMSE plots for varying Gaussian coefficient (κ_g) with 1-delay and probability of delay 0.3.

$$\mathbf{y}_k = \mathcal{H}_k \mathbf{x}_k + \mathcal{V}_k, \quad (3.36)$$

where $\mathcal{H}_k = [1 \ 1]^T$. The process noise covariance is taken as

$$\mathbf{Q}_k = \wp \begin{bmatrix} T^3/3 & T^2/2 \\ T^2/2 & T \end{bmatrix},$$

where $\wp = 10$. Similar to the previous example, \mathcal{V}_k consists of two Gaussian components, as $\mathcal{V}_{j,k} = \mathcal{N}(\mathbf{0}, \mathbf{R}_{j,k}) \forall j \in \{1, 2\}$, where $\mathbf{R}_{1,k}$ and $\mathbf{R}_{2,k}$ are taken as 0.01 and 100, respectively. The initial true data for the simulation is considered as $\mathbf{x}_0 = [1, 1]^T$ and the initial error covariance is taken as $\mathbf{P}_{0|0} = \text{diag}([0.01, 0.01])$. The initial estimate is $\hat{\mathbf{x}}_{0|0} = 1.5\mathcal{N}(\mathbf{x}_0, \mathbf{P}_{0|0})$. The true data simulation strategy is the same as Section 3.2.1. The simulation is performed for 200 time steps with $p = 0.7$ (probability of delay 0.3) and $p = 0.5$ (probability of delay 0.5), and where we don't specify the values of d , κ_g , and p , we consider $d = 1$, $\kappa_g = 0.9$ and $p = 0.7$.

Performance analysis

The true and estimated plots of the proposed MDKF are shown in Fig. 3.8, which concludes a successful estimation of the states using the proposed filter. Our further analysis is based on RMSE, computed by performing 500 Monte-Carlo simulations. In this regard, we plot the RMSEs for different scenarios in Figs. 3.9-3.12. The figures conclude a reduced RMSE of the proposed MDKF, which further concludes the improved accuracy of the proposed filter compared to the traditional filters. We further studied the performance of the proposed MDKF for varying delay probability in Table 3.3, where a consistent improvement in accuracy of the proposed MDKF for varying delay probability is observed.

We further extend the performance analysis of the proposed MDKF for varying Gaussian coefficient (κ_g) in Fig. 3.13. The figure concludes a consistently improved accuracy of the proposed MDKF for all values of κ_g . Finally, we studied the correlation between the true and estimated states in Table 3.4. From observations in Table 3.4, we can conclude that the correlation is highest for the proposed MDKF for all values of κ_g . Table 3.5 compares all the studied filtering method, such as MDKF, DKF, and KF.

Table 3.3: Example-2: 1-delay: Average RMSE of different filters as the delay probability varies.

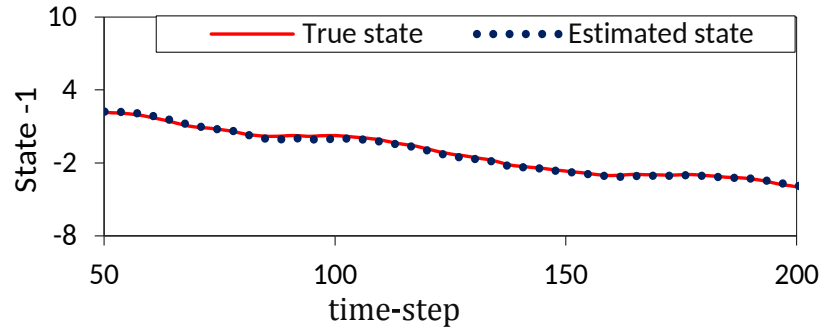
| Filter | 0.1 | 0.2 | 0.3 | 0.4 | 0.5 | 0.6 | 0.7 | 0.8 | 0.9 |
|--------|-------|-------|-------|-------|-------|-------|-------|-------|-------|
| MDKF | 0.384 | 0.395 | 0.406 | 0.414 | 0.430 | 0.427 | 0.431 | 0.427 | 0.425 |
| DKF | 1.000 | 0.977 | 1.031 | 1.052 | 1.023 | 1.029 | 1.063 | 1.026 | 1.040 |
| KF | 4.719 | 4.521 | 4.815 | 4.909 | 4.641 | 4.628 | 4.830 | 4.621 | 4.692 |

Table 3.4: Example-2: Correlation between the true and estimated states obtained for different filters with varying κ_g .

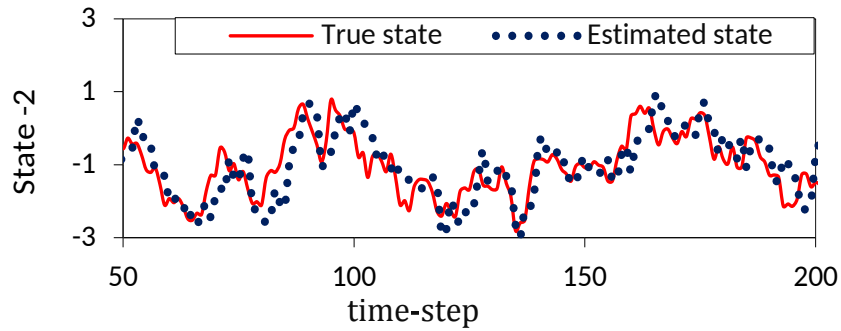
| Filter | 0.1 | 0.2 | 0.3 | 0.4 | 0.5 | 0.6 | 0.7 | 0.8 | 0.9 |
|--------|-------|-------|-------|-------|-------|-------|-------|-------|-------|
| MDKF | 0.884 | 0.988 | 0.984 | 0.986 | 0.986 | 0.842 | 0.988 | 0.954 | 0.987 |
| DKF | 0.888 | 0.975 | 0.980 | 0.984 | 0.978 | 0.815 | 0.990 | 0.929 | 0.984 |
| KF | 0.636 | 0.483 | 0.736 | 0.770 | 0.673 | 0.493 | 0.833 | 0.355 | 0.751 |

3.3 Discussion and conclusion

A wide range of practical problems involving uncertain information, *e.g.*, noisy sensor data and inaccurate experimental data, lead to high demand for the Kalman filter. The

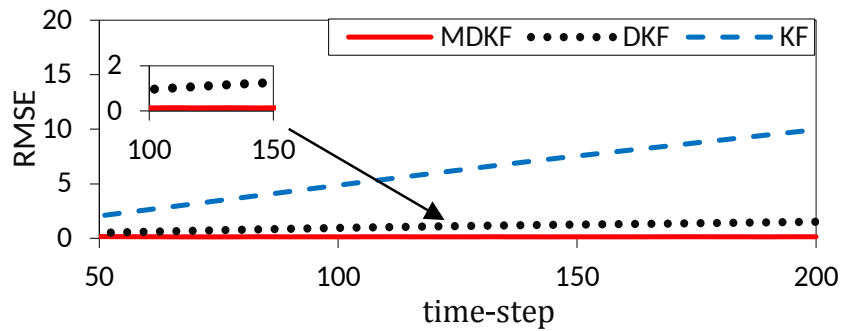


(a) State-1

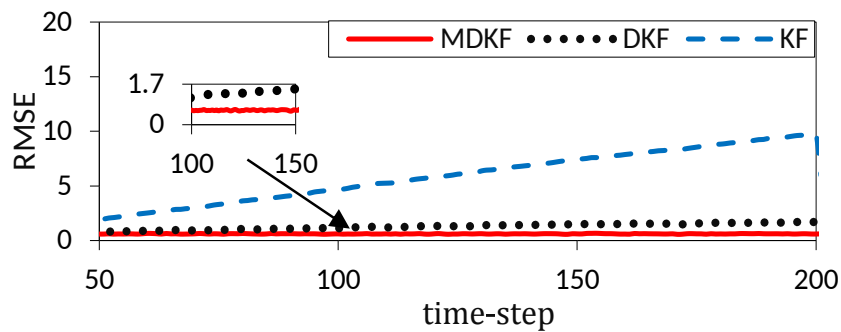


(b) State-2

Figure 3.8: Example-2: Comparison of true and estimated states obtained from MDKF for 1-delay and 0.3 probability of delay: (a) State-1 and (b) State-2.

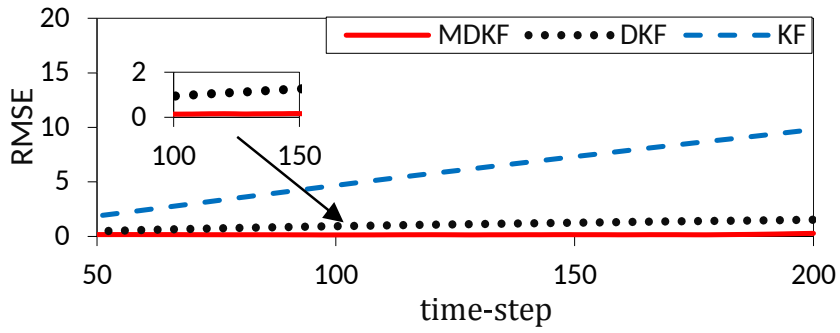


(a) State-1

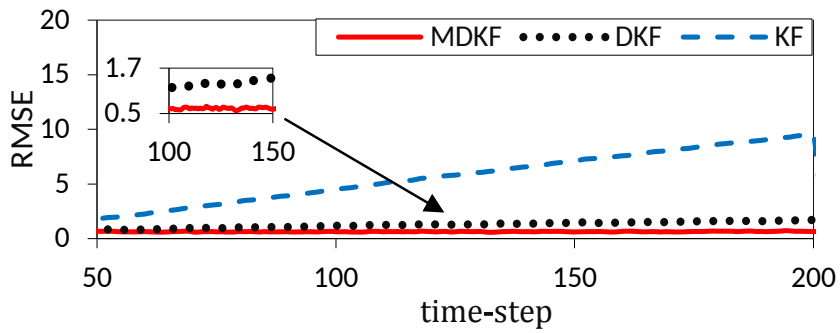


(b) State-2

Figure 3.9: Example-2: RMSE plots for 1-delay with probability of delay 0.3: (a) State-1 and (b) State-2.

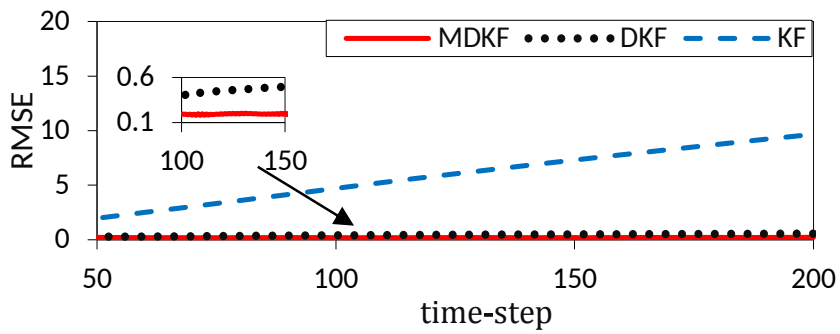


(a) State-1

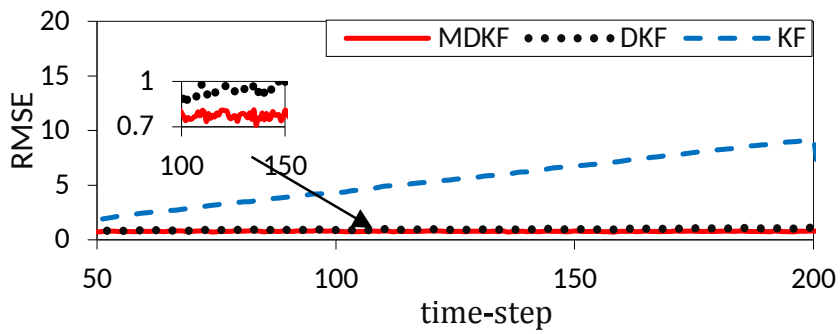


(b) State-2

Figure 3.10: Example-2: RMSE plots for 1-delay with probability of delay 0.5.

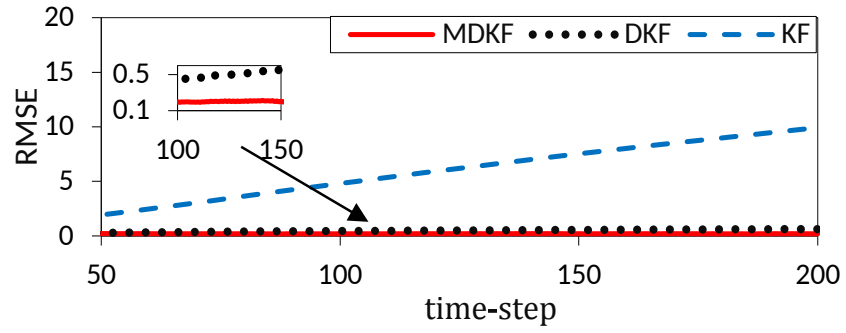


(a) State-1

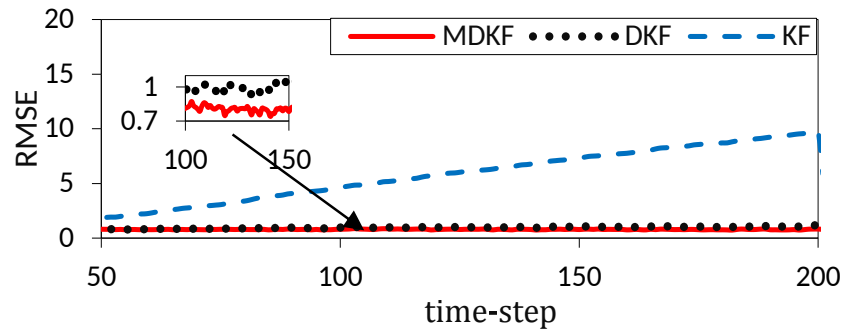


(b) State-2

Figure 3.11: Example-2: RMSE plots for 2-delay with probability of delay 0.3.

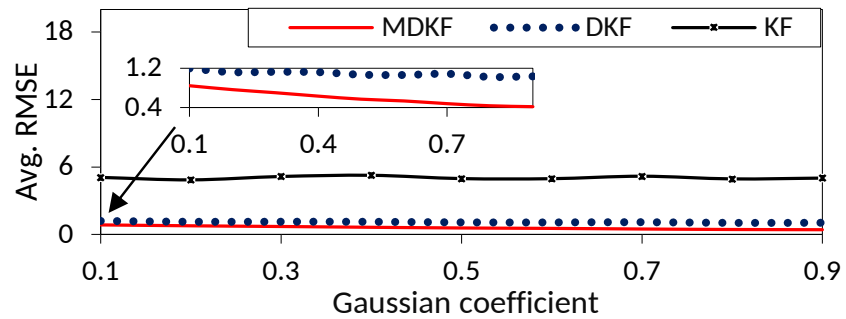


(a) State-1

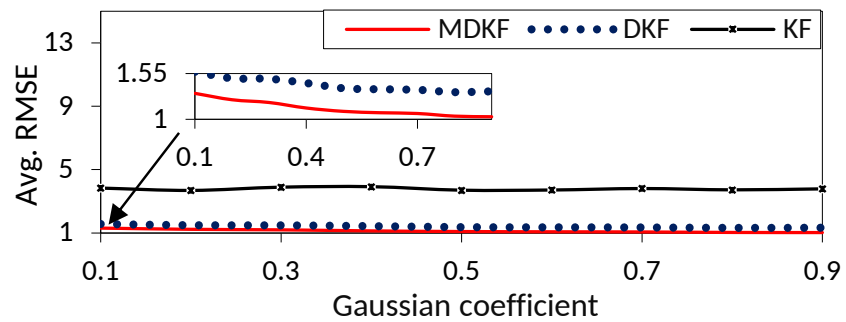


(b) State-2

Figure 3.12: Example-2: RMSE plots for 2-delay with probability of delay 0.5.



(a) State-1



(b) State-2

Figure 3.13: Example-2: Average RMSE plots for varying Gaussian coefficient (κ_g) with 1-delay and probability of delay 0.3.

Table 3.5: Computational time of the proposed MDKF with other existing filter, such as DKF, and KF.

| Filter | MDKF | DKF | KF |
|--------------------------|--------|--------|--------|
| Computational time (sec) | 0.3050 | 0.2788 | 0.2594 |

frequently appearing delayed measurements and non-Gaussian noises either restrict its application or harm the estimation accuracy for many practical problems. This chapter introduces a new modification to the Kalman filter to address these problems in a single algorithm.

The traditional Kalman filter is formulated to consider the statistical measures of the first and second orders. Subsequently, it ignores the higher order noise statistics and underperforms for non-Gaussian noises. To efficiently handle non-Gaussian noise and improve accuracy, we use the Kalman filtering technique under the correntropy maximization criterion, which considers the higher order statistics of noise.

In the case of delayed measurements, the states are updated with mismatched information, resulting in poor accuracy. The proposed modification mitigates this problem by identifying the delay using a likelihood based approach. Subsequently, the measurement is used to update the desired state at a past instant to which it corresponds. For real-time filtering, the estimated state is further updated up to the current instant using the state dynamics.

The proposed Kalman filtering algorithm is the first to simultaneously handle delayed measurements and non-Gaussian noise. We tested it on two filtering problems and compared its performance to the standard Kalman filter and an existing extension that addresses delayed measurements. The performance analysis demonstrates that the proposed method achieves improved estimation accuracy at the cost of a marginally higher computational time.

The current combination of delays in measurement and cyber-attacks may also deteriorate the already suboptimal performance of the wide application of Gaussian filter. As using cyber-physical systems becomes more prevalent, these uncertainties in measurement have become more prevalent and can potentially hinder the estimator's

effectiveness. Consequently, there is a need to extend the Kalman filter to address these issues simultaneously.

Chapter 4

Gaussian Filtering with False Data Injection and Randomly Delayed Measurements

4.1 Introduction

As discussed in Chapters 1 and 2, delay and FDI attack have been among the growing concerns in a cyber-physical system. The Cyber-physical system integrates communication and controller components to physical systems which may encompass elements such as [24][126] software, embedded systems, networks, and physical components. In cyber-physical systems, often state-of-the-art control systems incorporate a wireless communication network to transfer measurement data from geographically distant sensors to the remote estimator [62]. However, due to the unreliable nature of wireless communication networks, various irregularities, such as delays and cyber-attacks, can occur in measurement data. One such popular cyber-attack is a false data injection attack, where an attacker injects fake data into a target system or network. This is also called spoofing or data tampering and can be done through various methods like manipulating data packets or altering a database. The purpose of this attack is to mislead and deceive the target system or users, which can lead to unauthorized access, data theft, or other malicious actions. For instance, an attacker could inject false data into a financial system to manipulate stock prices or transfer

money to an unauthorized account [151]. In this context, Gaussian filtering, a commonly used technique, often underperforms or fails to produce accurate results in the presence of these irregularities[152]. This chapter focuses on two prevalent types of irregularities: unknown delay, caused by data propagation time, and cyber-attacks, where intruders inject false data into the true measurement data.

We refer to Chapter 2 for a comprehensive literature review of filtering methods designed to address delay and FDI attack in measurement. Notably, [104],[106],[108], and [28] have extended the EKF, UKF, and CKF methods to incorporate random delay, while [33] and [32] have reformulated the measurement model stochastically to incorporate the possibility of FDI attacks and re-derived traditional Gaussian filtering accordingly. Although these research developments address delay and cyber-attacks independently, they are incapable of handling their simultaneous occurrences.

In this chapter, to the best of author's knowledge, this filtering solution redesigns the traditional Gaussian filtering method for handling the simultaneously occurring delay and FDI attacks for the first time. The filtering solution provided is named as Gaussian filtering with delay and FDI attack (GFDF). The proposed GFDF reformulates the traditional measurement model using Bernoulli, geometric, and Gaussian random variables to incorporate the possibilities of delay and FDI attack. It re-derives the traditional Gaussian filtering method for a reformulated measurement model. The re-derivation of traditional Gaussian filtering method (for the modified measurement model) requires re-deriving the expressions of measurement estimation, covariance, and state-measurement cross-covariance. Interestingly, the proposed GFDF is a general extension of Gaussian filtering, which applies to any existing Gaussian filters, such as the EKF, CKF, and GHF. This problem studies the stability of the proposed GFDF for its EKF-based formulation. Furthermore, the improved accuracy of the proposed GFDF for its CKF-based formulation is validated. 72

4.2 Problem Description

Recalling Chapter 1, a nonlinear dynamical cyber-physical system can be represented by the following state space model,

$$\mathbf{x}_k = \mathcal{f}_{k-1}(\mathbf{x}_{k-1}) + \mathcal{Q}_{k-1} \quad (4.1)$$

$$\mathbf{y}_k = \mathcal{h}_k(\mathbf{x}_k) + \mathcal{V}_k, \quad (4.2)$$

Please note that this chapter's scope is limited to Gaussian approximated distribution, and refer to Chapter 1 for more details.

This problem considers that the true measurement \mathbf{y}_k may be subjected to two measurement irregularities, such as delayed measurement or FDI attacks. These irregularities can result in the actual observed measurement (\mathbf{z}_k) being different from \mathbf{y}_k . Consequently, the fundamental objective of filtering is to deduce the current \mathbf{x}_k based on the received measurement data \mathbf{z}_k .

Attackers frequently make intermittent changes to measurement data to conceal their intrusion. We hypothesize that the data may be manipulated through FDI and/or delayed measurement at specific instances. To accommodate these factors, The measurement model mentioned in Eq. (4.2) is modified for \mathbf{z}_k by adopting the following modeling techniques:

- To capture the occurrence of data alterations, two Bernoulli random variables, β_k and α_k are introduced. This approach comprises the following steps: i) employ a likelihood test to identify instances with no data alteration and to estimate the value of β_k , ii) perform a correlation analysis to detect delayed measurements and estimate the value of α_k , and iii) Inferred the presence of FDI attacks and estimated the value.
- After detecting an FDI attack, it is possible to model the uncertain false data using a Gaussian distribution. This is because the true measurement is randomly altered through an amplified/attenuated multiplicative process to bypass the pre-assigned

test. In this case, data pre-processing techniques are required to identify an appropriate Gaussian distribution. These steps are outlined in [33].

- Incorporating the geometric distribution is a viable approach for modeling uncertain measurement delays caused by limited resources. This approach enables delayed measurements to be incorporated into the analysis without requiring prior knowledge of the maximum delay. Moreover, using the geometric distribution to model instantaneous delays is an effective way to handle larger delays.

It is worth noting that data pre-analysis and pre-processing are conducted independently in this development, which is not included in the filtering methodology.

Throughout the rest of this chapter, the notations ϕ' and p' will be used to denote $(1 - \phi)$ and $(1 - p)$, respectively, for any random variable ϕ and any probability p . This notation applies to all random variables and probabilities.

The Bernoulli random variables β_k and α_k are subject to the following notion

$$\begin{cases} P(\beta_k = 1) = \mathbb{E}[\beta_k] = \mathbb{E}[(\beta_k)^c] = p_a \\ P(\alpha_k = 1) = \mathbb{E}[\alpha_k] = \mathbb{E}[(\alpha_k)^c] = p_d \end{cases} \quad (4.3)$$

where $\mathbb{E}[\cdot]$ denotes the statistical expectation operator and $c \in \mathbb{R}$ is a constant. Moreover, p_a and p_d denote the probabilities of no-attack and FDI attack, respectively. Similar to Eq. (4.3), corresponding to $P(\beta_k = 0) = p'_a$, we get $\mathbb{E}[\beta'_k] = \mathbb{E}[(\beta'_k)^c] = p'_a$ and $\mathbb{E}[(\beta_k - p_a)^2] = \mathbb{E}[(\beta_k)^2] - \mathbb{E}[\beta_k]^2 = p_a p'_a$. We get similar conclusions for α_k , corresponding to $P(\alpha_k = 0) = p'_d$, after simplification $\mathbb{E}[\alpha'_k] = \mathbb{E}[(\alpha'_k)^c] = p'_d$ and $\mathbb{E}[(\alpha_k - p_d)^2] = \mathbb{E}[(\alpha_k)^2] - \mathbb{E}[\alpha_k]^2 = p_d p'_d$. In addition, d -delay at time t_k can be represented by using a geometric random variable denoted by $G_{d,k}$. This random variable accounts for delays up to d sampling intervals. The probability of obtaining a value of

Table 4.1: α_k and β_k values for different attacks.

| Stochastic parameters | Form of attack |
|--------------------------------------|----------------|
| $\beta_k = 1, \alpha_k \in \{0, 1\}$ | No-attack |
| $\beta_k = 0, \alpha_k = 1$ | FDI-attack |
| $\beta_k = 0, \alpha_k = 0$ | Delayed data |

one for each entry of $G_{d,k}$ can be denoted by p_g . This random variable obeys

$$\begin{cases} P(G_{d,k}(i) = 1) = \mathbb{E}[(G_{d,k}(i))^c] = \Gamma_i \\ P(G_{d,k}(i) = 0) = \mathbb{E}[(G_{d,k}(i)')^c] = \Gamma'_i \\ \mathbb{E}[(G_{d,k}(i) - \Gamma_i)^2] = \Gamma_i \Gamma'_i, \end{cases} \quad (4.4)$$

where $\Gamma_i = (p'_g)^{i-1} p_g$ is the probability of i -delay $\forall i \in \{1, 2, \dots, d\}$ at t_k .

It is crucial to identify and account for false data to avoid its effects on filtering. Various techniques can be employed to achieve this [128] and [33]. Stochastic quantitative methods are instrumental in mitigating the impact of false data, as stochastic rules can be more effective in the presence of unknown intruders and arbitrary data injection. Pre-analysis rules, such as heuristic rules and normalization methods, can also aid in identifying and normalizing false data. In addition, stochastic heuristics can determine the probability of receiving a measurement and adjust amplification and attenuation factors accordingly. False data can be closely approximated as Gaussian data using appropriate heuristic rules and normalization methods. Suppose false data is injected at time t_k , represented as Δ_k , which can be approximated as $\mathcal{N}(\hat{\Psi}, \Sigma_\Psi)$ in the event of an FDI attack at t_k . It is important to note that $\mathbb{E}[\Delta_k^2] = \Sigma_\Psi + \hat{\Psi}^2$ is used in the next section. As discussed in [33], $\hat{\Psi}$ and Σ_Ψ can be determined based on predefined heuristic rules and normalization methods.

Additionally, the random variables are assumed to be independent and uncorrelated. Specifically, we express redesigned measurement model as $\mathbf{z}_k = \beta_k \mathbf{y}_k + \beta'_k [\alpha_k \Delta_k \mathbf{y}_k + \alpha'_k \sum_{i=1}^d G_{d,k}(i) \mathbf{y}_{k-i}]$. This equation can be further simplified to yield

$$\mathbf{z}_k = (\beta_k + \beta'_k \alpha_k \Delta_k) \mathbf{y}_k + \beta'_k \alpha'_k \sum_{i=1}^d G_{d,k}(i) \mathbf{y}_{k-i}. \quad (4.5)$$

Table 4.1 presents the values of α_k and β_k corresponding to different types of attacks. This study aims to re-derive the traditional Gaussian filtering method from a modified measurement model.

Remark 1 *In cyber-attacks, this modified measurement model is useful to counter both data replay attacks and FDI attacks jointly. Moreover, this approach ensures data security and integrity in various contexts and comprehensively controls cyber-attacks.*

4.3 Design methodology of GFDF

In this section, a proposed Gaussian filtering strategy is introduced to handle FDI and delayed measurements that occur concurrently. Prior research has shown that irregularities in measurements can affect the filtering accuracy in a way that is unrelated to the system's state dynamics. Therefore, the proposed filtering strategy only requires the re-derivation of measurement-related parameters because the traditional Gaussian filter prediction step is independent of measurement, and only the update step is influenced by measurement. Specifically, the measurement estimate, covariance, and cross-covariance for the true measurement (\mathbf{y}_k) are denoted as $\hat{\mathbf{y}}_{k|k-1}$, $\mathbf{P}_{k|k-1}^{\mathbf{y}\mathbf{y}}$, and $\mathbf{P}_{k|k-1}^{\mathbf{x}\mathbf{y}}$, respectively. Similarly, the corresponding parameters for an actually received measurement are denoted as $\hat{\mathbf{z}}_{k|k-1}$, $\mathbf{P}_{k|k-1}^{\mathbf{z}\mathbf{z}}$, and $\mathbf{P}_{k|k-1}^{\mathbf{x}\mathbf{z}}$. The proposed Gaussian filter replaces the parameters for a true measurement with those for an actually received measurement. In the subsequent discussion, the authors derive the modified measurement model parameters that account for the concurrent occurrence of FDI and delayed measurements.

We derive $\hat{\mathbf{z}}_{k|k-1}$, $\mathbf{P}_{k|k-1}^{\mathbf{z}\mathbf{z}}$, and $\mathbf{P}_{k|k-1}^{\mathbf{x}\mathbf{z}}$ with respect to \mathbf{z}_k (modeled in Eq. (4.5)) through the three subsequent lemmas.

Lemma 1 : The measurement \mathbf{z}_k can be estimated as follows as a result of jointly occurring delay and cyber-attacks: $\hat{\mathbf{z}}_{k|k-1}$

$$\hat{\mathbf{z}}_{k|k-1} = (p_a + p_a' p_d \hat{\Psi}) \hat{\mathbf{y}}_{k|k-1} + p_a' p_d' \sum_{i=1}^d \Gamma_i \hat{\mathbf{y}}_{k-i|k-1}. \quad (4.6)$$

Proof: Let us denote $\hat{\mathbf{z}}_{k|k-1} = \mathbb{E}[\mathbf{z}_k]$, for \mathbf{z}_k given in Eq. 4.5, computed as

$$\hat{\mathbf{z}}_{k|k-1} = \mathbb{E} \left[(\boldsymbol{\beta}_k + \boldsymbol{\beta}'_k \boldsymbol{\alpha}_k \Delta_k) \mathbf{y}_k + \boldsymbol{\beta}'_k \boldsymbol{\alpha}'_k \sum_{i=1}^d G_{d,k}(i) \mathbf{y}_{k-i} \right].$$

Please note that $\boldsymbol{\beta}_k$, $\boldsymbol{\alpha}_k$, Δ_k , and $G_{d,k}(i)$ characterize measurement irregularities, and they are independent of \mathbf{y}_k , which defines measurement values at the current instant. Thus, as $\mathbb{E}[\mathbf{y}_k] = \hat{\mathbf{y}}_{k|k-1}$, after simplification of $\boldsymbol{\beta}_k$, $\boldsymbol{\alpha}_k$, and $G_{d,k}$, we get

$$\hat{\mathbf{z}}_{k|k-1} = \mathbb{E} [\boldsymbol{\beta}_k + \boldsymbol{\beta}'_k \boldsymbol{\alpha}_k \Delta_k] \hat{\mathbf{y}}_{k|k-1} + \mathbb{E} [\boldsymbol{\alpha}'_k \boldsymbol{\beta}'_k] \sum_{i=1}^d \mathbb{E} [G_{d,k}(i)] \hat{\mathbf{y}}_{k-i|k-1}.$$

Substituting $\mathbb{E}[\boldsymbol{\alpha}_k]$, $\mathbb{E}[\boldsymbol{\beta}_k]$, and $\mathbb{E}[G_{d,k}(i)]$ from Eqs. (4.3) and (4.4), and their subsequent discussions, the above equation reduces to Eq. (4.6). \square

Lemma 2 : The covariance matrix $\mathbf{P}_{k|k-1}^{\mathbf{z}\mathbf{z}}$ for \mathbf{z}_k can be given as

$$\begin{aligned} \mathbf{P}_{k|k-1}^{\mathbf{z}\mathbf{z}} &= (p_a + p'_a p_d (\Sigma_\Psi + \hat{\Psi}^2)) + 2p_a p'_d \hat{\Psi} \mathbf{P}_{k|k-1}^{\mathbf{y}\mathbf{y}} + (p_a p'_a + p'_a p_d \hat{\Psi}^2 (1 - p'_a p_d) + p'_a p_d \Sigma_\Psi) \\ &\quad \hat{\mathbf{y}}_{k|k-1} \hat{\mathbf{y}}_{k|k-1}^T + p'_a p'_d \sum_{i=1}^d \Gamma_i \mathbf{P}_{k-i|k-1}^{\mathbf{y}\mathbf{y}} + \sum_{i=1}^d (p'_a p'_d \Gamma_i (1 - p'_a p'_d \Gamma_i)) \hat{\mathbf{y}}_{k-i|k-1} \hat{\mathbf{y}}_{k-i|k-1}^T + \\ &\quad \sum_{i \neq j=1}^d (p'_a p'_d (p'_g)^{i+j-2} p_g^2 (1 - p'_a p'_d (p'_g)^{i+j-2} p_g^2)) \hat{\mathbf{y}}_{k-i|k-1} \hat{\mathbf{y}}_{k-j|k-1}^T. \end{aligned} \quad (4.7)$$

Proof: The covariance matrix $\mathbf{P}_{k|k-1}^{\mathbf{z}\mathbf{z}}$ is given as

$$\mathbf{P}_{k|k-1}^{\mathbf{z}\mathbf{z}} = \mathbb{E} [(\mathbf{z}_k - \hat{\mathbf{z}}_{k|k-1})(\mathbf{z}_k - \hat{\mathbf{z}}_{k|k-1})^T]. \quad (4.8)$$

We can express the difference between \mathbf{z}_k and $\hat{\mathbf{z}}_{k|k-1}$ using Eqs. (4.5) and (4.6) as

$$\begin{aligned} \mathbf{z}_k - \hat{\mathbf{z}}_{k|k-1} &= \underbrace{(\boldsymbol{\beta}_k + \boldsymbol{\beta}'_k \boldsymbol{\alpha}_k \Delta_k)(\mathbf{y}_k - \hat{\mathbf{y}}_{k|k-1})}_{J_1} + \underbrace{(\boldsymbol{\beta}_k + \boldsymbol{\beta}'_k \boldsymbol{\alpha}_k \Delta_k - p_a - p'_a p_d \hat{\Psi}) \hat{\mathbf{y}}_{k|k-1}}_{J_2} \\ &\quad + \underbrace{\sum_{i=1}^d \boldsymbol{\beta}'_k \boldsymbol{\alpha}'_k G_{d,k}(i)(\mathbf{y}_{k-i} - \hat{\mathbf{y}}_{k-i|k-1})}_{J_3} + \underbrace{\sum_{i=1}^d (\boldsymbol{\beta}'_k \boldsymbol{\alpha}'_k G_{d,k}(i) - p'_a p'_d \Gamma_i) \hat{\mathbf{y}}_{k-i|k-1}}_{J_4}. \end{aligned} \quad (4.9)$$

By substituting $\mathbf{z}_k - \hat{\mathbf{z}}_{k|k-1}$ from Eq. (4.9) into Eq. (4.8), we obtain $\mathbf{P}_{k|k-1}^{\mathbf{z}\mathbf{z}} =$

$\sum_{i=1}^4 \sum_{j=1}^4 \mathbb{E} [J_i J_j^T]$. Stochastic filtering theory typically assumes that independent random variables possess stochastic independence properties. Applying this assumption, it can be concluded that $\mathbb{E}[J_i J_j^T] = 0$ for all $i \neq j$. As an example, we can write $\mathbb{E}[J_1 J_2^T] = \mathbb{E}[(\beta_k + \beta'_k \alpha_k \Delta_k)(\mathbf{y}_k - \hat{\mathbf{y}}_{k|k-1})(\beta_k + \beta'_k \alpha_k \Delta_k - (p_a + p'_a p_d \hat{\Psi})) \hat{\mathbf{y}}_k^T]$, which can be rewritten as $\mathbb{E}[J_1 J_2^T] = \mathbb{E}[(\beta_k + \beta'_k \alpha_k \Delta_k)] \mathbb{E}[(\mathbf{y}_k - \hat{\mathbf{y}}_{k|k-1})] \mathbb{E}[(\beta_k + \beta'_k \alpha_k \Delta_k - (p_a + p'_a p_d \hat{\Psi}))] \mathbb{E}[\hat{\mathbf{y}}_k^T]$. After further simplification and substituting the values from Eq. (4.3), we get $\mathbb{E}[J_1 J_2^T] = 0$. Similarly, we can easily conclude for other expressions $\mathbb{E}[J_i J_j^T] \forall i \neq j$. Thus,

$$\mathbf{P}_{k|k-1}^{zz} = \sum_{i=1}^4 \mathbb{E} [J_i J_i^T]. \quad (4.10)$$

We now derive $\mathbb{E}[J_i J_i^T] \forall i \in \{1, 2, \dots, 4\}$, which we add later to obtain $\mathbf{P}_{k|k-1}^{zz}$.

For J_1 given in Eq. (4.9), we can write

$$\mathbb{E} [J_1 J_1^T] = \mathbb{E} \left[(\beta_k + \beta'_k \alpha_k \Delta_k)^2 (\mathbf{y}_k - \hat{\mathbf{y}}_{k|k-1})(\mathbf{y}_k - \hat{\mathbf{y}}_{k|k-1})^T \right].$$

Please note that α_k and β_k are independent of \mathbf{y}_k and $\hat{\mathbf{y}}_{k|k-1}$. Moreover, as α_k and β_k are independent Bernoulli random variables, we obtain $\mathbb{E}[(\beta_k + \beta'_k \alpha_k \Delta_k)^2] = \mathbb{E}[(\beta_k^2 + \beta_k'^2 \alpha_k^2 \Delta_k^2 + 2\beta_k \beta_k' \alpha_k \Delta_k)]$. Substituting the values from Eq.(3) and $\Delta_k^2 = \Sigma_\Psi + \hat{\Psi}$, we get $\mathbb{E}[(\beta_k + \beta'_k \alpha_k \Delta_k)^2] = p_a + p'_a p_d (\Sigma_\Psi + \hat{\Psi}^2) + 2p_a p'_d \hat{\Psi}$. Subsequently, the above equation is simplified as

$$\mathbb{E} [J_1 J_1^T] = (p_a + p'_a p_d (\Sigma_\Psi + \hat{\Psi}^2) + 2p_a p'_d \hat{\Psi}) P_{k|k-1}^{yy}. \quad (4.11)$$

Similarly, for J_2 given in Eq. (4.9), we obtain

$$\mathbb{E} [J_2 J_2^T] = \mathbb{E} \left[(\beta_k + \beta'_k \alpha_k \Delta_k - (p_a + p'_a p_d \hat{\Psi}))^2 \hat{\mathbf{y}}_{k|k-1} \hat{\mathbf{y}}_{k|k-1}^T \right],$$

which is further simplified as

$$\mathbb{E} [J_2 J_2^T] = (p_a p'_a + p'_a p_d \hat{\Psi}^2 (1 - p'_a p_d) + p'_a p_d \Sigma_\Psi) \hat{\mathbf{y}}_{k|k-1} \hat{\mathbf{y}}_{k|k-1}^T. \quad (4.12)$$

Now substituting J_3 from Eq. (4.9) into $\mathbb{E} [J_3 J_3^T]$ to obtain

$$\mathbb{E} [J_3 J_3^T] = \mathbb{E} \left[\sum_{i=1}^d \beta'_k \alpha'_k G_{d,k}(i) (\mathbf{y}_{k-i} - \hat{\mathbf{y}}_{k-i|k-1}) \sum_{j=1}^d \beta'_k \alpha'_k G_{d,k}(j) (\mathbf{y}_{k-j} - \hat{\mathbf{y}}_{k-j|k-1})^T \right].$$

Here are some notes we ought to consider: 1) \mathbf{y}_{k-i} and \mathbf{y}_{k-j} are independent of $\forall i \neq j$, 2) $G_{d,k}(i)$ and $G_{d,k}(j)$ are independent of $\forall i \neq j$, and 3) α_k and β_k are independent of each other, and also independent of \mathbf{y}_{k-i} and $G_{d,k}(i) \forall i \in \{1, 2, \dots, d\}$. Based on their independently derived properties, we are able to simplify the above equation further as

$$\mathbb{E} [J_3 J_3^T] = p'_a p'_d \sum_{i=1}^d \Gamma_i \mathbf{P}_{k-i|k-1}^{\mathbf{y}\mathbf{y}}. \quad (4.13)$$

To this end, for J_4 given in Eq. (4.9), we get

$$\mathbb{E} [J_4 J_4^T] = \mathbb{E} \left[\sum_{i=1}^d (\beta'_k \alpha'_k G_{d,k}(i) - p'_a p'_d \Gamma_i)^2 \hat{\mathbf{y}}_{k-i|k-1} \hat{\mathbf{y}}_{k-i|k-1}^T \right]. \quad (4.14)$$

According to various independence properties for independent random variables, the above equation can be written as follows:

$$\begin{aligned} \mathbb{E} [J_4 J_4^T] &= \sum_{i=j=1}^d p'_a p'_d \Gamma_i (1 - p_a p'_d \Gamma_i) \hat{\mathbf{y}}_{k-i|k-1} \hat{\mathbf{y}}_{k-i|k-1}^T + \sum_{i \neq j=1}^d (p'_a \\ & p'_d (p'_g)^{i+j-2} p_g^2) (1 - (p'_a p'_d (p'_g)^{i+j-2} p_g^2)) \hat{\mathbf{y}}_{k-i|k-1} \hat{\mathbf{y}}_{k-j|k-1}^T. \end{aligned} \quad (4.15)$$

Substituting $\mathbb{E} [J_1 J_1^T]$, $\mathbb{E} [J_2 J_2^T]$, $\mathbb{E} [J_3 J_3^T]$, and $\mathbb{E} [J_4 J_4^T]$, from Eqs. (4.11), (4.12), (4.13), and (4.15), respectively, into Eq. (4.10), $\mathbf{P}_{k|k-1}^{\mathbf{z}\mathbf{z}}$ can be expressed in the form of Eq. (4.7).

□

Lemma 3 : The cross-covariance matrix between \mathbf{x}_k and \mathbf{z}_k can be obtained as

$$\mathbf{P}_{k|k-1}^{\mathbf{x}\mathbf{z}} = (p_a + p'_a p_d \hat{\Psi}) \mathbf{P}_{k|k-1}^{\mathbf{x}\mathbf{y}} + \sum_{i=1}^d p'_a p'_d \Gamma_i \mathbf{P}_{k-i|k-1}^{\mathbf{x}\mathbf{y}}. \quad (4.16)$$

Proof: For $\mathbf{z}_k - \hat{\mathbf{z}}_{k|k-1}$ given in Eq. (4.9), we get $\mathbf{P}_{k|k-1}^{\mathbf{x}\mathbf{z}} = \sum_{i=1}^4 \mathbb{E} [(\mathbf{x}_k - \hat{\mathbf{x}}_{k|k-1}) J_i^T]$. As $\hat{\mathbf{y}}_{k|k-1}$, $\hat{\mathbf{y}}_{k-i|k-1}$, and $\hat{\Psi}$ are constants and \mathbf{x}_k is independent of Δ_k , we can conclude that

$\sum_i \mathbb{E} [(\mathbf{x}_k - \hat{\mathbf{x}}_{k|k-1})J_i^T] = 0, \forall i \in \{2, 4\}$, giving

$$\mathbf{P}_{k|k-1}^{\mathbf{xy}} = \mathbb{E} [(\mathbf{x}_k - \hat{\mathbf{x}}_{k|k-1})J_1^T] + \mathbb{E} [(\mathbf{x}_k - \hat{\mathbf{x}}_{k|k-1})J_3^T]. \quad (4.17)$$

To this end, for J_1 given in Eq. (4.9), we obtain

$$\mathbb{E} [(\mathbf{x}_k - \hat{\mathbf{x}}_{k|k-1})J_1^T] = \mathbb{E} [(\mathbf{x}_k - \hat{\mathbf{x}}_{k|k-1})(\beta_k + \beta'_k \alpha_k \Delta_k)(\mathbf{y}_k - \hat{\mathbf{y}}_{k|k-1})^T]$$

which is simplified as

$$\mathbb{E} [(\mathbf{x}_k - \hat{\mathbf{x}}_{k|k-1})J_1^T] = (p_a + p'_a p_d \hat{\Psi}) \mathbf{P}_{k|k-1}^{\mathbf{xy}}. \quad (4.18)$$

Moreover, for J_3 given in Eq. (4.9), we get

$$\mathbb{E} [(\mathbf{x}_k - \hat{\mathbf{x}}_{k|k-1})J_3^T] = \mathbb{E} [(\mathbf{x}_k - \hat{\mathbf{x}}_{k|k-1}) \left(\sum_{i=1}^d \beta'_k \alpha'_k G_{d,k}(i) (\mathbf{y}_{k-i} - \hat{\mathbf{y}}_{k-i|k-1})^T \right)].$$

Applying the independent property, we get the following after a few simplifications and rearrangements.

$$\mathbb{E} [(\mathbf{x}_k - \hat{\mathbf{x}}_{k|k-1})J_3^T] = \mathbb{E} [\beta'_k \alpha'_k] \sum_{i=1}^d \left(\mathbb{E} [G_{d,k}(i)] \mathbb{E} [(\mathbf{x}_k - \hat{\mathbf{x}}_{k|k-1})(\mathbf{y}_{k-i} - \hat{\mathbf{y}}_{k-i|k-1})^T] \right).$$

As $\mathbb{E} [\beta'_k \alpha'_k] = p'_a p'_d$ and $\mathbb{E} [G_{d,k}(i)] = \Gamma_i$, we obtain

$$\mathbb{E} [(\mathbf{x}_k - \hat{\mathbf{x}}_{k|k-1})J_3^T] = \sum_{i=1}^d p'_a p'_d \Gamma_i \mathbf{P}_{k-i|k-1}^{\mathbf{xy}}. \quad (4.19)$$

Substituting Eqs. (4.18) and (4.19) into Eq. (4.17), we get $\mathbf{P}_{k|k-1}^{\mathbf{xz}}$ in the form of Eq. (4.16). \square

In light of the above discussion, we have derived a new method known as GFDF to counter cyber-attacks on measurements and delay measurements concurrently. This method replaces the traditional Gaussian filters estimated measurement vector $\hat{\mathbf{y}}_{k|k-1}$,

the covariance matrix of the measurement error $\mathbf{P}_{k|k-1}^{\mathbf{y}\mathbf{y}}$, and the cross-covariance matrix between the state and measurement $\mathbf{P}_{k|k-1}^{\mathbf{x}\mathbf{y}}$ with their counterparts for the altered measurements, namely the estimated measurement vector $\hat{\mathbf{z}}_{k|k-1}$, the covariance matrix of the measurement error $\mathbf{P}_{k|k-1}^{\mathbf{z}\mathbf{z}}$, and the cross-covariance matrix between the state and measurement $\mathbf{P}_{k|k-1}^{\mathbf{x}\mathbf{z}}$. These parameters are computed by utilizing the three lemmas mentioned above. Incorporating measurement irregularities into GFDF allows a more precise estimation of the system state even under attack and delayed measurement. The estimated measurement vector $\hat{\mathbf{z}}_{k|k-1}$ considers the impact of the attack and delayed measurement, while the covariance matrix of the measurement error $\mathbf{P}_{k|k-1}^{\mathbf{z}\mathbf{z}}$ captures the measurement uncertainty caused by these irregularities. The cross-covariance matrix between the state and measurement $\mathbf{P}_{k|k-1}^{\mathbf{x}\mathbf{z}}$ reflects the relationship between the system state and the altered measurement. For estimating the status of systems affected by cyber-attacks, GFDF is more resilient and accurate. By including the effects of these irregularities in the estimation process, the system becomes more resilient and remains uninterrupted in the scenario of malicious attacks.

Remark 2 *The proposed GFDF utilizes some estimate and covariance expressions from past instants, which increases its storage requirement.*

4.4 Stability of the GFDF

This section undertakes a stochastic stability analysis of the proposed filter, utilizing the concept of “exponential boundedness in mean square.” To accomplish this, we opt for the EKF-based formulation of the proposed filtering algorithm, abbreviated as EKDF. To begin, we construct the dynamic model for the estimation error of the EKDF. Subsequently, we demonstrate that the estimation error of the EKDF remains exponentially bounded in the mean square. To ensure stability, the associated parameters must be bounded, for which a detailed explanation is given in the later part of the chapter. Prior to continuing, we review the conventional notion used to evaluate the aforementioned stability concept [153].

Statement 4.4.1 A stochastic process is said to be exponential bounded in mean square sense if there are real numbers $\theta_1 > 0$, $\theta_2 > 0$, $\rho > 0$, and $0 < \kappa \leq 1$. There exists a positive definite function $\mathbb{V}(\zeta_k)$ for a stochastic process ζ_k , satisfying the following conditions

$$\begin{cases} \theta_1 \|\zeta_k\|^2 \leq \mathbb{V}(\zeta_k) \leq \theta_2 \|\zeta_k\|^2 \\ \mathbb{E}[\mathbb{V}(\zeta_k)|\zeta_{k-1}] - \mathbb{V}(\zeta_{k-1}) \leq \rho - \kappa \mathbb{V}(\zeta_{k-1}) \leq 0 \end{cases} \quad (4.20)$$

that jointly conclude

$$\mathbb{E}[\|\zeta_k\|^2] \leq \frac{\theta_2}{\theta_1} \mathbb{E}[\|\zeta_0\|^2] (1 - \kappa)^k + \frac{\rho}{\theta_1} \sum_{i=0}^{k-1} (1 - \kappa)^i, \quad (4.21)$$

where $\|\cdot\|$ denotes the spectral norm. For further elaboration, please refer to [153].

Remark 3 Eq. (4.21) is the mathematical definition of “exponential boundedness in a mean square” [153]. Therefore, if the stochastic process ζ_k satisfies this equation, it is stable in the sense of exponential boundedness. Moreover, Eq. (4.21) is inferred from Eq. (4.20); thus, ζ_k must satisfy the conditions in Eq. (4.20) to be exponentially stable in mean square.

To proceed with the dynamic model for the estimation error of the proposed filter, we recall the traditional EKF parameters [154].

$$\begin{cases} \hat{\mathbf{x}}_{k|k-1} = \mathcal{f}(\hat{\mathbf{x}}_{k-1|k-1}) \\ \mathbf{P}_{k|k-1} = \mathcal{F}_{k-1} \mathbf{P}_{k-1|k-1} \mathcal{F}_{k-1}^T + \mathbf{Q}_{k-1}, \end{cases} \quad (4.22)$$

where $\hat{\mathbf{x}}_{k|k-1}$ and $\mathbf{P}_{k|k-1}$ represent respectively the predicted state and its error covariance at t_k ; \mathcal{F}_{k-1} represents the Jacobian matrix of $\mathcal{f}(\mathbf{x}_{k-1})$. Now consider the measurement update parameters [154]

$$\begin{cases} \hat{\mathbf{y}}_{k|k-1} = \mathcal{h}(\hat{\mathbf{x}}_{k|k-1}) \\ \mathbf{P}_{k|k-1}^{\mathbf{y}\mathbf{y}} = \mathcal{H}_k \mathbf{P}_{k|k-1} \mathcal{H}_k^T + \mathbf{R}_k \\ \mathbf{P}_{k|k-1}^{\mathbf{x}\mathbf{y}} = \mathbf{P}_{k|k-1} \mathcal{H}_k^T \\ \hat{\mathbf{x}}_{k|k} = \hat{\mathbf{x}}_{k|k-1} + \mathbf{K} (\mathbf{y}_k - \hat{\mathbf{y}}_{k|k-1}), \end{cases} \quad (4.23)$$

with \mathcal{H}_k denoting the Jacobian of $\mathbf{h}(\mathbf{x}_k)$.

Moreover, the Taylor series approximations for $\mathbf{f}(\mathbf{x}_k)$ and $\mathbf{h}(\mathbf{x}_k)$ can be given as

$$\begin{cases} \mathbf{f}(\mathbf{x}_k) = \mathbf{f}(\hat{\mathbf{x}}_{k|k}) + \mathcal{F}_k \mathbf{e}_{k|k} + \mathcal{F}_t(\mathbf{x}_k, \hat{\mathbf{x}}_{k|k}) \\ \mathbf{h}(\mathbf{x}_k) = \mathbf{h}(\hat{\mathbf{x}}_{k|k-1}) + \mathcal{H}_k \mathbf{e}_{k|k-1} + \mathcal{H}_t(\mathbf{x}_k, \hat{\mathbf{x}}_{k|k-1}), \end{cases} \quad (4.24)$$

where $\mathbf{e}_{k|k} = \mathbf{x}_k - \hat{\mathbf{x}}_{k|k}$ and $\mathbf{e}_{k|k-1} = \mathbf{x}_k - \hat{\mathbf{x}}_{k|k-1}$ are the estimation and prediction errors, respectively; $\mathcal{F}_t(\mathbf{x}_k, \hat{\mathbf{x}}_{k|k})$ and $\mathcal{H}_t(\mathbf{x}_k, \hat{\mathbf{x}}_{k|k-1})$ denote the respective remainder terms.

The posterior estimate for \mathbf{z}_k is $\hat{\mathbf{x}}_{k|k} = \hat{\mathbf{x}}_{k|k-1} + \mathbf{K}(\mathbf{z}_k - \hat{\mathbf{z}}_{k|k-1})$, giving $\mathbf{e}_{k|k} = \mathbf{e}_{k|k-1} - \mathbf{K}(\mathbf{z}_k - \hat{\mathbf{z}}_{k|k-1})$. Subsequently, from Eqs. (4.1), (4.5), (4.6), (4.23), and (4.24), the dynamical model of $\mathbf{e}_{k|k}$ can be obtained as

$$\mathbf{e}_{k|k} = \bar{\mathcal{A}}_k \mathbf{e}_{k-1|k-1} + \bar{\mathcal{B}}_k + \bar{\mathcal{C}}_k + \bar{\mathcal{D}}_k, \quad (4.25)$$

where

$$\begin{cases} \bar{\mathcal{A}}_k = (\mathbb{I} - (p_a + p'_a p_d \hat{\Psi}) \mathbf{K} \mathcal{H}_k) \mathcal{F}_{k-1} \\ \bar{\mathcal{B}}_k = \mathcal{Q}_{k-1} - \mathbf{K}((\beta_k + \beta'_k \alpha_k \Delta_k) \mathcal{V}_k + \beta'_k \alpha'_k \sum_{i=1}^d G_{d,k}(i) \mathcal{V}_{k-i}) \\ \bar{\mathcal{C}}_k = \mathcal{F}_t(\mathbf{x}_k, \hat{\mathbf{x}}_{k|k}) - \mathbf{K}((\beta_k + \beta'_k \alpha_k \Delta_k) \mathcal{H}_t(\mathbf{x}_k, \hat{\mathbf{x}}_{k|k-1}) + \beta'_k \alpha'_k \sum_{i=1}^d G_{d,k}(i) \mathcal{H}_t(\mathbf{x}_{k-i}, \\ \hat{\mathbf{x}}_{k-i|k-1})) \\ \bar{\mathcal{D}}_k = -\mathbf{K} \left[(\beta_k + \beta'_k \alpha_k \Delta_k) \mathcal{H}_k \mathbf{e}_{k|k-1} + \beta'_k \alpha'_k \sum_{i=1}^d G_{d,k}(i) \mathcal{H}_{k-i} \mathbf{e}_{k-i|k-1} + ((\beta_k + \beta'_k \alpha_k \Delta_k) - \right. \\ \left. (p_a + p'_a p_d \hat{\Psi})) \times \mathbf{h}(\hat{\mathbf{x}}_{k|k-1}) + \sum_{i=1}^d (\beta'_k \alpha'_k G_{d,k}(i) - p'_a p'_d \Gamma_i) \mathbf{h}(\hat{\mathbf{x}}_{k-i|k-1}) + (p_a + p'_a p_d \hat{\Psi}) \right. \\ \left. \mathcal{H}_k \mathcal{F}_{k-1} \mathbf{e}_{k|k-1} \right]. \end{cases} \quad (4.26)$$

Following Remark 3, the error (4.25) should satisfy Eq. (4.20) for the EKDF to be exponentially bounded in the mean square. Let us first introduce the following bounds and conditions required to prove the stochastic stability of EKDF [153].

- \mathcal{F}_k is non-singular $\forall k$.
- Matrices and vectors are bounded via

where $\mathcal{V}_1, \mathcal{V}_2, \tau_1, \tau_2, \chi_1, \chi_2, \xi, \mathcal{H}, \mathcal{P}_1, \mathcal{P}_2, \mathcal{Q}_1, \mathcal{Q}_2, \mathcal{R}_1,$ and \mathcal{R}_2 are real numbers.

$$\left\{ \begin{array}{l} \|\mathcal{Q}_k\| \leq \mathcal{V}_1, \|\mathcal{V}_k\| \leq \mathcal{V}_2, \|\mathcal{F}_t(\mathbf{x}_{k-1}, \hat{\mathbf{x}}_{k-1|k-1})\| \leq \tau_1 \|\mathbf{x}_{k-1} - \hat{\mathbf{x}}_{k-1|k-1}\|^2, \\ \|\mathcal{H}_t(\mathbf{x}_k, \hat{\mathbf{x}}_{k|k-1})\| \leq \tau_2 \|\mathbf{x}_k - \hat{\mathbf{x}}_{k|k-1}\|^2, \|\mathcal{F}_k\| \leq \chi_1, \|\mathcal{H}_k\| \leq \chi_2, \|\mathbf{x}_{k-1} - \hat{\mathbf{x}}_{k-1|k-1}\| \\ = \|\mathbf{e}_{k-1|k-1}\| \leq \xi, \|\mathbf{x}_k - \hat{\mathbf{x}}_{k|k-1}\| = \|\mathbf{e}_{k|k-1}\| \leq \xi, \|\mathcal{R}(\hat{\mathbf{x}}_{k|k-1})\| \leq \mathcal{H}, \mathcal{P}_1 \mathbb{I} \leq \mathbf{P}_{k|k} \leq \\ \mathbf{P}_{k|k-1} \leq \mathcal{P}_2 \mathbb{I}, \mathcal{Q}_1 \mathbb{I} \leq \mathbf{Q}_k \leq \mathcal{Q}_2 \mathbb{I}, \text{ and } \mathcal{R}_1 \mathbb{I} \leq \mathbf{R}_k \leq \mathcal{R}_2 \mathbb{I}, \end{array} \right. \quad (4.27)$$

Theorem 1 For the bounds presented in Eq. (4.27), the stochastic dynamic model $\mathbf{e}_{k|k}$ (Eq. (4.25)) remains exponentially bounded in mean square. Alternatively, it satisfies

$$\mathbb{E} \left[\|\mathbf{e}_{k|k}\|^2 \right] \leq \frac{\theta_2}{\theta_1} \mathbb{E} \left[\|\mathbf{e}_{0|0}\|^2 \right] (1 - \kappa)^k + \frac{\rho}{\theta_1} \sum_{i=0}^{k-1} (1 - \kappa)^i, \quad (4.28)$$

Proof 1 We now consider the positive definite function as $\mathbb{V}(\mathbf{e}_{k|k}) = \mathbf{e}_{k|k}^T \mathbf{P}_{k|k} \mathbf{e}_{k|k}$, and substitute $\mathbf{e}_{k|k}$ from Eq. (4.25). Thus we can express $\mathbb{V}(\mathbf{e}_{k|k})$ as

$$\begin{aligned} \mathbb{V}(\mathbf{e}_{k|k}) = & \mathbf{e}_{k-1|k-1}^T \bar{\mathcal{A}}_k^T \mathbf{P}_{k|k}^{-1} \bar{\mathcal{A}}_k \mathbf{e}_{k-1|k-1} + \bar{\mathcal{C}}_k^T \mathbf{P}_{k|k}^{-1} (2\bar{\mathcal{A}}_k \mathbf{e}_{k-1|k-1} + \bar{\mathcal{C}}_k) + 2\bar{\mathcal{B}}_k^T \mathbf{P}_{k|k}^{-1} (\bar{\mathcal{A}}_k \mathbf{e}_{k-1|k-1} \\ & + \bar{\mathcal{C}}_k + \bar{\mathcal{D}}_k) + \bar{\mathcal{B}}_k^T \mathbf{P}_{k|k}^{-1} \bar{\mathcal{B}}_k + 2\bar{\mathcal{D}}_k^T \mathbf{P}_{k|k}^{-1} (\bar{\mathcal{A}}_k \mathbf{e}_{k-1|k-1} + \bar{\mathcal{C}}_k) + \bar{\mathcal{D}}_k^T \mathbf{P}_{k|k}^{-1} \bar{\mathcal{D}}_k. \end{aligned} \quad (4.29)$$

We now adopt the following steps for proving that $\mathbb{V}(\mathbf{e}_{k|k})$ satisfies the conditions given in Eq. (4.20).

- Similar to [155], we obtain $\bar{\mathcal{A}}_k^T \mathbf{P}_{k|k}^{-1} \bar{\mathcal{A}}_k \leq (1 - \kappa) \mathbf{P}_{k-1|k-1}^{-1}$, which further gives $\mathbf{e}_{k-1|k-1}^T \bar{\mathcal{A}}_k^T \mathbf{P}_{k|k}^{-1} \bar{\mathcal{A}}_k \mathbf{e}_{k-1|k-1} \leq (1 - \kappa) \mathbb{V}(\mathbf{e}_{k-1|k-1})$.
- Note that $\mathbb{V}(\mathbf{e}_{k|k})$ is scalar. Thus, following [155], we calculate: i) $\bar{\mathcal{C}}_k^T \mathbf{P}_{k|k}^{-1} (2\bar{\mathcal{A}}_k \mathbf{e}_{k-1|k-1} + \bar{\mathcal{C}}_k) \leq \lambda_1 \xi^2$, ii) $\bar{\mathcal{B}}_k^T \mathbf{P}_{k|k}^{-1} \bar{\mathcal{B}}_k \leq \lambda_2$, iii) $2\bar{\mathcal{D}}_k^T \mathbf{P}_{k|k}^{-1} (\bar{\mathcal{A}}_k \mathbf{e}_{k-1|k-1} + \bar{\mathcal{C}}_k) \leq \lambda_3 \xi^3 + \lambda_4 \xi^2 + \lambda_5 \xi + \lambda_6$, and iv) $\bar{\mathcal{D}}_k^T \mathbf{P}_{k|k}^{-1} \bar{\mathcal{D}}_k \leq \lambda_7 \xi^2 + \lambda_8 \xi + \lambda_9$, with $\lambda_1, \lambda_2, \lambda_3, \lambda_4, \lambda_5, \lambda_6, \lambda_7, \lambda_8$, and λ_9 being expressions in terms of $\mathcal{V}_1, \mathcal{V}_2, \tau_1, \tau_2, \chi_1, \chi_2, \xi, \mathcal{H}, \mathcal{P}_1, \mathcal{P}_2, \mathcal{Q}_1, \mathcal{Q}_2, \mathcal{R}_1$, and \mathcal{R}_2 . For more details, please refer to [155].
- The expectation operator afterwards gives $\mathbb{E}[2\bar{\mathcal{B}}_k^T \mathbf{P}_{k|k}^{-1} (\bar{\mathcal{A}}_k \mathbf{e}_{k-1|k-1} + \bar{\mathcal{C}}_k + \bar{\mathcal{D}}_k)] = 0$, as $\bar{\mathcal{B}}_k$ comprises the noises \mathcal{Q}_{k-1} and \mathcal{V}_k .

Following the discussion, we obtain

$$\begin{aligned} \mathbb{E}[\mathbb{V}(\mathbf{e}_{k|k})|\mathbf{e}_{k-1|k-1}] - \mathbb{V}(\mathbf{e}_{k-1|k-1}) &\leq \lambda_3 \xi^3 + (\lambda_1 + \lambda_4 + \lambda_7) \xi^2 + (\lambda_5 + \lambda_8) \xi \\ &+ \lambda_2 + \lambda_6 + \lambda_9 - \kappa \mathbb{V}(\mathbf{e}_{k-1|k-1}). \end{aligned} \quad (4.30)$$

Let us now define $\rho = \lambda_3 \xi^3 + (\lambda_1 + \lambda_4 + \lambda_7) \xi^2 + (\lambda_5 + \lambda_8) \xi + \lambda_2 + \lambda_6 + \lambda_9$. Subsequently, the above equation satisfies the second condition of Eq. (4.20).

Let us now apply the inverse operator and multiply $\mathbf{e}_{k|k}^T$ and $\mathbf{e}_{k|k}$ to the inequality of $\mathbf{P}_{k|k}$ given in Eq. (4.27). Thus, we get

$$\frac{1}{\mathcal{P}_2} \|\mathbf{e}_{k|k}\|^2 \leq \mathbb{V}(\mathbf{e}_{k|k}) \leq \frac{1}{\mathcal{P}_1} \|\mathbf{e}_{k|k}\|^2. \quad (4.31)$$

Substituting $\theta_1 = 1/\mathcal{P}_u$ and $\theta_2 = 1/\mathcal{P}_L$, the above inequality satisfies the first condition of Eq. (4.20).

We now emphasize that Eqs. (4.30) and (4.31) all together satisfy Eq. (4.20). Thus, for chosen $\mathbb{V}(\mathbf{e}_{k|k}) = \mathbf{e}_{k|k}^T \mathbf{P}_{k|k} \mathbf{e}_{k|k}$, the estimation error $\mathbf{e}_{k|k}$ (Eq. (4.25)) satisfies Eq. (4.21), which concludes the exponential boundedness of $\mathbf{e}_{k|k}$. Therefore, the EKDFD remains exponentially bounded in mean square if the inequalities presented in Eq. (4.27) hold true.

4.5 Simulation and Results

In this section, we use the CKF-based formulation of proposed GFDF to solve the nonlinear filtering problem. To compare its performance, benchmark filters, including i) ordinary CKF [64], ii) CKF with FDI attack handling [33], and iii) CKF with delayed measurement handling [156],[28] were considered. We will refer to the CKF-based formulations of CKF_FA[33], MLCKF[28], and CKF_GD[156]. We present two popular CPS examples, such as multiple sinusoid estimation and power system state estimation problem for this simulation-based studies.

This chapter presents the results for two simulation examples, such as multiple sinusoid estimation and power system state estimation problem.

4.5.1 Example-1: Multiple sinusoids estimation

Consider a problem of estimating multiple sinusoids [156, 157]. The state space model is given as

$$\mathbf{x}_k = \mathbf{I}\mathbf{x}_{k-1} + \boldsymbol{\omega}_{k-1} \quad (4.32)$$

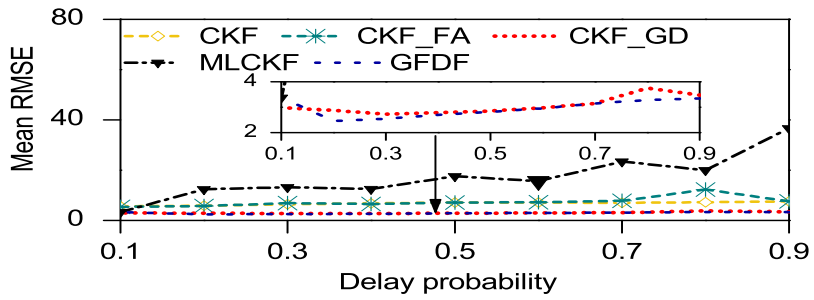
$$\mathbf{y}_k = \left[\sum_{j=1}^3 a_{j,k} \cos(2\pi f_{j,k} k \tau), \sum_{j=1}^3 a_{j,k} \sin(2\pi f_{j,k} k \tau) \right]^T + \zeta_k, \quad (4.33)$$

where $\mathbf{x} = [f_1, f_2, f_3, a_1, a_2, a_3]^T$ contains the frequencies f_i and amplitudes a_i of three sinusoids; $\tau = 0.25$ ms is the sampling time. The covariance matrices are assigned as $\mathbf{Q} = \text{diag}([\sigma_f^2 \ \sigma_f^2 \ \sigma_f^2 \ \sigma_a^2 \ \sigma_a^2 \ \sigma_a^2])$ and $\mathbf{R} = \text{diag}([\sigma_r^2 \ \sigma_r^2])$.

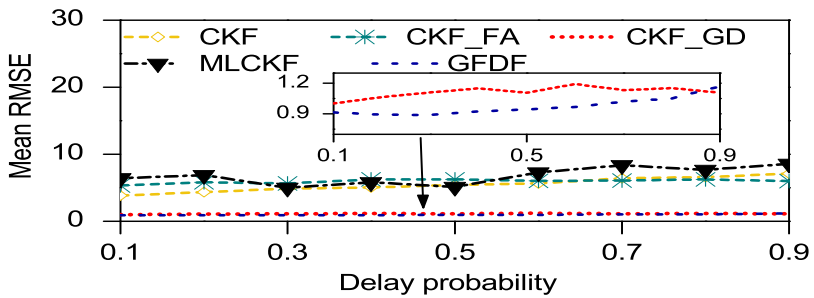
We perform the simulation for two cases i) $p_a = 0.2$, $\sigma_f = \sqrt{25}$ mHz, $\sigma_a = \sqrt{0.8}$ mV, and $\sigma_r = \sqrt{0.9}$ V and ii) Case 2: $p_a = 0.5$, $\sigma_f = \sqrt{0.9}$ Hz, $\sigma_a = \sqrt{0.1}$ mV, and $\sigma_r = \sqrt{0.1}$ V. The initial true state is chosen as $\mathbf{x}_0 = [200, 500, 1000, 3, 4, 3]^T$, and the estimate $\hat{\mathbf{x}}_{0|0}$ are considered to be normally distributed with mean \mathbf{x}_0 and covariance $\mathbf{P}_{0|0} = \text{diag}([20, 20, 20, 0.5, 0.5, 0.5])$. This study considers Δ_k to follow a normal distribution with a mean of 0.5 and a variance of 0.4. In the presence of an attack, it assumes $p_g = p_d = 0.5$. The filters are evaluated for 400 time-steps and 200 Monte-Carlo runs, and the mean RMSEs for amplitudes and frequencies are compared.

The mean RMSEs for all filters for two cases are presented in Figs. 4.1 and 4.2. The figures indicate that the proposed GFDF achieves improved accuracy compared to all existing filters. Table 4.2 presents a relative computational time of all simulated filters with CKF method. The table shows that the computational time of the proposed method is slightly increased compared to traditional CKF but remains comparable to existing CKF extensions for handling these irregularities.

This chapter presented the results obtained and derive some noteworthy conclusions. Figs. 4.1 to 4.2 demonstrate that the accuracy, as measured by average of RMSE, deteriorates with an increase in delay probability (p_g), as expected. However, it is found out that the average of RMSE variation is minimal for p_g values in the range of 0.1 to 0.5. This implies that the filtering performance is not significantly impacted if

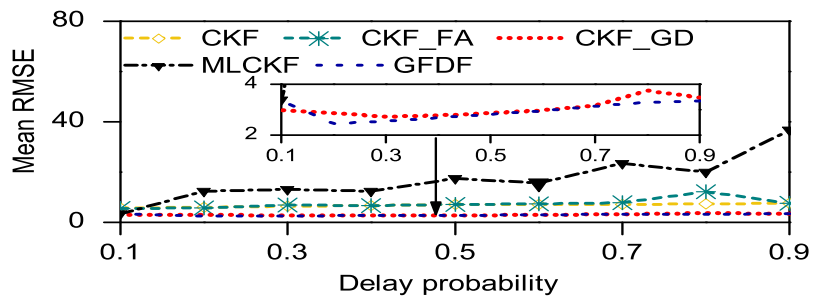


(a) Frequency

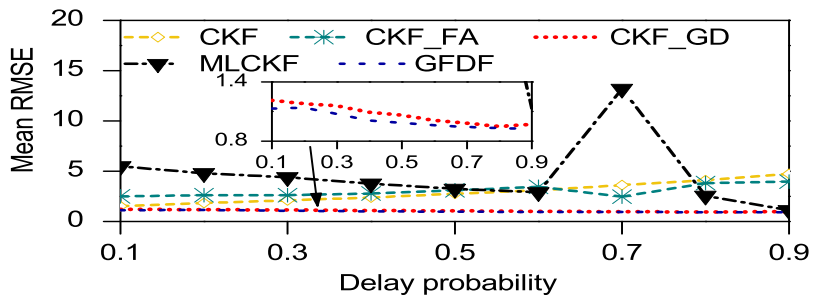


(b) Amplitude

Figure 4.1: Case 1: Average of RMSE comparison of CKF, MLCKF, CKF_FA, CKF_GD, and GFDF against varying delay probabilities.



(a) Frequency



(b) Amplitude

Figure 4.2: Case 2: Average of RMSE comparison of CKF, MLCKF, CKF_FA, CKF_GD, and GFDF against varying delay probabilities.

Table 4.2: Relative computational time of the proposed GFDF with other existing filter, such as MLCKF, CKF_FA, CKF_GD, CKF

| Filter | GFDF | CKF_GD | CKF_FA | MLCKF | CKF |
|--------|-------|--------|--------|-------|-----|
| Time | 1.171 | 1.063 | 1.045 | 1.734 | 1 |

only a few measurements experience delay while others are time-synchronized. Similar observations have been made in [28] and [156]. It is important to note that this trend may vary depending on the system dynamics and environmental factors.

Additionally, unlike existing filters, our proposed method is not significantly impacted by an increase in p_a . This indicates that our approach is adept at capturing irregularities and efficiently tracking state dynamics. To this end, it can be inferred that the current FDI attack methodology fails to address delayed measurements adequately. Likewise, existing delayed Gaussian filters like CKF_GD and MLCKF are ill-equipped to handle the potential intrusion of false data in a cyber-physical system. Conversely, the proposed GFDF method demonstrates its viability in simultaneously addressing the challenges posed by FDI attacks and delayed measurements.

4.5.2 Example-2: Power system state estimation

This example estimates the power system states, namely the voltage magnitude and phase angle at each bus or node, using a limited number of noisy measurements. The analysis is performed on the IEEE 14-bus benchmark power system network using Matlab on a personal computer with a 64-bit operating system, 32 GB RAM, and a 2 GHz Intel Core i3 processor.

Table 4.3 presents the measurement locations of phasor measurement units (PMUs) and remote terminal units (RTUs) in IEEE 14-bus benchmark power system as shown in Fig. 4.3. The PMUs are placed at specific locations to measure voltage and current phasors (\mathbf{V}_r , \mathbf{V}_i , \mathbf{I}_r , and \mathbf{I}_i), while the RTUs provide power injections (\mathbf{P}^i and \mathbf{Q}^i) at the installed buses and power flows (\mathbf{P}^f and \mathbf{Q}^f) through the specified branches. The detailed expressions for these measurements can be found in [48]. This simulation considers

that RTU data packets are updated every two seconds, and 30 PMU data packets were received between two adjacent RTU data packets. The proposed GFDF-based PSSE was implemented over 40 seconds at the PMU scan rate by incorporating the most recent PMU sensor data with the last available RTU sensor data.

The performance of the proposed GFDF is compared with i) ordinary CKF [48] [64], ii) CKF with FDI attack handling [33], iii) CKF with delayed measurement handling [156, 28], and CKF with delayed and missing measurements [155] were considered. To validate the findings, this chapter refers to the CKF-based formulations of as CKF_FA[157], MLCKF[28], CKF_GD[156], and CKF_DM[155]. However, unlike example-1, due to large numbers of measurements MLCKF[28] is not feasible to perform. This problem considers CKF_DM[155], including other benchmark filters as considered in 4.5.1.

Table 4.3: PMU and RTU measurements locations for the IEEE 14-bus benchmark power system networks.

| PMU | | RTU |
|---|--|---|
| $\mathbf{V}_r, \mathbf{V}_i, \mathbf{I}_r,$ and \mathbf{I}_i^\dagger | \mathbf{P}^i and $\mathbf{Q}^{i\dagger}$ | \mathbf{P}^f and $\mathbf{Q}^{f\dagger\dagger}$ |
| 2, 7, 9, 13 | 3, 5, 13, 14 | 1-5, 2-1, 2-5, 3-4, 4-5, 4-7, 6-11, 6-12, 6-13, 8-7, 9-4, 9-7, 9-10, 9-14, 10-11, 12-13, 13-14 |

The power system state dynamics are simplified as a random walk model due to the low likelihood of significant changes occurring between successive PMU scans. This simulation considers a 3% randomly changing load condition throughout the simulation period. For validating the proposed approach for large and random voltage fluctuations, a significantly larger process noise covariance, $\mathbf{Q}_k = 9 * 10^{-6} \mathbf{I}_{n \times n}$, is considered rather than a value mentioned in [134]. Here, δ_v^r , δ_{pi}^r , and δ_{pf}^r represent the standard deviations of sensor noises for RTU voltage, power injection, and power flow, respectively, and δ_v^p and δ_i^p are the corresponding values for PMU voltage and current of the measurements. To characterize sensor noises, the following values were considered [48]: $\delta_v^r = 0.001$, $\delta_{pi}^r = 0.02$, $\delta_{pf}^r = 0.02$, $\delta_v^p = 0.001$, and $\delta_i^p = 0.001$. The simulations were carried out with true initial bus voltages of $\mathbf{x}_0 = 1 \angle 0^\circ$ and the PSSE was performed with $\hat{\mathbf{x}}_{0|0} = \mathbf{x}_0$

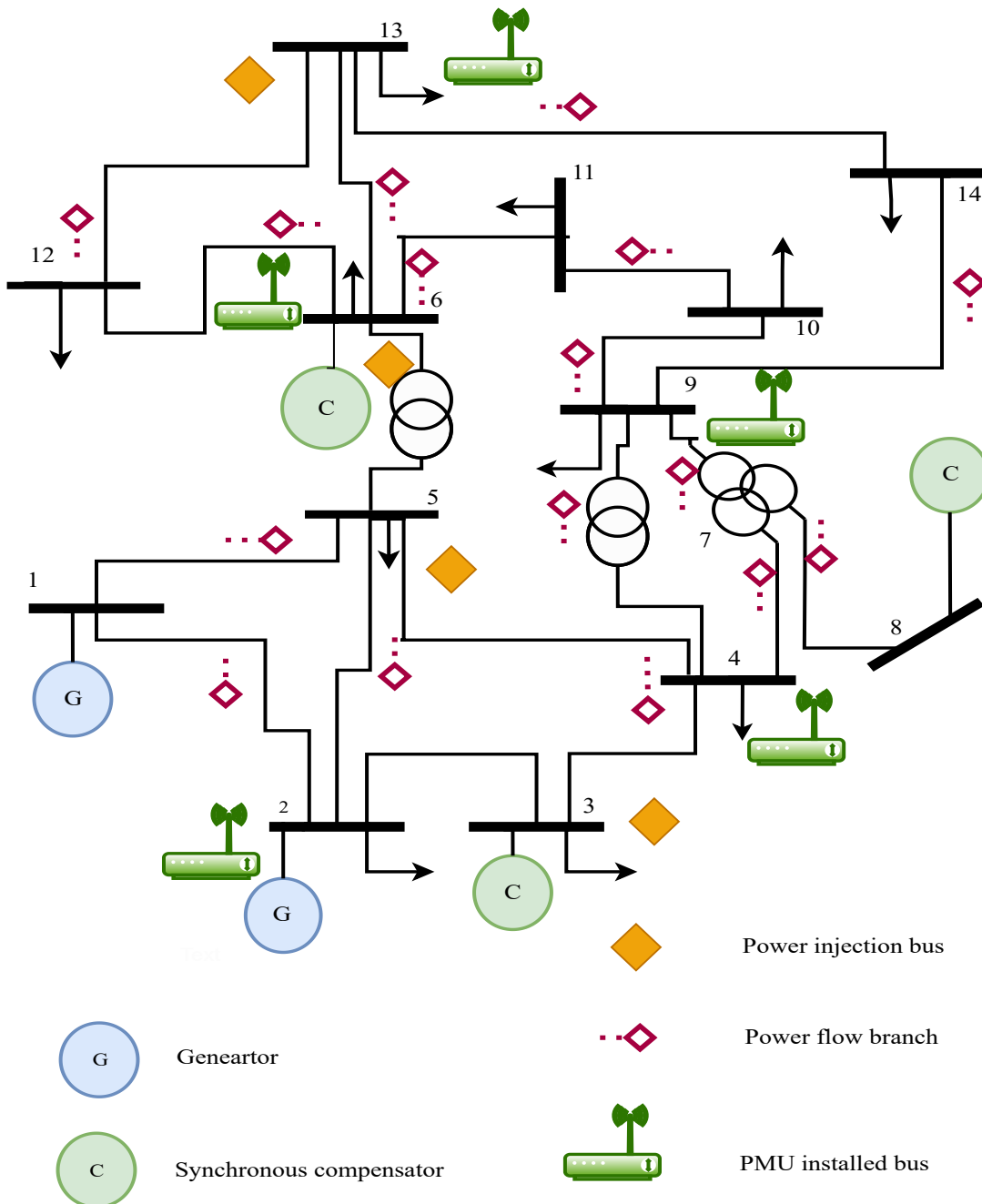
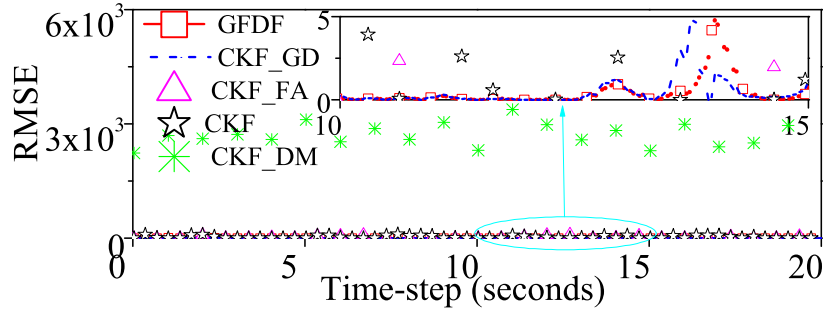
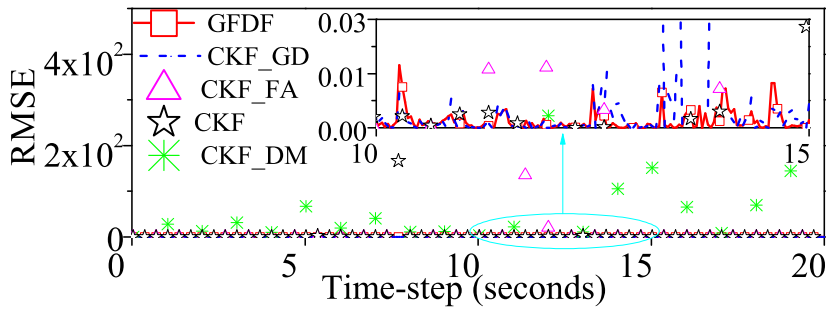


Figure 4.3: IEEE 14 bus benchmark.

and $\mathbf{P}_{0|0} = 10^{-6}\mathbf{I}_{n \times n}$. This problem sets Δ_k to follow a normal distribution with a mean of 0.5 and a variance of 0.4. In the presence of an attack, it assumes that $p_a = p_d = 0.5$.



(a) Voltage magnitude \mathbf{V} (p.u.)



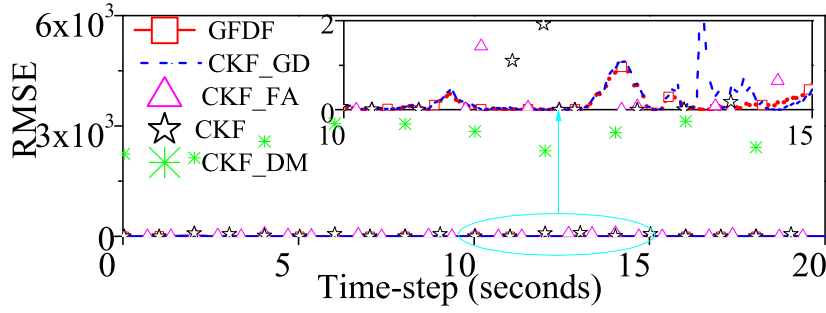
(b) Phase angle δ (radian)

Figure 4.4: RMSE comparison of CKF, CKF_FA, CKF_GD, CKF_DM, and GFDF at Bus-9 for 0.3 delay probabilities.

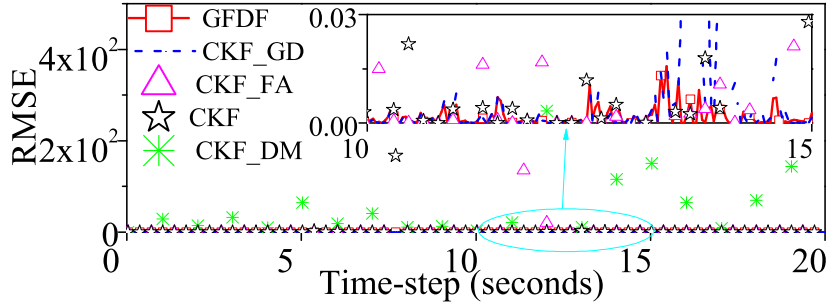
Table 4.4: Performance indices (in 10^{-3}) of the proposed GFDF-based PSSE with the existing benchmark filters obtained by averaging the voltage magnitude (\mathbf{V}) and phase angle δ across all buses.

| Delay prob. (p_g) | Error | \mathbf{V} | | | | | δ | | | | |
|-----------------------|-----------------|--------------|--------|--------|--------|--------|----------|--------|--------|--------|--------|
| | | GFDF | CKF_GD | CKF_FA | CKF | CKF_DM | GFDF | CKF_GD | CKF_FA | CKF | CKF_DM |
| 0.1 | Average of RMSE | 22 | 24 | 114 | 508 | 121 | 1.7 | 2.7 | 34.1 | 80.6 | 19.8 |
| 0.2 | | 22.1 | 24.9 | 113.7 | 508 | 120.7 | 1.4 | 2.6 | 34.1 | 80.8 | 19.7 |
| 0.3 | | 22.9 | 24.8 | 113.6 | 508.5 | 120.7 | 1.1 | 2.2 | 34.1 | 80.9 | 19.7 |
| 0.4 | | 21.8 | 23.6 | 113.4 | 508 | 120.5 | 0.9 | 1.9 | 34.4 | 80.8 | 19.8 |
| 0.5 | | 22.7 | 24 | 113.4 | 508.6 | 120.5 | 0.9 | 2 | 34.3 | 81.1 | 19.8 |
| 0.1 | Average of MAE | 3.55 | 3.61 | 18.4 | 361 | 19.6 | 0.238 | 0.366 | 1.88 | 22.33 | 0.95 |
| 0.2 | | 3.575 | 3.905 | 18.28 | 360.7 | 19.49 | 0.18 | 0.27 | 1.84 | 21.92 | 0.92 |
| 0.3 | | 3.68 | 3.97 | 18.27 | 361.2 | 19.49 | 0.16 | 0.23 | 1.82 | 21.75 | 0.91 |
| 0.4 | | 3.49 | 3.70 | 18.21 | 361.1 | 19.43 | 0.148 | 0.212 | 1.825 | 21.643 | 0.91 |
| 0.5 | | 3.491 | 3.70 | 18.21 | 361.27 | 19.43 | 0.143 | 0.2 | 1.815 | 21.608 | 0.904 |

We conducted a comparative study of the proposed GFDF-based PSSE and other existing filters, as shown in Figures 4.4(a) and 4.5(a) and Table 6.1. The RMSE plots for voltage magnitudes and voltage phase angles at bus 9 ($\mathbf{V}_{k,9}$ and $\delta_{k,9}$) are displayed in Figure 4.4(a) and 4.5(a) for delay probabilities of 0.3 and 0.5, respectively. These plots



(a) Voltage magnitude V (p.u.)



(b) Phase angle δ (radian)

Figure 4.5: RMSE comparison of CKF, CKF_FA, CKF_GD, CKF_DM, and GFDF at Bus-9 for 0.5 delay probabilities.

Table 4.5: Comparison of computational time for different filters.

| Filter | GFDF | CKF_GD | CKF_FA | MLCKF | CKF | CKF_DM |
|------------|-------|--------|--------|-------|--------|--------|
| Time (sec) | 4.877 | 5.1689 | 4.6438 | 5.929 | 4.6093 | 4.715 |

reveal that the CKF_DM filter has significantly higher RMSEs as it did not consider falsely injected data, resulting in poor performance compared to other filters. Furthermore, Figures 4.4(a) and 4.5(a) demonstrate that CKF and CKF_FA exhibit inferior estimation performance compared to the proposed GFDF-based PSSE.

Table 6.1 presents the average of RMSE and average of MAE of all considered filters for varying probabilities of delay. The results show that the proposed GFDF-based PSSE achieves the lowest average errors, including average of RMSE and average of MAE. Moreover, the table indicates that the filtering performance deteriorates with an increase in the probability of delay.

The computation times of simulation based study for PSSE on a 14-bus power system network is presented in Table 4.5. This implies that the computational time of

the proposed GFDF is marginally higher than traditional CKF but remains comparable to other existing CKF extensions for handling these irregularities.

4.6 Discussion and Conclusion

The practical applications of nonlinear estimation and filtering are vast, spanning fields such as defense, power, and network systems. However, the widely accepted Gaussian filtering method falls short in accounting for irregular measurements caused by delay and cyber-attacks. With practical measurements often exhibiting such irregularities, an advanced Gaussian filtering method is necessary.

The author introduced a method that employs stochastic modeling of delayed and cyber-attack measurements to meet this need. Our proposed stochastic model employs a Bernoulli random variable to indicate whether a measurement has been altered, either through an FDI attack or delay. The author then redesigned the traditional Gaussian filtering method to account for these modified measurements.

Our analysis demonstrates that the proposed method outperforms traditional Gaussian filtering, resulting in improved estimation accuracy even in the presence of both delay and cyber-attacks. However, it is important to note that our proposed method's computational budget and storage requirement are higher than the traditional Gaussian filtering method.

Up to this point, the extensions of Kalman filtering have demonstrated applicability to a wide range of filtering applications. Nevertheless, the complex nature of power system networks poses a significant challenge for state estimation that requires further exploration.

Chapter 5

Dynamic State Estimation of Power System Using Forecasting-Aided Cubature Quadrature Kalman Filter

5.1 Introduction

This chapter is focused on the PSSE problems. As discussed previously, the PSSE is an estimation problem of dynamical states of a complex power system network, which helps in online monitoring of the states of the power system networks. The bus voltages and phase angles are the typical dynamical states. Moreover, measurements follow the power flow equations, which are derived in Chapter 1.4, giving a nonlinear measurement equation. Therefore, unlike Chapter 3, this chapter uses a standard nonlinear state-space models, similar to Eqs. (1.3) and (1.4) of Chapter 1.

A detailed literature review is provided in Chapter 2 to present the chronological developments in PSSEs. As a summary of the literature review, we highlight [46], [49], [48], which develop advanced PSSE methods by utilizing EKF, UKF, and CKF. It is worth mentioning that the filtering literature witnessed some recent advancements that outperform EKF, UKF, and CKF. Thus, we can utilize such advancements in order to improve the PSSE accuracy. One such advanced filter is CQKF, an extension of CKF for improving accuracy.

This chapter introduces another contribution of this thesis, which develops an

advanced PSSE method by utilizing a forecasting-aided CQKF (FACQKF) over the state space model for DSE. The conventional CQKF requires mathematical state dynamics models, which are indeed unknown in PSSE design applications. The forecasting-aided feature of the proposed FACQKF relaxes this requirement. As a forecasting technique, the proposed FACQKF utilizes Holt's technique to compute the unknown state transition matrix. Additionally, the proposed FACQKF handles nonlinear dynamical equations by using a higher-order spherical-radial rule and a second order Gauss-Laguerre quadrature rule to approximate the intractable integrals appearing during the filtering [83]. For simplification, the proposed FACQKF will often be mentioned as CQKF-based PSSE. To achieve high accuracy, the proposed FACQKF has relatively higher computational demand than the UKF- and CKF-based PSSE methods. The improved accuracy of the modified CQKF-based PSSE is validated on the American Electric Power System located in the Midwest, a widely recognized benchmark for power system networks. The validation was performed on three commonly used benchmark power system networks: the IEEE 14-, 30-, and 118-bus systems.

5.2 Dynamic power system model

For a single set of data packets from sensors, the standard discrete form of nonlinear dynamic state space representation of real-time power flow model can be expressed using the Eqs. (1.1) and (1.2) [48] where $\mathbf{x}_k \in \mathbb{R}^n$ and $\mathbf{y}_k \in \mathbb{R}^m$ denote state and augmented measurement, respectively, with $k \in \{1, 2, \dots, N\}$. Moreover, $\mathcal{F}_{k-1} : \mathbf{x}_{k-1} \rightarrow \mathbf{x}_k$ and $\mathcal{H}_k : \mathbf{x}_k \rightarrow \mathbf{y}_k$ represent standard dynamical operators. Finally, $\mathcal{Q}_k \in \mathbb{R}^n$ and $\mathcal{V}_k \in \mathbb{R}^m$ represent the process and sensor noises, respectively, approximated as zero-mean Gaussian with covariances \mathbf{Q}_k and \mathbf{R}_k , respectively.

The process noise \mathcal{Q}_k compensates for the modeling inaccuracy of the state dynamics due to random fluctuations around the nominal operating conditions. Additionally, the measurement noise \mathcal{V}_k compensates for the sensor errors caused by time skewness and transmission interference in the RTUs and the data packet errors in the PMUs, respectively. For a detailed discussion on the measurement model received at time t_k , readers may follow Chapter 1.5.2.

5.3 Forecasting-aided modified CQKF-based PSSE

For the given state space model (Eqs. (1.1) and (1.2)), the modified CQKF [83] sequentially estimates the unknown states $\mathbf{x}_k \forall k \in \{1, 2, \dots, N\}$, as the sensor $\mathbf{y}_k \forall k \in \{1, 2, \dots, N\}$ is received sequentially. The CQKF is a popular Gaussian filter [21],[30], performed under the Bayesian framework [21], involving prediction and update steps. The Eq. (1.21) is spherical-radial transformed as

$$I = \frac{1}{\sqrt{(2\pi)^n}} \int_{\rho=0}^{\infty} \int_{U_n} \mathbb{F}(\mathbf{S}\rho\mathbf{Z} + \hat{\mathbf{x}}) ds(Z) \rho^{n-1} e^{-\rho^2/2} d\rho, \quad (5.1)$$

where \mathbf{S} is the Cholesky decomposition of \mathbf{P} , U_n is the surface of an n-dimensional unit hyper-sphere, $\|Z\| = 1$, and $\rho \in [0, \infty)$ is a radial variable. Please note that $\|\cdot\|$ denotes l_2 norm. The CQKF utilizes third-degree spherical cubature rule Eq. (5.2) for approximating

$$\int_{U_n} \mathbb{F}(\mathbf{S}\rho\mathbf{Z} + \hat{\mathbf{x}}) ds(Z) \approx \frac{2\sqrt{\pi^n}}{2n\Gamma(n/2)} \sum_{j=1}^{2n} \mathbb{F}(\rho [u]_j + \hat{\mathbf{x}}), \quad (5.2)$$

where $[u]$ is a set of indices representing the intersection points of unit hyper-sphere and coordinate axes. Substituting the approximation from Eq. (5.2) into Eq. (5.1) results I as a radial integral in ρ . The resulting expression can be transformed by substituting $\lambda = \rho^2/2$, which simplifies the remaining integral term in the form of $Z = \int_{\lambda=0}^{\infty} \mathbb{F}(\lambda) \lambda^t e^{-\lambda} d\lambda$ (with additional constant terms), where t is constant. The CQKF approximates this, thereby resulting in the integral using the higher-order Gauss-Laguerre quadrature rule is given as [30]

$$\int_{\lambda=0}^{\infty} \mathbb{F}(\lambda) \lambda^t e^{-\lambda} d\lambda \approx \sum_{i'=1}^{n'} \omega_{i'} \mathbb{F}(\lambda_{i'}), \quad (5.3)$$

where t is constant, n' denotes the number of Gauss-Laguerre quadrature points, while $\lambda_{i'}$ and $\omega_{i'} \forall i' \in \{1, 2, \dots, n'\}$ represent the Gauss-Laguerre quadrature points and associated weights. We obtain $\lambda_{i'} \forall i' \in \{1, 2, \dots, n'\}$ as roots of n' -order Chebyshev-Laguerre polynomial equation, given as $\mathcal{L}_{n'}^t = (-1)^{n'} \lambda^{-t} e^{\lambda} \frac{d^{n'}}{d\lambda^{n'}} \lambda^{t+n'} e^{-\lambda} = 0$ [83]. Subsequently,

the weights $\omega_{i'} \forall i' \in \{1, 2, \dots, n'\}$ are given as $\omega_{i'} = \frac{(n')\Gamma(1+n'+1)}{\lambda_{i'}[\mathcal{L}_{n'}^1(\lambda_{i'})]^2}$, [30] where $\Gamma[\cdot]$ represents the gamma function, while $\mathcal{L}_{n'}^1(\lambda)$ represents the first derivative of $\mathcal{L}_{n'}^1(\lambda_{i'})$ at $\lambda = \lambda_{i'}$. Finally, the CQKF combines the third-degree spherical cubature and higher-order Gauss-Laguerre quadrature rule to approximate the desired I as [30]

$$I \approx \sum_{j=1}^{N_s} \mathbf{W}_j \mathbb{F}(\hat{\mathbf{x}} + \mathbf{S}\boldsymbol{\xi}_j), \quad (5.4)$$

where $\mathbf{W}_j = \frac{1}{2n\Gamma(n/2)}\omega_{i'}$ and $\boldsymbol{\xi}_j = \sqrt{2\lambda_{i'}}[u]_j \forall j \in \{1, 2, \dots, N_s\}$, with $N_s = 2nn'$ representing the total number of sample points.

Remark 4 *The approximation of I in Eq. (5.4) by the n' -order Gauss Laguerre quadrature rule increases the required quadrature points by n' -times. In turn, this leads to an improvement in the estimation performance. The CQKF performance coincides with CKF performance when applying for a first order Gauss Laguerre quadrature rule. Additionally, number of required sample points is directly proportional to the dimension of the system. Similarly, in GHF [30] and Szegőquadrature Kalman filter (SQKF) [159], the number of support points requirement is $n^{n'}$ for an n -dimensional system. Therefore, ECKF, and GHF are ineffective for PSSE design applications because of the curse of dimensionality.*

Considering Eq. (5.4) for approximating I , we discuss below the computational aspects of the FACQKF-based PSSE.

Prediction: The prediction step involves computation of state dynamics by Holt's double exponential forecasting technique and computation of apriori state mean and covariance as discussed below:

A real-time power system process model is dynamic and complex. The state transition function is modeled using a forecasting tool [134] that accommodates variations in state from one time-step to the next. This chapter adopted a popular Holt's double exponential smoothing method for state forecasting $\mathcal{F}_k(\hat{\mathbf{x}}_{k-1|k-1})$, owing to its simplicity and reliability [49], [160]. Moreover, it is well suited for nonlinear optimization problems. The state model parameters mentioned in Eq. (1.1), $\mathcal{F}(\cdot)$ are computed using the

exponential smoothing technique. It considers two components: level factor \mathcal{L} and trend factor \mathcal{T} .

$$\mathbf{f}(\mathbf{x}_{k-1}) = \mathcal{L}_k + \mathcal{T}_k, \quad (5.5)$$

where

$$\mathcal{L}_k = \alpha_h \mathbf{x}_{k-1|k-1} + (1 - \alpha_h) \mathcal{L}_{k-1}, \quad (5.6)$$

$$\mathcal{T}_k = \beta_h (\mathcal{L}_k - \mathcal{L}_{k-1}) + (1 - \beta_h) \mathcal{T}_{k-1}, \quad (5.7)$$

$$\mathbf{f}(\mathbf{x}_{k-1}) = \mathcal{L}_k = \alpha_h (1 + \beta_h) \mathbf{x}_{k-1}, \quad (5.8)$$

$$\mathcal{T}_k = (1 - \alpha_h) (1 + \beta_h) \mathbf{x}_{k-1} - \beta_h \mathcal{L}_k - (1 - \beta_h) \mathcal{T}_k, \quad (5.9)$$

where $\alpha, \beta \in (0, 1)$ are called smoothing parameters, which are obtained in offline simulation. This paper adopts α and β values from [48] as 0.8 and 0.5, respectively. Moreover, the initial values of \mathcal{L} and \mathcal{T} are initial state and zero, respectively. Subsequently, it computes \mathcal{L}_{k-1} , to implement traditional derivative-less Gaussian filtering algorithm given in Appendix C.

Update: The update step of proposed PSSE is modified to incorporate various bad data in measurements received at control center. These bad data may occur due to various factors, such as measurement instrument failures, communication errors, sudden spikes, temporary equipment failures, switching operations, etc. This chapter focuses on identifying and isolating these flawed data while performing estimation operation.

Bad data identifier: To address the issue of large errors caused by like erroneous telemetered data or circuit breaker status changes, and to prevent their adverse effect on estimation accuracy and PSSE reliability, this chapter incorporated a resilient method for rejecting flawed measurements. This method aims to enhance the robustness of the proposed estimator by effectively identifying and handling sensor outliers caused by temporary measurement failures. By incorporating this approach, we aim to mitigate the

adverse effects of outliers and improve the reliability and accuracy of the PSSE results.

1. The time iterated $|\beta_k| = \frac{|(\mathbf{y}_k - \hat{\mathbf{y}}_{k|k-1})|}{\sqrt{(\mathbf{P}_{k|k-1}^{\mathbf{y}\mathbf{y}^{-1}})}}$ should be less than the positive threshold value β_{th} and include a precondition for state update to be followed. In this chapter, the positive threshold value (β_{th}) is an adjustable parameter determined by the user.
2. If $|\beta_k| > \beta_{th}$ we skip the state update step *i.e* $\mathbf{x}_k = \hat{\mathbf{x}}_{k|k-1}$, and $\mathbf{P}_k = \mathbf{P}_{k|k-1}$.

Assuming all state variables are mutually independent and the meter error follows normal distribution, then L_2 norm of innovation follows χ^2 distribution. A detection threshold value represents the level of confidence. If the detection threshold adopted for normalized residual test is 2, then the confidence level is 94.46%. If the detection threshold is 2.5, then the confidence level is 98.76%. In this paper, the bad data threshold β_{th} is considered as 3 for a 99.72% of detection confidence probability [161].

Remark 5.3.1 *The third central moment μ_3 express the skewness of a distribution. Hence, to differentiate between sudden change in states and bad data type of anomaly, an innovation skewness based test is conducted.*

$$b_k = \frac{\mu_3}{\sqrt{\mathbf{P}_{k|k-1}^{\mathbf{y}\mathbf{y}^{-1}}}} < \beta_{th}, \quad (5.10)$$

Under normal conditions, skewness maintains a symmetrical distribution with a zero mean and standard deviation, resulting in a magnitude of zero. However, when confronted with bad data, the skewness magnitude exceeds a predefined threshold, β_{th} , due to the loss of symmetry. In the presence of abrupt state changes, the skewness magnitude remains small relative to β_{th} . In this scenario, the skewness of the measurement distribution retains its symmetry but with altered mean and standard deviation.

In the modified CQKF-based PSSE, we implement the CQKF through the prediction and update steps as discussed in Appendix C with including bad data identifier condition, through PSSE state space model. The outcome $\hat{\mathbf{x}}_{k|k}$ gives the desired estimate of the PSSE parameters, such as the voltage magnitude and phase angle of all buses. The

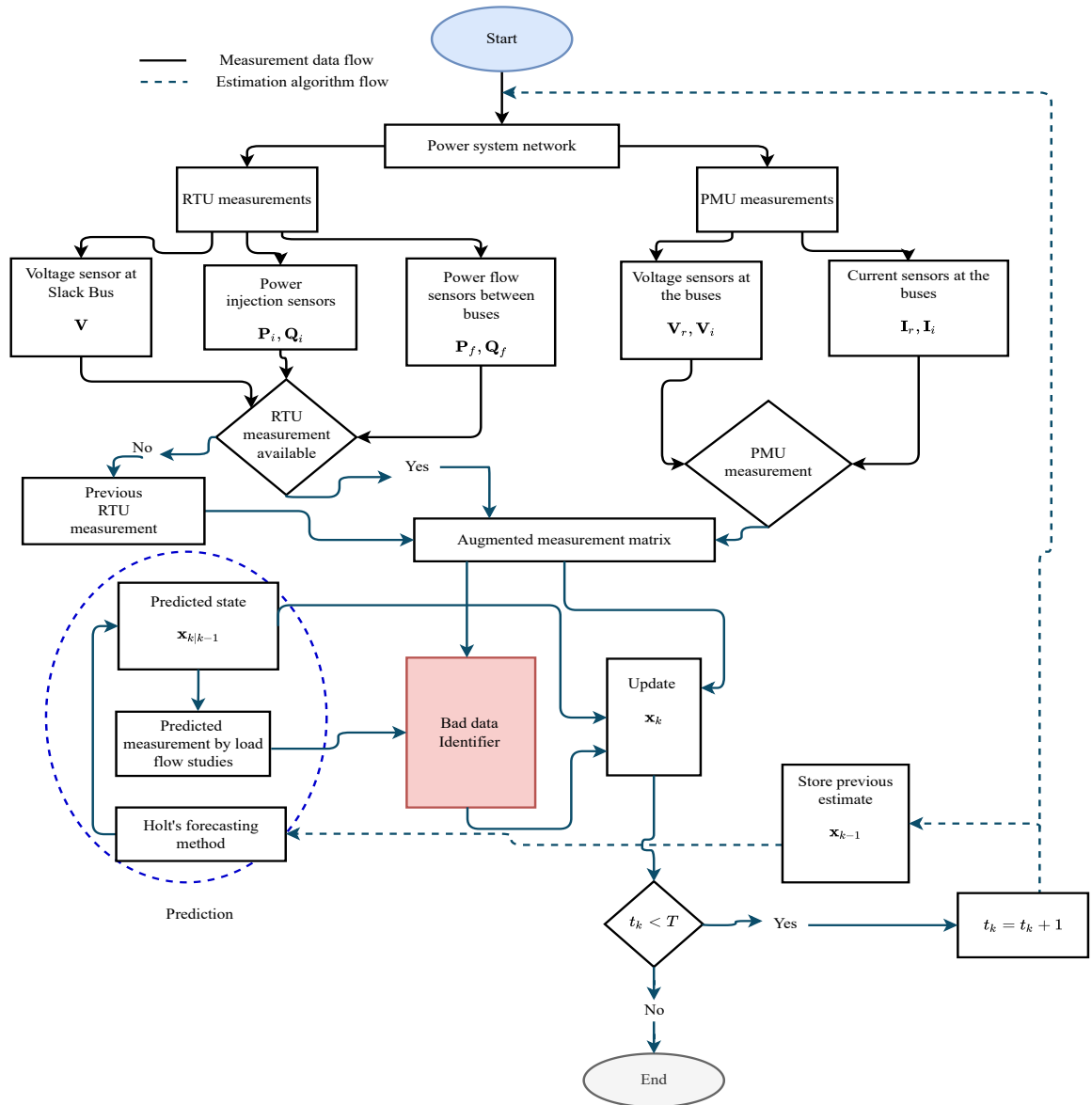


Figure 5.1: Modified CQKF-based PSSE algorithm.

step-by-step procedure for implementing the modified CQKF-based PSSE in a real-time power system network using a flow-chart is shown in Fig. 5.1. The author considered a standardized IEEE benchmark power system of 14-, 30-, and 118-bus for validating the modified CQKF algorithm, which is discussed in the subsequent section.

Remark 5.3.2 *An accurate PSSE helps to formulate efficient and reliable energy management strategies. Thus, the improved PSSE accuracy using the modified CQKF can enhance the efficiency and reliability of modern power system networks.*

Table 5.1: PMU and RTU measurements locations for the considered IEEE 14-, 30-, and 118-bus power system networks.

| Network | PMU $V_r, V_i, I_r,$ and I_i^\dagger | P^i and $Q^{i\dagger\dagger}$ | RTU P^f and $Q^{f\dagger\dagger\dagger}$ |
|---------|---|--|---|
| 14-bus | 2, 7, 9, 13 | 3, 5, 13, 14 | 1-5, 2-1, 2-5, 3-4, 4-5, 4-7, 6-11, 6-12, 6-13, 8-7, 9-4, 9-7, 9-10, 9-14, 10-11, 12-13, 13-14 |
| 30-bus | 2, 3, 10, 12, 18, 24, 30 | 2, 3, 4, 6, 8, 10, 11, 12, 15, 16, 19, 21, 24, 27, 30 | 1-3, 2-4, 2-5, 2-6, 3-4, 4-6, 5-7, 10-22, 12-15, 12-16, 14-15, 17-10, 17-16, 18-15, 18-19, 19-20, 20-10, 21-22, 23-15, 24-23, 25-26, 28-8, 30-27 |
| 118-bus | 1, 6, 8, 12, 15, 17, 21, 25, 29, 34, 40, 45, 49, 53, 56, 62, 72, 75, 77, 80, 85, 86, 90, 94, 101, 105, 110, 114 | 11, 19, 25, 27, 33, 34, 38, 40, 42, 44, 45, 47, 48, 49, 50, 66, 68, 70, 73, 75, 79, 88, 92, 99, 100, 101, 103, 104, 106, 107, 109, 110, 111, 112, 113, 114, 116, 117, 118, | 1-2, 3-5, 3-1, 4-5, 5-8, 5-6, 7-12, 8-9, 9-10, 12-11, 14-12, 15-13, 15-33, 16-12, 17-15, 17-16, 19-34, 19-18, 21-20, 22-21, 23-24, 23-22, 24-72, 24-70, 25-27, 26-25, 27-32, 27-115, 28-27, 29-31, 30-17, 30-26, 30-38, 30-8, 32-23, 32-31, 34-43, 36-35, 37-40, 38-65, 39-40, 40-42, 41-42, 43-44, 46-45, 46-48, 47-46, 49-54, 49-66, 50-49, 51-49, 51-52, 52-53, 54-55, 54-59, 57-56, 58-56, 58-51, 59-60, 59-61, 61-64, 63-59, 66-67, 66-62, 67-62, 68-81, 69-68, 70-74, 70-75, 71-73, 72-71, 75-118, 75-77, 76-77, 77-82, 77-78, 77-80, 83-82, 83-85, 83-84, 85-88, 85-89, 86-85, 87-86, 88-89, 89-92, 89-90, 90-91, 91-92, -93, 94-93, 96-82, 96-94, 96-95, 96-97, 98-80, 99-100, 99-80, 100-106, 100-101, 103-110, 103-100, 104-100, 104-105, 105-108, 106-107, 106-105, 108-109, 110-109, 116-68, 118-76 |

[†]PMU measurements, such as voltage phasor (V_r, V_i), and current phasors (I_r, I_i).

^{††}Active and reactive power injections.

^{†††}active and reactive power injections power flow between lines respectively.

5.4 Simulation and result

This section discusses validating the performance of the modified CQKF-, CKF-, and UKF-based PSSE techniques for IEEE 14-, 30-, and 118-bus power system networks.

A standard IEEE-14bus benchmark power system is illustrated in Fig. 4.3, for the convenience of the reader. 30 PMU data packets were considered between the two adjacent RTU data packets in this simulation study. The simulation study used data from Table 5.1, including the PMU locations to measure voltage and current phasor, the buses with power injection measurements, and the branches with power flow measurements [47], [162], assuming that RTU data packets are updated every two seconds.

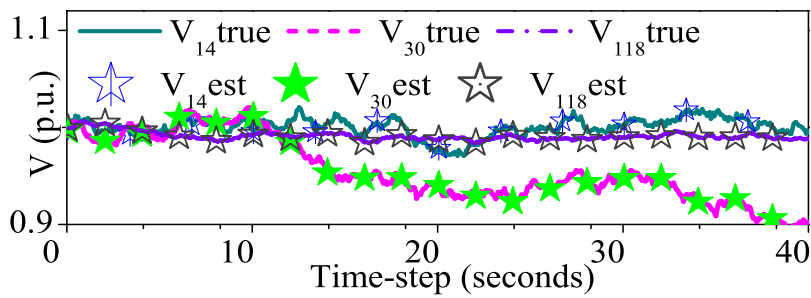
By adding the most recent PMU sensor data to the last available RTU sensor data, the modified CQKF-based PSSE was implemented over 40 seconds period at PMU scan rate.

True data generation: Due to the low likelihood of a significant change between two successive PMU scans, this design reduces the complexity of the power system state dynamics to a random walk model. The measuring model used in this work is adopted from [47] and [162]. Validating the proposed approach for large and random voltage fluctuations, significantly larger process noise covariance, $\mathbf{Q}_k = 9 * 10^{-6} \mathbb{I}_{n \times n}$, is considered rather than a value mentioned in [134]. Here, δ_v^r , δ_{pi}^r , and δ_{pf}^r represent the standard deviations of sensor noises for RTU voltage, power injection, and power flow, respectively, and δ_v^p and δ_i^p are the corresponding values for PMU voltage and current of the measurements. To characterize sensor noises, the following values were considered [161]: $\delta_v^r = 0.001$, $\delta_{pi}^r = 0.02$, $\delta_{pf}^r = 0.02$, $\delta_v^p = 0.001$, and $\delta_i^p = 0.001$.

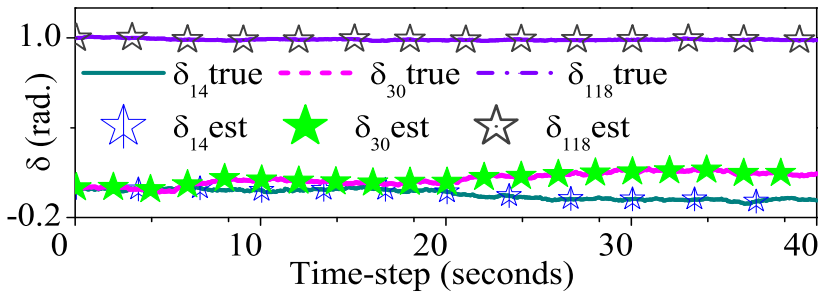
5.4.1 Case-1: Study of various benchmark electric power system under random voltage fluctuation.

Validating the proposed approach for large and random voltage fluctuations upto 3% of normal load, a significantly larger process noise covariance, $\mathbf{Q}_k = 9 * 10^{-6} \mathbb{I}_{n \times n}$, is considered rather than a value mentioned in [134]. To begin, the simulations were carried out with initial bus voltages of $\mathbf{x}_0 = 1 \angle 0^\circ$ as true data, and the PSSE was performed with $\hat{\mathbf{x}}_{0|0} = \mathbf{x}_0$ and $\mathbf{P}_{0|0} = 10^{-6} \mathbb{I}_{n \times n}$. The modified CQKF-based PSSE was validated on IEEE 14-, 30-, and 118-bus networks. The true and estimation plots for voltage magnitudes and voltage phase angles at bus 9 ($\mathbf{V}_{k,9}$ and $\delta_{k,9}$) are shown in Fig. 5.2. For each network

considered, Fig. 5.2(a) shows true-estimation plots of voltage magnitude, and Fig. 5.2(b) shows true-estimation plots of phase angle. The voltage phasor of an estimated value converged to the true value for all the considered IEEE system networks, as shown in Figs. 5.2(a), 5.2(b) for magnitude and phase angle, respectively. Thus, the simulation results indicated that the modified CQKF based PSSE technique suits the PSSE of IEEE 14-, 30-, and 118-bus networks. Furthermore, the modified CQKF-based PSSE technique was validated across all buses in the selected power networks (IEEE 14-, 30-, and 118-bus) and compared to the existing CKF- and UKF-based PSSE methods.



(a)



(b)

Figure 5.2: Case-1: True and estimate plots at bus-9 (subscripts 14, 30, and 118 represent the 14-, 30-, and 118-bus networks, respectively): (a) Voltage magnitude V (p.u.) and (b) Phase angle δ (radian).

The modified CQKF-based PSSE was verified using 50 Monte-Carlo (M_c) simulations to validate its improved accuracy and gain additional insights into its comparison with CKF- and UKF-based PSSE. Average of mean square error, average of mean of absolute error, and maximum error (MAXE) were chosen as the performance metrics and listed in Table 5.2, along with their execution time. The performance metrics, such as average of MSE, MAE, and MAXE are computed using Eqs. (1.29), (1.31), and (1.32), respectively.

Table 5.2: Case-1: Estimation error performance indices (in 10^{-5}) of the modified CQKF-based PSSE with the existing PSSEs obtained by averaging the voltage magnitude (V) and phase angle δ across all buses.

| Network | PSSE | Average of MSE | | Average of MAE | | MAXE | | Computational time |
|---------|------|----------------|----------|----------------|----------|--------|----------|--------------------|
| | | V | δ | V | δ | V | δ | |
| 118-bus | CQKF | 2.284 | 2.3 | 910 | 943.1 | 125.5 | 128.5 | 0.50 |
| | CKF | 2.296 | 2.319 | 920.4 | 943.3 | 125.6 | 128.7 | 0.31 |
| | UKF | 2.312 | 2.320 | 921.3 | 943.37 | 125.69 | 128.9 | 0.32 |
| 30-bus | CQKF | 1.0 | 0.8 | 230 | 187 | 900 | 820 | 0.027 |
| | CKF | 1.1 | 81.3 | 235 | 191 | 921 | 830 | 0.0162 |
| | UKF | 1.13 | 83 | 240 | 194 | 940 | 841 | 0.0163 |
| 14-bus | CQKF | 0.50 | 0.1836 | 168 | 95.8 | 575.2 | 406 | 0.006 |
| | CKF | 0.5078 | 0.1837 | 168.3 | 96.34 | 580.4 | 410 | 0.0037 |
| | UKF | 0.5091 | 0.1837 | 168.6 | 96.57 | 581.8 | 410.3 | 0.0038 |

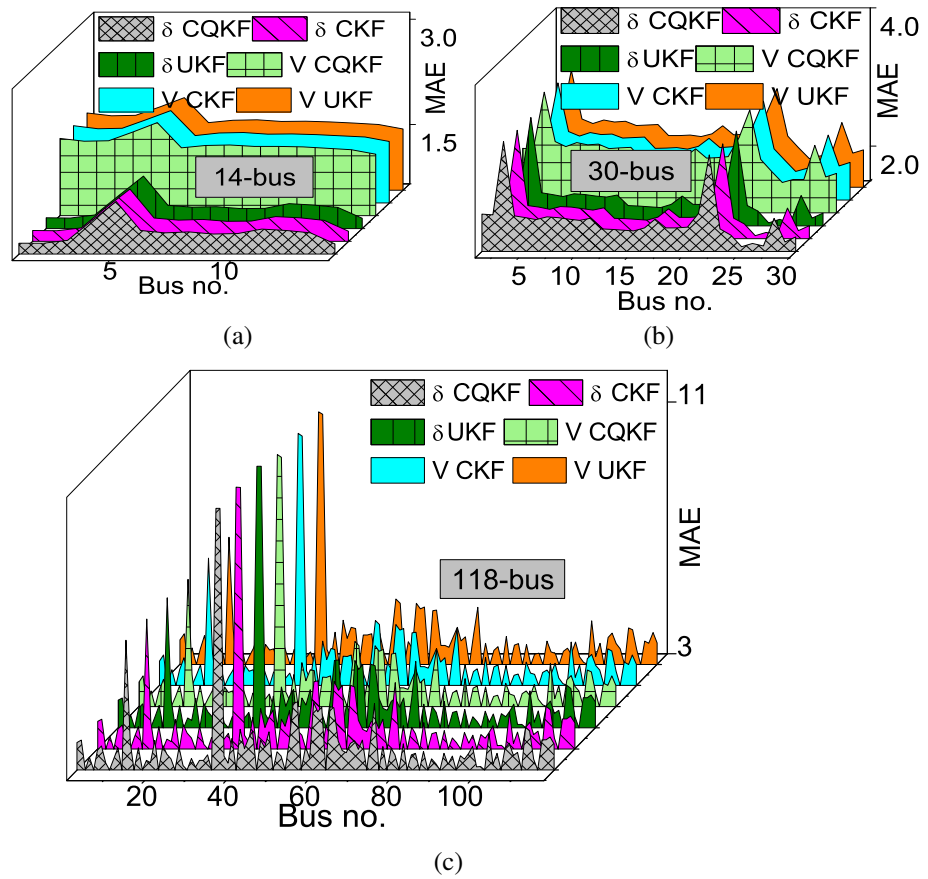


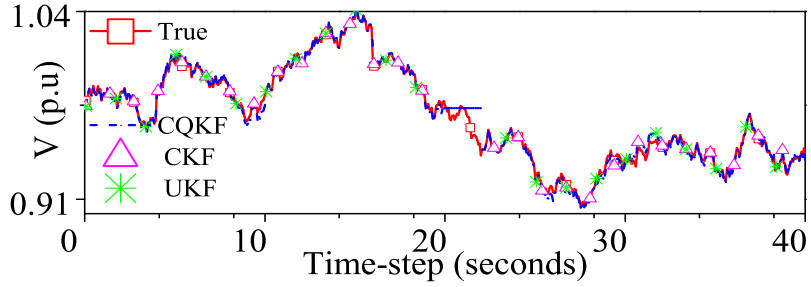
Figure 5.3: Case-1: MAE (in 10^{-2}) for voltage magnitude (V) and phase angle (δ) of all buses for the proposed (CQKF) and existing PSSE methods. **The modified CQKF-base PSSE method voltage magnitude (V) shown in black color and phase angle (δ) shown in green color.**

The MAEs of voltage magnitude and phase angle obtained using the proposed (shown in black and green color) and the existing PSSE methods for all power networks under consideration were compared, as shown in Fig. 5.3. It can be observed that spikes are displayed on bus-5 for 14-bus system (Refer Fig. 5.3(a)), bus-22 for 30-bus system (Refer Fig. 5.3(b)), and bus-36 for 118-bus system (Refer Fig. 5.3(c)). The spikes at these buses revealed an increase in MAE value and can be further reduced by installing PMU at the associated bus in the 14-, 30-, and 118-bus power system networks. It is evident from Table 5.2 that the CQKF-based PSSE has superior estimation performance with the least performance index values, such as average of MSE, average of MAE, and MAXE. Combining Figs. 5.2, 5.3, and Table 5.2 yield the lowest error values for the modified CQKF-based PSSE, indicating an improved accuracy but requiring a modest increase in computational storage.

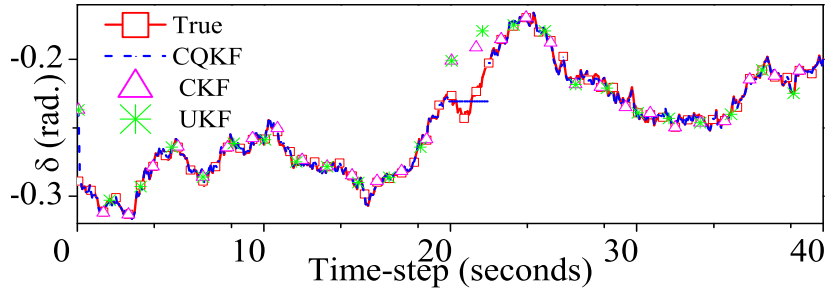
5.4.2 Case-2: To study handling of sudden load change and temporary sensor failure

This case investigates the robustness of the proposed estimator under load change conditions. This case studies the proposed estimator considering a 10% load change at 8 second in bus-3 and 10% power generation change at 16 second in bus-2 a false data packets of null matrix is sent to the estimator as sensor failure occurred in PMU at bus-2. Figure 6.4 illustrates the true and estimated plot of voltage and phase angle at bus-9 of a 14-bus power system. The proposed estimator demonstrates satisfactory performance by accurately estimating the true states following an 8 second 10% load change at bus-3 and a 16 second 10% power generation change at bus-2. In addition, the proposed estimator takes into account the predicted mean and covariance in the event of sensor failure between 20-24 seconds, whereas other existing PSSEs tend to diverge under similar conditions. This feature of the proposed estimator ensures its robustness and reliability in handling sensor failures, ultimately improving the accuracy and reliability of the state estimation. Additionally, error performances of the PSSEs are also presented in tabulated

format as shown in Table 5.3. It clearly validates that the proposed estimator performance bettered during load change and sensor failure. This figure demonstrates the successful estimation capability of the proposed robust forecasting-aided CQKF-based PSSE, even in adverse effects. Moreover, it is evident from Figure 5.4 that the performance indices of the existing PSSEs are inferior to those of the proposed PSSE.



(a) Voltage magnitude V (p.u.)



(b) Phase angle δ (radian)

Figure 5.4: True and estimate plots at bus-9 of 14-bus under load changing and sensor failure condition.

Table 5.3: Case-2: Performance indices (in 10^{-3}) of all PSSEs obtained by averaging the voltage magnitude (V) and phase angle δ across all buses for 14-bus power system.

| PSSE | Average of MSE | | Average of MAE | | MAXE | |
|------|----------------|----------|----------------|----------|------|----------|
| | V | δ | V | δ | V | δ |
| CQKF | 1.6 | 1.3 | 3.6 | 6 | 6.3 | 3.1 |
| CKF | 3 | 1.6 | 11 | 13.9 | 13 | 5 |
| UKF | 3.2 | 1.6 | 12 | 14.1 | 14.5 | 6 |

5.5 Discussion and conclusion

This chapter proposed a CQKF-based PSSE algorithm and its design methodology for the power system dynamic state estimation problem. The main advantage of the proposed technique over the conventional approach is the increased accuracy with comparatively few calculations to achieve improved estimation performance. The improvements in accuracy were made possible by utilizing the spherical cubature and the Gauss-Laguerre quadrature rule to approximate the nonlinear intractable integrals.

The proposed PSSE was validated using benchmark power system networks, including IEEE 14-, 30-, and 118-bus systems. Simulation-based studies were conducted on these systems, and the results showed significant improvements in estimation performance when using the modified CQKF-based PSSE compared to CKF- and UKF-based PSSEs. Specifically, in terms of mean absolute error deviation, the 118-bus study demonstrated improvements of 1.14% and 1.24%, while the 30-bus study showed improvements of 2.17% and 4.34%, respectively. The 14-bus study showed improvements of 0.56% and 0.81% with respect to CKF- and UKF-based PSSEs, respectively.

Generally, voltage at any point in the power system should not deviate more than 5% above or below the nominal voltage level. That means improvements are significant in estimation performance for sensitive power networks, specifically with high voltage magnitudes (measured in KV or MV). This can enhance online monitoring of voltage and load angle and help to improve energy management strategy and grid stability with reduced risk. This work implements a second order Gauss-Laguerre quadrature rule for numerical approximation of the intractable integrals in its Gaussian PDF. Applying higher order quadrature rules improves estimation accuracy at the cost of an increased computational storage requirement. However, with the advent of intelligent high storage devices, this storage may not be a major concern. However, a good trade-off can be made between estimation accuracy and computational storage capacity for selecting the order of Gauss-Laguerre quadrature rule. In addition, the modified CQKF-based PSSE also characterizes a CKF-based PSSE when a Gauss-Laguerre quadrature rule is used.

In light of numerous real-life irregularities, including unknown state dynamics, outliers in Gaussian noises, temporary sensor failure, and unknown noise statistical information, the GF-based PSSE requires an extension to handle such abnormalities effectively.

Chapter 6

Self-Adaptive Forecasting-Aided Gaussian Filtering-based Power System State Estimation under non-Gaussian Outliers

As discussed earlier in Chapter 1, the growing usage of electric vehicles, traction loads, and distributed energy resources (DERs), such as solar, wind, and others, introduce harmonics and frequent load fluctuations into the grid, making them highly unpredictable and fault sensitive, which needs fast online monitoring. An accurate PSSE is critical for developing effective energy management strategies and ensuring stable, secure, and reliable power delivery [134]. In this chapter, we propose a more robust and computationally efficient extension of the previously existing Gaussian filter (GF)-based PSSE approach, building upon the work presented in Chapter 5. Our proposed approach aims to address the practical challenges discussed in Chapter 2.2 that arise in non-ideal scenarios of complex power system networks and develop a more effective estimator, as discussed in Chapter 5.

Recalling Chapter 2, the state-of-the-art PSSEs implement Gaussian filters, such as EKF [46], UKF[163], and CKF [48], to recursively estimate bus voltages. The CKF-based PSSE outperforms the EKF- and UKF-based PSSEs both in terms of accuracy, stability,

and computational cost. In the literature review of filtering methods, several traditional approaches, including GHF [30], SQKF [159] have been identified. However, we avoided their implementation in the design of PSSE due to their extensively high computational cost, making real-time monitoring for large buses difficult.

The Gaussian filtering-based traditional PSSE methods suffer from several drawbacks, such as: i) in the prediction step, they essentially require mathematical models of state dynamics, which is practically unknown in dynamic power networks; ii) they require exact statistical information on noises, again unknown in real-life PSSE problems, and iii) the process and measurements often consist of non-Gaussian outliers due to randomly disturbed power generation-demand scenarios in a process model, and temporal instrument failures due to various limitations of communication links, and uncertainties in intelligent electronic devices.

The filtering and estimation literature specifically witnesses a few contributions [46], [164], [117], [160], [165], [137], and [139]. To deal with the above limitations, Holt's double exponential smoothing introduced for state prediction [46], [160], introduced a forgetting-factor based adaptive noise filtering approach [164], [139]. Maximum correntropy (MC) and minimum entropy (ME)-based design criteria are used to address non-Gaussian outliers, respectively, in [117], [125], and [140]. However, existing methods only address one limitation of traditional PSSE methods, while the simultaneous existence of all limitations can not be denied. This chapter introduces a robust self-adaptive maximum correntropy forecasting-aided Gaussian filter (FSMCGF)-based PSSE technique to simultaneously address the drawbacks of typical existing PSSE methods. Through the following notes, we summarize the contributions of the proposed FSMCGF-based PSSE method.

- A novel robust self-adaptive maximum correntropy forecasting-aided cubature Kalman filter (FSMCGF)-based PSSE method is proposed for real-time monitoring of power system states (voltage and phase angle) under noisy environments.
- State dynamics do not require mathematical models that are practically unknown.

- This chapter adaptively estimates process and measurement noise covariance by innovation- and residual-based forgetting factor method of Sage-Husa estimator.
- Numerous simulation shows the performance of FSMCGF depends on the Kernel's bandwidth, *e.g.*, A smaller Kernel's bandwidth considerably improves outlier rejections and vice-versa. An adaptive approach is implemented by auto-adjusting the bandwidth of the Kernel using the proposed FSMCGF-based PSSE method.
- In addition, it detects large faulty conditions sensor outliers as bad-data conditions and eliminates them while accurately estimating the power system states.
- This chapter further includes the identifiability of noise statistics and \mathbf{Q}/\mathbf{R} ratio, bad data conditions, random load fluctuation, and non-Gaussian noises in process and measurement model. We validate our findings through extensive simulations using different case scenarios.
- Under the proposed method, any existing Gaussian filters, such as the EKF, UKF, and CKF, can be formulated according to the practitioner's convenience.
- The consistency of the proposed FSMCGF-based PSSE is computed along with all other existing PSSEs.

This chapter implements a relatively stable, more accurate, and computationally efficient CKF-based formulation of the proposed FSMCGF-based PSSE method and validated on American electric power systems (in the Midwest) popularly known as IEEE 14-, 30-, and 118-bus power system networks.

6.1 Problem formulation

For a single set of data packets from sensors, the standard discrete form of nonlinear dynamic state space representation of real-time power flow model can be expressed using the Eqs. (1.1) and (1.2) [48], $\mathbf{x}_k \in \mathbb{R}^n$ and $\mathbf{y}_k \in \mathbb{R}^m$ denote state and augmented measurement, respectively with $k \in \{1, 2, \dots, N\}$. Moreover, $\mathcal{f}_{k-1} : \mathbf{x}_{k-1} \rightarrow \mathbf{x}_k$ and $\mathcal{h}_k : \mathbf{x}_k \rightarrow \mathbf{y}_k$ represent standard dynamical operators. Finally, $\mathcal{Q}_k \in \mathbb{R}^n$ and $\mathcal{V}_k \in \mathbb{R}^m$ represent the process and sensor noises, respectively, approximated as zero-mean

Gaussian with covariances \mathbf{Q}_k and \mathbf{R}_k , respectively. For a detailed discussion on dynamic power system model, readers may please refer to Chapter 5.2.

The process noise \mathcal{Q}_k compensates for the modeling inaccuracy of the state dynamics due to random fluctuations around the nominal operating conditions. Additionally, the measurement noise \mathcal{V}_k compensates for the sensor errors caused by time skewness and transmission interference in the RTUs and the data packet errors in the PMUs, respectively.

To this end, let us take the following notes:

- Unknown state dynamics should not be assumed constant to maintain accuracy in PSSE and reflect the transient behavioral changes in the power system.
- Traditional PSSE methods assume process and measurement noise covariance to be known and time-independent, potentially harming accuracy.
- Non-Gaussian outliers should not be ignored in process and measurements to maintain accuracy in PSSE.

The complex and dynamic power system can not be modeled as a certain state transition function \mathcal{f}_{k-1} . Hence, the proposed filter implements a forecasting tool to predict the dynamic states before reaching the actual measurement. In this regard, We implement a simplified forecasting method based on an auto-regressive integrated moving average (ARIMA) model named Holt's double exponential smoothing technique for tracking the dynamics of the process model in a real-time manner [160]. The proposed method is designed under the MC criterion for handling the non-Gaussian outliers in Gaussian distributed noises. This design criterion uses a Kernel window between the estimated and predicted values to characterize the nature of the non-Gaussian outliers. The proposed method considers a time-dependent Kernel width to efficiently address the outliers' time-varying nature. Moreover, the suggested filter employs the computationally efficient Sage-Husa adaptive (SGA) technique, which is inspired by the Sage-Husa adaptive Kalman filter (SHAKF) [139], to dynamically identify the noise statistics in each recursive step. Additionally, a robust algorithm is devised to mitigate temporal faults in

sensors without compromising the accuracy of the estimation process. This algorithm is commonly referred to as a bad-data identifier and can effectively detect sudden false data injected via sensors.

6.2 FSMCGF-Based PSSE method

The objective of the proposed FSMCGF-based PSSE is to estimate the unknown state \mathbf{x}_k (bus voltages) recursively as it receives noisy measurements \mathbf{y}_k from RTU and PMU sensors while also addressing the limitations of existing PSSEs.

We design the proposed FSMCGF-based PSSE method under the Gaussian filtering structure [21], involving prediction and update steps. The Gaussian filtering approximates the prior state, prior measurement, and posterior state as $\mathfrak{N}(\mathbf{x}_{k|k-1}; \hat{\mathbf{x}}_{k|k-1}, \mathbf{P}_{k|k-1})$, $\mathfrak{N}(\mathbf{y}_{k|k-1}; \hat{\mathbf{y}}_{k|k-1}, \mathbf{P}_{k|k-1}^{\mathbf{y}\mathbf{y}})$ and $\mathfrak{N}(\mathbf{x}_{k|k}; \hat{\mathbf{x}}_{k|k}, \mathbf{P}_{k|k})$, where \mathfrak{N} denotes a Gaussian distribution as discussed earlier in Chapter 1 and 5.3.

The computation of estimates and covariances involves multivariate Gaussian weighted intractable integrals, which are numerically approximated as a weighted sum of deterministically computed sample points. The sample points and weights, denoted as $\boldsymbol{\xi}$ and \mathbf{W} , respectively, are determined offline. Every Gaussian filter uses different sets of $\boldsymbol{\xi}$ and \mathbf{W} . For example, the CKF uses the third-degree spherical cubature rule of numerical integration, with $N_s = 2n$ sample points and weights. It obtains the j^{th} sample point $\boldsymbol{\xi}_j$ as $\sqrt{n}[\mathbf{I}_n \quad -\mathbf{I}_n]$, while the j^{th} weight is given as $\mathbf{W}_j = 1/2n, \forall j \in \{1, 2, \dots, N_s\}$.

As the proposed FSMCGF-based PSSE method is designed for a general Gaussian filter, we discuss its design aspects for general sample points and weights, *i.e.*, $\boldsymbol{\xi}$ and \mathbf{W} . In the following discussions, we introduce the design aspects of the proposed FSMCGF-based PSSE method in prediction and update steps.

6.2.1 Prediction

In Gaussian filtering-based PSSEs, the state prediction step aims to determine prediction parameters $\hat{\mathbf{x}}_{k|k-1}$ and $\mathbf{P}_{k|k-1}$ as discussed in Chapter 5.3, by following the Eqs. (5.5) to (5.9), and subsequently using algorithm given in Appendix C.

6.2.2 Update

The objective of this step is to compute the desired posterior estimate $\hat{\mathbf{x}}_{k|k}$ in GF-based PSSE method, using deterministic cubature points and weights, to estimate unknown bus voltages with occasional non-Gaussian noises. This step computes the measurement estimate $\hat{\mathbf{y}}_{k|k-1}$, its covariance $\mathbf{P}_{k|k-1}^{yy}$, and state-measurement cross-covariance $\mathbf{P}_{k|k-1}^{xy}$ [48].

$$\begin{cases} \hat{\mathbf{y}}_{k|k-1} = \sum_{i=1}^{N_s} \mathbf{W}_i \xi_{i,k|k-1}^\gamma, \\ \mathbf{P}_{k|k-1}^{yy} = \sum_{i=1}^{N_s} \mathbf{W}_i (\xi_{i,k|k-1}^\gamma - \hat{\mathbf{y}}_{k|k-1}) (\xi_{i,k|k-1}^\gamma - \hat{\mathbf{y}}_{k|k-1})^T + \mathbf{R}_k, \\ \mathbf{P}_{k|k-1}^{xy} = \sum_i \mathbf{W}_i (\xi_{i,k|k-1} - \hat{\mathbf{x}}_{k|k-1}) (\xi_{i,k|k-1}^\gamma - \hat{\mathbf{y}}_{k|k-1})^T, \end{cases}$$

with $\xi_{i,k|k-1}^\gamma = \gamma_k(\mathbf{S}_{k|k-1} \xi_i + \hat{\mathbf{x}}_{k|k-1})$ and $\xi_{i,k|k-1} = \mathbf{S}_{k|k-1} \xi_i + \hat{\mathbf{x}}_{k|k-1}$. The Proposed estimator uses a nonlinear kernel to suppress outliers/noise. Unlike the traditional GF-based PSSE, which relies on vulnerable Euclidean distance in mean square error and are prone to large outliers from demand changes, power fluctuations, instrument failures, and communication limitations.

As discussed previously, the real-life PSSE problems witness large non-Gaussian outliers. However, the traditional PSSEs underperform for non-Gaussian outliers. The proposed FSMCGF-based PSSE is designed under MC criterion to overcome this problem [115]. A definition for the correntropy is provided below:

Definition 1 *Let us consider two random variables, \mathbf{U} , and \mathbf{V} . Then, the correntropy $\mathcal{C}_{\mathbf{U},\mathbf{V}}$ between \mathbf{U} and \mathbf{V} is the measure of similarity between the two random variables, which is mathematically given as [35], [166]*

$$\mathcal{C}_{\mathbf{U},\mathbf{V}} = E [\mathcal{K}_{\mathbf{U},\mathbf{V}}(\mathbf{u}, \mathbf{v})] = \int \mathcal{K}_{\mathbf{U},\mathbf{V}} dF_{\mathbf{U},\mathbf{V}}(\mathbf{u}, \mathbf{v}), \quad (6.1)$$

where $\mathbb{E}[\cdot]$ denotes the expectation. Moreover, $\mathcal{K}_{\mathbf{U},\mathbf{V}}$ denotes nonlinear mapping of \mathbf{U} and \mathbf{V} into a Kernel space. We consider the usually chosen Gaussian kernel, giving

$$\kappa_{U,V} = \sum_{n=0}^{\infty} \frac{(-1)^n}{2^n \sigma^{2n}} \mathbb{E} [(U - V)^{2n}]. \quad (6.2)$$

where $\mathbf{e}(i) = u(i) - v(i)$ and $\sigma > 0$ denotes kernel width. As the joint probability of \mathbf{U} and \mathbf{V} is mostly unknown and only a limited number of l_s samples $\{u(i), v(i)\}_{i=1}^{l_s}$ of \mathbf{U} and \mathbf{V} are available, the correntropy is computed as Parzen Kernel estimator. As discussed earlier in Eq. (3.13), the cost function of the nonlinear estimator can be formulated as

$$\mathbf{J}_k = \hat{\mathbf{C}}_{U,V} = \frac{1}{l_s} \sum_{i=1}^{l_s} G_{\sigma}(\mathbf{e}_k(i)). \quad (6.3)$$

In the filter design, we consider the maximization of correntropy between the true state \mathbf{x}_k and estimated state $\hat{\mathbf{x}}_{k|k}$ i.e., maximization of cost function \mathbf{J}_k . Hence, the best estimate $\hat{\mathbf{x}}_{k|k}$ is a solution of $\mathbf{J}_k|_{max}$.

Under the MC-based design criterion, the best estimate $\hat{\mathbf{x}}_{k|k}$ must ensure the maximum correntropy between the true state \mathbf{x}_k and estimated state $\hat{\mathbf{x}}_{k|k}$. In this criterion, $\hat{\mathbf{x}}_{k|k}$ is obtained by solving a regression model that takes into account the augmented states, given as [166][138]

$$\begin{bmatrix} \hat{\mathbf{x}}_{k|k-1} \\ \mathbf{y}_k \end{bmatrix} = \begin{bmatrix} \mathbf{x}_k \\ \gamma(\mathbf{x}_k) \end{bmatrix} + \mathbf{e}_k. \quad (6.4)$$

Before proceeding further, we define two error quantities, $\boldsymbol{\varepsilon}_{k|k-1}^x$ and $\boldsymbol{\varepsilon}_{k|k}^x$, as

$$\begin{aligned} \boldsymbol{\varepsilon}_{k|k-1}^x &= \mathbf{x}_k - \hat{\mathbf{x}}_{k|k-1}, \\ \boldsymbol{\varepsilon}_{k|k}^x &= \mathbf{x}_k - \hat{\mathbf{x}}_{k|k}, \end{aligned} \quad (6.5)$$

To this end, objective is to compute the $\hat{\mathbf{x}}_{k|k}$ from the regression model in Eq. (6.4). However, nonlinear function $\gamma(\mathbf{x}_k)$ in regression model may result in a non-trivial solution. To improve its numerical stability, the measurement model is statistically

linearized as [167]

$$\mathbf{y}_k = \hat{\mathbf{y}}_{k|k-1} + \Gamma_k \boldsymbol{\varepsilon}_{k|k-1}^x + \mathcal{S}_k + \mathcal{V}_k, \quad (6.6)$$

where $\Gamma_k = (\mathbf{P}_{k|k-1}^{-1} \mathbf{P}_{k|k-1}^{\mathbf{xy}})^T$ is measurement slope matrix, and \mathcal{S}_k stands for statistical linearization error. Substituting linearized \mathbf{y}_k in Eq. (6.4), and simplified to compute augmented error [117]

$$\mathbf{e}_k = \begin{bmatrix} \hat{\mathbf{x}}_{k|k-1} \\ \boldsymbol{\varepsilon}_{k|k-1}^y + \Gamma_k \hat{\mathbf{x}}_{k|k-1} \end{bmatrix} - \begin{bmatrix} \mathbb{I}_n \\ \Gamma_k \end{bmatrix} \mathbf{x}_k = \mathbf{U}_k - \mathbf{V}_k, \quad (6.7)$$

where measurement innovation $\boldsymbol{\varepsilon}_{k|k-1}^y$ and residual $\boldsymbol{\varepsilon}_{k|k}^y$ errors are

$$\begin{aligned} \boldsymbol{\varepsilon}_{k|k-1}^y &= \mathbf{y}_k - \hat{\mathbf{y}}_{k|k-1} = \Gamma_k \boldsymbol{\varepsilon}_{k|k-1}^x + \mathcal{V}_k, \\ \boldsymbol{\varepsilon}_{k|k}^y &= \mathbf{y}_k - \hat{\mathbf{y}}_{k|k} = \Gamma_k \boldsymbol{\varepsilon}_{k|k}^x + \mathcal{V}_k, \end{aligned} \quad (6.8)$$

with covariance as

$$\mathbb{E}[\mathbf{e}_k \mathbf{e}_k^T] = \begin{bmatrix} \mathbf{S}_{k|k-1}^{\mathbf{p}} (\mathbf{S}_{k|k-1}^{\mathbf{p}})^T & \mathbf{0} \\ \mathbf{0} & \mathbf{S}_k^{\mathbf{r}} (\mathbf{S}_k^{\mathbf{r}})^T \end{bmatrix} = \mathbf{S}_{k|k-1} (\mathbf{S}_{k|k-1})^T. \quad (6.9)$$

and $\mathbb{E}[\cdot]$ denotes the expectation operator with

$$\begin{cases} \mathbf{S}_{k|k-1} = \text{chol}(\mathbb{E}[\mathbf{e}_k \mathbf{e}_k^T]), \\ \mathbf{S}_{k|k-1}^{\mathbf{p}} = \text{chol}(\mathbf{P}_{k|k-1}), \\ \mathbf{S}_k^{\mathbf{r}} = \text{chol}(\mathbb{E}[(\mathcal{L}_k + \mathcal{V}_k)(\mathcal{L}_k + \mathcal{V}_k)^T]), \\ \quad = \text{chol}(\mathbb{E}[\mathbf{P}_{k|k-1}^{\mathbf{yy}} - \Gamma_k \mathbf{P}_{k|k-1} \Gamma_k^T]), \end{cases} \quad (6.10)$$

normalizing Eq. (6.7) by multiplying $\mathbf{S}_{k|k-1}^{-1}$ on both sides, gives

$$\bar{\mathbf{e}}_k = \mathbf{S}_{k|k-1}^{-1} \begin{bmatrix} \hat{\mathbf{x}}_{k|k-1} \\ \mathcal{E}_{k|k-1}^y + \Gamma_k \hat{\mathbf{x}}_{k|k-1} \end{bmatrix} - \mathbf{S}_{k|k-1}^{-1} \begin{bmatrix} \mathbb{I} \\ \Gamma_k \end{bmatrix} \mathbf{x}_k = \mathcal{D}_k - \mathcal{W}_k \mathbf{x}_k. \quad (6.11)$$

where \mathcal{D}_k , \mathcal{W}_k , and $\bar{\mathbf{e}}_k = \mathbf{S}_{k|k-1}^{-1} \bar{\mathbf{e}}_k$ are $(n+m)$ -dimensional arrays.

The value of \mathbf{x}_k that maximizes \mathbf{J}_k is the desired posterior estimate of \mathbf{x} at t_k , i.e.,

$$\mathbf{x}_k = \arg \max_{\mathbf{x}_k} \mathbf{J}_k. \quad (6.12)$$

Therefore, $\hat{\mathbf{x}}_{k|k}$ is a solution of

$$\frac{d\mathbf{J}_k}{d\mathbf{x}_k} = 0. \quad (6.13)$$

Eq. (6.13) computes the solution of cost function at t_k as [35]

$$\begin{aligned} \mathbf{x}_k = g(\mathbf{x}_k) &= \left(\sum_{l=1}^{l_s} G_\sigma(\bar{\mathbf{e}}_k(l)) (\mathcal{W}_k(l))^T \mathcal{W}_k(l) \right)^{-1} \\ &\times \left(\sum_{l=1}^{l_s} G_\sigma(\bar{\mathbf{e}}_k(l)) (\mathcal{W}_k(l))^T \mathcal{D}_k(l) \right), \end{aligned} \quad (6.14)$$

where $\mathcal{D}_k(l)$, $\mathcal{W}_k(l)$, and $\bar{\mathbf{e}}_k(l)$ represent l^{th} element of \mathcal{D}_k and \mathcal{W}_k , and $\bar{\mathbf{e}}_k$, respectively, $\forall l \in \{1, 2, \dots, n+m\}$. Please note that $g(\mathbf{x}_k)$ is an exponential function of \mathbf{x}_k due to the Gaussian kernel $G_\sigma(\bar{\mathbf{e}}_k(l))$. Therefore, Eq. (6.14) fails to offer a closed-form solution. A fixed-point iteration based numerical approximation method [166]

$$\mathbf{x}_k^t = (\mathcal{W}_k^T \boldsymbol{\vartheta}_k \mathcal{W}_k)^{-1} (\mathcal{W}_k^T \boldsymbol{\vartheta}_k \mathcal{D}_k), \quad (6.15)$$

where $\boldsymbol{\vartheta}_k = \text{diag}(\boldsymbol{\vartheta}_k^x, \boldsymbol{\vartheta}_k^y)$, with $\boldsymbol{\vartheta}_k^x = \text{diag}(\bar{\mathbf{e}}_k(1), \dots, \bar{\mathbf{e}}_k(n))$, and $\boldsymbol{\vartheta}_k^y = \text{diag}(\bar{\mathbf{e}}_k(n+1), \dots, \bar{\mathbf{e}}_k(n+m))$. Expanding Eq. (6.15), a detailed expression of \mathbf{x}_k^t is provided in Appendix A. As a result, as discussed in [35], the estimate and covariance of \mathbf{x}_k in every iteration at t_k time instant can be obtained as

$$\begin{aligned}\hat{\mathbf{x}}_{k|k}^t &= \hat{\mathbf{x}}_{k|k-1} + \bar{\mathbf{K}}_k^{t-1} (\mathbf{y}_k - \hat{\mathbf{y}}_{k|k-1}), \\ \mathbf{P}_{k|k}^t &= \left(\mathbb{I}_n - \bar{\mathbf{K}}_k^{t-1} \Gamma_k \right) \mathbf{P}_{k|k-1} \left(\mathbb{I}_n - \bar{\mathbf{K}}_k^{t-1} \Gamma_k \right)^T + \bar{\mathbf{K}}_k^{t-1} \mathbf{R}_k \left(\bar{\mathbf{K}}_k^{t-1} \right)^T,\end{aligned}\quad (6.16)$$

where superscript t represents t^{th} fixed-point iteration for the t_k time instant. Moreover, other parameters used in Eq. (6.16) can be obtained as

$$\begin{cases} \bar{\mathbf{K}}_k^{t-1} = \bar{\mathbf{P}}_{k|k-1}^{t-1} \Gamma_k^T \left(\bar{\mathbf{P}}_{k|k-1}^{yy^{t-1}} \right)^{-1}, \\ \bar{\mathbf{P}}_{k|k-1}^{yy^{t-1}} = \Gamma_k \bar{\mathbf{P}}_{k|k-1}^{t-1} \Gamma_k^T + \bar{\mathbf{R}}_k^{t-1}, \\ \bar{\mathbf{P}}_{k|k-1}^{t-1} = \mathbf{S}_{k|k-1}^p (\vartheta_k^x)^{-1} (\mathbf{S}_{k|k-1}^p)^T, \\ \bar{\mathbf{R}}_k^{t-1} = \mathbf{S}_k^r (\vartheta_k^y)^{-1} (\mathbf{S}_k^r)^T. \end{cases}\quad (6.17)$$

As a stopping criterion for the iterative process, we compute a relative error quantity E_{rr} is smaller than the predefined tolerance level χ in every recursion,

$$E_{rr} = \frac{\|\hat{\mathbf{x}}_{k|k}^t - \hat{\mathbf{x}}_{k|k}^{t-1}\|}{\|\hat{\mathbf{x}}_{k|k}^{t-1}\|}.\quad (6.18)$$

where $\|\cdot\|$ denotes a second norm. Consequently, the iterative process stopped when E_{rr} became smaller than a predefined tolerance level χ . At the end of iterative process, the optimal solutions are computed as

$$\begin{cases} \hat{\mathbf{x}}_{k|k} = \hat{\mathbf{x}}_{k|k}^t, \\ \mathbf{P}_{k|k} = \mathbf{P}_{k|k}^t. \end{cases}\quad (6.19)$$

Furthermore, we calculate the process error terms $\boldsymbol{\varepsilon}_{k|k}^x$ and $\boldsymbol{\varepsilon}_{k|k-1}^x$, as well as the measurement error terms $\boldsymbol{\varepsilon}_{k|k}^y$ and $\boldsymbol{\varepsilon}_{k|k-1}^y$, to be utilized at a later time.

To this point, the proposed estimator optimizes \mathbf{x}_k in a time-independent Kernel space, with σ prioritizing second-order moments over higher order moments (as shown in Eq. (6.2)). The optimality of the MC criterion is dependent on the value of σ , which must be adapted to handle varying outlier conditions. The existing PSSEs assume

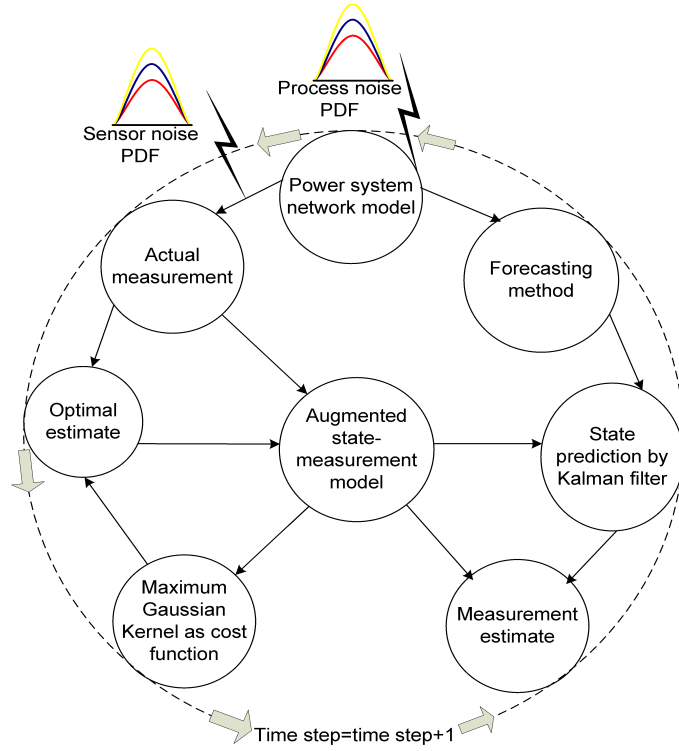


Figure 6.1: Modified MC-based PSSE algorithm

the noise covariances \mathbf{Q}_k and \mathbf{R}_k , which in real-time power systems may be unknown and time-dependent. Thus, the proposed estimator's robust and adaptive features are presented in the following sections.

Remark 6.2.1 *Large sensor outliers due to system failure may produce singular ϑ_k matrix, which in turn may fail estimation algorithm. So a robust approach is given below:*

- We compared $|\phi_k| = |\boldsymbol{\varepsilon}_{k|k-1}^y (\boldsymbol{\Gamma}_k \mathbf{P}_{k|k-1} \boldsymbol{\Gamma}_k^T + \mathbf{R}_k)^{-1} \boldsymbol{\varepsilon}_{k|k-1}^{yT}|$ with positive threshold value ϕ_{th} and included a precondition for state update to be followed.
- If $|\phi_k| > \phi_{th}$, the measurement data is considered to have temporal bad data. Hence state update is skipped, i.e $\mathbf{x}_{k|k} = \hat{\mathbf{x}}_{k|k-1}$, and $\mathbf{P}_k = \mathbf{P}_{k|k-1}$.

The proposed estimator adaptively updates σ_k^t through t^{th} fixed-point iteration at t_k time-step in accordance with dynamically varying Gaussian Kernel, its innovation covariance, and covariance with measurement residual at time t_k .

$$\sigma_k^t = \begin{cases} \sigma_{k-1}^t, & \text{if } tr(\bar{\mathbf{P}}_{k|k-1}^{yy^t}) \leq tr(\boldsymbol{\varepsilon}_{k|k}^y \boldsymbol{\varepsilon}_{k|k}^{yT}) \\ \sigma_{k-1}^t \frac{tr(\bar{\mathbf{P}}_{k|k-1}^{yy^t})}{tr(\boldsymbol{\varepsilon}_{k|k}^y \boldsymbol{\varepsilon}_{k|k}^{yT})}, & \text{otherwise} \end{cases} \quad (6.20)$$

where $\boldsymbol{\varepsilon}_{k|k}^y$ denotes residual error, $\bar{\mathbf{P}}_{k|k-1}^{yy^t}$ denote innovation covariance at t^{th} fixed-point iteration and $tr(\cdot)$ denotes the trace. Please note that $\sigma_k^t \rightarrow \infty$ leads to $\boldsymbol{\vartheta}_k \rightarrow \mathbb{I}$. Thus FSMCGF behaves as a CKF method. Conversely, $\sigma_k^t \rightarrow 0$ leads to $\boldsymbol{\vartheta}_k \rightarrow 0$, resulting in filter divergence.

The proposed PSSE adaptively estimates the unknown statistical noise information. The nonlinear filters implemented in [168],[169] proposes Bayesian and maximum likelihood methods, which are reliable. However, these filtering solutions are computationally costly, and assume time-invariant dynamic error, which is unrealistic for online monitoring. Covariance matching methods, such as SHAKF [137],[138], estimate noise statistics using innovation or residual sequences and then employ a matching technique. This work proposes a computationally efficient self-adaptive covariance matching method for the MCGF-based PSSE. Based on innovation and residual measurement error, the estimated \mathbf{R}_k is calculated based on measurement covariance as

$$\begin{aligned}\mathbf{R}_k &= \boldsymbol{\varepsilon}_{k|k-1}^y \boldsymbol{\varepsilon}_{k|k-1}^{y^T} - \Gamma_k \mathbf{P}_{k|k-1} \Gamma_k^T, \\ \mathbf{R}_k &= \boldsymbol{\varepsilon}_{k|k}^y \boldsymbol{\varepsilon}_{k|k}^{y^T} + \Gamma_k \mathbf{P}_{k|k} \Gamma_k^T.\end{aligned}\tag{6.21}$$

Readers may follow [137] and Appendix D.1 for a detailed derivation. To ensure positive definiteness \mathbf{R}_k at time-step k , is computed using second expression of Eq. (6.21), and thus, we will use the same expression. at time-step t_k Here-onwards, this chapter represents $\hat{\mathbf{Q}}_k$, and $\hat{\mathbf{R}}_k$ to represent adaptive noise covariance. similarly, adaptive process noise covariance [139] $\hat{\mathbf{Q}}_k$ can be obtained as

$$\hat{\mathbf{Q}}_k = \mathbb{E} [\mathcal{Y}_k \mathcal{Y}_k^T] = \mathbf{K}_k \mathbb{E} [\boldsymbol{\varepsilon}_{k|k}^y \boldsymbol{\varepsilon}_{k|k}^{y^T}] \mathbf{K}_k^T = \bar{\mathbf{K}}_k \boldsymbol{\varepsilon}_{k|k}^y \boldsymbol{\varepsilon}_{k|k}^{y^T} \bar{\mathbf{K}}_k^T,\tag{6.22}$$

where $\boldsymbol{\varepsilon}_{k|k}^y$ and $\boldsymbol{\varepsilon}_{k|k-1}^y$ are measurement errors. Please note that a wrong selection of \mathbf{R}_k is reflected in measurement residual error. Therefore, we define a weighting parameter μ . Thus, we obtain the final error value as a weighted summation of $\hat{\mathbf{R}}_k$ and measurement error.

A weight is given to process and measurement noise based on the innovation in

measurement sequence and standard deviation in current measurement covariance.

$$\hat{\mathbf{R}}_k = \mu_k \hat{\mathbf{R}}_{k-1} + (1 - \mu_k) \left(\boldsymbol{\varepsilon}_{k-1|k-1}^y \boldsymbol{\varepsilon}_{k-1|k-1}^{yT} + \Gamma_k \mathbf{P}_{k-1|k-1} \Gamma_k^T \right), \quad (6.23)$$

where

$$\mu_k = \begin{cases} 1, & \text{if } \phi_{th}^{ar} \geq 1 \\ \phi_{th}^{ar}, & \text{otherwise} \end{cases} \quad (6.24)$$

with $\phi_{th}^{ar} = \frac{\text{tr}(\bar{\mathbf{P}}_{k|k-1}^{yy^t})}{\text{tr}(\boldsymbol{\varepsilon}_{k-1|k-1}^y \boldsymbol{\varepsilon}_{k-1|k-1}^{yT})}$. Observing state model variation and innovation sequence, complex PSSE method needs to be online tracking with self-adaptive nature of noise covariance. The innovation sequence given in Eq. (6.24) is a judging criterion for evaluating the change of measurement noise dynamics.

$$\hat{\mathbf{Q}}_k = \begin{cases} \hat{\mathbf{Q}}_k, & \text{if } 0.98 \leq \hat{\mathbf{R}}_k / \bar{\mathbf{P}}_{k|k-1}^{yy^t} \leq 1 \\ \mu_k \hat{\mathbf{Q}}_{k-1} + (1 - \mu_k) \bar{\mathbf{K}}_k \boldsymbol{\varepsilon}_{k|k}^y \boldsymbol{\varepsilon}_{k|k}^{yT} \bar{\mathbf{K}}_k^T, & \text{otherwise} \end{cases} \quad (6.25)$$

The steps to be implemented for this iterative method are shown in Algorithm-3.

6.3 Simulation and result

In this section, we validate the improved accuracy of the proposed FSMCGF-based PSSE method compared to the AGF- and GF-based PSSE techniques for 14-, 30-, and 118-bus networks from the American electric power system (in the Midwest). 30 PMU data packets were received between adjacent RTU measurements in the interval of two seconds. Readers may follow Table 5.1 for information on buses with PMU locations (giving voltage and current phasors), power injection, and power flow for 14-, 30-, and 118-bus power system networks [47][162].

True data generation: The power system state dynamic data are same as Section 5.4. The power system state dynamics were modeled as a random walk due to the low likelihood of significant changes between two successive PMU scans. The measurement model used was adopted from [47], [162], and the Gaussian component of process noise

Algorithm 3 Pseudo code for computing $\hat{\mathbf{x}}_{k|k}$ and $\mathbf{P}_{k|k}$.

Input: $\hat{\mathbf{x}}_{k-1|k-1}$, $\hat{\mathbf{x}}_{k|k-1}$, $\mathbf{P}_{k|k-1}$, n , m , χ , and ϕ_{th}

Output: $\hat{\mathbf{x}}_{k|k}$ and $\mathbf{P}_{k|k}$

Initialization: $\hat{\mathbf{x}}_{k|k}(1) = \hat{\mathbf{x}}_{k|k-1}$, $E_{rr} = 1000$ (any large value), and $t = 1$

- 1: $\boldsymbol{\varepsilon}_{k|k-1}^y$, $\boldsymbol{\varepsilon}_{k-1|k-1}^y$, $\boldsymbol{\varepsilon}_{k|k-1}^x$ and $\boldsymbol{\varepsilon}_{k|k}^x$ using Eqs. (6.5) and (6.8)
 - 2: $|\phi_k| = |\boldsymbol{\varepsilon}_{k|k-1}^y (\boldsymbol{\Gamma}_k \mathbf{P}_{k|k-1} \boldsymbol{\Gamma}_k^T + \hat{\mathbf{R}}_k)^{-1} \boldsymbol{\varepsilon}_{k|k-1}^{yT}|$
 - 3: **if** $|\phi_k| > \phi_{th}$ **then**
 - 4: $\mathbf{x}_k = \hat{\mathbf{x}}_{k|k-1}$ and $\mathbf{P}_k = \mathbf{P}_{k|k-1}$
 - 5: **else**
 - 6: **while** $E_{rr} > \chi$ **do**
 - 7: Compute $\mathbf{S}_{k|k-1}^p$, \mathbf{S}_k^R , and $\mathbf{S}_{k|k-1}$ from Eq. (6.10),
 - 8: find $\bar{\mathbf{e}}_k$ using Eq. (6.11),
 - 9: $\boldsymbol{\vartheta}_k = \text{diag}(\bar{\mathbf{e}}_k(1), \dots, \bar{\mathbf{e}}_k(n+m))$,
 - 10: compute $\hat{\mathbf{x}}_{k|k}^t$ and $\mathbf{P}_{k|k}^t$ using Eqs. (6.16) and (6.17),
 - 11: update σ_k^t using Eq. (6.20),
 - 12: compute E_{rr} using (6.18),
 - 13: $t = t + 1$
 - 14: **end while**
 - 15: $\hat{\mathbf{x}}_{k|k}$, and $\mathbf{P}_{k|k}$ using (6.19),
 - 16: update $\hat{\mathbf{Q}}_k$ and $\hat{\mathbf{R}}_k$ following Eqs. (6.23)- (6.25),
 - 17: **return** $\hat{\mathbf{x}}_{k|k}$ and $\mathbf{P}_{k|k}$.
 - 18: **end if**
-

covariance was considered as $\mathbf{Q}_{1,k} = 9 * 10^{-6} \mathbb{I}_{n \times n}$ [134]. Here, the Gaussian component of measurement noises with the following standard deviation values was considered [161]: From RTUs: slack voltage $\delta_v^r = 0.001$, power injections $\delta_{pi}^r = 0.02$, and $\delta_{qi}^r = 0.02$, power flows between buses $\delta_{pf}^r = 0.02$, and $\delta_{pf}^i = 0.02$, and from PMUs: voltages (both real and imaginary) $\delta_v^p = 0.001$, and currents between connected buses (both real and imaginary) $\delta_i^p = 0.001$. With the given values standard deviation of the augmented measurement model is given as

$$\boldsymbol{\delta} = \text{diag}([\delta_v^r \ \delta_{pi}^r \ \delta_{qi}^r \ \delta_{pf}^r \ \delta_{pf}^i \ \delta_v^p \ \delta_i^p]). \quad (6.26)$$

Then, we take the Gaussian noise component as $\mathcal{V}_{j,k} = \mathcal{N}(\mathbf{0}, \mathbf{R}_{j,k}) \forall j \in \{1, 2\}$, with $\mathbf{R}_{1,k} = \delta^2$.

Following our problem formulation, in addition to the above discussed non-Gaussian noise, we add a non-Gaussian outlier $\mathcal{V}_{2,k}$. Considering that outlier has an additive

effect, the net randomness in the data becomes $\mathcal{V}_k = \kappa_g \mathcal{V}_{1,k} + (1 - \kappa_g) \mathcal{V}_{2,k}$, which becomes non-Gaussian against the Gaussian assumption of the noise. Interestingly, even a Gaussian $\mathcal{V}_{2,k}$ makes the net randomness $\mathcal{V}_k = \kappa_g \mathcal{V}_{1,k} + (1 - \kappa_g) \mathcal{V}_{2,k}$ non-Gaussian. Thus, the purpose of non-Gaussian outlier is served even if we consider $\mathcal{V}_{2,k}$ as Gaussian. To incorporate non-Gaussian noises, this chapter consider weighted sum of Gaussian PDFs $f_{\mathcal{V}_k} = \sum_{i=1}^n \kappa_{gi} f_{\mathcal{V}_{i,k}}$, where $\sum_{i=1}^n \kappa_{gi} = 1$, n denotes number of components and $f_{\mathcal{V}_k}$, represents a weighted summation of Gaussian PDFs $\forall i$. Please note that weighted summation of several Gaussian PDFs gives a non-Gaussian PDF. A similar modeling approach is followed for the process noise $f_{\mathcal{Q}_k} = \sum_{i=1}^n \kappa_{qi} f_{\mathcal{Q}_{i,k}}$ with $\sum_{i=1}^n \kappa_{qi} = 1$.

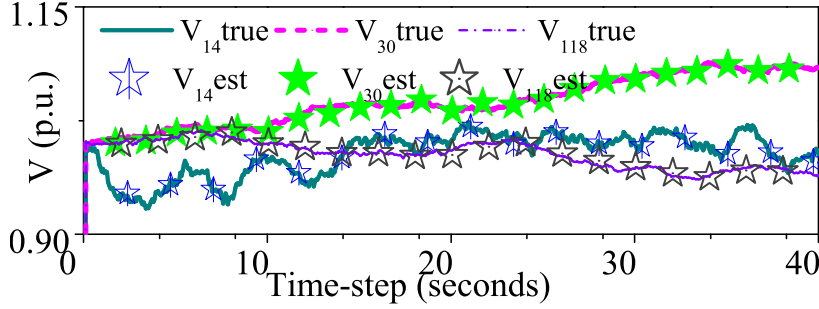
In order to evaluate the adaptability of the proposed estimator, correction factors $\gamma_{\mathbf{Q}} = 10$ and $\gamma_{\mathbf{R}} = 100$ are multiplied with the true noise covariances $\mathbf{Q}_{1,k}$ and $\mathbf{R}_{1,k}$, respectively, to account for the wrongly assumed noise covariances $\hat{\mathbf{Q}}_{1,k}$ and $\hat{\mathbf{R}}_{1,k}$. This approach is employed to validate the performance of the proposed estimator under adaptive conditions. Unless otherwise specified, the aforementioned parameters will remain unchanged.

Performance indices: 100 Monte-Carlo (M_c) simulations were conducted to test the estimators' performances under uncertain states and measurements of the power system. Considering the complexity of the power system dynamic, we study the behavior of the buses transiently. This simulation study compares the proposed estimator with existing GF and AGF methods using performance metrics like RMSE, MAE, and MAXE as mentioned in Chapter 1.10.4. MSE and MAE measure overall square error and absolute deviation between true and estimated states. MAXE computes the maximum deviation between true and estimated states throughout M_c runs.

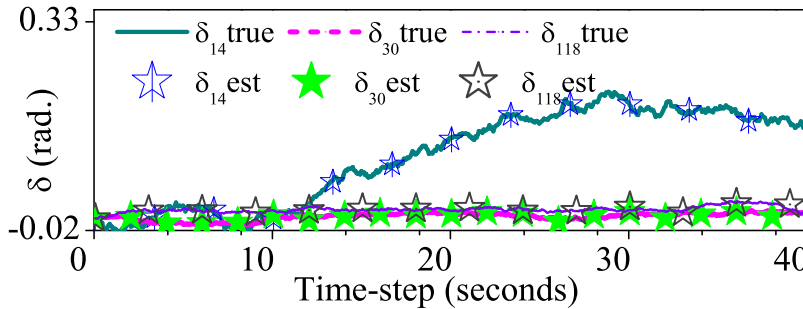
We conducted various simulated environments for performance validation, which are discussed through 4 different case studies. Case-1 considered nominal base voltage, Case-2 and 3 used $\mathbf{x}_0 = 1 \angle 0^\circ$ as true initial states. Case-1 and 2 discussed performance under different irregularities, Case-3 studies the performance of the proposed estimator for handling irregularities simultaneously under loading conditions. Finally, Case-4 analyzes the consistence of the proposed PSSE with other existing PSSEs.

Case-1: Only measurement with non-Gaussian outliers

In this case, we consider that only measurement consists of non-Gaussian outliers with $f_{\mathcal{V}_k} \sim 0.9 \times f_{\mathcal{V}_{1,k}} + 0.1 \times f_{\mathcal{V}_{2,k}}$ where $f_{\mathcal{V}_{1,k}}$ and $f_{\mathcal{V}_{2,k}}$ are pdfs of $\mathcal{N}(\mathbf{0}, \mathbf{R}_{1,k})$ and $\mathcal{N}(\mathbf{0}, \mathbf{R}_{2,k})$, respectively with $\mathbf{R}_{2,k} = 10^4 \delta^2$. Thus, as discussed above, the net randomness in the measurement (including measurement noise and outliers) will be considered as summation of two non-Gaussian. We consider the model and noise parameters same as the above discussion, while we assign the initial estimate and covariance as $\hat{\mathbf{x}}_{0|0} = \mathbf{x}_0$ and $\mathbf{P}_{0|0} = 10^{-6} \mathbb{I}_{n \times n}$, respectively. Sample true and estimation plots obtained using the proposed FSMCGF-based PSSE technique for voltage magnitude and phase angle at bus 9 ($\mathbf{V}_{k,9}$ and $\delta_{k,9}$) are shown in Fig. 6.2. We observed other bus voltages are also successfully estimated. The close match between true and estimated plots shows a successful PSSE for the proposed FSMCGF-based PSSE technique. We analyze the errors for more complex scenarios in the coming subsections.



(a) Voltage magnitude V (p.u.)



(b) Phase angle δ (radian)

Figure 6.2: Case-1: True and estimate plots at bus-9 (subscripts 14, 30, and 118 represent the 14-, 30-, and 118-bus networks, respectively).

Case-2: Gaussian process and measurement noise with random outliers

In this case, process and measurement noise have been non-Gaussian. The measurement noise distribution remains the same as in case-1. Here, the power network is disrupted with hunting condition, represented by non-Gaussian outliers modeled as

$f_{\mathcal{V}_k} \sim 0.9 \times f_{\mathcal{V}_{1,k}} + 0.1 \times f_{\mathcal{V}_{2,k}}$ where $f_{\mathcal{V}_{1,k}}$ and $f_{\mathcal{V}_{2,k}}$ are pdfs of $\mathcal{N}(\mathbf{0}, \mathbf{R}_{1,k})$ and $\mathcal{N}(\mathbf{0}, \mathbf{R}_{2,k})$, respectively with $\mathbf{R}_{2,k} = 10^4 \delta^2$.

$$f_{\mathcal{Q}_k} \sim 0.9 \times f_{\mathcal{Q}_{1,k}} + 0.1 \times f_{\mathcal{Q}_{2,k}} \mathcal{N}(\mathbf{0}, \mathbf{Q}_{2,k}), \quad (6.27)$$

where $f_{\mathcal{Q}_{1,k}}$ and $f_{\mathcal{Q}_{2,k}}$ are pdfs of $\mathcal{N}(\mathbf{0}, \mathbf{Q}_{1,k})$ and $\mathcal{N}(\mathbf{0}, \mathbf{Q}_{2,k})$, respectively with $\mathbf{Q}_{2,k} = 10^3 \mathbf{Q}_{1,k}$.

In this test case, the proposed FSMCGF-based PSSE method was compared with the AGF- and GF-based PSSE methods using different networks. Multiple performance metrics, such as RMSE, MAE, and MAXE, were computed. The average MAE at each bus for voltage and phase angle are plotted in Fig. 6.3, and it is observed that the proposed FSMCGF method (shown in black and magenta) outperforms the GF and AGF methods in terms of MAE for all tested environments. The minimum MAE values are achieved for voltage (in black color) and phase angles (in pink color) for 14-, 30-, and 118-bus networks, as shown in Fig. 6.3(a) to 6.3(c).

Case-3: Performance validation with different non-Gaussian measurement values and $\hat{\mathbf{Q}}_k$ and $\hat{\mathbf{R}}_k$

This case includes a performance comparison of the proposed FSMCGF-based PSSE method with existing AGF- and GF-based PSSE under a wide range of scenarios.

- Performance metrics when both process and measurement noises include random outliers by varying process and measurement noise Gaussian co-efficients κ_q , and κ_r , respectively.
- Performance metrics for different random outliers in measurement noise by varying measurement noise Gaussian co-efficient κ_r .
- Performance comparison for selecting $\hat{\mathbf{Q}}_k$ and $\hat{\mathbf{R}}_k$ values different from respective true values \mathbf{Q}_k and \mathbf{R}_k , respectively.

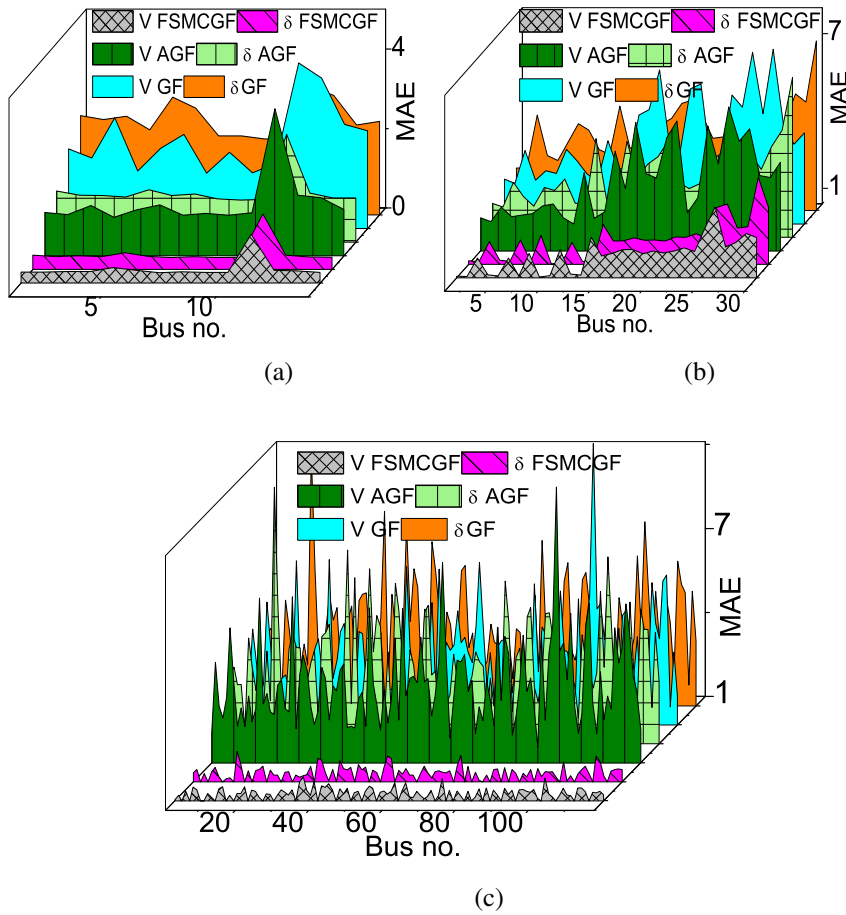


Figure 6.3: Case-2: MAE (in 10^{-3}) for voltage magnitude (V) and phase angle (δ) of all buses for the proposed (FSMCGF) and existing PSSE methods: (a) 14-bus, (b) 30-bus, and (c) 118-bus.

The proposed FSMCGF-base PSSE method voltage magnitude (V) shown in black color and phase angle (δ) shown in magenta color.

This case has the same estimation parameters as Case-2 if not stated otherwise. A thorough investigation was carried out for 14-, 30-, and 118-bus power system networks to evaluate estimation accuracy in terms of average of MSE, average of MAE, and MAXE obtained by averaging the per unit voltage and phase angle δ across all buses. Table 6.1 shows average of MSE, MAE and MAXE for the proposed FSMCGF-based is minimum for all tested environments, such as 14-, 30-, and 118-bus, respectively, with a slightly higher computational time.

A high value Gaussian co-efficient κ_g in a Gaussian mixture model makes the Gaussian mixture more Gaussian and less heavy-tailed. A performance comparison test was carried out for 14-, 30-, and 118-bus power system networks to validate the estimation superiority of the proposed filter. κ_g with a step variation of 0.2 with an initial value of 0.2 is considered for tabulation. Table 6.2 indicates that the increase in κ_g , *i.e.*, less heavy-tailed or more Gaussian value, reduces the average of MAEs for all PSSE estimators. The Value of average of MAEs reduces for all of the mentioned PSSE estimators, and the proposed estimator was found to be adaptive to Kernel bandwidth. This is due to increase in κ_g value, which assigns less weight to the outlier distribution. By doing so, measurement noise becomes less heavy-tailed, or, alternately, more Gaussian.

The proposed FSMCGF-based PSSE estimator considers adaptive Kernel bandwidth, \mathbf{Q}_k , and \mathbf{R}_k throughout its operation. To validate this, mean of error deviations are computed by carrying out PSSE in 14-, 30-, and 118-bus environments, respectively. Table 6.3 highlights two points:

- i) Despite any mis-assumption about sensitive process and measurement noise covariance, the proposed FSMCGF-based PSSE MAEs are minimal among other existing PSSEs.
- ii) PSSE methods perform optimally when $\hat{\mathbf{Q}}_k$ and $\hat{\mathbf{R}}_k$ are equal to their true values or $\mathbf{Q}_k/\mathbf{R}_k = 1$.
- ii) The robust nature of the proposed FSMCGF-based PSSE enables it to outperform

other existing AGF- and GF-based PSSE methods when $\mathbf{Q}_k/\mathbf{R}_k$ is equal to 1, as it can handle non-Gaussian outliers effectively.

Table 6.1: Case-3: Average of error performance (in 10^{-4}) and computational time (in ms) comparison for voltage (V) and phase angle (δ) of all buses.

| Network | PSSE method | Average of MSE | | Average of MAE | | MAXE | | Execution time (ms) |
|---------|-------------|----------------|----------|----------------|----------|------|----------|---------------------|
| | | V | δ | V | δ | V | δ | |
| 14-bus | FSMCGF | 0.38 | 0.32 | 40 | 30 | 15 | 14 | 6.2 |
| | AGF | 3.96 | 2.93 | 130 | 120 | 550 | 51 | 6 |
| | GF | 9.8 | 9.5 | 227 | 210 | 92 | 94 | 5 |
| 30-bus | FSMCGF | 4 | 3 | 100 | 100 | 57 | 50 | 39 |
| | AGF | 17 | 20 | 290 | 310 | 110 | 125 | 38 |
| | GF | 24 | 28 | 370 | 380 | 150 | 150 | 34 |
| 118-bus | FSMCGF | 2 | 2 | 100 | 100 | 71 | 75 | 82 |
| | AGF | 25 | 27 | 370 | 380 | 260 | 270 | 80 |
| | GF | 22 | 24 | 350 | 370 | 250 | 260 | 74 |

Table 6.2: Case-3: Comparison of average of MAEs for different PSSEs (in 10^{-3}) with Gaussian noise co-efficient κ_g for the states.

| Network | Filter | $\kappa_g = 0.2$ | | $\kappa_g = 0.4$ | | $\kappa_g = 0.6$ | | $\kappa_g = 0.8$ | | $\kappa_g = 1$ | |
|---------|--------|------------------|----------|------------------|----------|------------------|----------|------------------|----------|----------------|----------|
| | | V | δ | V | δ | V | δ | V | δ | V | δ |
| 14-bus | FSMCGF | 10 | 9 | 9 | 8 | 7 | 6 | 4.5 | 4.4 | 1 | 2 |
| | AGF | 25 | 26 | 23 | 20 | 10 | 20 | 16 | 16 | 04 | 5 |
| | GF | 38 | 42 | 37 | 41 | 35 | 38 | 29 | 31 | 9.5 | 10.4 |
| 30-bus | FSMCGF | 23 | 19 | 21 | 18 | 18 | 16 | 15 | 14 | 6 | 5 |
| | AGF | 32 | 27 | 30 | 26 | 28 | 24 | 27 | 23 | 10 | 10 |
| | GF | 41 | 36 | 40 | 34 | 37 | 31 | 31 | 26 | 12 | 13 |
| 118-bus | FSMCGF | 34 | 36 | 32 | 33 | 29 | 30 | 23 | 23 | 10 | 10 |
| | AGF | 40 | 042 | 39 | 041 | 39 | 41 | 38 | 40 | 37 | 38 |
| | GF | 33 | 35 | 41 | 43 | 41 | 42 | 40 | 41 | 35 | 37 |

Case-4: Concurrent effect of sudden load change, a sudden increase in power generation with measurement noise having outliers as a mixture of Gaussian and Laplacian noise and bad data

This case tests and validates the performance superiority of the proposed FSMCGF-based PSSE under extremely bad power system monitoring situation, such as the concurrent effect of the following condition:

Table 6.3: Case-3: Comparison of average of MAEs for different PSSEs (in 10^{-3}) with noise mis-assumption factor $\gamma_{\mathbf{Q}}$ and $\gamma_{\mathbf{R}}$ for the V , and δ states.

| Bus | Filter | $\gamma_{\mathbf{Q}} = 0.01, \gamma_{\mathbf{R}} = 100$ | | $\gamma_{\mathbf{Q}} = 1, \gamma_{\mathbf{R}} = 1$ | | $\gamma_{\mathbf{Q}} = 1, \gamma_{\mathbf{R}} = 10$ | | $\gamma_{\mathbf{Q}} = 10, \gamma_{\mathbf{R}} = 10$ | | $\gamma_{\mathbf{Q}} = 10, \gamma_{\mathbf{R}} = 100$ | |
|-----|--------|---|----------|--|----------|---|----------|--|----------|---|----------|
| | | V | δ | V | δ | V | δ | V | δ | V | δ |
| 14 | FSMCGF | 10 | 12 | 4 | 4 | 5 | 5 | 4 | 4 | 4 | 3 |
| | AGF | 10 | 12 | 13 | 12 | 10 | 11 | 10 | 12 | 13 | 13 |
| | GF | 21 | 12 | 13 | 12 | 22 | 24 | 13 | 12 | 23 | 24 |
| 30 | FSMCGF | 12 | 10 | 3 | 3 | 5 | 4 | 3 | 3 | 7 | 5 |
| | AGF | 13 | 11 | 13 | 9 | 13 | 11 | 11 | 9 | 17 | 16 |
| | GF | 23 | 15 | 13 | 9 | 16 | 15 | 13 | 9 | 19 | 18 |
| 118 | FSMCGF | 12 | 13 | 6 | 6 | 8 | 8 | 6 | 6 | 8 | 8 |
| | AGF | 13 | 14 | 12 | 13 | 12 | 13 | 12 | 13 | 11 | 12 |
| | GF | 22 | 23 | 12 | 13 | 19 | 17 | 12 | 13 | 20 | 22 |

- A sudden 10% increase load occur at bus-3 after 8 second and input power generation at bus-2 is increased by 10% after 16 seconds. Consequently, the dynamics of the power network change considerably.
- After 20 seconds, the PMU located at the 13th bus sends falsely injected measurement data to control center, which is inaccurate, indicating a value of 1 per unit and a phase angle of 0 degrees.
- Unlike Case-1 and 2, here, power system measurement noises are disrupted by random outliers due to both Gaussian distributed and Laplace distributed noise.

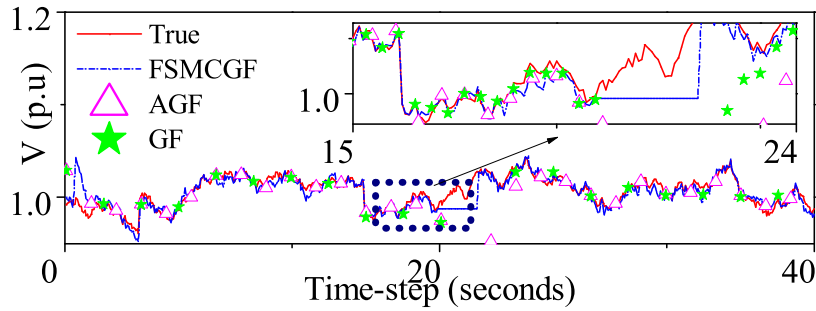
$$f_{\mathcal{V}_k} \sim 0.8f_{\mathcal{V}_{1,k}}\mathcal{N}(\mathbf{0}, \mathbf{R}_{1,k}) + 0.15f_{\mathcal{V}_{2,k}}\mathcal{N}(\mathbf{0}, \mathbf{R}_{2,k}) + 0.05f_{\mathcal{V}_{3,k}}, \quad (6.28)$$

where $f_{\mathcal{V}_{1,k}}$, $f_{\mathcal{V}_{2,k}}$, and $f_{\mathcal{V}_{3,k}}$ are pdfs of $\mathcal{N}(\mathbf{0}, \mathbf{R}_{1,k})$, $\mathcal{N}(\mathbf{0}, \mathbf{R}_{2,k})$, and $L(\mathbf{0}, 0.05)$, respectively.

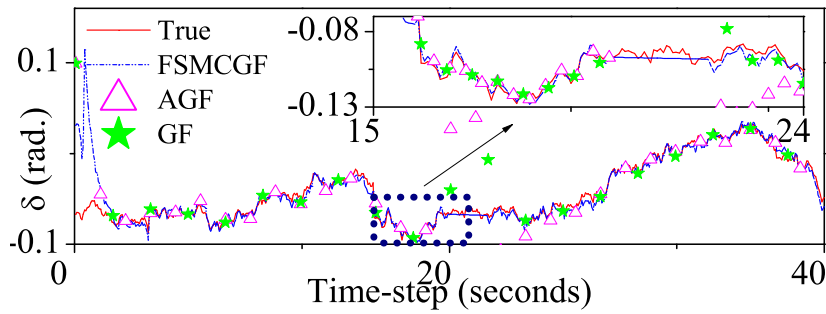
Please note that \mathcal{N} and L denote Gaussian distribution, and Laplace distribution, respectively. A true and estimation plot for the above testing condition is shown in Fig. 6.4. This figure shows that the proposed FSMCGF-based PSSE was successfully estimated during the concurrent occurrence of the above-mentioned adverse effects.

6.3.1 Case-5: Consistency evaluation

The consistency (or credibility) analysis of an estimator is crucial for its implementation in practical application like PSSE design. The consistency of an



(a) Voltage magnitude V (p.u.)



(b) Phase angle δ (radian)

Figure 6.4: Case-4: True and estimate plots at bus-2 for the sudden load change condition with non-Gaussian measurement.

estimator is evaluated by computing its normalized estimation error squared (NEES). The NEES is computed by taking square error in the states *i.e.*, $\hat{\mathbf{x}}_{k|k} - \mathbf{x}_k$ normalized with the estimated state error covariance *i.e.*, $\mathbf{P}_{k|k}$. We consider M_c number of Monte-Carlo simulations was considered to compute NEES at k^{th} time-step of i^{th} Mont-Carlo run.

$$NEES_k^{(i)} = \boldsymbol{\varepsilon}_{k|k}^{xT} \mathbf{P}_{k|k} \boldsymbol{\varepsilon}_{k|k}^x, \quad (6.29)$$

Average of NEES (ANEES) over M_c simulation runs is

$$ANEES_k = \frac{1}{nM_c} \sum_{i=1}^{M_c} NEES_k^{(i)}, \quad (6.30)$$

A consistently high value of NEES implies that the estimator underestimates the uncertainty in the system and vice versa. A reliable estimator makes accurate predictions with a reasonable level of uncertainty, NEES is close to 1. ANEES belongs to chi-square distribution, with a degree of freedom 1 was considered for this testing on a 14-bus power

system network.

$$\begin{aligned}
 LB &= n \left[\left(1 - \frac{2}{9nM_c} \right) - 1.96 \sqrt{\frac{2}{9nM_c}} \right]^3, \\
 UB &= n \left[\left(1 - \frac{2}{9nM_c} \right) + 1.96 \sqrt{\frac{2}{9nM_c}} \right]^3,
 \end{aligned} \tag{6.31}$$

The proposed estimator NEES value with two sided 95% probability value for a significance level of 0.05 lies well within its confidence region (between lower bound LB=0.78 and upper bound UB=1.25), thus guaranteeing the estimator's reliability. $NEES_k$ of all PSSE estimator are plotted in Fig. 6.5 to test their consistency or credibility. This figure shows that the AGF-based PSSE is inconsistent as the averaged NEES takes all values outside UB and is said to be an optimistic estimator as the error covariance is too small. $NEES_k$ for the proposed FSMCGF-based PSSE lies between LB and UB. Hence, the proposed estimator behaves neither as a pessimist nor as optimistic around the power system process and measurement uncertainties. Thus, the proposed estimator is the most credible PSSE estimator.

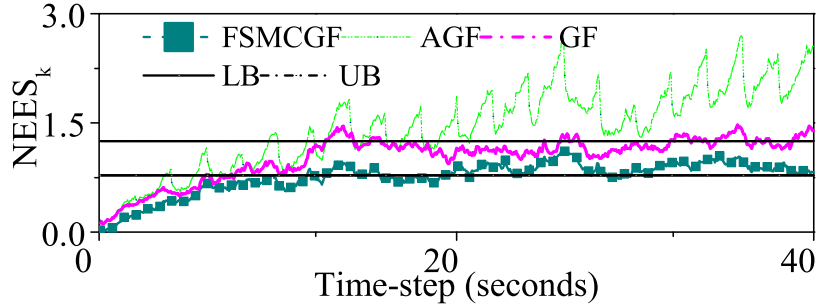


Figure 6.5: Case-5: NEES plot for consistency evaluation for 14-bus.

6.4 Discussion and conclusion

An accurate and robust PSSE is of utmost importance as it enables the development of effective energy management plans and guarantees a secure, reliable, and stable power distribution, particularly in light of the rise of electric vehicles, traction loads, and distributed energy resources. The traditional PSSEs performance degrades when the noises are inaccurately assumed and/or are variable and sensitive to non-Gaussian

outliers. The proposed PSSE estimator optimally considers the higher order moments through correntropy and fixed-point iteration method and, subsequently, implements a self-adaptive Kernel bandwidth, self-adaptive \mathbf{Q}_k , and \mathbf{R}_k method to obtain the optimal estimation. Numerous simulation experiments were carried out on IEEE 14-, 30-, and 118-bus, including normal loading conditions, sudden load change, Gaussian noise, Laplacian noise, mixture of Gaussian and Laplacian noises, bad data injection, show that the proposed FSMCGF-based PSSE outperforms the traditional estimators, such as AGF and GF in terms of performance index, such as average of MSE, MAE and MAXE. This chapter implements a CKF based formulation of the proposed FSMCGF-based PSSE implemented this performance validation. Results validate that estimation accuracy of proposed FSMCGF improves by nearly 60% with a negligible higher computational cost under proven circumstances. The proposed estimator was also found to be the most credible estimator from their normalized estimation error squared with a 0.05 significance level.

The contribution of this work lies in developing a robust PSSE that can withstand various power grid abnormalities, thereby advancing power system applications. However, the researcher also encountered another challenging case of online estimation during their research work, which was the Covid-19 pandemic that caused countless financial losses and human lives without a vaccine. As a scientific responsibility, the author took the initiative to extend the CKF method for ESE applications, specifically to estimate the population under different groups affected by the coronavirus infection.

Chapter 7

Kalman-based Compartment Estimation for Covid-19 Pandemic using Advanced Epidemic Model

This chapter introduces a Gaussian filter-based advanced ESE method. Alternatively, this chapter utilizes Gaussian filtering algorithm to estimate the compartmental populations, including susceptible (S), exposed (E), infected (I), recovered from exposed (R_e), recovered from infected (R), passed away (P), and vaccinated individual (V) populations of an advanced epidemic model. Although the proposed ESE method applies to any pandemic or epidemic, this chapter will be focused on Covid-19.

Recalling Chapters 1.6, and 2.4, this chapter attempts to implement Gaussian filtering algorithm to estimate the quantified population who are susceptible (S), exposed (E), infected (I), recovered from exposed (R_e), recovered from infected (R), passed away (P), and vaccinated individual (V) compartments.

Covid-19, caused by SARS-CoV-2, is an airborne viral infection that originated from Wuhan, People's Republic of China. Since its inception, it has infected half a billion people, killed close to 6 million people, and forced almost every country across the world to impose strict lockdowns, resulting in significant economic losses. New variants of the virus may make vaccines less effective over time. Mathematical analysis, such as in [170],[171], and [172], can help reduce the burden on medical infrastructure.

Aggressive non-pharmaceutical interventions (nPIs) may increase financial burdens [52], so minimal financial burden nPIs should be prioritized. Furthermore, recent research suggests that coronavirus mutates its genome sequence, resulting in new variants that make the vaccine less effective over time. But in absence of life-time immunity providing vaccine, dynamical model-based analytical results can help authorities frame appropriate strategies and guidelines for the public to stop or slow the transmission of widespread epidemic.

It is expected that model (*SIR* model) analysis-based strategy making should be superior if the models comprise more parameters. With this motivation, the later developments incorporated more compartments, including susceptible (*S*), exposed (*E*), infected (*I*), recovered from exposed (R_e), recovered from infected (*R*), passed away (*P*), and vaccinated individual (*V*) compartments. With different combinations of such compartments, various models, including *SIRP* [54],[55], *SEIR* [58], *SEIRP* [59], *SEIRRP* [60], *SIRV* [61] models, are introduced in the recent literature. These models are nonlinear in order to characterize the nonlinear disease dynamics. Moreover, these models become stochastic in order to characterize the modeling errors and uncertainties of the disease dynamics. Subsequently, the author develops GF-based ESE to online monitor the quantified information of compartments, such as susceptible, exposed, infected, *etc.* Literature on GF-based ESE, such as the EKF, UKF, and their extensions, used in the [54], [55], [141], [73], are known for their poor accuracy and stability. Thus, introducing an efficient estimation method can further improve the accuracy.

Summarizing the above discussions, we highlight the motivations of this chapter below:

- Consider the exposed and infected populations separately in order to address their inconsistent recovery pattern.
- Consider the stochastic nature of the model in order to address the limitations of [173].
- Consider the exposed and vaccinated populations in a single model, which is yet not considered in the literature.

- Implement a state-of-the-art estimation technique, like the CKF, for estimating the compartment populations with improved accuracy.
- Finally, the motivation of this chapter is to improve the accuracy of the model-based Covid-19 spread analysis by accomplishing the above mentioned motivations.

To accomplish the above mentioned motivations, this chapter modeled an advanced *SIR* model and a popularly known estimation technique named CKF to derive analytical conclusions helpful in non-pharmaceutical policy-making. We include various coronavirus disease impacting parameters, such as infection rate, recovery rate, reinfection rate, mortality rate, incubation rate, recovery rate of exposed group, and vaccination rate to model complex Covid-19 disease dynamics. The model considers seven stages of infections: susceptible (S), exposed (E), infected (I), recovered from exposed (R_e), recovered from infected (R), passed away (P), and vaccinated (V) population; abbreviated as *SEIRRPV* epidemic model. Henceforth, we will refer to the advanced *SIR* model as *SEIRRPV* model in the acronym form of its compartment. To validate, a mathematical analysis of the proposed epidemic model is demonstrated, which identifies the non-negativity, uniqueness, boundary condition, basic reproduction rate, sensitivity analysis, and stability analysis. A stochastic *SEIRRPV* model is then combined with a novel estimation technique, the CKF, to derive analytical conclusions about epidemic transmission. The CKF is a nonlinear Bayesian approximation filtering method, performed in prediction and update steps. The implementation of the prediction and update steps involves intractable integrals. The CKF uses third-degree spherical cubature rule for approximating the intractable integrals. Finally, we compared our results with existing *SIR*, *SIRP*, *SEIRP*, *SEIRRP*, *SIRV* models [60], [61], and [174]. The meaning of these models can be derived from the descriptions of every word provided. Please note that ‘recover’ represents those recovered from Covid-19 infection for *SIR*, *SIRP*, *SEIRP*, and *SIRV* models where exposed compartment is not considered.

7.1 Compartment based SEIRRPV model for analyzing Covid-19 spread

This section gives an overview of the compartment-based epidemic model used to analyze the spread of Covid-19. In general, the behavior of real-life systems or processes is complex, and modeling their exact dynamics is challenging. However, in many cases, the physical laws are well established in the literature to derive an approximated model, *e.g.*, the laws of motion can be used for approximate modeling of the motion of a moving object [6]. On the other hand, modeling dynamics of a biological process, such as the transmission of a new pandemic, is complex and lacks well-established physical laws characterizing their dynamics. The Covid-19 transmissibility is dynamic and ever-changing. It is new and unique for the scientific community, and no physical law has yet been developed to define its transmission rate and other behavior precisely. In such cases, the standard mathematical models are established in the literature for modeling disease behavior based on certain hypotheses applied to the pandemic behavior. Before introducing the proposed *SEIRRPV* model, we mention the following hypotheses on any pandemic [53], [175]:

- (a) The disease is contagious and spreads through direct and indirect contact or even airborne transmission.
- (b) The population remains constant during the period of the study. The deaths (excluding those caused by pandemic) and births during the study duration are ignored. It is worth mentioning that these numbers are expected to be small compared to the total population.
- (c) There may be some latency period during which an infected individual is not infectious. Similarly, There may be an exposure period during which an individual may be both infected and contagious but does not show any visible symptoms, *i.e.*, asymptomatic.
- (d) Every individual in the considered population has the same immunity.

- (e) Every individual in the considered population interacts equally with others in other compartments.

It should be mentioned that the hypotheses may not be unique across the practitioners. However, the resulting accuracy and the model complexity should be key factors in specifying a particular set of hypotheses.

The above mentioned hypotheses are generally common for all compartment-based modeling. A deterministic *SEIRRPV* model follows these hypotheses. Any modeling study comes with inherent limitations. Here, hypotheses (b), (d), and (e) condition are not true for coronavirus epidemic. However, we can approximate a study of shorter duration and associated uncertainty in our model. We consider the scenario of Covid-19 pandemic in Delhi, the capital city of India, with a population of 32 million. We implemented the proposed model to estimate the disease transmission in Delhi between 17 January 2021 and 26 April 2021. The simulation study period is important because Delhi witnessed its second wave from March and stretched to June 2021. There was a Covid outbreak throughout the city of Delhi. Hence, our assumption stands true that the entire population is equally susceptible to the Covid-19 pandemic. Although the birth rate (approximately 0.003% of total population) and natural death rate (0.03% of total population) are negligible compared to the total population of Delhi (approximately 32 million), the imperfection in these models could result in uncertainty in the predictive capability of Covid-19. Therefore, the author remodeled the deterministic epidemic model as a stochastic-based *SEIRRPV* epidemic model. In stochastic systems, there is no disease-endemic state, so persistence of the disease cannot be observed.

Based on the aforementioned hypothesis, we have identified several influencing parameters of the Covid-19 pandemic that are used to model the *SEIRRPV* deterministic epidemic model. These parameters are listed in below subsection.

7.1.1 Parameters involved in Covid-19 pandemic

The real-world scenarios, such as medical infrastructure, geographic demographics, social structure, public awareness, government strategies, *etc.*, may be linked to a

mathematical model. These epidemic models estimate different compartments and simulate various parameters influencing the transmission of the Covid-19 pandemic. Some of these parameters have been explained below.

Infection rate (α)

As mentioned in the previous section, the α number of susceptible people get infected with Covid-19 from an infected or exposed individual per unit of time. The Covid-19 disease can be transmitted through direct and indirect contact and airborne transmission. So, the infection rate parameter considers the level of social interaction, population density, environment healthiness, and social cleanliness. A high contact rate increases the infected population at a faster pace. However, strict measures and social awareness can slow down the transmission of the SARS-COV-2 virus even in densely populated cities or places with poor healthcare facilities. One such example is Asia's largest slum bearer, Dharavi, which successfully controlled the pandemic by stricter social measures imposed by Brihanmumbai Municipal Corporation (BMC), Maharashtra, India [176], as acknowledged by the world health organization (WHO). Government authority's decisions include critical social distancing at the workplace, masks in populated areas, protection against virulence and lockdown, and others.

Recovery rate (β)

It is the rate at which infected individuals are reported to have recovered on a given day. The speedy recovery of people depends on the healthcare facilities and medication they get. Hence, state hospitalization facilities, number of intensive care units (ICUs), availability of clinical drugs, transportation facilities, *etc.*, impact the recovery speed for the pandemic. The value of β may be different for all pandemics. One influenza-infected individual gets ill for 3-7 days (mean time =5 days), so the recovery rate β is 1/5 [60].

Reinfection rate (γ)

It is the rate at which recovered individuals get reinfected with Covid-19. In recent times, few Covid-19 fully vaccinated people have also been infected. So, vaccination does not make an individual fully immunized. Thus, γ is the inverse of the immunity rate. It is

otherwise called the immunity loss rate. Preliminary studies claim the immunity rate for Covid-19 stands for up to 4 months [177]. In *SEIRP*, *SEIRRP*-models segregate infected people into exposed and infected compartments. Recovered people may get exposed or infected with Covid-19. In *SEIRP*, *SEIRRP*, reinfection rate terms are specified as γ_e and γ , respectively. Moreover, we have one compartment to address contaminated people ('infected' compartment), so the reinfection rate for *SIR*, *SIRV*, and *SIRP*-models is γ .

Mortality rate (μ)

The Covid-19 pandemic has caused more than 5.8 million human deaths (updated on February 2022) [50]. The mortality rate of the pandemic is the ratio of the daily number of deceased people to the total infected population on the same day. Hence, the influencing constraints for mortality rate are the same as infection rate.

Incubation rate (κ)

The transition of an asymptotically infected individual (E) to be symptomatically infectious individual (I) is called an incubation rate. In some cases, people are infected and contagious. Still, they do not show any symptoms or are medically declared as Covid-19 -ve due to the poor medical facility or by an error in real-time polymerase chain reaction (RT-PCR) test or antigen test [178]. These exposed people act as active virus carriers, and the host may die or recover in both cases. So screening policies, contact tracing, *etc.*, like aspects may influence κ .

Recovery rate of exposed group (ρ)

It is the rate at which exposed group individuals recover without being infectious. However, it can not be inspected and needs lab-based proof. It may be considered equal to or greater than β .

Vaccination rate (Ω)

It is the rate at which people are vaccinated to be immune from the variants of coronavirus. Vaccination drive speed not only provides a weapon to reduce infection rate but also reduces human fatalities. However, vaccine inefficiency, v , may reduce the

vaccine's effectiveness. During the vaccine testing and clinical trials, its efficiency is evaluated.

7.1.2 Mathematical representation

We introduce the compartment models to analyze the Covid-19 transmission behavior based on the above mentioned hypotheses. Our model is inspired by the *SIR* epidemic model with inclusion of other pandemic spread impacting parameters, such as rate of asymptotically infection α_e , infection rate α , recovery rate β , reinfection rate for Covid-19 recovered individual from exposed γ_e and infected compartment γ , mortality rate μ , incubation rate κ , recovery rate of exposed population ρ as discussed in Chapter 7.1.1. Additionally, the recent vaccine rollout by Pfizer, AstraZeneca, and others will favor the physical epidemic model. Here, vaccination rate, Ω , and vaccination inefficacy, ν , play a vital role in controlling the pandemic. Hence, our proposed model is also more diversified in the model formulation of complex disease transmission.

We follow transmission patterns of the pathogens in classified compartments in terms of ordinary differential equations to formulate the proposed *SEIRRPV* epidemic model. According to the World Health Organization, there are two varieties of people infected by coronavirus: one does not have symptoms (E), and the other does (I). We consider the scenario of Covid-19 pandemic in Delhi, the capital city of India, with a population of 32 million. We implemented the proposed model to estimate the disease transmission in Delhi between 17 January 2021 and 26 April 2021. The period of the simulation study is important in the fact that Delhi witnessed its second wave of Covid-19 pandemic from March and stretched up to June of 2021. Here is assumption stands true with the Covid-19 pandemic transmission in Delhi, *i.e.*, total population of Delhi is equally susceptible to the Covid-19 pandemic.

- (a) Susceptible compartment individual transfer to exposed (E) asymptotically, and symptomatically, respectively, with infection rates of α_e and α . Additionally, recovered individuals from R_e and R compartments become susceptible with recovery rates γ_e and γ , respectively. Further, A small portion of vaccinated population becomes susceptible due to vaccination at a rate of Ω .

- (b) Population from susceptible (S) and vaccinated (V) compartment transfer to exposed (E) compartment with $\alpha_e E + \alpha I$ and $v\alpha_e V$, respectively.
- (c) Incubation rate κ of exposed population and $v\alpha I$ of vaccinated population coming to the infected (I) compartment from exposed (E) and vaccinated (V) population compartment.
- (d) Recovered populations from asymptotically infected or not hospitalized or those populations recovered from Covid-19 but went unnoticed by the government data are included in the R_e compartment. It includes the net population of inclusion of recovery rate ρ of exposed population and exclusion of reinfected population at a rate of γ_e .
- (e) R compartment includes individuals β rate of infected population (I) by excluding reinfected rate of recovered population (R).
- (f) Passed away (P) compartment are the mortality rate μ of infected population (I).
- (g) Vaccinated population is the net population of vaccinated people from susceptible compartment S with Ω rate by excluding infected people both symptomatically with $v\alpha_e I$ and asymptotically infected with $v\alpha E$.

We follow the fundamental steps (a)-(g) to formulate our proposed deterministic epidemic model. The following set of differential equations mathematically represents

compartments of the *SEIRRPV* model.

$$\begin{aligned}
 \frac{dS}{dt} &= -\alpha_e SE - \alpha SI + \gamma_e R_e + \gamma R - \Omega S \\
 \frac{dE}{dt} &= \alpha_e SE + \alpha SI - \kappa E - \rho E + vV\alpha_e E \\
 \frac{dI}{dt} &= \kappa E - \beta I - \mu I + vV\alpha I \\
 \frac{dR_e}{dt} &= \rho E - \gamma_e R_e \\
 \frac{dR}{dt} &= \beta I - \gamma R \\
 \frac{dP}{dt} &= \mu I \\
 \frac{dV}{dt} &= \Omega S - vV\alpha_e E - vV\alpha I
 \end{aligned} \tag{7.1}$$

An infection flow graph of advanced epidemic model is presented in Fig. 7.1 The system

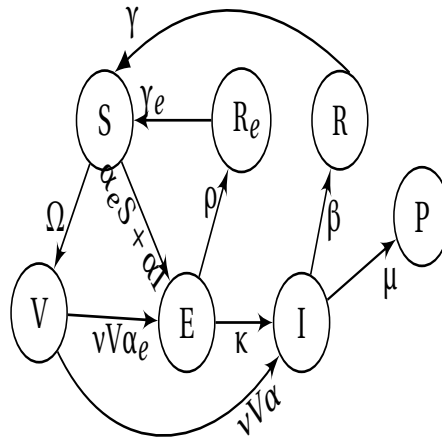


Figure 7.1: Infection flow graph *SEIRRPV* epidemic model

model obeys mass conservation property. We have

$$\frac{dS}{dt} + \frac{dE}{dt} + \frac{dI}{dt} + \frac{dR_e}{dt} + \frac{dR}{dt} + \frac{dP}{dt} + \frac{dV}{dt} = 0 \tag{7.2}$$

Hence, the sum of states will be equal to total population. Expressing states in terms of population ratio, we will get the following;

$$S + E + I + R_e + R + P + V = 1, \tag{7.3}$$

where 1 is the total population, including deceased. The sum of system states is 1, considering the system is a closed one *i.e.*, no natural death and births are considered.

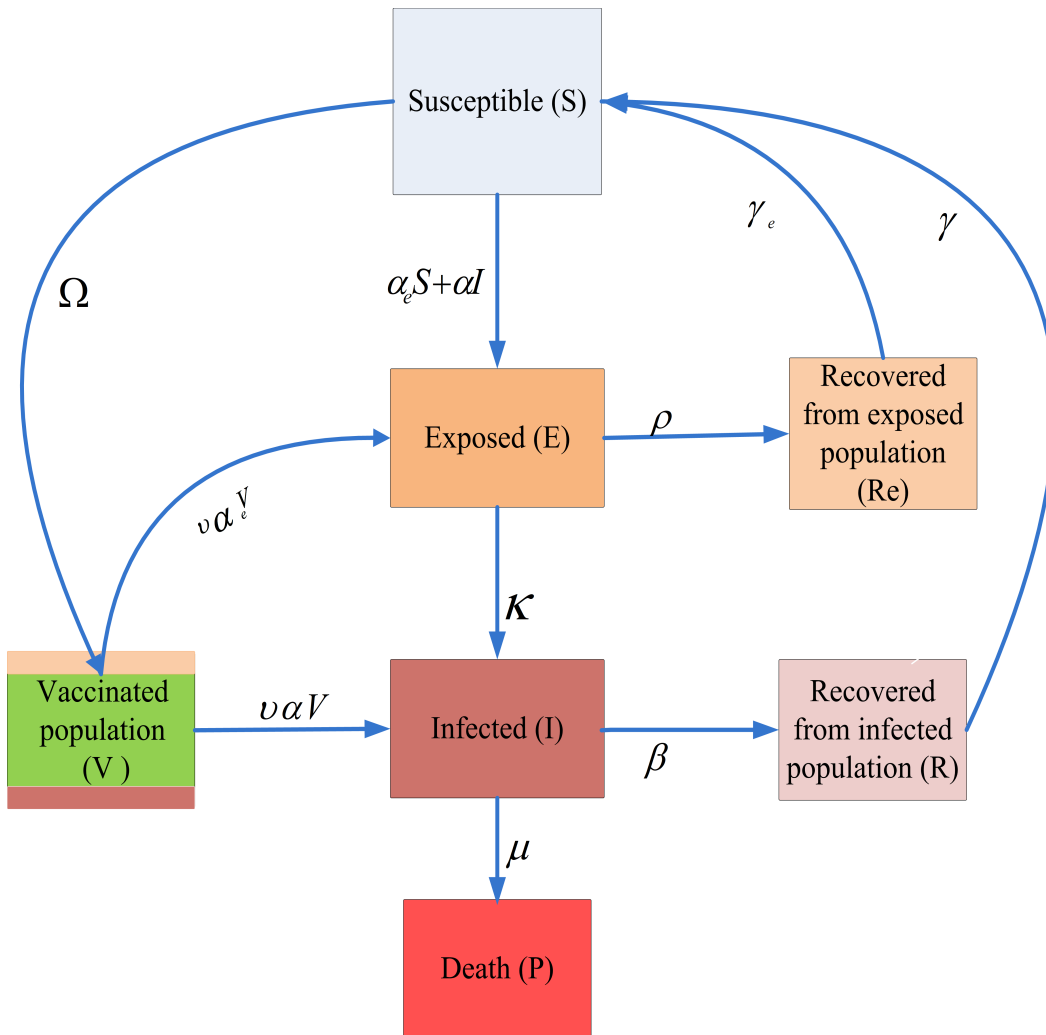


Figure 7.2: Block diagram of *SEIRRPV* epidemic model.

7.2 Problem formulation

The *SEIRRPV* epidemic model presented in Fig. 7.2, has been briefly discussed in nonlinear ordinary differential equation given in Eq. (7.1). However, it is difficult to model all the states accurately for estimation purposes in a real-world scenario. These modeling inaccuracies can be dealt with by including a random error, $\mathcal{Q}_k \in \mathbb{R}^n$, which follows Gaussian distribution with mean zero and covariance of \mathbf{Q} in the state model of Eq. (1.3). Similarly, a measurement for the epidemic model includes the number of

infected individuals, \mathcal{I} , recovered individuals, \mathcal{R} , passed away people, \mathcal{P} , and vaccine inoculated people, \mathcal{V} by the Covid-19 pandemic. These measurements are available through government data, surveys, testing, and the medical health update register. These data may not be error free. Furthermore, the RTPCR and other available coronavirus tests are not perfect. Hence, we model this measurement noise as $\mathcal{V}_k \in \mathbb{R}^m$ for Covid-19, and without loss of generality, it is assumed to be a Gaussian distribution with zero mean and \mathbf{R} as covariance. All groups of different Compartment models are expressed in ordinary differential equations as derived in Section 7.1.2. The state space representation of the proposed *SEIRRPV* model can be expressed as a state model and measurement model referring to Eqs. (1.3) and (1.4) in Chapter 1.

$$\begin{bmatrix} \frac{dS}{dt} \\ \frac{dE}{dt} \\ \frac{dI}{dt} \\ \frac{dR_e}{dt} \\ \frac{dR}{dt} \\ \frac{dP}{dt} \\ \frac{dV}{dt} \end{bmatrix} = \begin{bmatrix} -\alpha_e SE - \alpha SI + \gamma_e R_e + \gamma R - \Omega S \\ \alpha_e SE + \alpha SI + (v\alpha V - \kappa - \rho)E \\ \kappa E + (v\alpha V - \beta - \mu)I \\ \rho E - \gamma_e R_e \\ \beta I - \gamma R \\ \mu I \\ \Omega S - vV(\alpha_e E + \alpha I) \end{bmatrix} + \mathcal{Q}, \quad (7.4)$$

and observed equation for *SEIRRPV* model is

$$\begin{bmatrix} \mathcal{I} \\ \mathcal{R} \\ \mathcal{P} \\ \mathcal{V} \end{bmatrix} = \begin{bmatrix} 1 & 0 & 0 & 0 \\ 0 & 1 & 0 & 0 \\ 0 & 0 & 1 & 0 \\ 0 & 0 & 0 & 1 \end{bmatrix} \begin{bmatrix} I \\ R \\ P \\ V \end{bmatrix} + \mathcal{V}, \quad (7.5)$$

In this chapter, our objective is to estimate the states (each compartment). We will implement a popular nonlinear Kalman filtering algorithm called as CKF, as discussed in Section 7.4, which has better estimation accuracy among traditional filters, such as EKF [73], and UKF [82].

7.3 Mathematical analysis of the Proposed epidemic Model

Considering the initial condition of epidemic model, we derived disease-free condition and basic reproduction rate \mathcal{R}_0 . Additionally, we also discussed the well-posedness of our proposed deterministic epidemic model.

Theorem 2 (Existence and uniqueness of solution): Let $t^* \in \mathbb{R}_+^7$. The dynamical system Eq. (7.1) admits a unique solution on interval $(0, t^*)$ for initial conditions satisfying $S_0 > 0, E_0 > 0, I_0 > 0, R_{e0} > 0, R_0 > 0, P_0 > 0$ and $V_0 > 0$ [179].

Proof 2 Let us consider, $Y(t) = (S_t, E_t, I_t, R_{et}, R_t, P_t, V_t)^T$. Then Eq. (7.8) is expressed as $Y'(t) = F(Y(t)) = (f_1, f_2, f_3, f_4, f_5, f_6, f_7)^T$ where f_i are the generalized function of $Y(t)$. At initial condition, $Y_0 = (S_0, E_0, I_0, R_{e0}, R_0, P_0, V_0)^T > 0$. Jacobian matrix of $F(Y(t))$ can be expressed as in the form of $\mathbf{J}(F(Y(t))) = \frac{\delta f_i}{\delta Y}$ with $i \in \{1, 2, \dots, 7\}$. For simplicity, we mention few elements of the $\mathbf{J}(F(Y(t)))$ as

$$\begin{aligned}
 J_{11} &= \left| \frac{\delta f_1}{\delta S} \right| = |-\alpha_e E - \alpha I - \Omega| \leq \infty, & J_{12} &= \left| \frac{\delta f_1}{\delta E} \right| = |-\alpha_e S| \leq \infty, \\
 J_{13} &= \left| \frac{\delta f_1}{\delta I} \right| = |-\alpha S| \leq \infty, & J_{14} &= \left| \frac{\delta f_1}{\delta R_e} \right| = |\gamma_e| \leq \infty, \\
 J_{15} &= \left| \frac{\delta f_1}{\delta R} \right| = |\gamma| \leq \infty, & J_{16} &= \frac{\delta f_1}{\delta P} = 0 \leq \infty, \\
 J_{17} &= \left| \frac{\delta f_1}{\delta V} \right| = |0| \leq \infty, & J_{21} &= \left| \frac{\delta f_2}{\delta S} \right| = |\alpha_e E + \alpha I| \leq \infty, \\
 J_{22} &= \left| \frac{\delta f_2}{\delta E} \right| = |\alpha_e S - \kappa - \rho + v \alpha_e V| \leq \infty, & J_{23} &= \left| \frac{\delta f_2}{\delta I} \right| = |\alpha S| \leq \infty, \text{ etc.}
 \end{aligned} \tag{7.6}$$

The partial derivative of model Eq. (7.1) expressed in Eq. (7.6) exists, are finite and bounded. The system model presented in Eq. (7.1) and $\mathbf{J}(F(Y'))$, are continuous for $t > 0$. Hence, F satisfies a Lipschitz condition on \mathbb{R}_+^7 . The existence and uniqueness of solution for some time interval $(0, t^*)$ follows from Picard-Lindelof Theorem. \square

Theorem 3 (Positivity of solution): The set

$$\mathbb{D} = \{(S, E, I, R_e, R, P, V) \in \mathbb{R}_+^7 : S + E + I + R_e + R + P + V \leq N, S \geq 0, E \geq 0, I \geq 0, R_e \geq 0, R \geq 0, P \geq 0, V \geq 0\}, \quad (7.7)$$

i.e, the dynamical system state variables of Eq. (7.1) are $(S_t, E_t, I_t, R_{et}, R_t, P_t, V_t)$ non-negative $\forall t > 0$ [180].

Proof 3 Let us consider, $Y(t) = (S_t, E_t, I_t, R_{et}, R_t, P_t, V_t)^T$. Then Eq. (7.1) is expressed as $Y'(t) = F(Y(t)) = (f_{1t}(\cdot), f_{2t}(\cdot), f_{3t}(\cdot), f_{4t}(\cdot), f_{5t}(\cdot), f_{6t}(\cdot), f_{7t}(\cdot))^T$ where f_{it} are the generalized function of $Y(t) \forall i \in \{1, 2, \dots, 7\}$. Rewriting Eq. (7.1),

$$\frac{dS}{dt} = \psi_{1t}(\cdot), \quad \text{where} \quad \psi_{1t}(\cdot) = -\alpha_e E - \alpha I + \frac{\gamma_e R_e}{S} + \frac{\gamma R}{S} - \Omega$$

Integrating the above expression, we get

$$S_t = S_0 e^{\int_0^t \psi_{1t}(S, E, I, R_e, R) dt} \geq 0 \quad \forall t.$$

$$\frac{dE}{dt} = \psi_{2t}(\cdot), \quad \text{where} \quad \psi_{2t}(\cdot) = \alpha_e S + \frac{\alpha SI}{E} - \kappa - \rho + \nu V \alpha_e$$

Integrating the above expression result,

$$E_t = E_0 e^{\int_0^t \psi_{2t}(S, E, I, V) dt} \geq 0 \quad \forall t.$$

$$\frac{dI}{dt} = \psi_{3t}(\cdot), \quad \text{where} \quad \psi_{3t}(\cdot) = \frac{\kappa E}{I} - \beta - \mu + \nu V \alpha$$

Infected population is computed as

$$I_t = I_0 \exp^{\int_0^t \psi_{3t}(E, I, V) dt} \geq 0 \quad \forall t.$$

$$\frac{\delta R_e}{dt} = \psi_{4t}(\cdot), \quad \text{where} \quad \psi_{4t}(\cdot) = \frac{\rho E}{R_e} - \gamma_e$$

Population recovered from exposed compartment are,

$$R_{et} = R_{e0} e^{\int_0^t \psi_{4t}(E, R_e) dt} \geq 0 \quad \forall t. \quad \frac{\delta R}{dt} = \psi_{5t}(\cdot), \quad \text{where} \quad \psi_{5t}(\cdot) = \frac{\rho E}{R_e} - \gamma$$

Integrating the above expression, we get

$$R_t = R_0 \exp^{\int_0^t \psi_{5t}(I, R) dt} \geq 0 \quad \forall t.$$

$$\delta P = \psi_{6t}(\cdot), \quad \text{where} \quad \psi_{6t}(\cdot) = \mu I_t$$

Integrating above equation, we get

$$P_t = P_0 + \mu I_t(t) \geq 0 \quad \forall t. \quad \frac{\delta V}{dt} = \psi_{7t}(\cdot), \quad \text{where} \quad \psi_{7t}(\cdot) = \frac{\Omega S}{V} - \nu \alpha_e E - \nu \alpha I$$

Simplifying above equation

$$V_t = V_0 \exp^{\int_0^t \psi_{7t}(S, E, I, V) dt} \geq 0 \quad \forall t. \quad \text{Therefore, all solutions to model system Eq. (7.1)}$$

are non-negative. \square

Theorem 4 (Boundedness of solution): The solutions of proposed model in Eq. (7.1) are uniformly bounded with non-negative initial conditions in the region \mathbb{D} .

Proof 4 The proposed deterministic epidemic model given in Eq. (7.1) can be expressed as

$$\begin{aligned}
\frac{dS}{dt} + (\alpha_e E + \alpha I + \Omega) S &= \gamma_e R_e + \gamma R \\
\frac{dE}{dt} + (\kappa + \rho - \alpha_e S - \nu V \alpha_e) E &= \alpha S I \\
\frac{dI}{dt} + (\beta + \mu - \nu V \alpha) I &= \kappa E \\
\frac{dR_e}{dt} + \gamma_e R_e &= \rho E \\
\frac{dR}{dt} + \gamma R &= \beta I \\
\frac{dP}{dt} &= \mu I \\
\frac{dV}{dt} + (\nu \alpha_e E + \nu \alpha I) V &= \Omega S
\end{aligned} \tag{7.8}$$

Considering initial conditions of the epidemic model as $(S_0, E_0, I_0, R_{e0}, R_0, P_0, V_0)$, we simplified Eq. (7.8) by taking the Laplace transformation method. The simplified equations are given below

$$\begin{aligned}
S_t &= \frac{\gamma_e R_{et} + \gamma R_t}{\phi_{1t}} \left(1 - e^{-\phi_{1t}t}\right) + S_0 e^{-\phi_{1t}t}, \quad \phi_{1t} = \alpha_e E_t + \alpha I_t + \Omega \\
E_t &= \frac{\alpha S_t I_t}{\phi_{2t}} \left(1 - e^{-\phi_{2t}t}\right) + E_0 e^{-\phi_{2t}t}, \quad \phi_{2t} = \kappa_e \rho - \alpha_e S_t - \nu \alpha V_t \\
I_t &= \frac{\kappa E_t}{\phi_{3t}} \left(1 - e^{-\phi_{3t}t}\right) + I_0 e^{-\phi_{3t}t}, \quad \phi_{3t} = \beta + \mu - \nu \alpha V_t \\
R_{et} &= \frac{\rho E_t}{\phi_{4t}} \left(1 - e^{-\phi_{4t}t}\right) + R_{e0} e^{-\phi_{4t}t}, \quad \phi_{4t} = \gamma_e \\
R_t &= \frac{\beta I_t}{\phi_{5t}} \left(1 - e^{-\phi_{5t}t}\right) + R_0 e^{-\phi_{5t}t}, \quad \phi_{5t} = \gamma \\
P_t &= \phi_{6t} \int_0^t I_t dt + P_0, \quad \phi_{6t} = \mu \\
V_t &= \frac{\Omega S_t}{\phi_{7t}} \left(1 - e^{-\phi_{7t}t}\right) + V_0 e^{-\phi_{7t}t}, \quad \phi_{7t} = \nu \alpha_e V_t + \nu \alpha V_t.
\end{aligned} \tag{7.9}$$

Taking the smallest of the upper bound *i.e.*, supremum (sup) of the Eq. (7.9), we get

$$\begin{aligned}
\limsup_{t \rightarrow \infty} S_t &= \frac{\gamma_e R_{et} + \gamma R_t}{\phi_{1t}} \\
\limsup_{t \rightarrow \infty} E_t &= \frac{\alpha S_t I_t}{\phi_{2t}} \\
\limsup_{t \rightarrow \infty} I_t &= \frac{\kappa E_t}{\phi_{3t}} \\
\limsup_{t \rightarrow \infty} R_{et} &= \frac{\rho E_t}{\phi_{4t}} \\
\limsup_{t \rightarrow \infty} R_t &= \frac{\beta I_t}{\phi_{5t}} \\
\limsup_{t \rightarrow \infty} P_t &= \phi_{6t} \int_0^t I_t dt + P_0 \leq \infty \\
\limsup_{t \rightarrow \infty} V_t &= \frac{\Omega S_t}{\phi_{7t}}.
\end{aligned} \tag{7.10}$$

Adding equations given in Eq. (7.10) and rewriting the expression,

$$\begin{aligned}
\limsup_{t \rightarrow \infty} (S_t + E_t + I_t + R_{et} + R_t + P_t + V_t) &= \frac{\gamma_e R_{et} + \gamma R_t}{\phi_{1t}} + \frac{\alpha S_t I_t}{\phi_{2t}} + \frac{\kappa E_t}{\phi_{3t}} \\
&+ \frac{\rho E_t}{\phi_{4t}} + \frac{\kappa E_t}{\phi_{3t}} + \frac{\Omega S_t}{\phi_{7t}} = 1,
\end{aligned} \tag{7.11}$$

since $S_t + E_t + I_t + R_{et} + R_t + P_t + V_t = 1$. Therefore, the solution of the system given in Eq. (7.1) remains closed and uniformly bounded in the region \mathbb{R}_+^7 . \square

7.3.1 Basic reproduction rate \mathcal{R}_0

It is an indicator of emerging infections and plays a critical role in designing control interventions for existing infections. A basic reproduction rate \mathcal{R}_0 is usually determined by the basic reproduction number \mathcal{R}_0 , which measures how many secondary infections will occur from introducing one infected individual into a population of entirely susceptible individuals. Therefore, it determines the extent to which the infection spreads throughout the population.

Basic reproduction number \mathcal{R}_0 is defined as the spectral radius of negative of next generation matrix (\mathbf{N}_g) *i.e.*, $\mathcal{R}_0 = \rho(\mathbf{N}_g)$, where spectral radius (ρ) is a dominant eigen value of the \mathbf{N}_g . From Eq. (7.1), it is evident that there are two infected compartments

and five uninfected compartments. We will calculate the value of \mathcal{R}_0 by the next generation matrix (NGM) method, as discussed in [180], [181], [182]. We compute the transmission matrix \mathbf{T} and transition matrix $\mathbf{\Xi}$ from the epidemic model. Matrices \mathbf{T} , and $\mathbf{\Xi}$, respectively, represent the production of new infections and changes in states *i.e.*, removal of existing infections production of new infections.

$$\mathbf{T} = \begin{bmatrix} (\alpha_e S_0 + v\alpha_e V_0) & \alpha S_0 \\ 0 & 0 \end{bmatrix}, \quad \mathbf{\Xi} = \begin{bmatrix} -(\kappa + \rho) & 0 \\ \kappa & -(\beta + \mu - v\alpha V_0) \end{bmatrix}, \quad (7.12)$$

and next generation matrix (\mathbf{N}_g) can be computed from \mathbf{T} and $\mathbf{\Xi}$ as $\mathbf{N}_g = -\mathbf{T}\mathbf{\Xi}^{-1}$. The next generation matrix for the proposed model is expressed as

$$\mathbf{N}_g = -\mathbf{T}\mathbf{\Xi}^{-1} = - \begin{bmatrix} (\alpha_e S_0 + v\alpha_e V_0) & \alpha S_0 \\ 0 & 0 \end{bmatrix} \left\{ \begin{bmatrix} -(\kappa + \rho) & 0 \\ \kappa & -(\beta + \mu - v\alpha V_0) \end{bmatrix}^{-1} \right\}, \quad (7.13)$$

simplifying Eq. (7.13), we get

$$\mathbf{N}_g = -\mathbf{T}\mathbf{\Xi}^{-1} = \begin{bmatrix} \frac{\alpha_e S_0 + v\alpha_e V_0}{\kappa + \rho} + \frac{\alpha \kappa S_0}{(\beta + \mu - vV_0\alpha)(\kappa + \rho)} & \frac{\alpha \kappa S_0}{(\beta + \mu - vV_0\alpha)} \\ 0 & 0 \end{bmatrix}, \quad (7.14)$$

as we discussed earlier, we computed the dominant eigen value from the linearized infected subsystem *i.e.*, $\rho(-\mathbf{T}\mathbf{\Xi}^{-1})$. Hence, basic reproduction rate for the proposed *SEIRRPV* model is found to be:

$$\mathcal{R}_0 = -\rho(-\mathbf{T}\mathbf{\Xi}^{-1}) = \frac{\alpha_e S_0 + v\alpha_e V_0}{\kappa + \rho} + \frac{\alpha \kappa S_0}{(\beta + \mu - vV_0\alpha)(\kappa + \rho)}, \quad (7.15)$$

Eq. (7.15) can be simplified as

$$\mathcal{R}_0 = \frac{(\alpha_e S_0 + v\alpha_e V_0)(\beta + \mu - vV_0\alpha) + \alpha \kappa S_0}{(\kappa + \rho)(\beta + \mu - vV_0\alpha)}. \quad (7.16)$$

Considering total population of the city as susceptible and vaccine inoculation is not started *i.e.*, $S_0 = 1$ and $V_0 = 0$ the simplified basic reproduction rate \mathcal{R}_0 will be

$$\mathcal{R}_0 = \frac{\alpha_e(\beta + \mu) + \alpha\kappa}{(\kappa + \rho)(\beta + \mu)}. \quad (7.17)$$

7.3.2 Sensitivity analysis \mathcal{S}

Sensitivity indices assist us with relative variation in \mathcal{R}_0 when a parameter value changes. Additionally, it improves the robustness of our model when different parameters are used. The normalized sensitive index of \mathcal{S}_p for a generalized parameter p (such as, $\alpha_e, \alpha, \beta, \kappa$, *etc.*) [181]

$$\mathcal{S}_p = \frac{\partial \mathcal{R}_0}{\partial p} \frac{p}{\mathcal{R}_0} \quad (7.18)$$

7.3.3 Stability analysis

A detailed stability analysis of the proposed *SEIRRPV* epidemic model was presented using the following theorems:

Theorem 5 (*Disease-free condition*): *Non-infectious equilibrium conditions for epidemic models with non-negative parameters can be computed as*

$$\begin{aligned} (S, E, I) &= (0, 0, 0) \\ R + R_e + P + V &= 1, \quad (R_e \leq 1, R \leq 1, P \leq 1, 0 \leq V) \end{aligned} \quad (7.19)$$

Eq. (7.19) describes a disease-free condition when there is no disease within the presence of vaccine combination.

Proof 5 Equating Eq. (7.1) to zero and considering Eq. (7.2) along with Eq. (7.3), we obtain equilibrium condition in Eq. (7.19).□

Theorem 6 (*Endemic condition*): A model with non-negative parameters can obtain infectious equilibrium conditions as $(S^*, E^*, I^*, R_e^*, R^*, P^*, V^*)$. The total population is assumed to be susceptible due to the pandemic outbreak. This equilibrium condition is termed an endemic equilibrium condition.

Proof 6 We obtain endemic compartment population by equating Eq. (7.1) to zero. By simplifying equations, we get

$$\begin{aligned}
S^* &= \frac{\gamma_e \gamma \rho (\beta + \mu + vV^* \alpha) + \gamma \gamma_e \beta \kappa}{(\alpha_e + v)(\beta + \mu + vV^* \alpha) + \kappa \alpha_e} \\
E^* &= \frac{\alpha S^* I^*}{\kappa + \rho - vV^* \alpha_e - \alpha_e S^*} \\
I^* &= \frac{\kappa E^*}{(\beta + \mu + vV^* \alpha)} \\
R_e^* &= \frac{\rho E^*}{\gamma_e}, \quad R^* = \frac{\beta I^*}{\gamma} \\
P^* &= \int_0^t \mu I(t) dt \Big|_{t=t^*} \\
V^* &= \frac{\Omega S^*}{v(\alpha_e E^* + \alpha I^*)}
\end{aligned} \tag{7.20}$$

Theorem 7 (*Local stability of disease-free condition*): The disease-free equilibrium point $Y^* (S^*, E^*, I^*, R_e^*, R^*, P^*, V^*)$ is locally asymptotically stable in \mathbb{D} when $\mathcal{R}_0 < 1$ and unstable for $\mathcal{R}_0 > 1$.

$$\lambda + \kappa + \rho - vV^* \alpha_e \leq 0 \tag{7.21}$$

Proof 7 Here, we presented an illustration of the stability of the epidemic system model for the disease-free condition. We thus analyze the eigen values of the system model by evaluating its Jacobian matrix. The *SEIRRPV* epidemic model is expressed in matrix

linearization form as:

$$\mathbf{J} = \begin{pmatrix} \mathbf{J}_{11} & -\alpha_e S & -\alpha I & \gamma_e & \gamma & 0 & 0 \\ \alpha_e E & \mathbf{J}_{22} & \alpha S & 0 & 0 & 0 & \mathbf{J}_{27} \\ 0 & \kappa & \mathbf{J}_{33} & 0 & 0 & 0 & \mathbf{J}_{37} \\ 0 & \rho & 0 & -\gamma_e & 0 & 0 & 0 \\ 0 & 0 & \beta & 0 & -\gamma & 0 & 0 \\ 0 & 0 & \mu & 0 & 0 & 0 & 0 \\ \Omega & \mathbf{J}_{72} & \mathbf{J}_{73} & 0 & 0 & 0 & \mathbf{J}_{77} \end{pmatrix}, \quad (7.22)$$

where $\mathbf{J}_{11} = -(\alpha_e E + \alpha I + \Omega)$, $\mathbf{J}_{22} = (\alpha_e S - \kappa - \rho + vV\alpha_e)$, $\mathbf{J}_{27} = v\alpha_e E$, $\mathbf{J}_{33} = -(\beta + \mu - vV\alpha)$, $\mathbf{J}_{37} = v\alpha I$, $\mathbf{J}_{72} = -vV\alpha_e$, $\mathbf{J}_{73} = -vV\alpha$, and $\mathbf{J}_{77} = -v\alpha_e E -$

$v\alpha I$. We compute the characteristic function of the system as

$$\lambda \mathbb{I} - \mathbf{J} = \begin{pmatrix} (\lambda - \mathbf{J}_{11}) & \alpha_e S & \alpha I & -\gamma_e & -\gamma & 0 & 0 \\ -\alpha_e E & (\lambda - \mathbf{J}_{22}) & -\alpha S & 0 & 0 & 0 & -\mathbf{J}_{27} \\ 0 & -\kappa & (\lambda - \mathbf{J}_{33}) & 0 & 0 & 0 & -\mathbf{J}_{37} \\ 0 & -\rho & 0 & \lambda + \gamma_e & 0 & 0 & 0 \\ 0 & 0 & -\beta & 0 & \lambda + \gamma & 0 & 0 \\ 0 & 0 & -\mu & 0 & 0 & \lambda & 0 \\ -\Omega & -\mathbf{J}_{72} & -\mathbf{J}_{73} & 0 & 0 & 0 & (\lambda - \mathbf{J}_{77}) \end{pmatrix}, \quad (7.23)$$

In a disease-free condition $(S^*, E^*, I^*) = (0, 0, 0)$. The associated Jacobian is evaluated at the disease-free equilibrium to determine its local stability. The generalized form of the Jacobian matrix of the associated model is given in Eq. (7.22). Thus Jacobian matrix at

disease-free equilibrium point $P^*(S^*, E^*, I^*) = P^*(0, 0, 0)$ is expressed as J^n

$$\mathbf{J}^n = \begin{pmatrix} \mathbf{J}_{11}^n & 0 & 0 & \gamma_e & \gamma & 0 & 0 \\ 0 & \mathbf{J}_{22}^n & 0 & 0 & 0 & 0 & \mathbf{J}_{27}^n \\ 0 & \kappa & \mathbf{J}_{33}^n & 0 & 0 & 0 & \mathbf{J}_{37}^n \\ 0 & \rho & 0 & -\gamma_e & 0 & 0 & 0 \\ 0 & 0 & \beta & 0 & -\gamma & 0 & 0 \\ 0 & 0 & \mu & 0 & 0 & 0 & 0 \\ \Omega & \mathbf{J}_{72}^n & \mathbf{J}_{73}^n & 0 & 0 & 0 & \mathbf{J}_{77}^n \end{pmatrix}, \quad (7.24)$$

where superscript n stands for disease-free condition, $\mathbf{J}_{11}^n = -\Omega$, $\mathbf{J}_{22}^n = -\kappa - \rho + vV^* \alpha_e$, $\mathbf{J}_{27}^n = 0$, $\mathbf{J}_{33}^n = -(\beta + \mu - vV^* \alpha)$, $\mathbf{J}_{37}^n = 0$, $\mathbf{J}_{72}^n = -vV^* \alpha_e$, $\mathbf{J}_{73}^n = -vV^* \alpha$, and $\mathbf{J}_{77}^n = 0$.

We compute the characteristic function of the system as

$$\lambda \mathbb{I} - \mathbf{J}^n = \begin{pmatrix} m(\lambda - \mathbf{J}_{11}^n) & 0 & 0 & -\gamma_e - \gamma & 0 & 0 \\ 0 & (\lambda - \mathbf{J}_{22}^n) & 0 & 0 & 0 & -\mathbf{J}_{27}^n \\ 0 & \kappa & (\lambda - \mathbf{J}_{33}^n) & 0 & 0 & -\mathbf{J}_{37}^n \\ 0 & -\rho & 0 & \gamma_e & 0 & 0 \\ 0 & 0 & -\beta & 0 & \gamma & 0 \\ 0 & 0 & -\mu & 0 & 0 & \lambda \\ -\Omega & -\mathbf{J}_{72}^n & -\mathbf{J}_{73}^n & 0 & 0 & 0 & (\lambda - \mathbf{J}_{77}^n) \end{pmatrix}, \quad (7.25)$$

We computed the eigen values (λ) of Jacobian matrix \mathbf{J}^n by simplifying $\det(\lambda \mathbb{I} - \mathbf{J}^n) = 0$. Eigen values are $\lambda = 0, 0, -\Omega, -\gamma, \gamma_e, \lambda + \beta + \mu + vV^* \alpha \leq 0$ and $\lambda + \beta + \mu + vV^* \alpha_e \leq 0$. The dominant eigen value of \mathbf{J}^n is evaluated as

$$\lambda + \kappa + \rho - vV^* \alpha_e \leq 0 \quad (7.26)$$

Solving Eq. (7.17) we get,

$$\mathcal{R}_0 = \frac{vV^* \alpha_e}{\kappa + \rho}. \quad (7.27)$$

We computed λ is by replacing simplified \mathcal{R}_0 in Eq. (7.26)

$$\begin{aligned} (\kappa + \rho)(\mathcal{R}_0 - 1) &\leq 0 \\ \mathcal{R}_0 &\leq 1 \end{aligned} \tag{7.28}$$

We, therefore, conclude that the pandemic will be disease-free when $\mathcal{R}_0 \leq 1$. \square

Theorem 8 (*Population to be vaccinated for a disease-free condition*): *The disease-free equilibrium point $Y^*(S^*, E^*, I^*, R_e^*, R^*, P^*, V^*)$ is stable in \mathbb{D} then vaccinated population compartment must satisfy*

$$V^* \leq \frac{(\kappa + \rho)}{v\alpha_e}, \tag{7.29}$$

Proof 8 As we know, the eigen values of a characteristic equation must be negative or zero to be locally stable. From Eq. (7.26), we can easily observe that eigen values are negative when $vV^*\alpha_e - (\kappa + \rho) \leq 0$. So critical vaccinated population is simplified as $V^* \leq \frac{(\kappa + \rho)}{v\alpha_e}$. This concludes our proof. \square

Theorem 9 (*Local stability for endemic condition*): *The endemic equilibrium point $Y^*(S^*, E^*, I^*, R_e^*, R^*, P^*, V^*)$ is locally asymptotically stable in \mathbb{D} when $\mathcal{R}_0 > 1$.*

Proof 9 With a similar approach as the previous theorem, we will calculate eigen values to validate local stability of the epidemic in an endemic condition. Therefore, characteristic function at equilibrium point $Y^*(S^*, E^*, I^*, R_e^*, R^*, P^*, V^*)$ is $\lambda \mathbb{I} - \mathbf{J}^i$

$$\lambda \mathbb{I} - \mathbf{J}^i = \begin{pmatrix} (\lambda - \mathbf{J}_{11}^i) & \alpha_e S & \alpha I & -\gamma_e & -\gamma & 0 & 0 \\ -\alpha_e E^* & (\lambda - \mathbf{J}_{22}^i) & -\alpha S^* & 0 & 0 & 0 & -\mathbf{J}_{27}^i \\ 0 & -\kappa & (\lambda - \mathbf{J}_{33}^i) & 0 & 0 & 0 & -\mathbf{J}_{37}^i \\ 0 & -\rho & 0 & \lambda + \gamma_e & 0 & 0 & 0 \\ 0 & 0 & -\beta & 0 & \lambda + \gamma & 0 & 0 \\ 0 & 0 & -\mu & 0 & 0 & \lambda & 0 \\ -\Omega & -\mathbf{J}_{72}^i & -\mathbf{J}_{73}^i & 0 & 0 & 0 & (\lambda - \mathbf{J}_{77}^i) \end{pmatrix}, \tag{7.30}$$

where $\mathbf{J}_{11}^i = -(\alpha_e E^* + \alpha I + \Omega)$, $\mathbf{J}_{22}^i = (\alpha_e S^* - \kappa - \rho + \nu V^* \alpha_e)$, $\mathbf{J}_{27}^i = \nu \alpha_e E^*$, $\mathbf{J}_{33}^i = -(\beta + \mu - \nu V^* \alpha)$, $\mathbf{J}_{37}^i = \nu \alpha I^*$, $\mathbf{J}_{72}^i = -\nu V^* \alpha_e$, $\mathbf{J}_{73}^i = -\nu V^* \alpha$, and $\mathbf{J}_{77}^i = -\nu \alpha_e E^* - \nu \alpha I^*$. We further simplified endemic equilibrium point Y^* and expressed it in simplified basic reproduction rate \mathcal{R}_0 as mentioned in Eq. (7.27). After simplification, we get,

$$\nu V^* \alpha_e = \mathcal{R}_0 (\kappa + \rho), \quad \nu V^* \alpha = \frac{\mathcal{R}_0 \alpha (\kappa + \rho)}{\alpha_e} \quad (7.31)$$

$$I^* = \frac{\{(\mathcal{R}_0 - 1)(\kappa + \rho) + \alpha_e\} \Omega}{(1 - \mathcal{R}_0)(\kappa + \rho)(\alpha - \beta) - \alpha_e \beta + \rho \alpha} \quad (7.32)$$

$$E^* = \frac{\alpha I^*}{(1 - \mathcal{R}_0)(\kappa + \rho) - \alpha_e} = \frac{\alpha \Omega}{(1 - \mathcal{R}_0)(\kappa + \rho)(\alpha - \beta) - \alpha_e \beta + \rho \alpha} \quad (7.33)$$

The characteristic equation of the matrix is given in Eq. (7.30), $\det(\lambda \mathbb{I} - \mathbf{J}^n) = 0$ is expressed as

$$\lambda^7 + a_1 \lambda^6 + a_2 \lambda^5 + a_3 \lambda^4 + a_4 \lambda^3 + a_5 \lambda^2 + a_6 \lambda + a_7 = 0, \quad (7.34)$$

where

$$\begin{aligned} a_1 &= (\gamma + \gamma_e + \Omega), \\ a_2 &= (\alpha_e \kappa + \gamma \gamma_e + \gamma \Omega + \gamma_e \Omega), \\ a_3 &= \gamma \gamma_e \Omega + 2\alpha_e \kappa \Omega + \alpha_e \kappa \gamma + \alpha_e \kappa \gamma_e - \gamma_e \alpha_e E^* \rho, \\ a_4 &= \gamma \beta (\alpha_e E^* \kappa + \Omega \beta \nu V^* \alpha) + \alpha_e \kappa \{(1 + \Omega)(\gamma + \gamma_e + \Omega) + \gamma \gamma_e + \gamma \Omega + \gamma_e \Omega\} \\ &\quad - \gamma \gamma_e \alpha_e E^* \rho - \Omega \gamma_e \nu V^* \alpha_e - \Omega \nu V^* (\alpha_e^2 - \alpha^2 I^* - \alpha \alpha_e I^*) \\ a_5 &= \gamma \gamma_e \alpha_e E^* \kappa \beta + \gamma \alpha_e E^* \kappa \beta + \gamma \gamma_e \Omega \beta \nu V^* \alpha + \alpha_e \kappa (2\gamma \gamma_e \Omega + \gamma_e \Omega^2 + \gamma \Omega^2) \\ &\quad - \gamma_e \alpha_e E^* \rho \Omega \gamma - \Omega \gamma \nu V^* (\alpha_e^2 - \alpha^2 I^* - \alpha \alpha_e I^*) \\ a_6 &= \gamma \alpha_e \kappa \Omega (E^* \beta + \gamma_e \Omega) \end{aligned} \quad (7.35)$$

For endemic stability, $a_i \forall i \in \{1, 2, \dots, 6\}$ should be positive. Neglecting α^2 , α_e^2 and $\alpha \alpha_e$

terms of the Eq. (7.35) and using the \mathcal{R}_0 , E^* , I^* and V^* we can derive a_4 as

$$\{(\mathcal{R}_0 - 1)(\kappa + \rho)(\alpha - \beta) \geq (\alpha\beta - \rho\alpha) + \rho\alpha - \alpha\beta\} \gamma\gamma_e\Omega\beta\mathcal{R}_0\alpha(\kappa + \rho) \geq 0, \quad (7.36)$$

solving Eq. (7.36) we get

$$\mathcal{R}_0 = 1 + \frac{\rho\alpha - \alpha\beta}{(\kappa + \rho)(\alpha - \beta)} \geq 1, \quad (7.37)$$

□

Theorem 10 (*Global stability for disease-free condition*): *The disease-free equilibrium point $Y^*(S^*, E^*, I^*, R_e^*, R^*, P^*, V^*)$ is globally asymptotically stable in \mathbb{D}_+^7 when $\mathcal{R}_0 < 1$.*

Proof 10 Consider a Lyapunov function L as follows

$$L(Y^*) = \frac{1}{2}(S^* + E^* + I^*)^2, \quad (7.38)$$

It satisfies $L(Y^*) > 0 \forall Y^* \in \mathbb{D}_+^7$ and $L(Y^*) \Big|_{(S^*=0, E^*=0, I^*=0)} = 0$ necessary for the stability of the system model. Differentiating Eq. (7.38) with respect to time and using Eq. (7.1), we get

$$\begin{aligned} \dot{L}_0 &= (S^* + E^* + I^*)(\dot{S}^* + \dot{E}^* + \dot{I}^*), \\ \dot{L}_0 &= (S^* + E^* + I^*)(\gamma_e R_e^* + \gamma R^* - \Omega S^* - \rho E^* + \nu V^* \alpha_e E^* + \nu \alpha V^* I^* - \mu I^* - \beta I^*) \end{aligned} \quad (7.39)$$

where disease-free condition compartment population from Eq. (19) of the chapter confirms that $\dot{L}_0 = 0$ at the equilibrium condition. Further, Eq. (7.39) is strictly negative, considering the positive epidemic quantities. Thus, the global stability of the epidemic model during disease-free conditions is validated. □

Theorem 11 (*Global stability for endemic condition*): *The endemic equilibrium point $Y^*(S^*, E^*, I^*, R_e^*, R^*, P^*, V^*)$ is globally asymptotically stable in \mathbb{D}_+^7 when $\mathcal{R}_0 > 1$.*

Proof 11 An endemic disease has been present for a sufficiently long period of time where both asymptomatic and infected people are above a certain positive level. The global stability of endemic scenarios can be represented and analyzed by uniform persistence. Epidemic model is called uniformly persistent if there exists a constant $0 < \varepsilon < 1$ such that any solution $Y^*(S^*, E^*, I^*, R_e^*, R^*, P^*, V^*)$ with

$$\min \{ \limsup_{t \rightarrow \infty} (S_t, E_t, I_t, R_{et}, R_t, P_t, V_t) \} \geq \varepsilon \in \mathbb{D}_+^7$$

We follow the geometric approach's salient features for testing the endemic equilibrium's global stability. In this regard, following the research work of [182] sixth additive compound matrix is computed as

$$\mathbf{J}^{[6]} = \begin{pmatrix} \mathbf{J}_{11}^a & 0 & 0 & 0 & -\mathbf{J}_{37}^a & \mathbf{J}_{27}^a & 0 \\ 0 & \mathbf{J}_{22}^a & 0 & 0 & 0 & 0 & 0 \\ 0 & 0 & \mathbf{J}_{33}^a & 0 & 0 & 0 & -\gamma \\ 0 & 0 & 0 & \mathbf{J}_{44}^a & 0 & 0 & \gamma_e \\ -\mathbf{J}_{73}^a & \mu & -\beta & 0 & \mathbf{J}_{55}^a & \alpha_e S & \alpha_e I \\ \mathbf{J}_{72}^a & 0 & 0 & -\rho & \kappa & \mathbf{J}_{66}^a & -\alpha_e S \\ -\Omega & 0 & 0 & 0 & 0 & \alpha_e E & \mathbf{J}_{77}^a \end{pmatrix}, \quad (7.40)$$

where $\mathbf{J}_{11}^a = \mathbf{J}_{11} + \mathbf{J}_{22} + \mathbf{J}_{33} + \mathbf{J}_{44} + \mathbf{J}_{55} + \mathbf{J}_{66}$, $\mathbf{J}_{22}^a = \mathbf{J}_{11} + \mathbf{J}_{22} + \mathbf{J}_{33} + \mathbf{J}_{44} + \mathbf{J}_{55} + \mathbf{J}_{77}$, $\mathbf{J}_{27}^a = v\alpha_e E$, $\mathbf{J}_{33}^a = \mathbf{J}_{11} + \mathbf{J}_{22} + \mathbf{J}_{33} + \mathbf{J}_{44} + \mathbf{J}_{66} + \mathbf{J}_{77}$, $\mathbf{J}_{37}^a = v\alpha I$, $\mathbf{J}_{72}^a = -vV\alpha_e$, $\mathbf{J}_{44}^a = \mathbf{J}_{11} + \mathbf{J}_{22} + \mathbf{J}_{33} + \mathbf{J}_{55} + \mathbf{J}_{66} + \mathbf{J}_{77}$, $\mathbf{J}_{55}^a = \mathbf{J}_{11} + \mathbf{J}_{22} + \mathbf{J}_{44} + \mathbf{J}_{55} + \mathbf{J}_{66} + \mathbf{J}_{77}$, $\mathbf{J}_{66}^a = \mathbf{J}_{11} + \mathbf{J}_{33} + \mathbf{J}_{44} + \mathbf{J}_{55} + \mathbf{J}_{66} + \mathbf{J}_{77}$, $\mathbf{J}_{73}^a = -vV\alpha$, and $\mathbf{J}_{77}^a = \mathbf{J}_{11} + \mathbf{J}_{33} + \mathbf{J}_{44} + \mathbf{J}_{55} + \mathbf{J}_{66} + \mathbf{J}_{77}$. From Eq. (21) of Theorem 4.6 in the chapter, we found values of the diagonal elements of \mathbf{J} as $\mathbf{J}_{ii} \forall i \in \{1, 2, \dots, 7\}$.

With the validation of continuity and uniqueness, boundedness solution, initial disease-free condition, and unique endemic equilibrium condition which satisfies $\mathbf{J}(F(Y(t))) = \frac{\delta f_i}{\delta Y}$ with $i \in \{1, 2, \dots, 7\} = 0$ we can consider the following differential equation.

$$z_t' = \left[M_f M^{-1} + M \mathbf{J}^{[6]} M^{-1} \right] z_t =: \mathbf{B}(F(t, F(Y(0)))) z_t, \quad (7.41)$$

where $Y(t) \mapsto M(F(Y(t)))$ is a \mathbb{D}^1 non-singular $\begin{pmatrix} n \\ m+2 \end{pmatrix} \times \begin{pmatrix} n \\ m+2 \end{pmatrix}$ matrix-valued function in \mathbb{D} such that $\|M(F(Y(t)))^{-1}\|$ is uniformly bounded and M_f is the directional derivative of M in the direction field F and $\mathbf{J}^{[m+2]}$ is the $m+2$ additional compound matrix of the Jacobian matrix of Eq. (7.22).

$$\begin{aligned} \mathbf{M} &= \text{diag} \left[V \quad P \quad R \quad R_e \quad c_1 I \quad c_2 E \quad S \right], \\ \mathbf{M}_f &= \text{diag} \left[V' \quad P' \quad R' \quad R'_e \quad c_1 I' \quad c_2 E' \quad S' \right], \end{aligned} \quad (7.42)$$

Eq. (7.1) in the chapter for a small time deviation is simplified as

$$\alpha_e E + \alpha I + \Omega = -\frac{\gamma_e R_e + \gamma R}{S} + \frac{S'}{S}, \quad \kappa + \rho - vV\alpha_e - \alpha_e S = -\frac{\alpha SI}{E} + \frac{E'}{E}, \quad (7.43)$$

$$\beta + \mu - vV\alpha = -\frac{\kappa E}{I} + \frac{I'}{I}, \quad \frac{\rho E}{R_e} = \gamma_e + \frac{R'_e}{R_e}, \quad \frac{\beta I}{R} = \gamma + \frac{R'}{R}, \quad \frac{\mu I}{P} = \frac{P'}{P}, \quad (7.44)$$

$$-v\alpha_e E - v\alpha I = -\frac{\Omega S}{V} + \frac{V'}{V}, \quad (7.45)$$

Substituting Eqs. (7.40) and (7.42)- (7.45) in Eq. (7.41) and rederived in form of six hyper-planes from the \mathbf{B} matrix.

$$\mathbf{B}_t = \begin{pmatrix} \mathbf{B}_{11} & 0 & 0 & 0 & \mathbf{B}_{15} & \mathbf{B}_{16} & 0 \\ 0 & \mathbf{B}_{22} & 0 & 0 & 0 & 0 & 0 \\ 0 & 0 & \mathbf{B}_{33} & 0 & 0 & 0 & \mathbf{B}_{37} \\ 0 & 0 & 0 & \mathbf{B}_{44} & 0 & 0 & \mathbf{B}_{47} \\ \mathbf{B}_{51} & \mathbf{B}_{52} & \mathbf{B}_{53} & 0 & \mathbf{B}_{55} & \mathbf{B}_{56} & \mathbf{B}_{57} \\ \mathbf{B}_{61} & 0 & 0 & \mathbf{B}_{64} & \mathbf{B}_{65} & \mathbf{B}_{66} & \mathbf{B}_{67} \\ \mathbf{B}_{71} & 0 & 0 & 0 & 0 & \mathbf{B}_{67} & \mathbf{B}_{77} \end{pmatrix} \quad (7.46)$$

where

$$\begin{aligned}
\mathbf{B}_{11} &= -(\alpha_e E + \alpha I + \mu) - (\kappa + \rho - \alpha_e S - \nu \alpha_e V) - (\mu + \beta - \nu \alpha V) - \gamma - \gamma_e + \frac{V'}{V}, \\
\mathbf{B}_{15} &= -c_1^{-1} \nu \alpha V, \quad \mathbf{B}_{16} = -c_2^{-1} \nu \alpha_e V \\
\mathbf{B}_{22} &= -(\alpha_e E + \alpha I + \Omega) - (\kappa + \rho - \alpha_e S - \nu \alpha_e V) - (\mu + \beta - \nu \alpha V) - (\alpha_e E + \alpha I) \nu \\
&\quad - \gamma - \gamma_e + \frac{P'}{P}, \\
\mathbf{B}_{33} &= -(\alpha_e E + \alpha I + \Omega) - (\kappa + \rho - \alpha_e S - \nu \alpha_e V) - (\mu + \beta - \nu \alpha V) - (\alpha_e E + \alpha I) \nu \\
&\quad - \gamma_e + \frac{R'}{R}, \\
\mathbf{B}_{37} &= \frac{-\gamma R}{S}, \\
\mathbf{B}_{44} &= -(\alpha_e E + \alpha I + \Omega) - (\kappa + \rho - \alpha_e S - \nu \alpha_e V) - (\mu + \beta - \nu \alpha V) - (\alpha_e E + \alpha I) \nu \\
&\quad - \gamma + \frac{R'_e}{R_e}, \\
\mathbf{B}_{47} &= \frac{\gamma_e R_e}{S}, \\
\mathbf{B}_{51} &= \alpha I \nu c_1, \quad \mathbf{B}_{52} = \frac{\mu I c_1}{P}, \quad \mathbf{B}_{53} = -\frac{\beta I c_1}{R} \\
\mathbf{B}_{55} &= -(\alpha_e E + \alpha I + \Omega) - (\kappa + \rho - \alpha_e S - \nu \alpha_e V) - (\alpha_e E + \alpha I) \nu - \gamma_e - \gamma + \frac{I'}{I}, \\
\mathbf{B}_{56} &= \frac{\alpha S I c_1}{E c_2}, \quad \mathbf{B}_{57} = \frac{I^2 \alpha c_1}{S}, \\
\mathbf{B}_{61} &= \alpha_e E \nu c_2, \quad \mathbf{B}_{64} = \frac{\rho E c_2}{R_e}, \quad \mathbf{B}_{65} = -\frac{\kappa E c_2}{I c_1} \\
\mathbf{B}_{66} &= -(\alpha_e E + \alpha I + \Omega) - (\alpha_e E + \alpha I) \nu - \gamma_e - \gamma + \frac{E'}{E}, \\
\mathbf{B}_{71} &= -\frac{\Omega S}{V}, \quad \mathbf{B}_{76} = \frac{\alpha_e S}{c_2}, \\
\mathbf{B}_{77} &= -(\kappa + \rho - \alpha_e S - \nu \alpha_e V) - (\mu + \beta - \nu \alpha V) - (\alpha_e E + \alpha I) \nu - \gamma - \gamma_e + \frac{S'}{S},
\end{aligned} \tag{7.47}$$

$\mathbf{B}_{ij} \forall i, j \in \{1, 2, \dots, 7\}$ represent rows and column index of \mathbf{B} . The vector norm, $|\cdot|$ of $F(Y(t))$ in \mathbb{D}_+^7 is implemented for stability analysis purpose. may be expressed as Our approach is based on Li and Muldowney's theorem [183] to determine the parametric value of the epidemic to ensure its globally asymptotically stable. Applying Lozinskiĭ

measure,

$$\mathbb{M}(B) \leq \sup \{h_i \forall i \in \{1, 2, \dots, 7\}\}, \quad (7.48)$$

where \mathbb{M} is Lozinskiĭ measure with respect to l_1 norm consisting of h_i hyper-planes. B_{ij} are the matrix norms with respect to l_1 vector norms by following the detailed derivation in Theorem 13 of [182]. Consequently, We use Eqs. (7.43) to (7.45) to simplify h_i as

$$\begin{aligned} \mathbf{h}_{1t} &= \mathbf{B}_{11} + \sum_{j \neq 1} |\mathbf{B}_{1j}| \\ &= -\frac{\gamma_e R_e + \gamma R}{S} + \frac{-\alpha SI}{E} - \frac{\kappa E}{I} - \gamma - \gamma_e - \left(\frac{\alpha}{c_1} + \frac{\alpha_e}{c_2} \right) \nu V + \frac{S'}{S} + \frac{E'}{E} + \frac{I'}{I} + \frac{V'}{V} := \bar{h}_{1t}, \end{aligned}$$

$$\begin{aligned} \mathbf{h}_{2t} &= \mathbf{B}_{22} + \sum_{j \neq 2} |\mathbf{B}_{2j}| \\ &= -\frac{\gamma_e R_e + \gamma R}{S} + \frac{-\alpha SI}{E} - \frac{\kappa E}{I} - \gamma - \gamma_e - \frac{\Omega S}{V} + \frac{S'}{S} + \frac{E'}{E} + \frac{I'}{I} + \frac{P'}{P} + \frac{V'}{V} := \bar{h}_{2t}, \end{aligned}$$

$$\begin{aligned} \mathbf{h}_{3t} &= \mathbf{B}_{33} + \sum_{j \neq 3} |\mathbf{B}_{3j}| \\ &= -\frac{\gamma_e R_e}{S} + \frac{-\alpha SI}{E} - \frac{\kappa E}{I} - \gamma_e - \frac{\Omega S}{V} + \frac{S'}{S} + \frac{E'}{E} + \frac{I'}{I} + \frac{R'}{R} + \frac{V'}{V} := \bar{h}_{3t}, \end{aligned}$$

$$\begin{aligned} \mathbf{h}_{4t} &= \mathbf{B}_{44} + \sum_{j \neq 4} |\mathbf{B}_{4j}| \\ &= -\frac{\gamma R}{S} + \frac{-\alpha SI}{E} - \frac{\kappa E}{I} - \gamma - \frac{\Omega S}{V} + \frac{S'}{S} + \frac{E'}{E} + \frac{I'}{I} + \frac{R'_e}{R_e} + \frac{V'}{V} := \bar{h}_{4t}, \end{aligned}$$

$$\begin{aligned} \mathbf{h}_{5t} &= \mathbf{B}_{55} + \sum_{j \neq 5} |\mathbf{B}_{5j}| \\ &= \nu c_1 (-\alpha_e E - \Omega) (1 + \nu c_1) \left(-\frac{\gamma_e R_e + \gamma R}{S} + \frac{S'}{S} \right) + \frac{-\alpha SI}{E} - (1 - c_1) \gamma - \gamma_e - \frac{\Omega S}{V} + \frac{E'}{E} + \frac{I'}{I} + \frac{(1+c_1)R'}{R} + \frac{P'}{P} + \frac{V'}{V} := \bar{h}_{5t}, \end{aligned}$$

$$\begin{aligned} \mathbf{h}_{6t} &= \mathbf{B}_{66} + \sum_{j \neq 6} |\mathbf{B}_{6j}| \\ &= \nu c_2 (-\alpha I - \Omega) (1 + \nu c_2) \left(-\frac{\gamma_e R_e + \gamma R}{S} + \frac{S'}{S} \right) + \frac{-\kappa E}{I} - \gamma - (1 - c_1) \gamma_e - \frac{\Omega S}{V} + \frac{E'}{E} + \frac{I'}{I} + \frac{(1+c_2)R'}{R} + \frac{P'}{P} + \frac{V'}{V} := \bar{h}_{6t}, \end{aligned}$$

$$\begin{aligned} \mathbf{h}_{7t} &= \mathbf{B}_{77} + \sum_{j \neq 7} |\mathbf{B}_{7j}| \\ &= \frac{-\alpha SI}{E} - \frac{\kappa E}{I} - \gamma - \gamma_e - \frac{\Omega S}{V} + \frac{S'}{S} + \frac{E'}{E} + \frac{I'}{I} + \frac{V'}{V} := \bar{h}_{7t}, \end{aligned}$$

The simplified \bar{h}_{it} values are negative for non-negative values of epidemic parameters.

Following LaSalle's invariance principle [184]

$$\therefore \lim_{t \rightarrow \infty} \frac{1}{t} \int_0^t \bar{h}_i(s) ds < 0, \quad i \in \{1, 2, \dots, 7\} \quad (7.49)$$

This proves that the epidemic model is globally asymptotically stable during endemic conditions for $\mathcal{R}_0 > 1$. \square

7.4 Cubature Kalman filter (CKF)-based epidemic state estimator

With the state space model of the system already discussed in Chapter 7.2, the CKF is performed under a popular Bayesian framework of filtering [185]. The Bayesian framework involves two steps: prediction and update. The computation of mean and covariance involves intractable integrals of the form [64],[186] are approximated using the third-degree spherical cubature rule [186],[187] of numerical approximation as earlier discussed in Chapter 5.3 and second para of Chapter 6.2. The prediction and update steps for implementing the CKF are presented in Appendix C.

The CKF algorithm in Appendix C is implemented over the state space model corresponding to the proposed *SEIRRPV* model in order to estimate the desired compartment populations. We use the standard CKF, while the state-of-the-art filtering literature witnesses few advancements in order to marginally improve the accuracy at the cost of increased computational budget. For example, [83] replaces the third-degree spherical cubature rule with higher-degree spherical cubature rule while [188] redesigns the CKF under maximum correntropy criterion in order to improve the accuracy. A practitioner can use such advancements to marginally improve the accuracy but with an additional computational budget.

7.5 Simulation and Results

This section discusses the performance validation of the proposed *SEIRRPV* model integrated with CKF techniques. To demonstrate the superiority of the proposed *SEIRRPV* model over the various epidemic parameters discussed in Section 7.1.1, a simulation-based comparative analysis is performed. Epidemic models, such as *SIR* [142], *SIRV* [61], *SIRP* [54], *SEIRP* [59], *SEIRRP* [60], along with the proposed *SEIRRPV* models, are represented in the state-space model as stated in Eqs. (1.1) and (1.2). Each model has a different state and measurement model, as suggested in Section 7.2. In this simulation-based study, two scenarios are examined. First, vaccinated models

are validated through real-data of an epidemic outbreak that occurred in Delhi caused by the SARS-COV-2 virus, and second, a comparison with *SIR* family models is performed. We categorize simulation parameters as estimation parameters and epidemic parameters for better understanding. We consider the below parameter values in our simulation.

Estimation parameter: We study the propagation of disease dynamics of the city for $T=200$ days with a sampling period of 1 day. Here, epidemic compartments are put in the state matrix *i.e.*, state of a *SEIRRPV* model is considered as $\mathbf{x}_k = [S_k E_k I_k R_{ek} R_k P_k V_k]^T$, with k in subscript representing the time instant t_k . The initial compartment values for Covid-19 pandemic $E_0, I_0, R_{e0}, R_0, P_0, V_0$ are 100, 200, 0, 1, 0, and 0, respectively. Rest of the population is assumed to be equally susceptible to being sick due to the ongoing pandemic. \mathcal{Q}_k is the process noise that follows $\mathcal{Q}_k \approx \mathcal{N}(\mathbf{0}, \mathbf{Q}_k)$, where \mathfrak{N} denotes Gaussian distribution. Process noise standard deviation, σ_x for susceptible, exposed, infected, recovered from exposed, recovered from infection, passed away, and vaccine inoculation are 31.622, 6.3245, 7.071, 2.236, 2.236, 1, and 7.746, respectively. Similarly, \mathcal{V}_k measurement noise follows $\mathcal{V}_k \approx \mathfrak{N}(\mathbf{0}, \mathbf{R}_k)$. Standard deviation σ_y for the measurements of infected, recovered, passed away, and vaccine inoculation groups are 10, 8.944, 3.162, and 10^{-4} , respectively. $x \in \{1, 2, \dots, n\}$, and $y \in \{1, 2, \dots, m\}$ in subscript represent the state and measurement vector, where n and m are the number of states and measurement vectors, respectively. The initial estimate of state $\hat{\mathbf{x}}_{0|0}$ is generated as a Gaussian random number with mean \mathbf{x}_0 , and initial covariance $\mathbf{P}_{0|0} = \text{diag}([1000, 1000, 1000, 100, 100, 1, 500])$, where diag represents diagonal matrix. Hence, we implement the CKF technique over different epidemic models for 200 days with a sample time of 1 day.

Epidemic parameter: Let us consider that the coronavirus causes pandemics in an anonymous city with a population of 35 million. Epidemic parameters have been adopted from [60] and are shown in Table 7.1.

| Case | N | α_e | α | β | γ_e | γ | μ | κ | ρ | ν | Ω |
|------|------------------|------------|----------|---------|------------|----------|-------|----------|--------|-------|----------|
| 1 | 32×10^6 | 0.3 | 0.13 | 0.05 | 10^{-4} | 0.08 | 0.04 | 0.9 | 0.8 | 0.35 | 0.002 |
| 2 | 35×10^6 | 2 | 2 | 0.05 | 0.071 | 0.1 | 0.032 | 0.2 | 0.08 | 0.35 | 0.002 |

Table 7.1: Epidemic parameters values considered.

7.5.1 Case-1: Vaccinated model validation through real-data of epidemic outbreak in Delhi caused by SARS-COV-2 virus

Publicly available Covid-19 pandemic data, which provide insights into epidemic dynamics in Delhi, the capital city of India, have been implemented for simulation-based research [50][51]. For our simulated modeling, we collected information on per day infection, recovered, death, and vaccinated compartments. We used these data as measurements to model our true state model between 17 January 2021 and 26 April 2021. Please note that the extensive stress on the healthcare system left many without access to adequate healthcare. As a result, we have more noisy information about the epidemic outbreak. Hence, we verified the proposed model to be validated with a hundred times more process noise standard deviation, σ_x for susceptible, exposed, infected, recovered from exposed, recovered from infection, passed away, and vaccine inoculation, as discussed earlier.

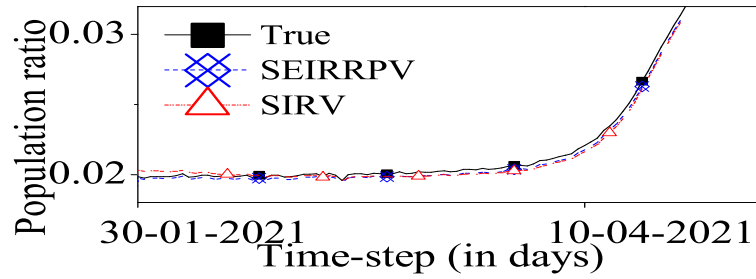
Table 7.2: Average % RMSE comparison of the *SEIRRPV* and *SIRV* model using real-data.

| Epidemic model | I | R | P | V |
|----------------|------|------|---------------|-------|
| <i>SEIRRPV</i> | 2.09 | 2.78 | 19.7 | 29.20 |
| <i>SIRV</i> | 2.60 | 2.60 | nan^\dagger | 29.42 |

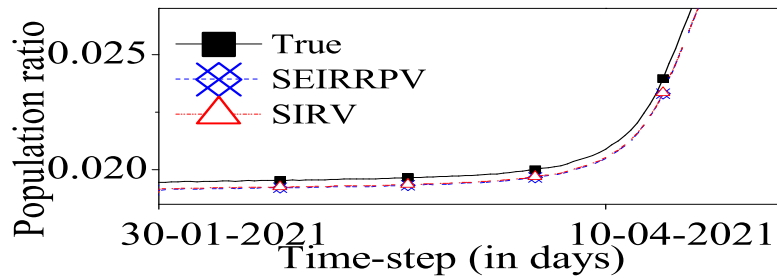
nan^\dagger : %RMSE does not exist for the given compartment.

For evaluating the performances, the matrices root mean square error (RMSE) and percentage RMSE are considered by taking $M_c = 1000$ number of Monte-Carlo simulations, using Eqs. (1.29) and (1.30).

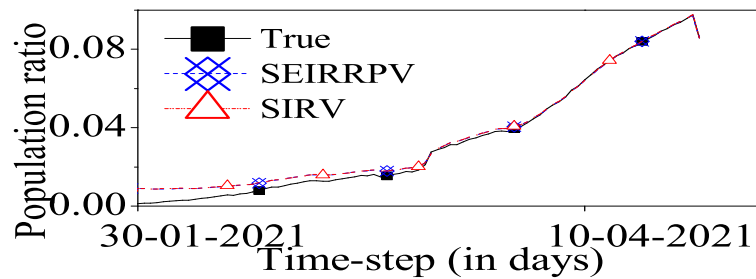
Please note that the true values of compartment populations, i.e. real-data of \mathbf{x}_k are collected from [50] and [51]. Subsequently, the RMSE and %RMSE are obtained for the error between the true compartment population data and the estimated compartment population $\hat{\mathbf{x}}_{k|k}$. Fig. 7.3 shows that the proposed *SEIRRPV* model successfully tracks the Covid-19 spread. Moreover, Fig. 7.4 and Table 7.2 collectively infer that the RMSE is reduced for the proposed *SEIRRPV* model in comparison to the *SIRV* model.



(a)

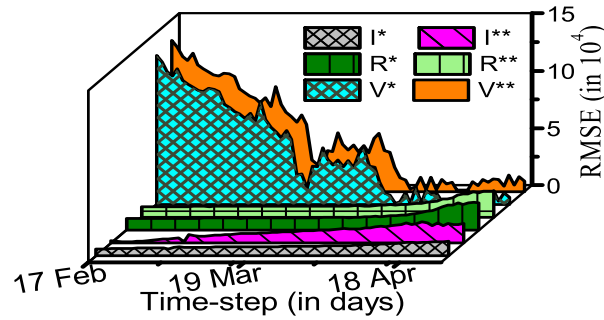


(b)



(c)

Figure 7.3: Case-1: Estimates of different compartments in form of population ratio (a) infected compartment, (b) recovered people from infected compartment, (c) vaccinated people compartment.



*, and ** in superscript represent *SEIRRPV*, and *SIRV* epidemic model, respectively.

Figure 7.4: Case-1: RMSE based performance comparison between *SEIRRPV* and *SIRV* model

7.5.2 Case-2: Comparison with *SIR* family models

In the above discussions, we limited the comparison of the proposed *SEIRRPV* model with the *SIRV* model, as the two models commonly include the vaccinated population. We now extend the comparison of the proposed *SEIRRPV* model with all famous existing models under the *SIR* family, including the *SIR*, *SIRP*, *SIRV*, *SEIRP*, and *SEIRRP* models. In this regard, we compare the percentage RMSEs for all models in Table 7.3. The table concludes an improved accuracy of the proposed *SEIRRPV* model in comparison to the existing models. To ensure that the estimation errors of the proposed *SEIRRPV* model for different compartment populations are within acceptable ranges, we plot the RMSEs of compartment populations obtained using the proposed *SEIRRPV* model in Fig. 7.5.

Table 7.3: %RMSE for different models with 1000 Monte-Carlo simulations.

| Model | S | E | I | Re | R | P | V |
|----------------|--------|---------------|--------|---------------|---------|---------------|---------------|
| <i>SIR</i> | 10.57 | nan^\dagger | 1.607 | nan^\dagger | 0.0041 | nan^\dagger | nan^\dagger |
| <i>SIRP</i> | 11.06 | nan^\dagger | 1.974 | nan^\dagger | 0.0901 | 0.0131 | nan^\dagger |
| <i>SIRV</i> | 5.359 | nan^\dagger | 2.246 | nan^\dagger | 0.0289 | nan^\dagger | 0.00015 |
| <i>SEIRP</i> | 45.19 | 60.57 | 10.31 | nan^\dagger | 0.0901 | 0.0131 | nan^\dagger |
| <i>SEIRRP</i> | 4.15 | 3.535 | 0.0765 | 1.996 | 0.00017 | 0.00017 | nan^\dagger |
| <i>SEIRRPV</i> | 0.0020 | 0.0022 | 0.0011 | 0.0004 | 0.00001 | 0.00001 | 0.00002 |

nan^\dagger : % RMSE does not exist for the given compartment.

For a comprehensive analysis of the pandemic's persistence, all parameters

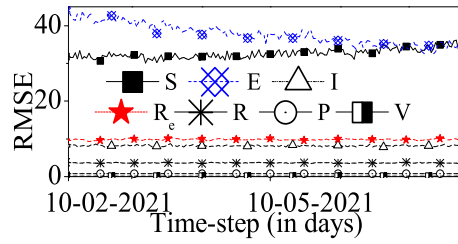


Figure 7.5: Case-2: RMSE of different compartments by *SEIRRPV* model.

corresponding to the basic reproduction number have been analyzed for sensitivity. In this regard, we implemented Eqs. (7.16), and (7.17) in Eq. (7.18) to compute the sensitivity index \mathcal{S} for different epidemic parameters.

The Table 7.4 shows the sensitivity of the epidemic parameters, such as α_e , α , β , μ , κ , ρ , ν and Ω on the epidemic. Sensitive analysis shows that the most important factor

Table 7.4: Sensitive index for different epidemic parameters

| Parameter | α_e | α | β | μ | κ | ρ | ν | Ω |
|---------------|------------|----------|---------|-------|----------|--------|-------|----------|
| \mathcal{S} | 1.00 | 0.784 | -0.98 | -0.63 | 0.11 | -0.28 | 0.79 | -4.27 |

in containing the epidemic is vaccination rate, followed by infection rate, which shows no symptoms and recovery rate. The least sensitive parameter is incubation rate. Positive sensitivity indicates that increases in relevant parameters lead to increases in \mathcal{R}_0 and vice versa. Lower α_e and higher Ω are necessary constraints for lower \mathcal{R}_0 values. As a result of the sensitivity analysis, vaccine rate appears to be more important than the following different nPIs.

7.6 Discussion

Covid-19 pandemic caused by SARS-COV-2 started in Wuhan city of China and jolted the entire world within a few months. Its uniqueness is not only its speed of transmission but also life-threatening. In this article, we estimate the dynamics of the Covid-19 from the noisy process and measurement model. Process noise is due to various real-life complex constraints involved in it. So, accurate information about disease transmission is imperative to strategize correctly. Considering new developments in vaccination, we focus on the proposed *SEIRRPV* epidemic model to estimate the

susceptible, exposed, infected, recovered from exposed, recovered from infected, and passed away people during this pandemic. In this chapter, we observed the positive impact of various nPIs, such as social distancing, social awareness, and cleanliness, on the Covid-19 pandemic. In addition to this, we observed a rapid decline in the infected population by improving healthcare infrastructure and increasing the mass vaccination drive, as shown in Table 7.4. We compared the estimation performance of the proposed *SEIRRPV* model with the existing *SIRV* model using the real-data of Delhi and compared it with the existing *SIRV* model using CKF-based method. Fig. 7.3, 7.4 and Table 7.2 validated that the proposed *SEIRRPV* has considerably higher estimation accuracy in comparison to the existing *SIRV* models.

The monitoring and analysis of Covid-19 spread using the epidemic models, like the proposed *SEIRRPV* model, give an edge in formulating appropriate administrative strategies for its control. However, for efficient control of its spread, public awareness is also equally important, and the public must take care of other measures, like social distancing, use of face-masks, non-pharmaceutical interventions, hand sanitization, *etc.*, seriously. In spreading such awareness, the role of print and electronic media has been appreciated, and we may have similar expectations from the media in the future. It has been observed that the spread of the first wave of Covid-19 (approximately between April to July months of 2020) was relatively slower in India when people's awareness was considered to be at its best. However, the spread was severely faster in the second wave, when the media reports frequently highlighted a lack of public precautions.

7.7 Conclusion

An advanced *SIR* epidemic model named *SEIRRPV* with the required mathematical analysis is presented in this chapter. We present uniqueness, positivity, boundedness, and stability analysis (local and global) for both infection-free and endemic conditions. Epidemic model parameters functionalities are computed from their sensitivity indices. A novel CKF technique is implemented on the proposed epidemic model to dynamically estimate the compartments population. We implemented the proposed model to estimate the disease transmission in Delhi, between 17 January 2021 to 26 April 2021. The

simulation study period is important because it witnessed its second wave from March and stretched until June 2021. Through simulation-based analysis, we conclude that the proposed *SEIRRPV* has better performance and also provides additional information to policy-makers about the people who are infected but non-infectious, improving the overall efficiency of the model. However, the proposed algorithm does not give information about the evolution of new variants of Covid-19, which may stimulate further research. We present a comparative analysis of *SIR* family's different epidemic models. Additionally, we validate the proposed *SEIRRPV* model provides more accurate information to the policy-maker to implement the social and clinical strategy with minimal economic loss. Table 7.3 and Table 7.4, respectively, are the estimation accuracy of the proposed epidemic model and sensitivity indices for different epidemic parameters. It concludes that by improving healthcare infrastructure and increasing the mass vaccination drive, epidemic outbreaks can be contained, *i.e.*, \mathcal{R}_0 brought below one.

Chapter 8

Discussion and Conclusion

8.1 Discussion

The Kalman filter and its nonlinear extension, the Gaussian filter, have become widely popular mathematical tools for various applications such as target tracking, power systems, disease transmission monitoring, financial modeling, biomedical diagnosis, remaining useful-life prediction for industrial equipment, fault diagnosis, prognosis, *etc.* Despite the widespread applications of filtering algorithms, the literature lacks a well-performed filtering method for accurately estimating dynamical state of systems under various practical environment. This is mainly due to the fact that the existing filters exhibit significant performance degradation in the presence of irregularities such as delayed measurements, false data injection (cyber-attack), unknown or varying statistical noise, and non-Gaussian noise. Even though the linear Kalman filtering method is optimal for linear systems with Gaussian noises, its performance significantly deteriorates in the presence of the above said irregularities. Although some extensions of the nonlinear filtering algorithms are available to address such irregularities marginally, they are generally insufficient for handling the real-life problems. Therefore, one of the motivations of this thesis is to develop advanced filtering algorithms for handling various irregularities.

Beyond the general filtering algorithms, this thesis also focuses on contributing

towards improving the performance of some practical applications that utilize filtering algorithms. Under this motivation, this thesis primarily focuses on PSSE algorithms for improving the performance of power system networks. Moreover, since the duration of completing the thesis work witnessed the deadly outbreak of Covid-19, as a scientific responsibility, the author decided to utilize the knowledge of filtering algorithms in fight against Covid-19. With this motivation, this thesis also utilizes filtering algorithms for developing an efficient ESE method for effectively monitoring the spread of Covid-19.

In real-life PSSE design applications, traditional Gaussian filters have been extended with forecasting techniques to compute complex power system network process models in a generalized function form. Fortunately, existing nonlinear filters are adequately accurate for general real-life applications, with minimal measurement irregularities. However, measurement irregularities can severely compromise the accuracy of filtering algorithms, which limits their practical applicability.

To discuss the contribution of developing ESE methods for efficient monitoring of Covid-19 spread, it should be mentioned that the ESE methods are composed of a compartment-based epidemic model, and an advanced estimation method. Thus, this thesis is motivated to introduce an advanced compartment-based epidemic model and subsequently, Gaussian filter is implemented to efficiently estimate the compartmental populations. It should be mentioned that an efficient ESE helps in accurate modeling of epidemic spread, which further helps in framing efficient administrative policies for containing the spread of the epidemic, such as the Covid-19.

8.2 Conclusion

- The linear Kalman filter is redesigned to efficiently address the simultaneously occurring delayed measurements and non-Gaussian noises. It utilizes the maximum correntropy-based design criterion for handling non-Gaussian noises.
- An advanced nonlinear Gaussian filtering method, abbreviated as GFDF, is developed for handling cyber-attacks (FDI attacks) and delayed measurements

simultaneously. The proposed GFDF uses geometric and Bernoulli random variables to characterize the delay and FDI attack.

- The significance of efficient PSSE methods are well discussed in Chapter 1 and 2 for efficient and reliable power delivery. With this motivation, Chapter 5 introduced a new PSSE, the FACQKF-based PSSE method. The proposed FACQKF-based PSSE method improves the accuracy as compared to the existing PSSE methods, which are mainly based on the EKF, UKF, and CKF. However, the improved accuracy comes at the cost of marginally increased computational demand.
- An efficient, computationally effective, and reliable power system state estimator is essential for stable power distribution with the rise of DERs. In this regard, Chapter 6 introduces a further advanced Gaussian filter-based PSSE method named FSMCGF-based PSSE method. In Gaussian filtering, the CKF method is adopted due to its higher estimation accuracy, stability, and computational storage requirement. The proposed FSMCCKF-based PSSE method eliminates various drawbacks of typical PSSE methods, including the ambiguous approximation of unknown process models, inefficacy in handling non-Gaussian outliers, inefficacy in handling unknown time-varying noises, and temporal sensor failure.
- We propose a diversified epidemic model, SEIRRPV, which considers various disease impacting parameters. The model's existence, uniqueness, boundness, boundary values, and local and global stability are validated mathematically. A CKF-based ESE is applied to estimate disease transmission in Delhi from January to April 2021. Analysis suggests improving healthcare infrastructure and increasing vaccination efforts can help contain outbreaks.

8.3 Future Research Scope

Following the contributions of this thesis, some future research scopes are as follows:

- This thesis, particularly Chapter 3, introduced the concept of simultaneously handling more than one measurement irregularities, including the delay and non-Gaussian noises. The future research scope may be to handle more than two irregularities simultaneously.
- The filtering algorithm designed in Chapter 4 requires some pre-processing of data to ensure that the FDI attack can be compensated with an appropriate Gaussian PDF. Such pre-processing ultimately requires various assumptions and approximations, which often influence the accuracy adversely. In future research, the proposed method can be extended further to relax the need for such data pre-processing.
- The PSSE algorithm designed in Chapter 5 can be extended further to implement particle filter based PSSE for distributed networks. Depending on the application, state dynamics may be complex or unknown. Therefore, machine learning or deep learning techniques can be useful to identify these dynamics, and the above solutions can also be applied to unknown dynamics.
- Chapter 6, introduces the concept of simultaneously handling irregularities, including the noise adaptive and non-Gaussian noises in power systems. The future research scope may be to handle other irregularities, such as intermittently missing and delayed measurements.

Appendix A

Simplifying Eq. (3.23) in terms of Eq.

(3.27)

Let us expand $(\mathcal{W}_{(r^*,j^*)}^T \boldsymbol{\vartheta}_{(r^*,j^*)}^{t-1} \mathcal{W}_{(r^*,j^*)})^{-1}$ and $(\mathcal{W}_{(r^*,j^*)}^T \boldsymbol{\vartheta}_{(r^*,j^*)}^{t-1} \mathcal{D}_{(r^*,j^*)})$. To expand $(\mathcal{W}_{(r^*,j^*)}^T \boldsymbol{\vartheta}_{(r^*,j^*)}^{t-1} \mathcal{W}_{(r^*,j^*)})^{-1}$, we rewrite $\mathcal{W}_{(r^*,j^*)}$ given in Eq. (3.18) by substituting $\mathbf{S}_{(r^*,j^*)|(k)}$ from Eq. (3.16). Then, given $\boldsymbol{\vartheta}_{(r^*,j^*)} = \text{diag}(\boldsymbol{\vartheta}_{(r^*,j^*)}^x, \boldsymbol{\vartheta}_{(r^*,j^*)}^y)$ and the resulting $\mathcal{W}_{(r^*,j^*)}$ expression, we obtain $(\mathcal{W}_{(r^*,j^*)}^T \boldsymbol{\vartheta}_{(r^*,j^*)}^{t-1} \mathcal{W}_{(r^*,j^*)})^{-1}$ in the form of Eq. (A.1).

$$\begin{aligned} \left(\mathcal{W}_{(r^*,j^*)}^T \boldsymbol{\vartheta}_{(r^*,j^*)}^{t-1} \mathcal{W}_{(r^*,j^*)} \right)^{-1} &= \left((\mathbf{S}_{(r^*,j^*)|(k)}^{pT})^{-1} \boldsymbol{\vartheta}_{(r^*,j^*)}^{y^{t-1}} (\mathbf{S}_{(r^*,j^*)|(k)}^p)^{-1} + \mathcal{H}_{(r^*,j^*)}^T (\mathbf{S}_{(r^*,j^*)|(k)}^{rT})^{-1} \right. \\ &\quad \left. \boldsymbol{\vartheta}_{(r^*,j^*)}^{x^{t-1}} (\mathbf{S}_{(r^*,j^*)|(k)}^r)^{-1} \mathcal{H}_{(r^*,j^*)} \right)^{-1}. \end{aligned} \quad (\text{A.1})$$

To further simplify Eq. (A.1), let us consider the following notations

$$\begin{cases} A = (\mathbf{S}_{(r^*,j^*)|(k)}^{pT})^{-1} \boldsymbol{\vartheta}_{(r^*,j^*)}^{x^{t-1}} (\mathbf{S}_{(r^*,j^*)|(k)}^p)^{-1}, & C = \mathcal{H}_{(r^*,j^*)}^T \\ D = (\mathbf{S}_{(r^*,j^*)|(k)}^{rT})^{-1} \boldsymbol{\vartheta}_{(r^*,j^*)}^{y^{t-1}} (\mathbf{S}_{(r^*,j^*)|(k)}^r)^{-1}, & E = \mathcal{H}_{(r^*,j^*)} \end{cases} \quad (\text{A.2})$$

Considering Woodbury matrix identity, $(A + CDE)^{-1} = A^{-1} - A^{-1}C(D^{-1} + EA^{-1}C)^{-1}$

EA^{-1} , which gives $(\mathcal{W}_{(r^*,j^*)}^T \boldsymbol{\vartheta}_{(r^*,j^*)}^{t-1} \mathcal{W}_{(r^*,j^*)})^{-1}$ expression in the form of Eq. (A.3).

$$\begin{aligned} & \left(\mathcal{W}_{(r^*,j^*)}^T \boldsymbol{\vartheta}_{(r^*,j^*)}^{t-1} \mathcal{W}_{(r^*,j^*)} \right)^{-1} = \mathbf{S}_{(r^*,j^*)|(k)}^p (\boldsymbol{\vartheta}_{(r^*,j^*)}^{x^{t-1}})^{-1} \mathbf{S}_{(r^*,j^*)|(k)}^{pT} - \mathbf{S}_{(r^*,j^*)|(k)}^p (\boldsymbol{\vartheta}_{(r^*,j^*)}^{x^{t-1}})^{-1} \mathbf{S}_{(r^*,j^*)|(k)}^{pT} \\ & \mathcal{H}_{(r^*,j^*)}^T \left(\mathbf{S}_{(r^*,j^*)|(k)}^r (\boldsymbol{\vartheta}_{(r^*,j^*)}^{y^{t-1}})^{-1} \mathbf{S}_{(r^*,j^*)|(k)}^{rT} + \mathcal{H}_{(r^*,j^*)} \mathbf{S}_{(r^*,j^*)|(k)}^p (\boldsymbol{\vartheta}_{(r^*,j^*)}^{x^{t-1}})^{-1} \mathbf{S}_{(r^*,j^*)|(k)}^{pT} \mathcal{H}_{(r^*,j^*)}^T \right)^{-1} \\ & \mathcal{H}_{(r^*,j^*)} \mathbf{S}_{(r^*,j^*)|(k)}^p (\boldsymbol{\vartheta}_{(r^*,j^*)}^{x^{t-1}})^{-1} \mathbf{S}_{(r^*,j^*)|(k)}^{pT}. \end{aligned} \quad (\text{A.3})$$

To obtain $\mathcal{W}_{(r^*,j^*)}^T \boldsymbol{\vartheta}_{(r^*,j^*)}^{t-1} \mathcal{D}_{(r^*,j^*)}$, let us rewrite $\mathcal{D}_{(r^*,j^*)}$ by substituting $\mathbf{S}_{(r^*,j^*)|(k)}$ from Eq. (3.16) into Eq. (3.17) and expressed as

$$\mathcal{D}_{(r^*,j^*)} = \begin{bmatrix} (\mathbf{S}_{(r^*,j^*)|(k)}^p)^{-1} \hat{\mathbf{x}}_{(r^*,j^*)|(k-1)} \\ (\mathbf{S}_{(r^*,j^*)|(k)}^p)^{-1} (\mathbf{y}_k - \mathcal{H}_{(r^*,j^*)} \hat{\mathbf{x}}_{(r^*,j^*)|(k-1)}) \end{bmatrix}. \quad (\text{A.4})$$

Then, for the resulting expression of $\mathcal{D}_{(r^*,j^*)}$, $\mathcal{W}_{(r^*,j^*)}$, and $\boldsymbol{\vartheta}_{(r^*,j^*)}^{t-1}$, we get $\mathcal{W}_{(r^*,j^*)}^T \boldsymbol{\vartheta}_{(r^*,j^*)}^{t-1} \mathcal{D}_{(r^*,j^*)}$ in the form of Eq. (A.5).

$$\begin{aligned} \mathcal{W}_{(r^*,j^*)}^T \boldsymbol{\vartheta}_{(r^*,j^*)}^{t-1} \mathcal{D}_{(r^*,j^*)} &= (\mathbf{S}_{(r^*,j^*)|(k)}^{pT})^{-1} \boldsymbol{\vartheta}_{(r^*,j^*)}^{x^{t-1}} (\mathbf{S}_{(r^*,j^*)|(k)}^p)^{-1} \hat{\mathbf{x}}_{(r^*,j^*)|(k-1)} + \mathcal{H}_{(r^*,j^*)}^T (\mathbf{S}_{(r^*,j^*)|(k)}^{rT})^{-1} \\ & \boldsymbol{\vartheta}_{(r^*,j^*)}^{y^{t-1}} (\mathbf{S}_{(r^*,j^*)|(k)}^r)^{-1} (\boldsymbol{\varepsilon}_{k|k-1}^y). \end{aligned} \quad (\text{A.5})$$

To this end, substituting $(\mathcal{W}_{(r^*,j^*)}^T \boldsymbol{\vartheta}_{(r^*,j^*)}^{t-1} \mathcal{W}_{(r^*,j^*)})^{-1}$ and $(\mathcal{W}_{(r^*,j^*)}^T \boldsymbol{\vartheta}_{(r^*,j^*)}^{t-1} \mathcal{D}_{(r^*,j^*)})$ from Eqs. (A.3) and (A.5), respectively into Eq. (3.23), we obtain the desired $\hat{\mathbf{x}}_{(r^*,j^*)|(k-1)}^t$ in the form of Eq. (3.27) for $\bar{\mathbf{K}}_{(r^*,j^*)}$, $\bar{\mathbf{P}}_{(r^*,j^*)|(k-1)}^{t-1}$, and $\bar{\mathbf{R}}_{(r^*,j^*)}^{t-1}$ given in Eqs. (3.28), (3.30), and (3.31), respectively.

Appendix B

Simplifying Eq. (6.15) in terms of Eq. (6.17)

Extending Appendix A for nonlinear system and replacing \mathcal{H} , (r^*, j^*) , respectively with non-linear measurement slope Γ_k , and $k - 1$. Eq. (6.15) is simplified using Eq. (6.21) as

$$\mathcal{D}_{(r^*, j^*)} = \begin{bmatrix} (\mathbf{S}_{(r^*, j^*)|^{(k)}}^p)^{-1} \hat{\mathbf{x}}_{(r^*, j^*)|^{(k-1)}} \\ (\mathbf{S}_{(r^*, j^*)|^{(k)}}^p)^{-1} (\boldsymbol{\varepsilon}_{k|k-1}^y + \Gamma_k \hat{\mathbf{x}}_{k|k-1}) \end{bmatrix}. \quad (\text{B.1})$$

Subsequently, Appendix A is followed to get Eq. (6.17).

Appendix C

Analytical steps of filtering

Sample points and Weights:

Compute the deterministic sample points and weights using numerical approximation method: ξ_j and $\mathbf{W}_j \forall i \in \{1, 2, \dots, N_s\}$.

Prediction:

- Determine the Cholesky decomposition of initial error covariance

$$\mathbf{P}_{k-1|k-1} = \Sigma_{k-1|k-1} \Sigma_{k-1|k-1}^T,$$

where $\Sigma_{k-1|k-1} = \text{chol}(\mathbf{P}_{k-1|k-1}, \text{lower})$

- Compute the transformed sampling points

$$\zeta_{i,k-1|k-1} = \Sigma_{k-1|k-1} \xi_j + \hat{\mathbf{x}}_{k-1|k-1}$$

- Propagate $\zeta_{i,k-1|k-1}$ through process model

$$\zeta_{i,k-1|k-1}^* = \phi_{k-1}(\zeta_{i,k-1|k-1}).$$

- Estimate the predicated mean

$$\hat{\mathbf{x}}_{k|k-1} = \sum_{j=1}^{N_s} \mathbf{W}_j \zeta_{i,k-1|k-1}^*.$$

- Compute the predicated error covariance

$$\mathbf{P}_{k|k-1} = \sum_{j=1}^{N_s} \mathbf{W}_j \zeta_{i,k-1|k-1}^* \zeta_{i,k-1|k-1}^{*T} - \hat{\mathbf{x}}_{k|k-1} \hat{\mathbf{x}}_{k|k-1}^T + \mathbf{Q}_k.$$

Update:

- Determine the Cholesky decomposition of predicted error covariance

$$\mathbf{P}_{k-1|k} = \Sigma_{k-1|k} \Sigma_{k-1|k}^T,$$

$$\text{where } \Sigma_{k-1|k} = \text{chol}(\mathbf{P}_{k-1|k}, \text{lower})$$

- Compute the transformed sample points

$$\zeta_{i,k|k-1} = \Sigma_{k|k-1} \xi_j + \hat{\mathbf{x}}_{k|k-1}$$

- Propagate $\zeta_{i,k|k-1}$ through measurement model

$$\zeta_{i,k|k-1}^* = \Psi_k(\zeta_{i,k|k-1})$$

- Compute the predicted measurement

$$\hat{\mathbf{y}}_{k|k-1} = \sum_{j=1}^{N_s} \mathbf{W}_j \zeta_{i,k|k-1}^*$$

- Compute the innovation error covariance

$$\mathbf{P}_{k|k-1}^{\mathbf{y}\mathbf{y}} = \sum_{i=1}^{N_s} \mathbf{W}_j \zeta_{i,k|k-1}^* \zeta_{i,k|k-1}^{*T} - \hat{\mathbf{y}}_{k|k-1} \hat{\mathbf{y}}_{k|k-1}^T + \mathbf{R}_k$$

- Compute the cross-covariance

$$\mathbf{P}_{k|k-1}^{\mathbf{x}\mathbf{y}} = \sum_{i=1}^{N_s} \mathbf{W}_j \zeta_{i,k|k-1} \zeta_{i,k|k-1}^{*T} - \hat{\mathbf{x}}_{k|k-1} \hat{\mathbf{y}}_{k|k-1}^T$$

- Determine the Kalman gain

$$\mathbf{K}_k = \mathbf{P}_{k|k-1}^{\mathbf{x}\mathbf{y}} (\mathbf{P}_{k|k-1}^{\mathbf{y}\mathbf{y}})^{-1}$$

- Compute the updated estimate of state

$$\hat{\mathbf{x}}_{k|k} = \hat{\mathbf{x}}_{k|k-1} + \mathbf{K}_k (\mathbf{y}_k - \hat{\mathbf{y}}_{k|k-1})$$

- Compute the updated error covariance of state

$$\mathbf{P}_{k|k} = \mathbf{P}_{k|k-1} - \mathbf{K}_k \mathbf{P}_{k|k-1}^{\mathbf{y}\mathbf{y}} \mathbf{K}_k^T$$

Appendix D

Innovation and residual covariance

D.1 Innovation covariance

Using Eqs. (1.1), (1.2), (6.5) and (6.8), the covariance of innovation is expressed as

$$\begin{aligned} \mathbb{E}[\boldsymbol{\varepsilon}_{k|k-1}^y \boldsymbol{\varepsilon}_{k|k-1}^{yT}] &= \mathbb{E}[(\Gamma_k \boldsymbol{\varepsilon}_{k|k-1}^x + \mathcal{V}_k)(\Gamma_k \boldsymbol{\varepsilon}_{k|k-1}^x + \mathcal{V}_k)^T] = \Gamma_k \mathbf{P}_{k|k-1} \Gamma_k^T \\ &\quad + \mathbf{R}_k \Rightarrow \mathbf{R}_k = \mathbb{E}[\boldsymbol{\varepsilon}_{k|k-1}^y \boldsymbol{\varepsilon}_{k|k-1}^{yT}] - \Gamma_k \mathbf{P}_{k|k-1} \Gamma_k^T, \quad (\text{D.1}) \end{aligned}$$

where $\boldsymbol{\varepsilon}_{k|k-1}^y$ and \mathcal{V}_k are uncorrelated.

D.2 Residual covariance

Using Eqs. (1.1), (1.2), (6.5) and (6.8) and using basic rules as $\hat{\mathbf{x}}_{k|k-1}$, $\boldsymbol{\varepsilon}_{k|k-1}^y$ and \mathcal{V}_k are uncorrelated, the simplified terms are :

$$\left\{ \begin{aligned} \mathbb{E}[\Gamma_k \boldsymbol{\varepsilon}_{k|k}^x \mathcal{V}_k^T] &= -\Gamma_k \mathbb{E}[\hat{\mathbf{x}}_{k|k} \mathcal{V}_k^T] = -\Gamma_k \mathbb{E}[(\hat{\mathbf{x}}_{k|k-1} + \mathbf{K}_k(\Gamma_k \boldsymbol{\varepsilon}_{k|k-1}^y + \mathcal{V}_k)) \mathcal{V}_k^T] \\ &= -\Gamma_k \mathbb{E}[\hat{\mathbf{x}}_{k|k-1} \mathcal{V}_k^T + \mathbf{K}_k \Gamma_k \boldsymbol{\varepsilon}_{k|k-1}^y \mathcal{V}_k^T + \mathbf{K}_k \mathcal{V}_k \mathcal{V}_k^T] = -\Gamma_k \mathbf{K}_k \mathbf{R}_k, \\ \mathbb{E}[\mathcal{V}_k \boldsymbol{\varepsilon}_{k|k}^x \Gamma_k^T] &= \mathbb{E}[\Gamma_k \boldsymbol{\varepsilon}_{k|k}^x \mathcal{V}_k^T]^T = -(\Gamma_k \mathbf{K}_k \mathbf{R}_k)^T = -\mathbf{R}_k \mathbf{K}_k^T \Gamma_k^T, \\ \Gamma_k \mathbf{P}_{k|k} \Gamma_k^T - \Gamma_k \mathbf{K}_k \mathbf{R}_k &= \Gamma_k (\mathbb{I} - \mathbf{K}_k \Gamma_k) \mathbf{P}_{k|k-1} \Gamma_k^T - \Gamma_k \mathbf{K}_k \mathbf{R}_k = \Gamma_k \mathbf{P}_{k|k-1} \Gamma_k^T - \Gamma_k \mathbf{K}_k \Gamma_k \\ &\quad \mathbf{P}_{k|k-1} \Gamma_k^T - \Gamma_k \mathbf{K}_k \mathbf{R}_k = \Gamma_k \mathbf{P}_{k|k-1} \Gamma_k^T - \Gamma_k \mathbf{P}_{k|k-1} \Gamma_k^T \mathbf{P}_{k|k-1}^{\text{yy}^{-1}} \mathbf{P}_{k|k-1}^{\text{yy}} = 0, \end{aligned} \right. \quad (\text{D.2})$$

thus, the residual covariance is simplified as

$$\begin{aligned}
\mathbb{E} \left[\boldsymbol{\varepsilon}_{k|k}^y \boldsymbol{\varepsilon}_{k|k}^{yT} \right] &= \mathbb{E} \left[(\Gamma_k \boldsymbol{\varepsilon}_{k|k}^x + \mathcal{V}_k) (\Gamma_k \boldsymbol{\varepsilon}_{k|k}^x + \mathcal{V}_k)^T \right] + \mathbf{R}_k = \Gamma_k \mathbf{P}_{k|k} \Gamma_k^T + \mathbb{E} \left[\Gamma_k \boldsymbol{\varepsilon}_{k|k}^x \mathcal{V}_k^T \right] \\
&+ \mathbb{E} \left[\mathcal{V}_k^T \Gamma_k \boldsymbol{\varepsilon}_{k|k}^{xT} \right] + \mathbf{R}_k = \Gamma_k \mathbf{P}_{k|k} \Gamma_k^T - \Gamma_k \mathbf{K}_k \mathbf{R}_k - \mathbf{R}_k \mathbf{K}_k^T \Gamma_k^T + \mathbf{R}_k = \mathbf{R}_k - \Gamma_k \mathbf{P}_{k|k} \Gamma_k^T.
\end{aligned}
\tag{D.3}$$

Bibliography

- [1] Robert Grover Brown, Patrick YC Hwang, et al. *Introduction to random signals and applied Kalman filtering*, volume 3. Wiley New York, 1992.
- [2] Yaakov Bar-Shalom, X Rong Li, and Thiagalingam Kirubarajan. *Estimation with applications to tracking and navigation: theory algorithms and software*. John Wiley & Sons, 2004.
- [3] Rudolph Emil Kalman. A new approach to linear filtering and prediction problems. *Journal of Basic Engineering*, 82(1):35–45, 1960.
- [4] Ali Abur and Antonio Gomez Exposito. *Power system state estimation: theory and implementation*. CRC press, 2004.
- [5] Alcir Monticelli. Electric power system state estimation. *Proceedings of IEEE Instruments Electrical Electronics Engineering*, 88(2):262–282, 2000.
- [6] William Ogilvy Kermack and Anderson G McKendrick. A contribution to the mathematical theory of epidemics. *Proceedings of the Royal Society A: Mathematical, Physical and Engineering Sciences*, 115(772):700–721, 1927.
- [7] Antonio Gomez-Exposito, Jose A Rosendo-Macias, and Miguel A Gonzalez-Cagigal. Monitoring and tracking the evolution of a viral epidemic through nonlinear Kalman filtering: Application to the Covid-19 case. *IEEE Journal of Biomedical Health Informatics*, 26(4):1441–1452, 2021.
- [8] Rajiv Ramaswami, Kumar Sivarajan, and Galen Sasaki. *Optical networks: a practical perspective*. Morgan Kaufmann, 2009.

- [9] Yun Fei, Tao Meng, and Zhonghe Jin. Nano satellite attitude determination with randomly delayed measurements. *Acta Astronautica*, 185:319–332, 2021.
- [10] Kebina Manandhar, Xiaojun Cao, Fei Hu, and Yao Liu. Detection of faults and attacks including false data injection attack in smart grid using Kalman filter. *IEEE Transactions on Control Network Systems*, 1(4):370–379, 2014.
- [11] Omid Sayadi and Mohammad Bagher Shamsollahi. ECG denoising and compression using a modified extended Kalman filter structure. *IEEE Transactions on Biomedical Engineering*, 55(9):2240–2248, 2008.
- [12] SY Chen. Kalman filter for robot vision: a survey. *IEEE Transactions on Industrial Electronics*, 59(11):4409–4420, 2011.
- [13] Rohit Rana, Vijyant Agarwal, Prerna Gaur, and Harish Parthasarathy. Design of optimal UKF state observer–controller for stochastic dynamical systems. *IEEE Transactions on Industry Applications*, 57(2):1840–1859, 2020.
- [14] Xiaolin Ning, Fan Wang, and Jiancheng Fang. An implicit UKF for satellite stellar refraction navigation system. *IEEE Transactions on Aerosp. Electronics Systems*, 53(3):1489–1503, 2017.
- [15] Ramaprasad Bhar. *Stochastic filtering with applications in finance*. World Scientific, 2010.
- [16] Federico Cassola and Massimiliano Burlando. Wind speed and wind energy forecast through Kalman filtering of numerical weather prediction model output. *Applied Energy*, 99:154–166, 2012.
- [17] Brian DO Anderson and John B Moore. *Optimal filtering*. Courier Corporation, 2012.
- [18] Simon S Haykin. *Kalman filtering and neural networks*, volume 284. Wiley Online Library, 2001.

- [19] Raman Mehra. Approaches to adaptive filtering. *IEEE Transactions on Automatic Control*, 17(5):693–698, 1972.
- [20] Bin Jia and Ming Xin. *Grid-based nonlinear estimation and its applications*. CRC Press, 2019.
- [21] Shovan Bhaumik and Paresh Date. *Nonlinear estimation: methods and applications with deterministic Sample Points*. CRC Press, 2019.
- [22] Badong Chen, , Yu Zhu, Jinchun Hu, and Jose C Principe. *System parameter identification: information criteria and algorithms*. Newnes, 2013.
- [23] Saleem A Kassam. *Signal detection in non-Gaussian noise*. Springer Science & Business Media, 2012.
- [24] Derui Ding, Qing-Long Han, Yang Xiang, Xiaohua Ge, and Xian-Ming Zhang. A survey on security control and attack detection for industrial cyber-physical systems. *Neurocomputing*, 275:1674–1683, 2018.
- [25] Wenli Duo, MengChu Zhou, and Abdullah Abusorrah. A survey of cyber attacks on cyber physical systems: Recent advances and challenges. *IEEE/CAA Journal of Automatica Sinica*, 9(5):784–800, 2022.
- [26] Izhak Rubin. An approximate time-delay analysis for packet-switching communication networks. *IEEE Transactions on Communications*, 24(2):210–222, 1976.
- [27] Rachana Ashok Gupta and Mo-Yuen Chow. Networked control system: Overview and research trends. *IEEE Transactions on Industrial Electronics*, 57(7):2527–2535, 2009.
- [28] Ramin Esmzad and Reza Mahboobi Esfanjani. Bayesian filter for nonlinear systems with randomly delayed and lost measurements. *Automatica*, 107:36–42, 2019.

- [29] Andrew H Jazwinski. *Stochastic processes and filtering theory*. Courier Corporation, 2007.
- [30] Abhinoy Kumar Singh. Major development under Gaussian filtering since unscented Kalman filter. *IEEE/CAA Journal of Automatica Sinica*, In press.
- [31] Zhe Chen. Bayesian filtering: From Kalman filters to particle filters, and beyond. *Statistics*, 182(1):1–69, 2003.
- [32] Shanmou Chen, Qiangqiang Zhang, Dongyuan Lin, and Shiyuan Wang. A class of nonlinear Kalman filters under a generalized measurement model with false data injection attacks. *IEEE Sig. Proc. Lett.*, 29:1187–1191, 2022.
- [33] Abhinoy Kumar Singh, Sumit Kumar, Nagendra Kumar, and Rahul Radhakrishnan. Bayesian approximation filtering with false data attack on network. *IEEE Transactions on Aerosp. Electronics Systems*, 58(2):976–988, 2021.
- [34] Yang Meng, Shesheng Gao, Yongmin Zhong, Gaoge Hu, and Aleksandar Subic. Covariance matching based adaptive unscented Kalman filter for direct filtering in INS/GNSS integration. *Acta Astronautica*, 120:171–181, 2016.
- [35] Badong Chen et al. Maximum correntropy Kalman filter. *Automatica*, 76:70–77, 2017.
- [36] Badong Chen, Lujuan Dang, Yuantao Gu, Nanning Zheng, and José C Príncipe. Minimum error entropy Kalman filter. *IEEE Transactions on Systems, Man, and Cybernetics: Systems*, 51(9):5819–5829, 2019.
- [37] Lyuzerui Yuan, Jie Gu, Honglin Wen, and Zhijian Jin. Improved particle filter for non-Gaussian forecasting-aided state estimation. *Journal of Modern Power Systems and Clean Energy*, 2022.
- [38] Shuchang Zhou, , Yujin Wang, Tingting Zhu, and Liming Xia. CT features of coronavirus disease 2019 (Covid-19) Pneumonia in 62 patients in Wuhan, China. *American Journal of Roentgenology*, 214(6):1287–1294, 2020.

- [39] Caifang Zheng, Weihao Shao, Xiaorui Chen, Bowen Zhang, Gaili Wang, and Weidong Zhang. Real-world effectiveness of Covid-19 vaccines: a literature review and meta-analysis. *International Journal of Infectious Disease*, 114:252–260, 2022.
- [40] Mukhtar Ahmad. *Power system state estimation*. Artech house, 2013.
- [41] Fred C Schweppe and J Wildes. Power system static-state estimation, part i: Exact model. *IEEE Transactions on Power Appar. Systems*, (1):120–125, 1970.
- [42] Fred C Schweppe and Douglas B Rom. Power system static-state estimation, part ii: Approximate model. *IEEE Transactions on Power Appar. Systems*, (1):125–130, 1970.
- [43] Fred C Schweppe. Power system static-state estimation, part iii: Implementation. *IEEE Transactions on Power Appar. Systems*, (1):130–135, 1970.
- [44] Sung-Kwan Joo, Jang-Chul Kim, and Chen-Ching Liu. Empirical analysis of the impact of 2003 blackout on security values of us utilities and electrical equipment manufacturing firms. *IEEE Transactions on Power Systems*, 22(3):1012–1018, 2007.
- [45] Vahid Madani. Western interconnection experience with phasor measurements. In *2006 IEEE PES Power Systems Conf. and Exposit.*, pages 343–352. IEEE, 2006.
- [46] Lingling Fan and Yasser Wehbe. Extended Kalman filtering based real-time dynamic state and parameter estimation using PMU data. *Elec. Power Systems Research*, 103:168–177, 2013.
- [47] George N Korres and Nikolaos M Manousakis. State estimation and bad data processing for systems including PMU and SCADA measurements. *Electrical Power Systems Research*, 81(7):1514–1524, 2011.
- [48] A Sharma, Suresh Chandra Srivastava, and Saikat Chakrabarti. A cubature

- Kalman filter based power system dynamic state estimator. *IEEE Transactions on Instrumentation and Measurement*, 66(8):2036–2045, 2017.
- [49] Gustavo Valverde and Vladimir Terzija. Unscented Kalman filter for power system dynamic state estimation. *IET Generation, Transmission & Distribution*, 5(1):29–37, 2011.
- [50] MultiMedia LLC. Covid-19 coronavirus pandemic, 2021.
- [51] Mygov. Covid-19 coronavirus pandemic, 2021.
- [52] Surindra Suthar, Sukanya Das, Nagpure, et al. Epidemiology and diagnosis, environmental resources quality and socio-economic perspectives for Covid-19 pandemic. *Journal of Environmental Management*,, 280:111700, 2021.
- [53] KM Ariful Kabir, Kazuki Kuga, and Jun Tanimoto. Analysis of SIR epidemic model with information spreading of awareness. *Chaos, Solitons & Fractals*, 119:118–125, 2019.
- [54] Agus Hasan and and others Susanto, Hadi. A new estimation method for Covid-19 time-varying reproduction number using active cases. *Scientific reports*, 12(1):1–9, 2022.
- [55] Md Shariful Islam, Md Enamul Hoque, and Mohammad Ruhul Amin. Integration of Kalman filter in the epidemiological model: a robust approach to predict Covid-19 outbreak in Bangladesh. *International Journal of Modern Physics*, 32(08):2150108, 2021.
- [56] Erik Cuevas. An agent-based model to evaluate the Covid-19 transmission risks in facilities. *Computers in Biology and Medicine*, 121:103827, 2020.
- [57] Jonatan Almagor and Stefano Picascia. Exploring the effectiveness of a Covid-19 contact tracing app using an agent-based model. *Scientific reports*, 10(1):1–11, 2020.

- [58] Martin CJ Bootsma and Neil M Ferguson. The effect of public health measures on the 1918 Influenza pandemic in US cities. *Proceedings of the National Academy of Sciences*, 104(18):7588–7593, 2007.
- [59] MR Sidi Ammi and M Tahiri. Study of transmission dynamics of Covid-19 virus using fractional model: case of Morocco. In *Analysis of Infectious disease problems (Covid-19) and their global impact*. Springer (2021) 617–627.
- [60] Reza Sameni. Mathematical modeling of epidemic diseases; a case study of the Covid-19 coronavirus. *ArXiv:2003.11371*, 2020.
- [61] Wei Yang, Chengjun Sun, and Julien Arino. Global analysis for a general epidemiological model with vaccination and varying population. *Journal of Math. Analysis and Application*, 372(1):208–223, 2010.
- [62] Zhen Zhao, Peter Xiaoping Liu, and Jinfeng Gao. Model-based fault diagnosis methods for systems with stochastic process—a survey. *Neurocomputing*, 2022.
- [63] Simon J Julier and Jeffrey K Uhlmann. New extension of the Kalman filter to nonlinear systems. In *Signal Processing, Sensor Fusion, and Target Recognition VI*, volume 3068, pages 182–194. International Society Optical Photonics, 1997.
- [64] Ienkaran Arasaratnam and Simon Haykin. Cubature Kalman filters. *IEEE Transactions on Automatic Control*, 54(6):1254–1269, 2009.
- [65] Ienkaran Arasaratnam, Simon Haykin, and Robert J Elliott. Discrete-time nonlinear filtering algorithms using Gauss–Hermite quadrature. *Proc. IEEE*, 95(5):953–977, 2007.
- [66] Inam Ullah, Siyu Qian, Zhixiang Deng, and Jong-Hyouk Lee. Extended Kalman filter-based localization algorithm by edge computing in wireless sensor networks. *Digital Communications and Networks*, 7(2):187–195, 2021.
- [67] Zheng Chen, Yuhong Fu, and Chunting Chris Mi. State of charge estimation of

- lithium-ion batteries in electric drive vehicles using extended Kalman filtering. *IEEE Transactions on Veh. Technol.*, 62(3):1020–1030, 2012.
- [68] Xinyue Li and Ralph Kennel. General formulation of Kalman-filter-based online parameter identification methods for VSI-fed PMSM. *IEEE Transactions on Industrial Electronics*, 68(4):2856–2864, 2020.
- [69] Shubhendra Vikram Singh Chauhan and Grace Xingxin Gao. Spoofing resilient state estimation for the power grid using an extended Kalman filter. *IEEE Transactions on Smart Grid*, 12(4):3404–3414, 2021.
- [70] James McNames and Mateo Aboy. Statistical modeling of cardiovascular signals and parameter estimation based on the extended Kalman filter. *IEEE Transactions on Biomedical Engineering*, 55(1):119–129, 2007.
- [71] Vangelis P Oikonomou et al. The use of Kalman filter in biomedical signal processing. *Kalman Filter: Recent Advances and Application*, 2009.
- [72] Paul Hamelmann, Rik Vullings, Massimo Mischi, Alexander F Kolen, Lars Schmitt, and Jan WM Bergmans. An extended Kalman filter for fetal heart location estimation during doppler-based heart rate monitoring. *IEEE Transactions on Instr. and Meas.*, 68(9):3221–3231, 2018.
- [73] Xinhe Zhu, Bingbing Gao, Yongmin Zhong, Chengfan Gu, and Kup-Sze Choi. Extended Kalman filter based on stochastic epidemiological model for Covid-19 modelling. *Computers in Biology and Medicine*, 137:104810, 2021.
- [74] Paolo Di Giamberardino and Daniela Iacoviello. Early estimation of the number of hidden hiv infected subjects: An extended Kalman filter approach. *Infectious Diseases Modelling*, 2023.
- [75] Vahid Azimi, Mojtaba Sharifi, Seyed Fakoorian, Thang Nguyen, and Van Van Huynh. State estimation-based robust optimal control of influenza epidemics in an interactive human society. *Information Sciences*, 592:340–360, 2022.

- [76] Michael Athans, Richard Wishner, and Anthony Bertolini. Suboptimal state estimation for continuous-time nonlinear systems from discrete noisy measurements. *IEEE Transactions on Automatic Control*, 13(5):504–514, 1968.
- [77] Manoranjan Majji, John L Junkins, and James D Turner. A high order method for estimation of dynamic systems. *Journal of Astronautical Sciences*, 56(3):401–440, 2008.
- [78] Y. J. Zhang and Z. Geng. Detection of target maneuver from bearings-only measurements. *IEEE Transactions on Aerosp. Electronics Systems*, 49(3):2028–2034, July 2013.
- [79] Maral Partovibakhsh and Guangjun Liu. An adaptive unscented Kalman filtering approach for online estimation of model parameters and state-of-charge of Lithium-ion batteries for autonomous mobile robots. *IEEE Transactions on Control Systems Technology*, 23(1):357–363, 2014.
- [80] Junjian Qi, Kai Sun, Jianhui Wang, and Hui Liu. Dynamic state estimation for multi-machine power system by unscented Kalman filter with enhanced numerical stability. *IEEE Transactions on Smart Grid*, 9(2):1184–1196, 2016.
- [81] Mahmoud El-Gohary and James McNames. Human joint angle estimation with inertial sensors and validation with a robot arm. *IEEE Transactions on Biomedical Engineering*, 62(7):1759–1767, 2015.
- [82] Vasileios E Papageorgiou and George Tsaklidis. An improved epidemiological-unscented Kalman filter (hybrid SEIHCRDV-UKF) model for the prediction of Covid-19. application on real-time data. *Chaos, Solitons & Fractals*, 166:112914, 2023.
- [83] Shovan Bhaumik et al. Cubature quadrature Kalman filter. *IET Signal Processing*, 7(7):533–541, 2013.
- [84] Shovan Bhaumik and Swati. Square-root cubature-quadrature Kalman filter. *Asian Journal of Control*, 16(2):617–622, 2014.

- [85] Abhinoy Kumar Singh and Shovan Bhaumik. Transformed cubature quadrature Kalman filter. *IET Signal Processing*, 11(9):1095–1103, 2017.
- [86] Shiyuan Wang, Jiuchao Feng, and K Tse Chi. Spherical simplex-radial cubature Kalman filter. *IEEE Signal Processing Lett.*, 21(1):43–46, 2013.
- [87] Zhaoming Li and Wenge Yang. Spherical simplex-radial cubature quadrature Kalman filter. *Journal of Electrical and Computer Engineering*, 2017, 2017.
- [88] Abhinoy Kumar Singh. Exponentially fitted cubature Kalman filter with application to oscillatory dynamical systems. *IEEE Transactions on Circuits and Systems I: Regul. Papers*, 67(8):2739–2752, 2020.
- [89] Abhinoy Kumar Singh, Mihailo V Rebec, and Ahmad Haidar. Kalman-based calibration algorithm for agamatrix continuous glucose monitoring system. *IEEE Transactions on Control Systems Technol.*, 29(3):1257–1267, 2020.
- [90] Rahul Radhakrishnan, Abhinoy Kumar Singh, Shovan Bhaumik, and Nutan Kumar Tomar. Quadrature filters for underwater passive bearings-only target tracking. In *Sensor Signal Processing for Defence (SSPD)*, pages 1–5. IEEE, 2015.
- [91] Selma Zoljic-Beglerovic, Georg Stettinger, Bernd Lubert, and Martin Horn. Railway suspension system fault diagnosis using cubature Kalman filter techniques. *IFAC-PapersOnLine*, 51(24):1330–1335, 2018.
- [92] Zheng Liu, Xuanju Dang, Benqin Jing, and Jianbo Ji. A novel model-based state of charge estimation for lithium-ion battery using adaptive robust iterative cubature Kalman filter. *Electrical Power Systems Research*, 177:105951, 2019.
- [93] Bin Jia, Ming Xin, and Yang Cheng. Sparse-grid quadrature nonlinear filtering. *Automatica*, 48(2):327–341, 2012.
- [94] Abhinoy Kumar Singh, Rahul Radhakrishnan, Shovan Bhaumik, and Paresh Date. Adaptive sparse-grid Gauss–Hermite filter. *Journal of Comput. Applied Math.*, 342:305–316, 2018.

- [95] Jenkaran Arasaratnam and Simon Haykin. Square-root quadrature Kalman filtering. *IEEE Transactions on Signal Processing*, 56(6):2589–2593, 2008.
- [96] Hermann Singer. Generalized Gauss–Hermite filtering. *AStA Advances in Statistical Analysis*, 92(2):179–195, 2008.
- [97] Rahul Radhakrishnan, Abhinoy Kumar Singh, Shovan Bhaumik, and Nutan Kumar Tomar. Multiple sparse-grid Gauss–Hermite filtering. *Applied Math. Modelling*, 40(7-8):4441–4450, 2016.
- [98] Xiao Lu, Huanshui Zhang, Wei Wang, and Kok-Lay Teo. Kalman filtering for multiple time-delay systems. *Automatica*, 41(8):1455–1461, 2005.
- [99] B Chen, L Yu, and W-A Zhang. Robust Kalman filtering for uncertain state delay systems with random observation delays and missing measurements. *IET Control Theory & Application*, 5(17):1945–1954, 2011.
- [100] Maryam Moayedi, Yung K Foo, and Yeng C Soh. Adaptive Kalman filtering in networked systems with random sensor delays, multiple packet dropouts and missing measurements. *IEEE Transactions on Signal Processing*, 58(3):1577–1588, 2009.
- [101] Ziyi Liu, Yingting Luo, and Yunmin Zhu. State estimation for linear dynamic system with multiple-step random delays using high-order Markov chain. *IEEE Access*, 8:76218–76227, 2020.
- [102] Xiao Lu, Huanshui Zhang, Wei Wang, and Kok-Lay Teo. Kalman filtering for multiple time-delay systems. *Automatica*, 41(8):1455–1461, 2005.
- [103] Xiao Lu, Lihua Xie, Huanshui Zhang, and Wei Wang. Robust Kalman filtering for discrete-time systems with measurement delay. *IEEE Transactions on Circuits & Systems II: Express Briefs*, 54(6):522–526, 2007.
- [104] Aurora Hermoso-Carazo and Josefa Linares-Pérez. Extended and unscented

- filtering algorithms using one-step randomly delayed observations. *Applied Math. Comp.*, 190(2):1375–1393, 2007.
- [105] Abhinoy Kumar Singh, Shovan Bhaumik, and Paresh Date. Quadrature filters for one-step randomly delayed measurements. *Applied Math. Mod.*, 40(19-20):8296–8308, 2016.
- [106] A Hermoso-Carazo and J Linares-Pérez. Unscented filtering algorithm using two-step randomly delayed observations in nonlinear systems. *Applied Math. Comp.*, 33(9):3705–3717, 2009.
- [107] Abhinoy Kumar Singh, Shovan Bhaumik, and Paresh Date. A modified Bayesian filter for randomly delayed measurements. *IEEE Transactions on Automatic Control*, 62(1):419–424, 2016.
- [108] Abhinoy Kumar Singh, Paresh Date, and Shovan Bhaumik. New algorithm for continuous-discrete filtering with randomly delayed measurements. *IET Control Theory and Application*, 10(17):2298–2305, 2016.
- [109] Svante Björklund. *A survey and comparison of time-delay estimation methods in linear systems*. PhD thesis, Dept. of EE, Linköpings universitet, SE-581, 83 Linköping, Sweden, 2003.
- [110] Stanislav Talaš and Vladimír Bobál. Predictive control adapting to fractional values of time delay. *Mathematical Problems in Engineering*, 2018, 2018.
- [111] Abhinoy Kumar Singh. Fractionally delayed Kalman filter. *IEEE/CAA Journal of Automatica Sinica*, 7(1):169–177, 2019.
- [112] Vimal Bhatia, Bernard Mulgrew, and Apostolos T Georgiadis. Stochastic gradient algorithms for equalisation in α -stable noise. *Signal Processing*, 86(4):835–845, 2006.
- [113] Vimal Bhatia and Bernard Mulgrew. Non-parametric likelihood based channel estimator for Gaussian mixture noise. *Sig. Proces.*, 87(11):2569–2586, 2007.

- [114] Jose C Principe. *Information theoretic learning: Renyi's entropy and Kernel perspectives*. Springer-Verlag, New york, 2010.
- [115] Xi Liu, Hua Qu, Jihong Zhao, and Badong Chen. Extended Kalman filter under maximum correntropy criterion. In *2016 International Joint Conference on Neural Networks (IJCNN)*, pages 1733–1737. IEEE, 2016.
- [116] Zhiyu Zhang, Jinzhe Qiu, and Wentao Ma. Adaptive extended Kalman filter with correntropy loss for robust power system state estimation. *Entropy*, 21(3):293, 2019.
- [117] Shanmou Chen et al. Robust state estimation with maximum correntropy rotating geometric unscented Kalman filter. *IEEE Transactions on Instrument and Measurement*, 71:1–14, 2021.
- [118] Jingjing He, Changku Sun, Baoshang Zhang, and Peng Wang. Maximum correntropy square-root cubature Kalman filter for non-Gaussian measurement noise. *IEEE access*, 8:70162–70170, 2020.
- [119] Xi Liu, Hua Qu, Jihong Zhao, and Pengcheng Yue. Maximum correntropy square-root cubature Kalman filter with application to SINS/GPS integrated systems. *ISA Transactions*, 80:195–202, 2018.
- [120] Wutao Qin, Xiaogang Wang, and Naigang Cui. Maximum correntropy sparse Gauss–Hermite quadrature filter and its application in tracking ballistic missile. *IET Radar, Sonar and Navigation*, 11(9):1388–1396, 2017.
- [121] Yu Liu, Hong Wang, and Chaohuan Hou. UKF based nonlinear filtering using minimum entropy criterion. *IEEE Transactions on Signal Processing*, 61(20):4988–4999, 2013.
- [122] Lujian Dang, Badong Chen, Yulong Huang, Yonggang Zhang, and Haiquan Zhao. Cubature Kalman filter under minimum error entropy with fiducial points for INS/GPS integration. *IEEE/CAA Journal of Automatica Sinica*, 9(3):450–465, 2021.

- [123] Jiacheng He, Gang Wang, Huijun Yu, JunMing Liu, and Bei Peng. Generalized minimum error entropy Kalman filter for non-Gaussian noise. *ISA Transactions on*, 2022.
- [124] Wentao Ma, Peng Guo, Xiaofei Wang, Zhiyu Zhang, Siyuan Peng, and Badong Chen. Robust state of charge estimation for li-ion batteries based on cubature Kalman filter with generalized maximum correntropy criterion. *Energy*, 260:125083, 2022.
- [125] Haiquan Zhao and Boyu Tian. Robust power system forecasting-aided state estimation with generalized maximum mixture correntropy unscented Kalman filter. *IEEE Transactions on Instr. and Meas.*, 71:1–10, 2022.
- [126] Arpan Chattopadhyay and Urbashi Mitra. Security against false data injection attack in cyber-physical systems. *IEEE Transactions on Control Network Systems*, 2019.
- [127] Dan Zhang, Qing-Guo Wang, Gang Feng, Yang Shi, and Athanasios V Vasilakos. A survey on attack detection, estimation and control of industrial cyber-physical systems. *ISA Transactions on*, 116:1–16, 2021.
- [128] Shuai Liu, Guoliang Wei, Yan Song, and Yurong Liu. Extended Kalman filtering for stochastic nonlinear systems with randomly occurring cyber attacks. *Neurocomputing*, 207:708–716, 2016.
- [129] Yan Liu and Guang-Hong Yang. Event-triggered distributed state estimation for cyber-physical systems under dos attacks. *IEEE Transactions on Cybernetics*, 52(5):3620–3631, 2022.
- [130] Wei Ao, Yongduan Song, and Changyun Wen. Distributed secure state estimation and control for cps under sensor attacks. *IEEE Transactions on Cybernetics*, 50(1):259–269, 2020.

- [131] Robert E Larson, William F Tinney, and John Peschon. State estimation in power systems part i: Theory and feasibility. *IEEE Transactions on Power Appar. Systems*, (3):345–352, 1970.
- [132] Robert E Larson, William F Tinney, Laszlo P Hajdu, and Dean S Piercy. State estimation in power systems part ii: Implementation and applications. *IEEE Transactions on Power Appar. Systems*, (3):353–363, 1970.
- [133] Felix F Wu. Power system state estimation: a survey. *International Journal of Electrical Power & Energy Systems*, 12(2):80–87, 1990.
- [134] AM Leite Da Silva, MB Do Coutto Filho, and JF De Queiroz. State forecasting in electric power systems. In *IEE Proc. C (Generation, Transmission & Distribution)*, volume 130, pages 237–244. IET, 1983.
- [135] Ankush Sharma, SC Srivastava, and S Chakrabarti. Testing and validation of power system dynamic state estimators using real time digital simulator (RTDS). *IEEE Transactions on Power Systems*, 31(3):2338–2347, 2015.
- [136] Vedik Basetti, Ashwani Kumar Chandel, and Chandan Kumar Shiva. Square-root cubature Kalman filter based power system dynamic state estimation. *Sustainable Energy, Grids and Networks*, 31:100712, 2022.
- [137] Mingming Song et al. Adaptive Kalman filters for nonlinear finite element model updating. *Mechanical Systems and Signal Processing*, 143:106837, 2020.
- [138] Yi Wang et al. Adaptive robust cubature Kalman filter for power system dynamic state estimation against outliers. *IEEE Access*, 7:105872–105881, 2019.
- [139] Shahrokh Akhlaghi, Ning Zhou, and Zhenyu Huang. Adaptive adjustment of noise covariance in Kalman filter for dynamic state estimation. In *2017 IEEE Power & Ener. Society General Meeting*, pages 1–5, 2017. IEEE.
- [140] Lujuan Dang, Badong Chen, Shiyuan Wang, Wentao Ma, and Pengju Ren. Robust power system state estimation with minimum error entropy unscented

- Kalman filter. *IEEE Transactions on Instrumentation and Measurement*, 69(11):8797–8808, 2020.
- [141] Jialu Song, Hujin Xie, Bingbing Gao, Yongmin Zhong, Chengfan Gu, and Kup-Sze Choi. Maximum likelihood-based extended Kalman filter for Covid-19 prediction. *Chaos, Soliton & Fractal*, 146:110922, 2021.
- [142] Marino Gatto, Enrico Bertuzzo, et al. Spread and dynamics of the Covid-19 epidemic in Italy: Effects of emergency containment measures. *Proc. Nat. Acad. Sc.*, 117(19):10484–10491, 2020.
- [143] Shuli Sun. Optimal linear filters for discrete-time systems with randomly delayed and lost measurements with/without time stamps. *IEEE Transactions on Automatic Control*, 58(6):1551–1556, 2012.
- [144] Abhinoy Kumar Singh, Paresh Date, and Shovan Bhaumik. A modified Bayesian filter for randomly delayed measurements. *IEEE Tran. Auto. Contr.*, 62(1):419–424, 2016.
- [145] Rangeet Mitra and Vimal Bhatia. Minimum error entropy criterion based channel estimation for massive-MIMO in VLC. *IEEE Transactions on Vehicular Technology*, 68(1):1014–1018, 2018.
- [146] Kursad Fevzi Tuncer. Non-Gaussian noise. Technical report, NASA, Washington, D.C, May 1970. progress report no.: 135-102.
- [147] Xiaoxu Wang, Yan Liang, Quan Pan, and Chunhui Zhao. Gaussian filter for nonlinear systems with one-step randomly delayed measurements. *Automatica*, 49(4):976–986, 2013.
- [148] Jhon A Isaza, Hector A Botero, and Hernan Alvarez. State estimation using non-uniform and delayed information: A review. *International Journal of Automation Computing*, 15(2):125–141, 2018.

- [149] Uday Kumar Singh, Rangeet Mitra, Vimal Bhatia, and Amit Kumar Mishra. Kernel LMS-based estimation techniques for radar systems. *IEEE Transactions on Aerospace & Electronic Systems*, 55(5):2501–2515, 2019.
- [150] Matthew P Wand and William R Schucany. Gaussian-based Kernels. *Canadian Journal of Statistics*, 18(3):197–204, 1990.
- [151] Ali Tajer. False data injection attacks in electricity markets by limited adversaries: Stochastic robustness. *IEEE Transactions on Smart Grid*, 10(1):128–138, 2017.
- [152] André Teixeira, Iman Shames, Henrik Sandberg, and Karl Henrik Johansson. A secure control framework for resource-limited adversaries. *Automatica*, 51:135–148, 2015.
- [153] Konrad Reif, Stefan Gunther, Engin Yaz, and Rolf Unbehauen. Stochastic stability of the discrete-time extended Kalman filter. *IEEE Transactions on Automatic Control*, 44(4):714–728, 1999.
- [154] Brian DO Anderson and John B Moore. *Optimal filtering*. Courier Corporation, 2012.
- [155] Amit Kumar Naik, Guddu Kumar, Prabhat Kumar Upadhyay, Paresh Date, and Abhinoy Kumar Singh. Gaussian filtering for simultaneously occurring delayed and missing measurements. *IEEE Access*, 10:100746–100762, 2022.
- [156] Guddu Kumar, Sumanta Kumar Nanda, Alok Kumar Verma, Vimal Bhatia, and Abhinoy Kumar Singh. Nonlinear Gaussian filtering with network-induced delay in measurements. *IEEE Transactions on Aerospace and Electronic Systems*, pages 1–7, 2022.
- [157] Abhinoy Kumar Singh, Sumit Kumar, Nagendra Kumar, and Rahul Radhakrishnan. Bayesian approximation filtering with false data attack on network. *IEEE Transactions on Aero. Elect. Systems*, 58(2):976–988, 2021.

- [158] Guddu Kumar, Paresh Date, Ram Bilas Pachori, R Swaminathan, and Abhinoy Kumar Singh. Wrapped particle filtering for angular data. *IEEE Access*, 10:90287–90298, 2022.
- [159] Abhinoy Kumar Singh. Szegő quadrature Kalman filter for oscillatory systems. *IEEE Access*, 8:194700–194708, 2020.
- [160] Vedik Basetti, Ashwani K Chandel, and Rajeevan Chandel. Power system dynamic state estimation using prediction based evolutionary technique. *Energies*, 107:29–47, 2016.
- [161] Zhaoyang Jin, Junbo Zhao, Lei Ding, Saikat Chakrabarti, Elena Gryazina, and Vladimir Terzija. Power system anomaly detection using innovation reduction properties of iterated extended Kalman filter. *International Journal of Electrical Power & Energy Systems*, 136:107613, 2022.
- [162] BK Saha Roy, AK Sinha, and AK Pradhan. An optimal PMU placement technique for power system observability. *International Journal of Electrical Power & Energy System*, 42(1):71–77, 2012.
- [163] Gustavo Valverde and Vladimir Terzija. Unscented Kalman filter for power system dynamic state estimation. *IET Generation, Transmission & Distribution*, 5(1):29–37, 2010.
- [164] Yi Wang et al. Robust forecasting-aided state estimation for power system against uncertainties. *IEEE Transactions on Power Systems*, 35(1):691–702, 2019.
- [165] Dapeng Wang, Hai Zhang, and Baoshuang Ge. Adaptive unscented Kalman filter for target tracking with time-varying noise covariance based on multi-sensor information fusion. *Sensors*, 21(17):5808, 2021.
- [166] Sumanta Kumar Nanda, Guddu Kumar, Vimal Bhatia, and Abhinoy Kumar Singh. Kalman filtering with delayed measurements in non-Gaussian environments. *IEEE Access*, 9:123231–123244, 2021.

- [167] Xi Liu, Zhigang Ren, Hongqiang Lyu, Zhihong Jiang, Pengju Ren, and Badong Chen. Linear and nonlinear regression-based maximum correntropy extended Kalman filtering. *IEEE Transactions on Systems, Man, and Cybernetics: Systems*, 51(5):3093–3102, 2019.
- [168] Rodrigo Astroza, Andrés Alessandri, and Joel P Conte. A dual adaptive filtering approach for nonlinear finite element model updating accounting for modeling uncertainty. *Mechanical Systems and Signal Processing*, 115:782–800, 2019.
- [169] Ali Almagbile, Jinling Wang, and Weidong Ding. Evaluating the performances of adaptive Kalman filter methods in GPS/INS integration. *Journal of Global Positioning Systems*, 9(1):33–40, 2010.
- [170] Paolo Di Giamberardino and Daniela Iacoviello. Evaluation of the effect of different policies in the containment of epidemic spreads for the Covid-19 case. *Biomedical Signal Processing & Control*, 65:102325, 2021.
- [171] Corentin Briat and Erik I Verriest. A new delay-SIR model for pulse vaccination. *Biomedical Signal Processing & Control*, 4(4):272–277, 2009.
- [172] C Treesatayapun. Epidemic model dynamics and fuzzy neural-network optimal control with impulsive traveling and migrating: Case study of Covid-19 vaccination. *Biomedical Signal Processing & Control*, 71:103227, 2022.
- [173] Giulia Giordano, Marta Colaneri, Alessandro Di Filippo, et al. Modeling vaccination rollouts, SARS-CoV-2 variants and the requirement for non-pharmaceutical interventions in italy. *Nature Medicine*, 27(6):993–998, 2021.
- [174] Marek B Trawicki. Deterministic SEIRs epidemic model for modeling vital dynamics, vaccinations, and temporary immunity. *Math.*, 5(1):7, 2017.
- [175] Julien Arino and Pauline Van Den Driessche. The basic reproduction number in a multi-city compartmental epidemic model. In *Positive Systems*. Springer (2003) 135–142.

- [176] Mahaveer Golechha. Covid-19 containment in Asia's largest urban slum Dharavi-Mumbai, India: Lessons for policy-makers globally. *Journal of Urban Health*, 97(6):796–801, 2020.
- [177] Adam K Wheatley, Juno, et al. Evolution of immune responses to SARS-CoV-2 in mild-moderate Covid-19. *Nature communications*, 12(1):1–11, 2021.
- [178] Ingrid Arevalo-Rodriguez, Buitrago, et al. False-negative results of initial RT-PCR assays for Covid-19: a systematic review. *PloS one*, 15(12):E0242958, 2020.
- [179] M. O. Oke, O. M. Ogunmiloro, et al. Mathematical modeling and stability analysis of a SIRV epidemic model with non-linear force of infection and treatment. *Communications in Mathematics and Applications*, 10(4):717–731, 2019.
- [180] Subhas Khajanchi, Sovan Bera, and Tapan Kumar Roy. Mathematical analysis of the global dynamics of a HTLV-I infection model, considering the role of cytotoxic T-lymphocytes. *Mathematics and Computers in Simulation*, 180:354–378, 2021.
- [181] Sovan Bera, Subhas Khajanchi, and Tapan Kumar Roy. Dynamics of an HTLV-I infection model with delayed CTLs immune response. *Applied Mathematics Computation*, 430:127206, 2022.
- [182] Stefania Ottaviano, Mattia Sensi, and Sara Sottile. Global stability of SAIRS epidemic models. *Nonlinear Analysis: Real World Application*, 65:103501, 2022.
- [183] Michael Y. Li and James S. Muldowney. On R.A. Smith's Autonomous Convergence Theorem. *The Rocky Mountain Journal of Mathematics*, 25(1):365 – 378, 1995.
- [184] Joseph P La Salle. *The stability of dynamical systems*. SIAM, 1976.
- [185] Ienkaran Arasaratnam, Simon Haykin, and Thomas R Hurd. Cubature Kalman filtering for continuous-discrete systems: theory and simulations. *IEEE Transactions on Signal Processing*, 58(10):4977–4993, 2010.

- [186] Abhinoy Kumar Singh and Shovan Bhaumik. Higher degree cubature quadrature Kalman filter. *International Journal of Control, Automation & Systems*, 13(5):1097–1105, 2015.
- [187] AH Stroud. Approximate calculation of multiple integrals. Prentice-Hall series in Automatic Computation. 1971.
- [188] Shengxin Li, Bo Xu, Lianzhao Wang, and Asghar A Razzaqi. Improved maximum correntropy cubature Kalman filter for cooperative localization. *IEEE Sensor*, 20(22):13585–13595, 2020.